ON THREE-DIMENSIONAL HYDRODYNAMIC NUMERICAL MODELLING OF WIND INDUCED FLOWS IN STABLY STRATIFIED WATERS: A GALERKIN-FINITE DIFFERENCE APPROACH

by

Kyung Tae Jung,

M.Sc., Seoul National University, Seoul.

Thesis submitted for the degree of

Doctor of Philosophy

in the

Department of Applied Mathematics

University of Adelaide

May 1989

TABLE OF CONTENTS

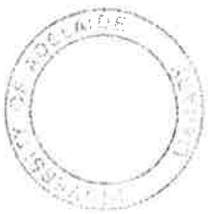

SUMMARY

The work presented in this thesis is concerned with the development of a linear three-dimensional hydrodynamic numerical model for wind induced flow in stably stratified flat-bottomed lakes or seas. The perturbed motion is assumed small and deepening of the interfaces under wind action is ignored. The vertical dependence of horizontal currents is determined using Galerkin methods, whereas a finite difference method is used for the integration in time and the horizontal spatial coordinates. Two types of basis functions are taken into consideration: B-spline functions (Galerkin-finite element method) and numerically determined eigenfunctions (Galerkin-spectral method).

The proposed Galerkin models can accommodate an arbitrary variation in the vertical eddy viscosity within each layer. Across the interface the eddy viscosity profile can be chosen to be either continuous or discontinuous.

Two types of interfacial conditions are examined. The first is that the horizontal velocities and shear stresses are continuous across the interface and the second is that of zero-stress (used by Heaps, 1966, Phil. Trans. Roy. Soc., Ser. A, **259**, 391–416). The condition of continuous horizontal velocities and shear stresses requires only one set of basis functions, whereas the stress-free condition effectively decouples the system into two parts, and hence requires two independent sets of basis functions.

The model performances are demonstrated for the Ekman problems with stratification. Steady state and time dependent responses of an unbounded sea, subject to the impulsive onset of wind stress, are computed using a point model. For the study of inertial motion subject to the local wind stress, a two-layer model composed of the surface layer and the pycnocline is proposed.

The methods are also applied to investigate the transient response of an ide-

alised narrow lake of uniform depth subject to the impulsive onset of wind. Time-dependent behaviour of internal vertical displacements and their convergence rates are compared for the one and two domain systems.

SIGNED STATEMENT

This thesis contains no material which has been accepted for the award of any other degree or diploma in any University and, to the best of my knowledge and belief, the thesis contains no material previously published or written by another person, except where due reference is made in the text. I consent to the thesis being made available for photocopying and loan.

Kyung Tae Jung.

ACKNOWLEDGEMENTS

I wish to thank my supervisor, Dr. J. Noye, for suggestions and help with the writing of this thesis. It is my pleasure to extend my grateful thanks to Dr. A.M. Davies who gave valuable advice on the details of Galerkin models, made his work available to me prior to printing, and helped me in various ways during the course of this study.

This thesis owes much to a number of people. Mr. M. Oxenham who read the manuscript thoroughly, found errors and improved immeasurably the content of the thesis. I am also grateful to his friendship. Mr. J. Nixon was always willing to help me. His comments and prompt reading were very much helpful in completing this thesis. Special thanks are due to Mr. P. Thorpe who read my earlier writings with patience. I would like to thank Mr. D. Beard for his *unlimited* support with respect to computing and also his friendship. I am also grateful to a number of people for helping me through this ordeal: To Mr. P. Bills, Mr. T. Davidson, Mr. G. Furnell, Mr. A. Larsson, Mr. G. Noone, Ms. D. Lucic, and Drs. A. Dixon, D. Hill and T. Marchant. I also wish to acknowledge the financial assistance provided during the part of my candidature in the form of a University of Adelaide Scholarship.

CHAPTER 1

INTRODUCTION

1.1 A survey of previous work

Over the past fifteen years the development of three-dimensional hydrodynamic numerical models for coastal and shelf environments has greatly accelerated. With the rapid growth of computing power it has become computationally realistic to solve the full set of governing hydrodynamic equations with respect to time and the three spatial coordinates. Typically, there have been two approaches used for integrating the governing equations over the horizontal space domain, namely finite difference and finite element methods.

The three-dimensional models diversify according to the way in which the vertical dependence of the hydrodynamic variables are represented. It is becoming increasingly evident that the numerical models cannot be classified by simple guide-lines. Nevertheless, it seems appropriate, for the purposes of this thesis, to classify the models into four groups: the Ekman-type model, the multilayered model, the finite difference grid model and the Galerkin-function model. No attempt will be made to discuss the first three models in detail. However, since the model to be described in this thesis is a mixture of the multilayered and Galerkin-function models, we do include a few comments outlining the salient features of each of these models, along with a few representative examples. The Ekman-type model is basically an extension of the work of Welander (1957). Many researchers have favoured this analytical approach for the purpose of obtaining physical insight into the dynamic characteristics of the system in three dimensions. For detailed

accounts of these approaches, see Cheng *et al.* (1976) and Simons (1980).

In the multilayered models the vertical fluid space is represented by a stack of immiscible discrete layers, within each layer the density being taken as constant. Each layer acts as a stream tube and only exchange of momentum can take place between the layers via interfacial stresses. Essentially, these models are analogous to a super-position of layer-averaged two-dimensional models. Some of the papers on layered models include: O'Brien and Hulburt (1972), McNider and O'Brien (1973), Abbott *et al.* (1975), Wang and Connor (1975), D'Alessio *et al.* (1983) and Preller (1986),

While numerical investigations in three-dimensions continue to use multilayered models, a great deal of effort has also been directed towards the development of numerical models based on finite difference approximations. In these finite difference grid models the vertical space is partitioned into a set of vertical grid boxes. Consequently the hydrodynamic equations are represented in finite difference form using the variables defined at the vertical grid-points. In contrast to the layered model the fluid is allowed to move through the vertical grid boxes. In order to represent turbulent mixing of physical properties, most models use the familiar eddy diffusion hypothesis. More recently, three-dimensional models have used high level turbulence closure schemes to dynamically calculate the turbulence intensity; in the majority of studies made thus far, finite difference grid models have been employed. Work on these models has been done by: Leendertse *et al.* (1973, 1977), Simon (1973), Bennett (1977), Blumberg and Mellor (1980), Noye *et al.* (1981), Sheng (1982), Davies (1985*c*) and Noye and Stevens (1986). These finite difference grid models can be grouped in various ways. Such considerations, however, are beyond the scope of the present discussion. For a detailed account of the fixed grid box and σ-transformed grid box models, see Davies and Stephens (1983).

Alternatives to the above numerical approaches include the Galerkin-function models which have increasingly attracted interest as valuable tools for investigation of coastal and shelf dynamics. In these methods the structure of horizontal components of the current in the vertical are represented by horizontally and time varying undetermined coefficients together with depth varying functions (basis functions). Application of the well-known Galerkin procedure (Fletcher, 1984) to the hydrodynamic equations yields a system of coupled equations for the expansion coefficients. These equations coupled with the continuity equation and appropriate lateral boundary conditions can be solved using any standard numerical method, for which finite difference methods have been overwhelmingly chosen up to now. Having determined the expansion coefficients, the continuous profiles of horizontal currents can be reproduced. The Galerkin-function models are mainly characterised by the nature of their basis functions, that is, according to whether the basis functions are defined either *locally* or *globally* and whether the basis functions are eigenfunctions of the vertical diffusivity operator or not. In the following review of Galerkin-function models our attention is directed to the choice of basis functions.

Heaps (1972) was the among the first to develop a mixed approach by combining the spectral expansion in the vertical direction and a standard hydrodynamic finite difference model in the horizontal plane. In essence, the method uses eigenfunctions of the vertical diffusivity operator as the basis functions. The spectral basis is sought by the requirement that each eigenfunction satisfies the homogeneous Neumann condition at the sea surface and the bottom boundary condition term by term. Consequently a linear friction law is required and eigenvalues and eigenfunctions become dependent upon the eddy viscosity and the bottom friction coefficient. Clarke (1974) has shown that such restrictions can be relaxed by incorporating the bottom boundary condition as a natural boundary condition which permits one to use nonlinear quadratic friction. Heaps' approach differs from the

usual finite-dimensional approximations in that a technique known as *completion of the expansion to the infinity* is applied to ensure the exact satisfaction of the surface boundary condition. In theory, Heaps' formulation does not restrict the form of the vertical eddy viscosity. However, since the eigenvalue problem is solved analytically, the eddy viscosity profile takes a simple functional form. In a series of works Heaps has refined the spectral model for applications to tides, wind-induced flows and density currents in Irish seas (Heaps, 1973, 1974; Heaps and Jones, 1975, 1977).

In the context of the Ekman-type model, that is, with the use of a constant eddy viscosity profile and a no-slip bottom boundary condition, two earlier contributions have been noted which resemble in spirit the Galerkin-function models. Yampol'skii (1966) used a Fourier cosine expansion to represent the vertical dependence of wind drift currents in a horizontally unbounded homogeneous sea. For wind induced flows in a bounded homogeneous basin of uniform depth, Liggett (1969) developed an Ekman-type three-dimensional model using Fourier cosine transforms in the vertical direction. The rigid-lid approximation imposed at the sea surface naturally leads to a second-order elliptic equation for pressure distribution which is solved at each time step by a finite difference method to estimate pressure gradients at the horizontal grid-points.

Studies have since been focused on the development of Galerkin-function models which are capable of handling arbitrary variation of the eddy viscosity with a more general set of basis functions as well as nonlinear effects. Cosine functions have been a popular choice even in the presence of external stresses at the sea surface. Cooper and Pearce (1977) and Pearce and Cooper (1981) used a mixed basis set which is composed of a set of cosine series and prescribed auxiliary functions. The auxiliary function was taken to be a linear combination of cubic polynomials and logarithmic functions. This was used in order to improve the convergence of

cosine series solutions near the sea surface, particularly with the use of an eddy viscosity profile which decreases near the sea surface. The bottom boundary condition was incorporated in a way similar to Heaps' approach. Koutitas (1978) has developed a three-dimensional tidal model which involves nonlinear advection and horizontal turbulent diffusion terms. Nonlinear effects associated with the free sea surface elevation are, however, neglected. Davies (1980*a*) has presented a Galerkin formulation which incorporates the surface and bottom stress conditions as natural boundary conditions. The advantage of this formulation is that each term in the expansion of continuous functions is not constrained to satisfy the stress boundary conditions, and subsequently the bottom boundary condition can take a non-linear form. Using a quadratic bottom friction the models have been applied to investigate tide and wind induced circulation in the North Sea and North-West European Shelf (Davies, 1980*c*, 1981*b*; Davies and Furnes, 1980; Davies and James, 1983). The extension of the Galerkin models to nonlinear hydrodynamic equations involving advective terms and a nonlinear free surface variation has been given by Davies (1980*b*). Wolf (1983) has developed a fully nonlinear three-dimensional model involving advective and horizontal diffusion terms. In an attempt to improve the efficiency of the model, particularly when high spatial resolution is required, the fast-moving gravity wave terms are treated by the Alternating Direction implicit scheme and the other terms, including friction, advection and diffusion, are treated explicitly. The investigations conducted by Davies and James (1983) and Proctor (1987) are also based on nonlinear Galerkin models with a basis set of cosine functions.

Developments of the Galerkin-function model with basis sets of Chebyshev and Legendre polynomials have been pursued as important alternatives to the use of cosine series (Davies and Owen, 1979; Owen, 1980; Gordon, 1982). Investigations conducted by Davies and Owen (1979) in idealised basins have shown that Chebyshev and Legendre polynomials, which are in fact eigenfunctions of singu-

lar Sturm-Liouville boundary value problems (Higgins, 1977), rapidly converge throughout the water column and are particularly suited to wind-induced flows in homogeneous seas. For the no-slip bottom boundary condition, odd Chebyshev and Legendre polynomials are chosen to exactly satisfy the essential constraint. Owen (1980) chose Legendre polynomials as a basis set in developing a three-dimensional non-linear hydrodynamic model which takes into account the continuous stratification through a Richardson number-dependent eddy viscosity and a slip condition at the sea bed. Gordon (1982) used a time-splitting algorithm in which the internal modes associated with baroclinic flow are integrated with a significantly longer time step than the external mode associated with barotropic flow. By reformulating the hydrodynamic equations at the outset into barotropic and baroclinic sets, Davies (1982*a*) has shown that a splitting algorithm can be applied with an arbitrary set of basis functions. An alternative to these approaches is using a basis set of eigenfunctions.

Although numerous applications of these classical polynomials can be found in various disciplines and their properties are well known, use of such a general basis set is disadvantageous in that physical insight into the vertical structure of a particular system cannot be readily inferred a general basis set. For that, the eigenfunction method is best suited, particularly when the vertical structure of the eddy viscosity profile is fixed. Using a spectral expansion of the horizontal currents through the vertical, Nihoul (1977) developed a transformation technique of extracting current profiles from a two-dimensional model. Legendre polynomials of even order are taken as a basis set of eigenfunctions with the choice of a parabolic eddy viscosity profile. In continuing his earlier analytical approach, Heaps (1981) developed a two-layered spectral method to improve the representation of the bottom frictional layer in tidal flows. The local forms of the eigenfunctions within each layer are derived first and are then matched at the interface by the requirement that the eigenfunctions and their derivatives must be continuous. This method

has been extended further to a three-layered stratified system in which the eigenfunctions are defined continuously throughout the depth but, due to the jump in the values of density and eddy viscosity at the interfaces, their derivatives are discontinuous (Heaps, 1983). Subsequently, the spectral models based on the *mode matching technique* have been applied to investigate the dynamic response to wind pulse forcings of idealised shelf seas with uniform and cross-shelf depth variation (Heaps and Jones, 1983; 1985). For continuously stratified seas of non-uniform depth, van Foreest and Brundit (1982) have developed a Galerkin-based mixed approach using the normal mode expansion over the vertical space and a finite difference approximation in time and over the horizontal plane. Wind stress has been incorporated as a body force acting over the mixed surface layer. Heaps (1984) has presented a full account of normal mode solutions for continuously stratified flat-bottomed seas in which the vertical eddy viscosity is assumed to be inversely proportional to the static stability and the linear bottom friction is related to the velocity at the sea bed. The modal model developed by Furnes and Mork (1987) employs a two-layered representation of the density profile. These models all include the variation of the free sea surface, whereas the modal ocean models (for example, McCreary, 1981) usually assume the rigid-lid approximation at the sea surface.

An extension of the analytical eigenfunction approaches for handling arbitrary variation of the vertical eddy viscosity in homogeneous seas has been established by Davies (1983*c*) and Furnes (1983) in different ways. In solving an eigenvalue problem numerically, Davies (1983*c*) has used a Galerkin method with a basis set of the fourth-order B-spline functions. In the Furnes' approach the eigensystem has been solved using the Runge-Kutta-Merson method. Although the essence of the method is mainly numerical, the analytic feature has been endowed by means of a mode matching technique. Local forms of eigenfunctions have been taken as Bessel functions by approximating the arbitrary eddy viscosity profile as

a sequence of composite-linear piecewise profiles. Comparison between the two approaches has shown that from the point of view of accuracy, the Runge-Kutta-Merson method has an advantage over the Galerkin method in that errors arising in the solution procedure can be monitored (Davies and Furnes, 1986). It should be mentioned that Davies' approach is based on a direct matrix operation, whereas Furnes' approach is based on iteration. To improve the slow convergence of the eigenfunction expansion at the sea surface, the *stressing* of boundary constraints has been introduced by Furnes (1983) and Davies (1983*b*), which results in a coupled system of equations for the expansion coefficients.

In parallel with the development of such global approaches as the above, considerable efforts have also been made to enable the employment of a local basis set. In a series of studies conducted by Davies (1977*a*,*b*,*c*, 1978*a*,*b*, 1982*b*, 1983*a*, 1985*a*) fourth-order B-spline functions are exclusively used. The advantage of using high-order B-spline functions is demonstrated by solving Burger's equation and by reproducing the propagation of gravity waves with various combinations of boundary conditions (Davies, 1978*a*,*b*). In earlier models Davies (1977*b*,*c*) has used the Galerkin-collocation method so that each term in the expansion of B-spline functions satisfies the boundary constraints exactly and hence integrating by parts is not necessary. The Galerkin method has been applied to continuously stratified seas with a basis set of B-spline functions (Davies, 1982*b*, 1983*a*). The arbitrary continuous variation of density and eddy viscosity is allowed and, neglecting diffusion of density, the internal displacement is introduced as a new prime variable. Two basis sets are additionally required to expand the continuous variation of internal displacement and density in the vertical direction.

Attempts to represent the vertical space in terms of a piecewise linear basis set have also been made (Koutitas and O'Connor, 1980*a*,*b*; Lynch and Werner, 1987). Koutitas and O'Connor (1980*a*) represent a horizontal space using the fi-

nite difference approximation in a way similar to Davies and incorporate nonlinear advective terms in the equations of motion. The models developed by Koutitas and O'Connor (1980*b*) and Lynch and Werner (1987) employ triangular finite elements for the horizontal plane. The solutions in all spatial dimensions are then obtained using a finite element model, but these models may still be regarded as mixed models in that the vertical space is represented in a layered fashion, that is, using locally one-dimensional finite elements. Koutitas and O'Connor (1980*b*) employed a fractional time stepping method in which diffusion and advection-propagation processes are evaluated at different time levels, while Lynch and Werner (1987) separate the time dependence from the spatial dependence of the motion, assuming that the solutions are periodic in time, and solve the Helmholtz-type equation for the surface elevation. Laible (1980) developed a mixed model in which the horizontal space is represented in terms of nine-node quadrilateral isoparametric finite elements and the vertical space is represented by continuous cubic polynomials with two undetermined coefficients. In a subsequent study the model was extended to a two-layer version (Laible, 1982).

It is known that the choice of a basis set is crucial to the success of Galerkin models (Gottlieb and Orszag, 1977). For wind-induced flows, the use of a Chebyshev and Legendre polynomial basis set was found to be very accurate and was obviously more efficient than using cosine functions and local basis sets (Davies and Owen, 1979). Davies and Stephens (1983) have shown that the eigenfunction method is more efficient than the finite-difference method, provided that the vertical structure of eddy viscosity is fixed. In comparing two finite difference methods with Galerkin methods using cosine functions and Legendre and Chebyshev polynomials in tidal channels of constant depth, Jung *et al.* (1987) have noted that the accuracy of the eigenfunction expansion is comparable to that of finite difference methods with optimised vertical grid distribution. However, for the general spectral basis finite difference methods are more accurate than Galerkin methods for

a wide range of model parameters. It is known that using spectral methods with a general basis set requires more computational effort per degree of freedom than finite difference or finite elements methods (Fletcher, 1984). Strict comparison between the numerical methods is very difficult and results may be characteristic to the problem. It appears that a suitable basis set must be chosen on a case by case consideration, depending upon the nature of the system to be modelled, the eddy viscosity profiles and their time-dependence, conditions of bottom topography and stratification and the tolerance limit of numerical errors. It is worth noting the strategy chosen by Davies (1985*b*) in which the B-spline basis set of order four has been used for reproducing quantitative values accurately, whereas for a physical interpretation the eigenfunction method has been used in a complementary manner.

Apart from the accuracy and computational efficiency of Galerkin-function methods, their use is very appealing in that there is a certain correspondence between the solution approach and the dynamics of long-wave motions in shelf seas which are *shallow* in nature. Use of a basis set of eigenfunctions is particularly attractive because the horizontal and vertical dependence of hydrodynamic variables can be separated. There is an important distinction between Galerkin and finite difference representations which should be pointed out. For finite difference methods the numerical scheme has to be modified locally near the boundaries (and also around the interfaces in conditions of layered stratification), while for Galerkin approximations, such a modification is not needed but the problem of choosing a basis set appropriate to specific situations remains a difficult task.

1.2 Introductory remarks on present work

Davies' numerical method (1983*c*) permits one to determine eigenfunctions numerically for the continuous arbitrary eddy viscosity profile. Heaps (1983) has

developed a mode matching technique which deals with conditions of layered stratification. Since his model is analytic in nature the eddy viscosity profile is restricted to specific functional forms, and in practice the eddy viscosity is taken as being constant within each layer. In this thesis, the two contributions are combined to introduce a set of new Galerkin-based linear three-dimensional multilayered hydrodynamic models which are flexible in that the vertical eddy viscosity profile can be prescribed arbitrarily within each layer. The detailed methodology is described for basis sets of fourth-order B-splines and eigenfunctions, respectively.

With the formulation of Galerkin solutions, the presence of discontinuities in the prescribed eddy viscosity profile is assumed at the outset. Physically this makes sense since such an assumption is consistent with the fundamental properties of the multilayered model in that the fluid system is modelled as a stack of homogeneous layers. Variational approaches have been used previously in other disciplines to handle strong discontinuities in the coefficient of the second-order diffusivity operator. By using linear basis functions Javandel and Witherspoon (1969) have developed a variational model for fluid flow in anisotropic multilayered aquifers, and Desai and Johnson (1973) solved the one-dimensional consolidation equation with piecewise varying coefficients. A key feature of these variational approaches is that the weak formulation of the system involves the summation of functionals defined over each layer. Thermal interactions between the soil and the atmosphere were investigated by Garder and Raymond (1974) in a similar manner. The extension of the present method to these problems is straightforward.

When approximating the vertical variation of horizontal current in stably stratified seas, numerical models designed for continuous stratification have certain advantages over layered models in their application. The layered model is restricted by the requirement that the interface is not allowed to intersect the surface; hence the model cannot simulate the observed frontal structure during upwelling. Never-

theless, in the presence of a distinct thermocline the application of a layered model provides a great deal of physical insight into the dynamics of stratified flows. Also the approach is conceptually simpler than that for continuous stratification.

Throughout this thesis it is assumed that the vertical structure of the eddy viscosity profile is fixed and, neglecting erosion or deepening of the surface layer, the well formed layered structure is undisturbed by any turbulent mechanisms. Still, the lack of observational data may be a hindrance to the applicability of three-dimensional hydrodynamic numerical models. Furthermore, the three-dimensional modelling of stratified flows on a realistic scale is a very expensive exercise. Therefore, prior to extensive numerical investigation of the real system, particularly keeping Bass Strait in mind, the numerical experiment in this thesis is focused on the sensitivity of the model response in idealised situations, and in that course the model can also be verified. Emphasis is on the role of the pycnocline in determining the vertical structure of wind-induced flows and the time evolution of the surface current. In most computations the eddy viscosity has been prescribed in a piecewise-constant form, since the ability to deal with discontinuous variation of eddy viscosity can be best shown in this manner. In recent years there has been increasing interest in the development of turbulence models (Blumberg and Mellor, 1980; Johns, 1979; Koutitas and O'Connor, 1980*a*; Leendertse and Liu, 1977) which aim to determine the eddy viscosity directly as part of dynamic solutions, but it appears that these models remain at an early stage of development and their applicability as a prediction tool has not been verified.

The present numerical investigation is characterised by interface conditions introduced at a thermocline level. Two types of interfacial conditions are examined. The first is that the horizontal velocities and shear stresses are continuous across the interface and the second is that of zero-stress at the interface. The condition that across the interface horizontal velocities and shear stresses be continuous leads

to a *one domain system* which requires only one set of basis functions, whereas the stress-free condition effectively uncouples the system into two parts, and hence yields a *two domain system* which requires two independent sets of basis functions. Such a stress-free assumption at the interfaces is not new; in fact it underlies many analytical studies using layered models (Veronis and Stommel, 1956; Heaps, 1966; Csanady, 1968). We focus our attention in this thesis on comparison of the wind induced motion between the one and two domain systems through various numerical experiments. Chapter 2 describes the notation for the multilayered system to be modelled and the Galerkin solutions in terms of basis sets of B-spline functions and eigenfunctions. The boundary constraints for basis functions will be called *limit conditions* (Lattès, 1969) in order to distinguish these from the usual boundary conditions such as wind stress and bottom friction. The solution procedure used by Heaps and Davies will be closely followed, and is self-contained except for the theoretical details about B-spline functions. The presence of discontinuities in the distribution of density and the vertical eddy viscosity requires a definition of a weighted scalar product for each domain. Once the solution space is equipped with a set of weighted scalar products, the solution procedure follows the standard Galerkin method. Use of the continuity condition for velocity and stress at all interface levels yields a one domain system equipped with one scalar product, whereas the imposition of a zero-stress condition at an interface level yields a two domain system with two independent definitions of scalar products.

Chapter 3 is concerned with the description of the methodology of determining the spectral basis numerically from a multilayered Sturm-Liouville boundary value problem. Following Davies (1983*b*) and Furnes (1983), the limit conditions are introduced in a generalised separable form. The eigenfunctions in the basis set are given various names: *modal functions*, *vertical modes*, *modes*, *vertical structural functions*, and so on. The term *vertical mode* is used in this thesis. In a manner similar to Davies (1983*a*), the transformation relation which projects the

coefficients of the B-spline basis set or the known values of currents onto those of the eigenfunctions is also developed for the multilayered system. This permits an estimate of modal composition in current profiles for a given eddy viscosity profile.

Chapters 4 and 5 are concerned with applications of the models in idealised stratified systems. More specifically, two and three-layer structures are considered for one and two domain systems. Following Davies (1985*b*) the B-spline basis set of order four has been used to reproduce the surface current and current profiles accurately, whereas for a physical interpretation an eigenfunction method has been used in a complementary manner. Since stratification reduces the vertical penetration scale of wind energy, we exclude the bottom frictional boundary layer from consideration.

Steady state and time dependent Ekman-type problems are considered in Chapter 4 using *point models* in horizontally unbounded seas. The surface and internal displacements are suppressed and the horizontal extent of the layered structure is assumed uniform throughout the domain. For time dependent motion, wind stresses in the form of a step-function and a constant pulse with finite duration, are considered. A two-layer version of the Pollard-Millard (1970) slab model, which is composed of a surface mixed layer and the pycnocline, is proposed for the study of local inertial motions. Instead of a bulk decay parameter, the pycnocline structure, eddy viscosity and thickness of the pycnocline control the rate at which wind shear diffuses downward out of the mixed layer.

In Chapter 5 a series of numerical experiments are conducted to investigate the transient response of the water subject to a step function wind stress in a narrow stratified lake of constant depth. The effects of eddy viscosity profiles on the vertical variation of currents and on the time-dependent behaviour of internal vertical displacements are investigated, with special attention being paid to com-

parison of the initial decay between the one and two domain systems. Effects of density distribution, eddy viscosity within the pycnocline and eddy viscosity at the bottom layer are also investigated.

Concluding remarks are made in Chapter 6 and suggestions are made for further research in this area. Appendix I describes some basic properties of the multilayered eigenvalue system; Appendix II summarises the form of the first few vertical modes and their modal characteristics computed numerically using various eddy viscosity profiles; Appendix III presents an eigenequation derived analytically for a three-layered piecewise constant profile; Appendix IV includes a transient solution for wind-induced flows in a two-layered horizontally unbounded sea derived using Laplace transforms with a linear slip condition imposed at the base of the pycnocline.

CHAPTER 2

LINEAR HYDRODYNAMIC EQUATIONS FOR MULTILAYERED SEAS AND THEIR NUMERICAL SOLUTIONS USING GALERKIN-FINITE DIFFERENCE METHODS

2.1 Linear hydrodynamic equations

The model assumes an incompressible fluid and that thermodynamic effects are negligible. The flow is predominantly horizontal so that any vertical acceleration is neglected and hence the pressure distribution is hydrostatic in the vertical direction. Also, horizontal shears and nonlinear terms involving the squares of the velocity components are ignored. The resulting hydrodynamic equations in Cartesian coordinates are

$$\frac{\partial U}{\partial t} - \gamma V = -\frac{1}{\rho}\left(\frac{\partial P}{\partial x} - \frac{\partial \tau_{zx}}{\partial z}\right) + X, \tag{2.1.1}$$

$$\frac{\partial V}{\partial t} + \gamma U = -\frac{1}{\rho}\left(\frac{\partial P}{\partial y} - \frac{\partial \tau_{zy}}{\partial z}\right) + Y, \tag{2.1.2}$$

$$\frac{\partial U}{\partial x} + \frac{\partial V}{\partial y} = -\frac{\partial W}{\partial z}, \tag{2.1.3}$$

$$-\frac{1}{\rho}\left(\frac{\partial P}{\partial z}\right) = g, \tag{2.1.4}$$

where

$$\tau_{zx} = \rho N \frac{\partial U}{\partial z}, \qquad \tau_{zy} = \rho N \frac{\partial V}{\partial z}, \tag{2.1.5}$$

The notation used is as follows:

t	time
x, y	Cartesian coordinates measured in the horizontal plane of the undisturbed sea surface
z	vertical coordinate, positive upward and with origin at the undisturbed sea surface
h	depth of the sea floor below the undisturbed surface level
P	pressure
N	coefficient of vertical eddy viscosity
ρ	density of sea water
γ	geostrophic coefficient ($= 2\omega_e \sin \phi_e$)
ω_e	angular speed of the Earth's rotation
ϕ_e	latitude, positive in the Northern Hemisphere and negative in the Southern Hemisphere
g	acceleration due to gravity
U, V	components of horizontal current in the x and y directions respectively
W	vertical component of current
τ_{zx}, τ_{zy}	components of the vertical shears in the x and y directions respectively
X, Y	components of direct tide-generating forces in the x and y directions, respectively.

Equation (2.1.4) may be integrated to give

$$P(z) = P_a + g \int_z^{\zeta} \rho \, dz, \tag{2.1.6}$$

where P_a is the atmospheric pressure at the free sea surface. In the homogeneous case equation (2.1.6) reduces to

$$P(z) = P_a + g\rho(\zeta - z). \tag{2.1.7}$$

As a result of formula (2.1.7), the pressure variable will not appear explicitly in the equations of motion and, since the density change arises in a discrete manner in

the present hydrodynamic system, the effects of density variation will be coupled with the gradients of the free and internal surfaces (Hutter, 1984).

2.2 The multilayered formulation

To proceed in the formulation of the equations of motion in a multilayered system, it is necessary to introduce some definitions and the basic notation. In this study two situations are considered in relation to the interfacial conditions; these involve the concepts of *one domain* and *two domain systems.* Each domain consists of an arbitrary number of layers. Throughout the depth of a one domain system, continuity of the horizontal components of current and shear stress is enforced, whereas in the two domain system, a stress-free condition is introduced at an undisturbed level of the interface in the system, which effectively blocks the transmission of vertical shears across the boundary and splits the system into upper and lower domains. The boundary between the two domains is called the *interior domain boundary.* In theory it is possible to introduce multiple stress-free conditions over the vertical space domain. However, in practice we employ this condition only once, at the base of the pycnocline. For the two layer system the condition is applied at the interface between the upper and lower layers.

Figure 2.1 illustrates the multilayered system of constant depth in which the real system, having continuously varying density, is represented by a stack of horizontal layers. Between these layers, there are impermeable but moving interfaces and the density within each layer is constant. For the one domain system the whole water column is denoted by Ω_0, and the jth layer is denoted by $\Omega_{0,j}$, while for the two domain system the upper and lower domains are denoted by Ω_1 and Ω_2, respectively, and the jth layers in these domains are denoted by $\Omega_{1,j}$ and $\Omega_{2,j}$, respectively. For physical reasons, the σ-transformation described in Section 2.3 is introduced to normalise the depth of each domain, not each layer. All the basic

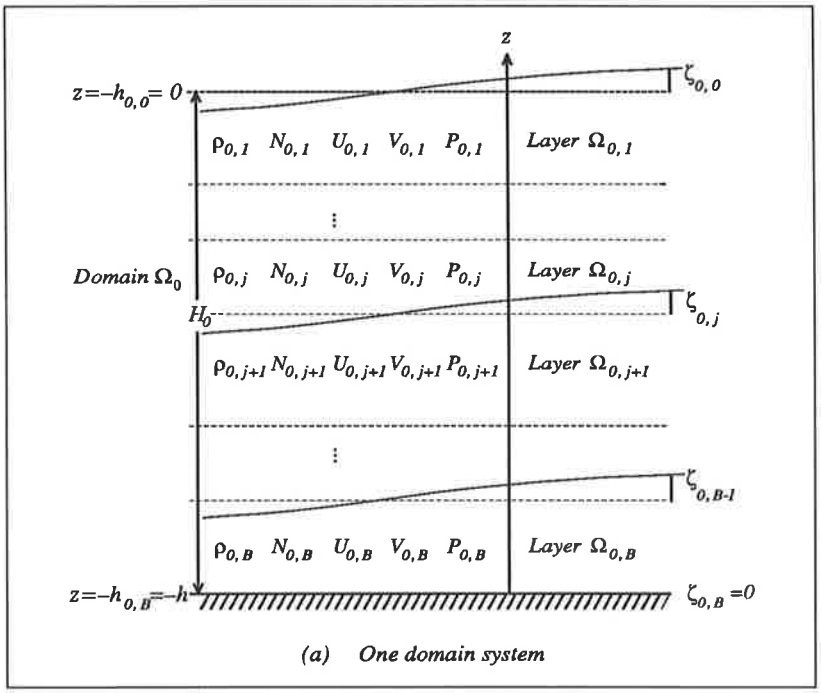

(a) One domain system

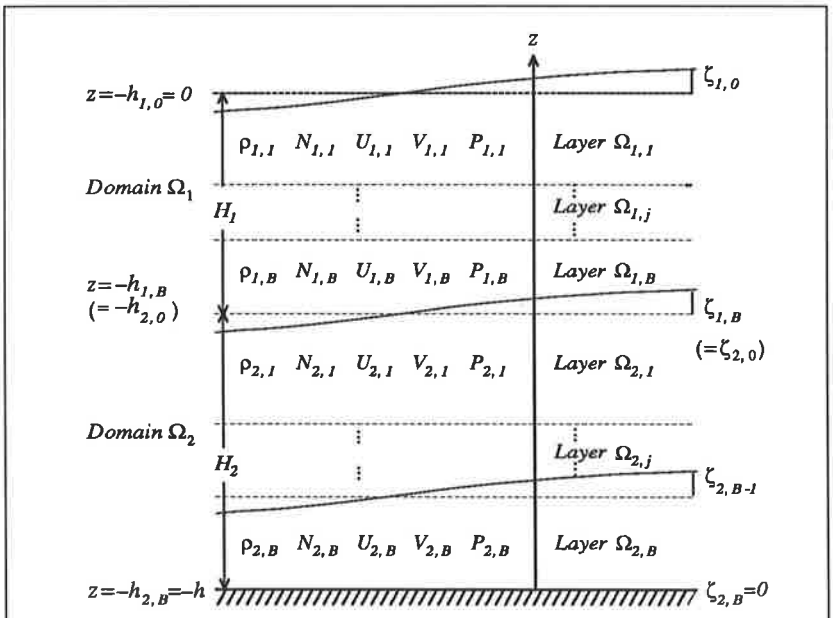

(b) Two domain system

Figure 2.1 The multilayered one and two domain systems.

parameters such as density, vertical eddy viscosity, pressure, the coordinates of the undisturbed levels of the interfaces and their displacements, and the U, V and W velocities, are labelled using double subscripts. For example, $\rho_{i,j}$ is the density at the jth layer of domain i. Symbols defined for the one domain system are identified by the subscript $i = 0$. In Section 2.5 where the Galerkin solutions are described for the one and two domain systems, the notations used for B-splines are similarly introduced. In addition, some quantities which are uniquely defined for each domain regardless of the number of layers within each, are denoted by a single index. For example, H_i is the thickness of domain i. To facilitate the formulation, we denote, for example, the density ρ at the bottom (J_i th) layer of the domain i by $\rho_{i,B}$. For stability of the fluid, the density increases downwards from the top layer, that is $\rho_{i,j} < \rho_{i,j+1}$, for all i and j within each domain, and $\rho_{1,B} < \rho_{2,1}$. Also, we assume that $\rho_{i,0} = 0$, $i = 0, 1$, and $\rho_{2,0} = \rho_{1,B}$.

The pressure P at a depth z in the top layers within each domain Ω_i is given by

$$P_{i,1} = P_a + g\rho_{i,1}(\zeta_{i,0} - z), \qquad (i = 0, 1), \quad (2.2.1)$$

$$P_{i,1} = P_a + g\sum_{\ell=1}^{J_1} \rho_{1,\ell}\Big(h_{1,\ell} + \zeta_{1,\ell-1} - \zeta_{1,\ell}\Big) + g\rho_{2,1}(\zeta_{2,0} - z), \qquad (i = 2), \quad (2.2.2)$$

and at a depth z in each $\Omega_{i,j}$, $j = 2, \cdots, J_i$, by

$$P_{i,j} = P_a + g\sum_{\ell=1}^{j-1} \rho_{1,\ell}\Big(h_{i,\ell} + \zeta_{i,\ell-1} - \zeta_{i,\ell}\Big) + g\rho_{i,j}\Big(\zeta_{i,j-1} - z\Big), \qquad (i = 0, 1), \quad (2.2.3)$$

$$P_{i,j} = P_a + g\sum_{\ell=1}^{J_1} \rho_{1,\ell}\Big(h_{1,\ell} + \zeta_{1,\ell-1} - \zeta_{1,\ell}\Big) + g\sum_{\ell=1}^{j-1} \rho_{2,\ell}\Big(h_{2,\ell} + \zeta_{2,\ell-1} - \zeta_{2,\ell}\Big) + g\rho_{2,j}(\zeta_{2,j-1} - z), \qquad (i = 2), \quad (2.2.4)$$

where $\zeta_{i,j}$ is the displacement of the lower interface of the jth layer in domain Ω_i.

For pressure to be continuous at all interior interfaces, it must satisfy

$$P_{i,j} = P_{i,j+1} \qquad \text{at} \quad z = -h_{i,j} + \zeta_{i,j}, \tag{2.2.5}$$

where $i = 0, 1, 2,\ j = 1, \cdots, J_i - 1$, and

$$P_{1,B} = P_{2,1} \qquad \text{at} \quad z = -h_{1,B} + \zeta_{1,B}. \tag{2.2.6}$$

Substituting (2.2.1) to (2.2.4) into (2.1.1) and (2.1.2), and using (2.1.5), (2.2.5) and (2.2.6), gives

$$\begin{aligned} \frac{\partial U_{i,j}}{\partial t} - \gamma V_{i,j} = &- \sum_{\ell=1}^{j} g\Big(\frac{\rho_{i,\ell} - \rho_{i,\ell-1}}{\rho_{i,j}}\Big)\frac{\partial \zeta_{i,\ell-1}}{\partial x} \\ &- \frac{\partial P_a}{\rho_{i,j}\partial x} + X + \frac{\partial}{\partial z}\Big(N_{i,j}\frac{\partial U_{i,j}}{\partial z}\Big), \end{aligned} \tag{2.2.7}$$

$$\begin{aligned} \frac{\partial V_{i,j}}{\partial t} + \gamma U_{i,j} = &- \sum_{\ell=1}^{j} g\Big(\frac{\rho_{i,\ell} - \rho_{i,\ell-1}}{\rho_{i,j}}\Big)\frac{\partial \zeta_{i,\ell-1}}{\partial y} \\ &- \frac{\partial P_a}{\rho_{i,j}\partial y} + Y + \frac{\partial}{\partial z}\Big(N_{i,j}\frac{\partial V_{i,j}}{\partial z}\Big), \end{aligned} \tag{2.2.8}$$

where $i = 0, 1,\ j = 1, \cdots, J_i$, and

$$\begin{aligned} \frac{\partial U_{2,j}}{\partial t} - \gamma V_{2,j} = &- \sum_{\ell=1}^{J_1} g\Big(\frac{\rho_{1,\ell} - \rho_{1,\ell-1}}{\rho_{2,j}}\Big)\frac{\partial \zeta_{1,\ell-1}}{\partial x} \\ &- \sum_{\ell=1}^{j} g\Big(\frac{\rho_{2,\ell} - \rho_{2,\ell-1}}{\rho_{2,j}}\Big)\frac{\partial \zeta_{2,\ell-1}}{\partial x} \\ &- \frac{\partial P_a}{\rho_{2,j}\partial x} + X + \frac{\partial}{\partial z}\Big(N_{2,j}\frac{\partial U_{2,j}}{\partial z}\Big), \end{aligned} \tag{2.2.9}$$

$$\begin{aligned} \frac{\partial V_{2,j}}{\partial t} + \gamma U_{2,j} = &- \sum_{\ell=1}^{J_1} g\Big(\frac{\rho_{1,\ell} - \rho_{1,\ell-1}}{\rho_{2,j}}\Big)\frac{\partial \zeta_{1,\ell-1}}{\partial y} \\ &- \sum_{\ell=1}^{j} g\Big(\frac{\rho_{2,\ell} - \rho_{2,\ell-1}}{\rho_{2,j}}\Big)\frac{\partial \zeta_{2,\ell-1}}{\partial y} \\ &- \frac{\partial P_a}{\rho_{2,j}\partial y} + Y + \frac{\partial}{\partial z}\Big(N_{2,j}\frac{\partial V_{2,j}}{\partial z}\Big), \end{aligned} \tag{2.2.10}$$

where $j = 1, \cdots, J_2$.

The body forcings involving the gradients of atmospheric pressure and direct tide-generating forces are hereafter denoted as

$$-\frac{\partial P_a}{\rho_{i,j}\partial x} + X = \widetilde{X}_{i,j}, \qquad -\frac{\partial P_a}{\rho_{i,j}\partial y} + Y = \widetilde{Y}_{i,j}. \tag{2.2.11}$$

Integrating (2.1.3) with respect to z over the interval $z = -h_{i,j}$ to $z = -h_{i,j-1}$, and noting that for small motion the vertical component of velocity is given by

$$W_{i,j} = \frac{\partial \zeta_{i,j}}{\partial t} \qquad \text{at} \quad z = -h_{i,j}, \tag{2.2.12}$$

we obtain

$$\frac{\partial \zeta_{i,j-1}}{\partial t} - \frac{\partial \zeta_{i,j}}{\partial t} + \frac{\partial}{\partial x}\int_{-h_{i,j}}^{-h_{i,j-1}} U_{i,j}\, dz + \frac{\partial}{\partial y}\int_{-h_{i,j}}^{-h_{i,j-1}} V_{i,j}\, dz = 0, \tag{2.2.13}$$

where $i = 0, 1, 2$, $j = 1, \cdots, J_i$. Note that the condition at the sea bed requires that $\partial \zeta_{i,B}/\partial t = 0$ in equation (2.2.14).

2.3 Surface, bottom and interfacial boundary conditions

In order to solve the system of equations (2.2.7) to (2.2.10), and (2.2.13) for the dependent variables $\zeta_{i,j}$, $U_{i,j}$ and $V_{i,j}$, boundary conditions have to be specified at the sea surface and the sea bed, along with appropriate interfacial conditions, and initial and lateral boundary conditions along the coastal and open boundaries. The initial and lateral boundary conditions used are given in Chapters 4 and 5, along with the application of the present model to wind induced currents in a horizontally unbounded open sea region and in a narrow lake. In this section the interfacial conditions and the boundary conditions at the sea surface and at the sea bed are described.

Evaluating the boundary conditions at the undisturbed levels gives the surface

boundary conditions at $z = 0$, $i = 0, 1$, as

$$\rho_{i,1}\Big(N_{i,1}\frac{\partial U_{i,1}}{\partial z}\Big) = \tau_{sx}, \qquad \rho_{i,1}\Big(N_{i,1}\frac{\partial V_{i,1}}{\partial z}\Big) = \tau_{sy}, \tag{2.3.1}$$

where τ_{sx} and τ_{sy} are components of external wind stress imposed at the sea surface. At the sea bed $z = -h_{i,J_i} = -h_{i,B}$ with $i = 0, 2$, we have either a *no-slip* boundary condition:

$$U_{i,B} = 0, \qquad V_{i,B} = 0, \tag{2.3.2}$$

or a *slip* boundary condition:

$$\rho_{i,B}\Big(N_{i,B}\frac{\partial U_{i,B}}{\partial z}\Big) = \tau_{bx}, \qquad \rho_{i,B}\Big(N_{i,B}\frac{\partial V_{i,B}}{\partial z}\Big) = \tau_{by}, \tag{2.3.3}$$

where τ_{bx} and τ_{by} are components of bottom frictional stress. The brackets in (2.3.1) and (2.3.3) are used to indicate that the quantity inside of them may vary within the layer.

Relating the bottom stresses, through a linear friction law, to the bottom current one has

$$\tau_{bx} = k_b \rho_{i,B}\, U_{i,B}(-h), \qquad \tau_{by} = k_b \rho_{i,B}\, V_{i,B}(-h), \tag{2.3.4}$$

where $i = 0, 2$ and k_b is the coefficient of linear bottom friction. Alternatively, bottom stresses may be represented by means of a quadratic friction law (for example, Davies, 1982*b*) or by a linear friction law based on velocities averaged over the bottom layer (Heaps, 1966).

At the undisturbed levels of the interior interfaces of each domain $z = -h_{i,j}$, the conditions to be satisfied are those of the continuity of the horizontal velocity and of the stress components. That is,

$$U_{i,j} = U_{i,j+1}, \qquad V_{i,j} = V_{i,j+1}, \tag{2.3.5}$$

$$\rho_{i,j}\Big(N_{i,j}\frac{\partial U_{i,j}}{\partial z}\Big) = \rho_{i,j+1}\Big(N_{i,j+1}\frac{\partial U_{i,j+1}}{\partial z}\Big), \tag{2.3.6}$$

$$\rho_{i,j}\Big(N_{i,j}\frac{\partial V_{i,j}}{\partial z}\Big) = \rho_{i,j+1}\Big(N_{i,j+1}\frac{\partial V_{i,j+1}}{\partial z}\Big), \tag{2.3.7}$$

where $i = 0, 1, 2,\ j = 1, \cdots, J_i - 1$, and the conditions at the interior domain boundary $z = -h_{1,B} = -h_{2,0}$ are

$$\rho_{1,B}\left(N_{1,B}\frac{\partial U_{1,B}}{\partial z}\right) = \rho_{2,1}\left(N_{2,1}\frac{\partial U_{2,1}}{\partial z}\right) = 0, \tag{2.3.8}$$

$$\rho_{1,B}\left(N_{1,B}\frac{\partial V_{1,B}}{\partial z}\right) = \rho_{2,1}\left(N_{2,1}\frac{\partial V_{2,1}}{\partial z}\right) = 0. \tag{2.3.9}$$

In these matching conditions we assume that there exist one-sided derivatives (from the above and below) of horizontal currents at all internal interfaces. In a rigorous sense, all physical quantities appearing in this thesis do in fact need to have one-sided limits at the interfaces because the system is discrete in nature. For simplicity, we ignore such rigour throughout the thesis.

Physically, conditions (2.3.8) and (2.3.9) state that the internal friction at the interface is zero, that is, the water bodies of the two domains slide freely relative to each other without frictional interaction. Heaps (1966) employed this condition as an approximate interface condition at the thermocline level in an analytical study of the dynamic response of a two-layer narrow lake to a suddenly applied constant wind. In an investigation of local inertial motions conducted by Gonella (1971*b*) such a stress-free condition was imposed at the base of the surface layer.

2.4 Transformed equations and boundary conditions

2.4.1 Transformation to the σ coordinate system

Before developing the solution of equations (2.2.7) to (2.2.10) and (2.2.13) using Galerkin expansions over the vertical space domain, these equations are transformed into σ-coordinates originally proposed by Phillips (1957) for numerical weather predictions. Using the σ-transformations

$$\sigma_i = -z/H_i, \qquad i = 0, 1, \tag{2.4.1}$$

$$\sigma_i = -(z + H_1)/H_2, \qquad i = 2, \tag{2.4.2}$$

where $H_0 = h_{0,B} = h$, $H_1 = h_{1,B}$ and $H_2 = h_{2,B} = h - H_1$, each of the domains is normalised by the σ-transformations such that the interval $-h_{i,B} \leq z \leq -h_{i,0}$ is transformed onto $0 \leq \sigma_i \leq 1$. The coordinates of the undisturbed levels of interfaces $h_{i,j}$ are accordingly transformed by

$$\xi_{i,j} = h_{i,j}/H_i, \qquad (i = 0, 1,\ j = 1, \cdots, J_i), \tag{2.4.3}$$

$$\xi_{i,j} = (h_{i,j} - H_1)/H_2, \qquad (i = 2,\ j = 0, \cdots, J_i). \tag{2.4.4}$$

Alternatively, each layer may be transformed to the interval $[0, 1]$, or Ω_1 and Ω_2 may be transformed to the intervals $[-1, 0]$ and $[0, 1]$, respectively. The transformations (2.4.1) and (2.4.2) have been chosen in this study mainly for physical reasons.

In layered models the interfacial surfaces are often assumed to be parallel to the undisturbed horizontal sea surface. It should be noted that in the presence of an uneven bottom the interfaces will be distorted through the σ-transformation (except for the upper domain of the two domain system).

2.4.2 Transformed equations

The transformed equations of motion for $\Omega_{i,j}$, $i = 0, 1$, are

$$\frac{\partial U_{i,j}}{\partial t} - \gamma V_{i,j} = -\sum_{\ell=1}^{j} g\Big(\frac{\rho_{i,\ell} - \rho_{i,\ell-1}}{\rho_{i,j}}\Big)\frac{\partial \zeta_{i,\ell-1}}{\partial x} + \widetilde{X}_{i,j} + \frac{\partial}{H_i^2 \partial \sigma_i}\Big(N_{i,j}\frac{\partial U_{i,j}}{\partial \sigma_i}\Big), \tag{2.4.5}$$

$$\frac{\partial V_{i,j}}{\partial t} + \gamma U_{i,j} = -\sum_{\ell=1}^{j} g\Big(\frac{\rho_{i,\ell} - \rho_{i,\ell-1}}{\rho_{i,j}}\Big)\frac{\partial \zeta_{i,\ell-1}}{\partial y} + \widetilde{Y}_{i,j} + \frac{\partial}{H_i^2 \partial \sigma_i}\Big(N_{i,j}\frac{\partial V_{i,j}}{\partial \sigma_i}\Big), \tag{2.4.6}$$

where $j = 1, \cdots, J_i$.

The transformed equations of motion for $\Omega_{2,j}$ are

$$\begin{aligned}\frac{\partial U_{2,j}}{\partial t} - \gamma V_{2,j} = &- \sum_{\ell=1}^{J_1} g\Big(\frac{\rho_{1,\ell} - \rho_{1,\ell-1}}{\rho_{2,j}}\Big)\frac{\partial \zeta_{1,\ell-1}}{\partial x} \\ &- \sum_{\ell=1}^{j} g\Big(\frac{\rho_{2,\ell} - \rho_{2,\ell-1}}{\rho_{2,j}}\Big)\frac{\partial \zeta_{2,\ell-1}}{\partial x} \\ &+ \widetilde{X}_{2,j} + \frac{\partial}{H_2^2 \partial \sigma_2}\Big(N_{2,j}\frac{\partial U_{2,j}}{\partial \sigma_2}\Big),\end{aligned} \tag{2.4.7}$$

$$\begin{aligned}\frac{\partial V_{2,j}}{\partial t} + \gamma U_{2,j} = &- \sum_{\ell=1}^{J_1} g\Big(\frac{\rho_{1,\ell} - \rho_{1,\ell-1}}{\rho_{2,j}}\Big)\frac{\partial \zeta_{1,\ell-1}}{\partial y} \\ &- \sum_{\ell=1}^{j} g\Big(\frac{\rho_{2,\ell} - \rho_{2,\ell-1}}{\rho_{2,j}}\Big)\frac{\partial \zeta_{2,\ell-1}}{\partial y} \\ &+ \widetilde{Y}_{2,j} + \frac{\partial}{H_2^2 \partial \sigma_2}\Big(N_{2,j}\frac{\partial V_{2,j}}{\partial \sigma_2}\Big),\end{aligned} \tag{2.4.8}$$

where $j = 1, \cdots, J_2$.

The transformed equation of continuity for $\Omega_{i,j}$ is

$$\frac{\partial \zeta_{i,j-1}}{\partial t} - \frac{\partial \zeta_{i,j}}{\partial t} + H_i\Big\{\frac{\partial}{\partial x}\int_{\xi_{i,j-1}}^{\xi_{i,j}} U_{i,j}\, d\sigma_i + \frac{\partial}{\partial y}\int_{\xi_{i,j-1}}^{\xi_{i,j}} V_{i,j}\, d\sigma_i\Big\} = 0, \tag{2.4.9}$$

where $i = 0, 1, 2$, $j = 1, \cdots, J_i$ and $\partial \zeta_{i,B}/\partial t = 0$.

2.4.3 Transformed boundary conditions

The transformed surface boundary conditions at $\sigma_i = 0$, $i = 0, 1$ are

$$-\frac{\rho_{i,1}}{H_i}\Big(N_{i,1}\frac{\partial U_{i,1}}{\partial \sigma_i}\Big) = \tau_{sx}, \qquad -\frac{\rho_{i,1}}{H_i}\Big(N_{i,1}\frac{\partial V_{i,1}}{\partial \sigma_i}\Big) = \tau_{sy}. \tag{2.4.10}$$

The transformed no-slip and slip boundary conditions at $\sigma_i = 1$, $i = 0, 2$ are

$$U_{i,B} = 0, \qquad V_{i,B} = 0, \tag{2.4.11}$$

and

$$-\frac{\rho_{i,B}}{H_i}\Big(N_{i,B}\frac{\partial U_{i,B}}{\partial \sigma_i}\Big) = \tau_{bx}, \qquad -\frac{\rho_{i,B}}{H_i}\Big(N_{i,B}\frac{\partial V_{i,B}}{\partial \sigma_i}\Big) = \tau_{by}, \tag{2.4.12}$$

where $i = 0, 2$.

The transformed conditions of continuity of velocity and stress within each domain $\sigma_i = \xi_{i,j}$ are

$$U_{i,j} = U_{i,j+1}, \qquad V_{i,j} = V_{i,j+1}, \tag{2.4.13}$$

$$\rho_{i,j}\Big(N_{i,j}\frac{\partial U_{i,j}}{\partial \sigma_i}\Big) = \rho_{i,j+1}\Big(N_{i,j+1}\frac{\partial U_{i,j+1}}{\partial \sigma_i}\Big), \tag{2.4.14}$$

$$\rho_{i,j}\Big(N_{i,j}\frac{\partial V_{i,j}}{\partial \sigma_i}\Big) = \rho_{i,j+1}\Big(N_{i,j+1}\frac{\partial V_{i,j+1}}{\partial \sigma_i}\Big), \tag{2.4.15}$$

where $i = 0, 1, 2,\ j = 1, \cdots, J_i - 1$.

The stress-free conditions at the interior domain boundary $\sigma_1 = \xi_{1,B} = 1$, or equivalently $\sigma_2 = \xi_{2,0} = 0$, are

$$\frac{\rho_{1,B}}{H_1}\Big(N_{1,B}\frac{\partial U_{1,B}}{\partial \sigma_1}\Big) = \frac{\rho_{2,1}}{H_2}\Big(N_{2,1}\frac{\partial U_{2,1}}{\partial \sigma_2}\Big) = 0, \tag{2.4.16}$$

$$\frac{\rho_{1,B}}{H_1}\Big(N_{1,B}\frac{\partial V_{1,B}}{\partial \sigma_1}\Big) = \frac{\rho_{2,1}}{H_2}\Big(N_{2,1}\frac{\partial V_{2,1}}{\partial \sigma_2}\Big) = 0. \tag{2.4.17}$$

2.5 Solutions via the use of a Galerkin method applied over the vertical space domain: a basis set of B-splines

For approximating solutions of differential equations, the Galerkin method is the most favoured of the various weighted residual methods. The first step in constructing the Galerkin solutions is to expand the U_i and V_i velocities through the vertical in terms of depth-dependent basis functions (test functions), $\phi_{i,k}(\sigma_i)$, and the corresponding time and horizontally varying coefficients, $A_i(x, y, t)$, $B_i(x, y, t)$, $k = 1, \cdots, m_i$, respectively. Let the U_i equation of motion be taken in operator

form as $\mathcal{L}_1(U_i, V_i) = 0$. The finite-dimensional representation of solutions produces a non-zero residual, $R^{(e)}$, given by

$$R^{(e)} = \mathcal{L}_1(U_i^{(M)}, V_i^{(M)}), \tag{2.5.1}$$

where $U_i^{(M)}$ and $V_i^{(M)}$ denote the finite-dimensional approximation to U_i and V_i. The next step is to set the integral of weighted residuals over the domain Ω_i to zero by choosing the weighting function to be the same as the basis function used for the expansion of $U_i^{(M)}$ and $V_i^{(M)}$, namely

$$\langle \phi_{i,k} \ \mathcal{L}_1(U_i^{(M)}, V_i^{(M)}) \rangle = 0, \qquad k = 1, \cdots, m_i, \tag{2.5.2}$$

where $\langle \ , \rangle$ denotes a scalar product. The same procedure is applied to the V_i equation of motion. Consequently, a system of equations for the unknown coefficients are derived which can be solved by any standard numerical methods available for depth-integrated dynamics. For detailed accounts on the principle of the Galerkin method see Prenter (1975) and Fletcher (1984). In the literature there have been some applications of the least squares method (for example, Stevens, 1976). However, this has not received much attention principally due to the sizable amount of computation required.

2.5.1 *B*-splines functions

Most realisations of the Galerkin procedure, with a basis set of continuous functions, implicitly assume that the solution is relatively smooth. The global dependence of continuous functions on localised changes usually limits the reproduction of the localised rapid variations in solutions (De Boor, 1978), although such a disadvantage can be avoided in certain circumstances by using a basis set of eigenfunctions (Davies, 1983*c*). In this respect the *B*-splines of order n_o which have restricted support and continuous derivatives up to $n_o - 2$ may be advantageous from a numerical point of view over other local basis sets, such as other

splines or piecewise sinusoidal functions. Details on the practical use of B-splines can be found in Cox (1972, 1975) and Davies (1977a).

Figure 2.2 illustrates the basis sets of the fourth order B-splines defined in the two-layer, one and two domain systems. The intervals $[0,1]$ are subdivided into units of length $\Delta\nu_{i,r} = (\nu_{i,r+1} - \nu_{i,r})$, by the partition

$$0 = \nu_{i,0} < \cdots < \nu_{i,r} < \cdots < \nu_{i,\overline{m}} = 1, \tag{2.5.3}$$

where $i = 0, 1, 2$ and $\overline{m} = m_i - n_o + 1$. Points denoted by $\nu_{i,r}$ are called knots and their separation can be arbitrary. For convenience, the distribution of knots shown in Figure 2.2 is uniform for each domain. The r th B-spline of order four has non-zero positive values over the knot interval $\nu_{i,r-4} < \sigma_i < \nu_{i,r}$, with its values and derivatives vanishing at $\nu_{i,r-4}$ and $\nu_{i,r}$. For the one domain system a set of B-splines spanning the entire depth from the surface to the sea bed is defined, while for the two domain system two independent sets of B-splines spanning the upper and lower domains are defined. Two sets of three supporting knots are defined to complete the basis set at the outside of each domain, that is $\nu_{0,-3}$ to $\nu_{0,-1}$, and $\nu_{0,1}$ to $\nu_{0,3}$, for Ω_0, and $\nu_{i,-3}$ to $\nu_{i,-1}$, and $\nu_{i,1}$ to $\nu_{i,3}$, for Ω_i, $i = 1, 2$. Use of the fourth-order B-splines results in a hepta-diagonal mass matrix.

For the one domain system there is no difference in the arrangement of knots between the homogeneous and layered systems except that for the latter, the positions of the knots are constrained to coincide with the undisturbed interface levels to avoid any undesirable oscillations in numerical results (Axelsson and Barker, 1984). For the two domain system two sets of knots are defined as shown in Figure 2.2 and, in this example, knots $\nu_{1,5}$ and $\nu_{2,0}$ are positioned on the domain boundaries. The two sets of three supporting knots around the domain boundary may overlap each other, but in any case their contribution to each domain is independent.

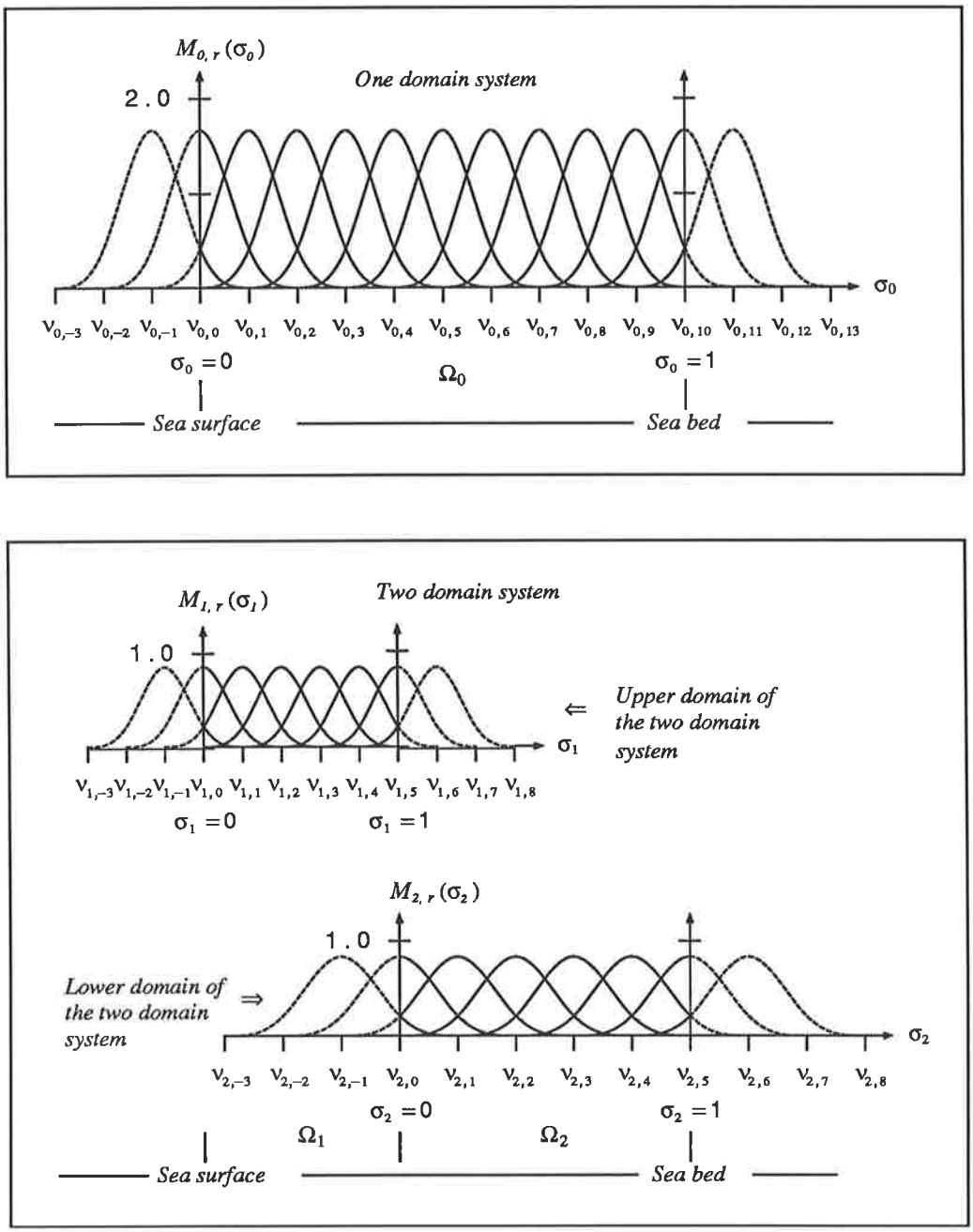

Figure 2.2 Configuration of the fourth-order B-spline functions in the one and two domain systems.

The Galerkin procedures for the one and two domain systems are described separately. The two horizontal components of current are expanded in terms of the fourth-order B-splines $M_{i,r}(\sigma_i)$, $i = 0, 1, 2$, with the introduction of a set of weighted scalar products.

2.5.2 One domain solutions

Galerkin solutions in $\Omega_{0,j}$ are sought with respect to the scalar product

$$\langle \phi, \psi \rangle = \sum_{j=1}^{J_0} \frac{\rho_{0,j}}{\rho_{0,1}} \int_{\xi_{0,j-1}}^{\xi_{0,j}} \phi_{0,j} \cdot \psi_{0,j} \, d\sigma_0 \ , \tag{2.5.4}$$

where $\phi_{0,j}$, $\psi_{0,j}$ is a pair of square integrable functions in a Lebesque sense. With this, the conventional Galerkin method can readily be applied.

For simplicity, it is assumed that the vertical variation of eddy viscosity has a fixed structure over the domain, that is,

$$N = N_{0,j}(x, y, \sigma_0, t) = \alpha_0(x, y, t)\mu_{0,j}(\sigma_0) \qquad \text{for} \quad \xi_{0,j-1} \le \sigma_0 \le \xi_{0,j}, \tag{2.5.5}$$

where $j = 1, \cdots, J_0$.

The two components of horizontal current, U_0 and V_0, at a depth σ_0, are expanded using m_0 basis functions of B-splines, so that

$$U_0(x, y, \sigma_0, t) = \sum_{r=1}^{m_0} A_{0,r}(x, y, t) \ M_{0,r}(\sigma_0) \ , \tag{2.5.6}$$

$$V_0(x, y, \sigma_0, t) = \sum_{r=1}^{m_0} B_{0,r}(x, y, t) \ M_{0,r}(\sigma_0), \tag{2.5.7}$$

where the coefficients $A_{0,r}$ and $B_{0,r}$ are to be determined.

Taking the scalar product (2.5.4) of (2.4.5) with $M_{0,k}$ gives

$$\begin{aligned} \frac{\partial \langle U_{0,k} \rangle}{\partial t} - \gamma \langle V_{0,k} \rangle = & - \sum_{\ell=1}^{J_0} g\left(\frac{\rho_{0,\ell} - \rho_{0,\ell-1}}{\rho_{0,1}} \right) \frac{\partial \zeta_{0,\ell-1}}{\partial x} \ a_{0,\ell-1,k} \\ & + \ \widetilde{X}_{0,1} \, a_{0,0,k} + I_{0,k}, \end{aligned} \tag{2.5.8}$$

where

$$\langle U_{i,k}\rangle = \langle U_i, M_{i,k}\rangle = \sum_{j=1}^{J_i}\left(\frac{\rho_{i,j}}{\rho_{i,1}}\int_{\xi_{i,j-1}}^{\xi_{i,j}} U_{i,j}\, M_{i,k}\; d\sigma_i\right), \tag{2.5.9}$$

$$\langle V_{i,k}\rangle = \langle V_i, M_{i,k}\rangle = \sum_{j=1}^{J_i}\left(\frac{\rho_{i,j}}{\rho_{i,1}}\int_{\xi_{i,j-1}}^{\xi_{i,j}} V_{i,j}\, M_{i,k}\; d\sigma_i\right), \tag{2.5.10}$$

$$a_{i,\ell,k} = \sum_{j=\ell+1}^{J_i}\int_{\xi_{i,j-1}}^{\xi_{i,j}} M_{i,k}\; d\sigma_i \;= \int_{\xi_{i,\ell}}^{1} M_{i,k}\; d\sigma_i, \tag{2.5.11}$$

and

$$I_{i,k} = \frac{\alpha_i}{H_i^2}\sum_{j=1}^{J_i}\left\{\frac{\rho_{i,j}}{\rho_{i,1}}\int_{\xi_{i,j-1}}^{\xi_{i,j}}\frac{\partial}{\partial\sigma_i}\left(\mu_{i,j}\frac{\partial U_{i,j}}{\partial\sigma_i}\right)M_{i,k}\; d\sigma_i\right\}, \tag{2.5.12}$$

with $i = 0$, $k = 1, \cdots, m_i$.

Integrating (2.5.12) by parts yields

$$\begin{aligned} I_{0,k} = \; & -\frac{1}{\rho_{0,1}H_0}\sum_{j=1}^{J_0}\Big\{\tau_{zx}(\xi_{0,j})\; M_{0,k}(\xi_{0,j}) - \tau_{zx}(\xi_{0,j-1})\; M_{0,k}(\xi_{0,j-1})\Big\} \\ & - \frac{\alpha_0}{H_0^2}\sum_{j=1}^{J_0}\left(\frac{\rho_{0,j}}{\rho_{0,1}}\int_{\xi_{0,j-1}}^{\xi_{0,j}}\mu_{0,j}\frac{\partial U_{0,j}}{\partial\sigma_0}\frac{dM_{0,k}}{d\sigma_0}d\sigma_0\right). \end{aligned} \tag{2.5.13}$$

Using the interfacial condition (2.4.14) and substituting the sea surface and bottom boundary conditions (2.4.10) and (2.4.12) gives

$$\begin{aligned} I_{0,k} = & -\frac{\tau_{bx}}{\rho_{0,B}H_0}M_{0,k}(1) + \frac{\tau_{sx}}{\rho_{0,1}H_0}M_{0,k}(0) \\ & - \frac{\alpha_0}{H_0^2}\sum_{j=1}^{J_0}\left(\frac{\rho_{0,j}}{\rho_{0,1}}\int_{\xi_{0,j-1}}^{\xi_{0,j}}\mu_{0,j}\frac{\partial U_{0,j}}{\partial\sigma_0}\frac{dM_{0,k}}{d\sigma_0}d\sigma_0\right). \end{aligned} \tag{2.5.14}$$

This integration by parts facilitates the inclusion of the boundary conditions, and it permits the use of linear basis functions.

Substituting the expansions (2.5.6) and (2.5.7) into (2.5.8), then using (2.5.9),

(2.5.10) and (2.5.14), yields

$$\sum_{r=1}^{m_0}\frac{\partial A_{0,r}}{\partial t}\langle M_{0,r},\ M_{0,k}\rangle\ -\ \gamma\sum_{r=1}^{m_0}B_{0,r}\langle M_{0,r},\ M_{0,k}\rangle$$

$$=-\sum_{\ell=1}^{J_0}g\Big(\frac{\rho_{0,\ell}-\rho_{0,\ell-1}}{\rho_{0,1}}\Big)\frac{\partial\zeta_{0,\ell-1}}{\partial x}\ a_{0,\ell-1,k}$$

$$-\frac{\tau_{bx}}{\rho_{0,B}H_0}M_{0,k}(1)+\frac{\tau_{sx}}{\rho_{0,1}H_0}M_{0,k}(0)+\widetilde{X}_{0,1}\,a_{0,0,k}$$

$$-\frac{\alpha_0}{H_0^2}\sum_{r=1}^{m_0}A_{0,r}\sum_{\ell=1}^{J_0}\Big(\frac{\rho_{0,\ell}}{\rho_{0,1}}\int_{\xi_{0,\ell-1}}^{\xi_{0,\ell}}\mu_{0,\ell}\frac{dM_{0,r}}{d\sigma_0}\frac{dM_{0,k}}{d\sigma_0}d\sigma_0\Big),\qquad k=1,\cdots,m_0. \tag{2.5.15}$$

Similarly,

$$\sum_{r=1}^{m_0}\frac{\partial B_{0,r}}{\partial t}\langle M_{0,r},\ M_{0,k}\rangle\ +\ \gamma\sum_{r=1}^{m_0}A_{0,r}\langle M_{0,r},\ M_{0,k}\rangle$$

$$=-\sum_{\ell=1}^{J_0}g\Big(\frac{\rho_{0,\ell}-\rho_{0,\ell-1}}{\rho_{0,1}}\Big)\frac{\partial\zeta_{0,\ell-1}}{\partial y}\ a_{0,\ell-1,k}$$

$$=-\frac{\tau_{by}}{\rho_{0,B}H_0}M_{0,k}(1)+\frac{\tau_{sy}}{\rho_{0,1}H_0}M_{0,k}(0)+\widetilde{Y}_{0,1}\,a_{0,0,k}$$

$$-\frac{\alpha_0}{H_0^2}\sum_{r=1}^{m_0}B_{0,r}\sum_{\ell=1}^{J_0}\Big(\frac{\rho_{0,\ell}}{\rho_{0,1}}\int_{\xi_{0,\ell-1}}^{\xi_{0,\ell}}\mu_{0,\ell}\frac{dM_{0,r}}{d\sigma_0}\frac{dM_{0,k}}{d\sigma_0}d\sigma_0\Big),\qquad k=1,\cdots,m_0. \tag{2.5.16}$$

Substituting (2.5.6) and (2.5.7) into the equation of continuity (2.4.9) and rearranging the set of resultant equations yields,

$$\frac{\partial\zeta_{0,j}}{\partial t}+\sum_{r=1}^{m_0}H_0\Big(\frac{\partial A_{0,r}}{\partial x}+\frac{\partial B_{0,r}}{\partial y}\Big)a_{0,j,r}=0, \tag{2.5.17}$$

where $j=0,\cdots,J_i-1$.

Writing (2.5.15), (2.5.16) and (2.5.17) in matrix form gives

$$\begin{aligned}\mathbf{C}_i\mathbf{A}_i^{\bullet}=\ &\gamma\mathbf{C}_i\mathbf{B}_i-\sum_{\ell=1}^{J_i}g\Big(\frac{\rho_{i,\ell}-\rho_{i,\ell-1}}{\rho_{i,1}}\Big)\frac{\partial\zeta_{i,\ell-1}}{\partial x}\mathbf{E}_i^{(\ell)}\\&+\frac{\tau_{sx}}{\rho_{i,1}H_i}\mathbf{E}_i^{s}-\frac{\tau_{bx}}{\rho_{i,1}H_i}\mathbf{E}_i^{b}+\widetilde{X}_{i,1}\mathbf{E}_i^{(1)}-\frac{\alpha_i}{H_i^2}\mathbf{D}_i\mathbf{A}_i,\end{aligned} \tag{2.5.18}$$

$$\begin{aligned}\mathbf{C}_i\mathbf{B}_i^{\bullet} = &-\gamma\mathbf{C}_i\mathbf{A}_i - \sum_{\ell=1}^{J_i} g\Big(\frac{\rho_{i,\ell}-\rho_{i,\ell-1}}{\rho_{i,1}}\Big)\frac{\partial\zeta_{i,\ell-1}}{\partial y}\mathbf{E}_i^{(\ell)} \\ &+ \frac{\tau_{sy}}{\rho_{i,1}H_i}\mathbf{E}_i^{s} - \frac{\tau_{by}}{\rho_{i,1}H_i}\mathbf{E}_i^{b} + \widetilde{Y}_{i,1}\mathbf{E}_i^{(1)} - \frac{\alpha_i}{H_i^2}\mathbf{D}_i\mathbf{B}_i,\end{aligned} \tag{2.5.19}$$

and

$$\mathbf{Z}_i^{\bullet} + H_i\,\mathbf{E}_i(\mathbf{A}_i' + \mathbf{B}_i') = 0, \tag{2.5.20}$$

where $i = 0$. In these equations:

$\mathbf{C}_i$ is a mass matrix of order $m_i \times m_i$ with (r,k) th element

$$\sum_{j=1}^{J_i}\frac{\rho_{i,j}}{\rho_{i,1}}\int_{\xi_{i,j-1}}^{\xi_{i,j}} M_{i,r}\,M_{i,k}\;d\sigma_i; \tag{2.5.21}$$

$\mathbf{D}_i$ is a diffusion matrix of order $m_i \times m_i$ with (r,k) th element

$$\sum_{j=1}^{J_i}\Big(\frac{\rho_{i,j}}{\rho_{i,1}}\int_{\xi_{i,j-1}}^{\xi_{i,j}} \mu_{i,j}\,M_{i,r}\,M_{i,k}\;d\sigma_i\Big); \tag{2.5.22}$$

$\mathbf{E}_i$ is a matrix of order $m_i \times m_i$ with (r,k) th element

$$\int_{\xi_{i,r-1}}^{1} M_{i,k}\;d\sigma_i; \tag{2.5.23}$$

$\mathbf{E}_i^{(\ell)}$, $\ell = 1,\cdots,J_i$, is a column vector of length m_i with k th element

$$\int_{\xi_{i,\ell-1}}^{1} M_{i,k}\;d\sigma_i; \tag{2.5.24}$$

$\mathbf{E}_i^{s}$ and $\mathbf{E}_i^{b}$ are column vectors of length m_i with k th element

$$M_{i,k}(0) \quad \text{and} \quad M_{i,k}(1), \text{ respectively;} \tag{2.5.25}$$

$\mathbf{A}_i$ and $\mathbf{B}_i$ are column vectors of length m_i with k th element

$$A_{i,k} \quad \text{and} \quad B_{i,k}, \text{ respectively;} \tag{2.5.26}$$

$\mathbf{A}_i^{\bullet}$ and $\mathbf{B}_i^{\bullet}$ are column vectors of length m_i with k th element

$$\frac{\partial A_{i,k}}{\partial t} \quad \text{and} \quad \frac{\partial B_{i,k}}{\partial t}, \text{ respectively;} \tag{2.5.27}$$

$\mathbf{Z}_i^{\bullet}$ is a column vector of length m_i with k th element

$$\frac{\partial \zeta_{i,k-1}}{\partial t}; \tag{2.5.28}$$

and $\mathbf{A}_i'$ and $\mathbf{B}_i'$ are column vectors of length m_i with k th element

$$\frac{\partial A_{i,k}}{\partial x} \quad \text{and} \quad \frac{\partial B_{i,k}}{\partial y}, \text{ respectively.} \tag{2.5.29}$$

The definitions of matrices (2.5.21) to (2.5.29) will also be used for the solutions of the two domain system which will be described in Section 2.5.2.

Following the usual strategy used in finite element methods, it is possible to incorporate the boundary conditions, thus modifying the basis sets and subsequently all of the integrals given in this formulation. In earlier studies Davies (1977*b*,*c*) has done this on the basis of the Galerkin-Collocation method. Therefore the integration by parts do not appear in the solution procedure.

In this study the surface stress conditions have been incorporated as natural boundary conditions in the course of integrating (2.5.12) by parts. Subsequently, when the slip-boundary conditions are enforced at the sea bed, all of the boundary constraints are natural conditions needing no special modifications. However, for the case in which a no-slip condition (an essential boundary condition) is enforced at the sea bed $\sigma_i = 1$, $i = 0$, it is required that the basis sets be modified. This is achieved by either specifying knots having the $n_o - 1$ multiplicity at $\sigma_i = 1$ (Davies, 1977*a*, 1978*b*) or by linearly combining the B-splines which do not vanish at $\sigma_i = 1$ (Davies, 1977*b*,*c*, 1980*a*). It has been revealed in preliminary computations that both approaches yield almost the same results. The latter approach is used in this study. Thus, for the total contribution of the B-spline basis set to vanish at $\sigma_i = 1$ we need

$$\sum_{r=1}^{m_i} A_{i,r} M_{i,r}(1) = 0 \quad \text{at} \quad \sigma_i = 1. \tag{2.5.30}$$

Since, for the B-splines of the fourth order, $M_{i,r}(\sigma_i)$ is non-zero at $\sigma_i = 1$ for each $r = m_i - n_o + 2$ to m_i, equation (2.5.30) reduces to

$$A_{i,m_i} = -A_{i,m_i-2}\frac{M_{i,m_i-2}(1)}{M_{i,m_i}(1)} - A_{i,m_i-1}\frac{M_{2,m_i-1}(1)}{M_{2,m_i}(1)}. \qquad (2.5.31)$$

Thus, by replacing the $(m_i - 1)$th and $(m_i - 2)$th B-splines by

$$\bar{M}_{i,m_i-1}(\sigma_i) = M_{i,m_i-1}(\sigma_i) - \frac{M_{i,m_i-1}(1)}{M_{i,m_i}(1)}M_{i,m_i}(\sigma_i), \qquad (2.5.32)$$

and

$$\bar{M}_{i,m_i-2}(\sigma_i) = M_{i,m_i-2}(\sigma_i) - \frac{M_{i,m_i-2}(1)}{M_{i,m_i}(1)}M_{i,m_i}(\sigma_i), \qquad (2.5.33)$$

we form a basis set, each element of which satisfies the essential constraint at $\sigma_i = 1$ exactly. With these modifications the order and length of matrices in (2.5.21) to (2.5.29) are reduced by one.

Once the coefficients of B-spline expansions are computed from (2.5.18), (2.5.19) and (2.5.20), along with the appropriate initial conditions and lateral boundary conditions, the two components of horizontal current at a depth σ_0 are obtained from (2.5.6) and (2.5.7).

For the general situation when the eddy viscosity profiles of the form (2.5.5) are not permitted, the problem of reformulating the resultant diffusion matrix at every time step might occur. In such circumstances, as described by Davies (1980*c*), it might be expedient to expand the eddy viscosity in terms of suitably chosen interpolation functions $\Psi_{0,\ell}$ with coefficients $E_{0,j,\ell}(x, y, t)$ so that

$$N_{0,j}(x, y, \sigma_0, t) = \sum_{\ell=1}^{m_e} E_{0,j,\ell}(x, y, t)\, \Psi_{0,j,\ell}(\sigma_0), \qquad j = 1, \cdots, J_0, \qquad (2.5.34)$$

where m_e is not necessarily equal to m_0.

Integrating these expansions over each layer and dividing by the thickness of the layer, we obtain for $\Omega_{i,j}$, $i = 0$,

$$\overline{U}_{i,j}(x,y,\sigma_i,t) = \frac{1}{\Delta\xi_{i,j}} \sum_{r=1}^{m_i} A_{i,r}(x,y,t) \int_{\xi_{i,j-1}}^{\xi_{i,j}} M_{i,r}\, d\sigma_i, \tag{2.5.35}$$

$$\overline{V}_{i,j}(x,y,\sigma_i,t) = \frac{1}{\Delta\xi_{i,j}} \sum_{r=1}^{m_i} B_{i,r}(x,y,t) \int_{\xi_{i,j-1}}^{\xi_{i,j}} M_{i,r}\, d\sigma_i, \tag{2.5.36}$$

where $\Delta\xi_{i,j} = \xi_{i,j} - \xi_{i,j-1}$, $j = 1, \cdots, J_i$.

Integrating these expansions over the domain Ω_i, $i = 0$, we obtain

$$\overline{U}_i(x,y,\sigma_i,t) = \sum_{r=1}^{m_i} A_{i,r}(x,y,t) \int_0^1 M_{i,r}\, d\sigma_i, \tag{2.5.37}$$

$$\overline{V}_i(x,y,\sigma_i,t) = \sum_{r=1}^{m_i} B_{i,r}(x,y,t) \int_0^1 M_{i,r}\, d\sigma_i, \tag{2.5.38}$$

with $j = 1, \cdots, J_i$.

2.5.3 Two domain solutions

Introducing a stress-free condition at an interface level leads to the representation of the vertical dependence in terms of two independent sets of basis functions. Use of a single set of basis functions forms a system of partial differential equations with overspecified boundary conditions. Approximate solutions to the system of equations (2.4.5) to (2.4.8) are sought with respect to the scalar products

$$\langle \phi_i, \psi_i \rangle = \sum_{j=1}^{J_i} \left(\frac{\rho_{i,j}}{\rho_{i,1}} \int_{\xi_{i,j-1}}^{\xi_{i,j}} \phi_{i,j} \cdot \psi_{i,j}\, d\sigma_i \right) \qquad \text{for} \quad \Omega_i, \tag{2.5.39}$$

where $i = 1, 2$.

Expanding the two components of horizontal current in Ω_i in terms of B-spline basis functions $M_{i,r}(\sigma_i)$ together with time and horizontally varying coefficients,

gives

$$U_i(x,y,\sigma_i,t) = \sum_{r=1}^{m_i} A_{i,r}(x,y,t)\ M_{i,r}(\sigma_i), \tag{2.5.40}$$

$$V_i(x,y,\sigma_i,t) = \sum_{r=1}^{m_i} B_{i,r}(x,y,t)\ M_{i,r}(\sigma_i), \tag{2.5.41}$$

where the coefficients $A_{i,r}$ and $B_{i,r}$, $i = 1,2$ are to be determined. Note that the number of B-spline functions and the order of the B-splines may also differ for each domain.

The variation in the vertical eddy viscosity is assumed to be of the form

$$N = N_{i,j}(x,y,\sigma_i,t) = \alpha_i(x,y,t)\ \mu_{i,j}(\sigma_i) \qquad \text{for} \quad \Omega_{i,j}, \tag{2.5.42}$$

where $i = 1,2$. For a more general form of time varying eddy viscosity, it is possible to expand the vertical eddy viscosity in terms of a set of interpolation functions similar to those described by equation (2.5.34).

Taking the scalar product (2.5.39) of equations (2.4.5) and (2.4.7), with $M_{i,k}$, $i = 1,2$, respectively, gives

$$\begin{aligned} \frac{\partial \langle U_{1,k}\rangle}{\partial t} - \gamma\langle V_{1,k}\rangle = &- \sum_{\ell=1}^{J_1} g\left(\frac{\rho_{1,\ell} - \rho_{1,\ell-1}}{\rho_{1,1}}\right)\frac{\partial \zeta_{1,\ell-1}}{\partial x}\ a_{1,\ell-1,k} \\ &+ \widetilde{X}_{1,1}\, a_{1,0,k} + I_{1,k} \qquad \text{for} \quad \Omega_1, \end{aligned} \tag{2.5.43}$$

$$\begin{aligned} \frac{\partial \langle U_{2,k}\rangle}{\partial t} - \gamma\langle V_{2,k}\rangle = &- \sum_{\ell=1}^{J_1} g\left(\frac{\rho_{1,\ell} - \rho_{1,\ell-1}}{\rho_{2,1}}\right)\frac{\partial \zeta_{1,\ell-1}}{\partial x}\ a_{2,0,k} \\ &- \sum_{\ell=1}^{J_2} g\left(\frac{\rho_{2,\ell} - \rho_{2,\ell-1}}{\rho_{2,1}}\right)\frac{\partial \zeta_{2,\ell-1}}{\partial x}\ a_{2,\ell-1,k} \\ &+ \widetilde{X}_{2,1}\, a_{2,0,k} + I_{2,k} \qquad \text{for} \quad \Omega_2, \end{aligned} \tag{2.5.44}$$

where

$$\langle U_{i,k}\rangle = \langle U_i, M_{i,k}\rangle = \sum_{j=1}^{J_i}\left(\frac{\rho_{i,j}}{\rho_{i,1}}\int_{\xi_{i,j-1}}^{\xi_{i,j}} U_{i,j}\, M_{i,k}\ d\sigma_i\right), \tag{2.5.9}$$

$$\langle V_{i,k}\rangle = \langle V_i, M_{i,k}\rangle = \sum_{j=1}^{J_i}\Big(\frac{\rho_{i,j}}{\rho_{i,1}}\int_{\xi_{i,j-1}}^{\xi_{i,j}} V_{i,j}\, M_{i,k}\; d\sigma_i\Big)\;, \tag{2.5.10}$$

$$a_{i,\ell,k} = \sum_{j=\ell+1}^{J_i}\int_{\xi_{i,j-1}}^{\xi_{i,j}} M_{i,k}\; d\sigma_i \;= \int_{\xi_{i,\ell}}^{1} M_{i,k}\; d\sigma_i, \tag{2.5.11}$$

and

$$I_{i,k} \;=\; \frac{\alpha_i}{H_i^2}\sum_{j=1}^{J_i}\Big\{\frac{\rho_{i,j}}{\rho_{i,1}}\int_{\xi_{i,j-1}}^{\xi_{i,j}}\frac{\partial}{\partial\sigma_i}\Big(\mu_{i,j}\frac{\partial U_{i,j}}{\partial\sigma_i}\Big)M_{i,k}\; d\sigma_i\Big\}, \tag{2.5.12}$$

with $i = 0$, $k = 1,\cdots,m_i$.

Integrating (2.5.12) by parts and substituting the boundary conditions (2.4.10) and (2.4.12) and the interfacial conditions (2.4.14) and (2.4.16), gives

$$I_{1,k} = \;\frac{\tau_{sx}}{\rho_{1,1}H_1}M_{1,k}(0) - \frac{\alpha_1}{H_1^2}\sum_{j=1}^{J_1}\Big(\frac{\rho_{1,j}}{\rho_{1,1}}\int_{\xi_{1,j-1}}^{\xi_{1,j}}\mu_{1,j}\frac{\partial U_{1,j}}{\partial\sigma_1}\frac{dM_{1,k}}{d\sigma_1}d\sigma_1\Big), \tag{2.5.45}$$

where $k = 1,\cdots,m_1$ and

$$I_{2,k} = -\frac{\tau_{bx}}{\rho_{2,1}H_2}M_{2,k}(1) - \frac{\alpha_2}{H_2^2}\sum_{j=1}^{J_2}\Big(\frac{\rho_{2,j}}{\rho_{2,1}}\int_{\xi_{2,j-1}}^{\xi_{2,j}}\mu_{2,j}\frac{\partial U_{2,j}}{\partial\sigma_2}\frac{dM_{2,k}}{d\sigma_2}d\sigma_2\Big), \tag{2.5.46}$$

where $k = 1,\cdots,m_2$.

Substituting the expansions (2.5.40) and (2.5.41) into (2.5.43) and (2.5.44), and using (2.5.9), (2.5.10), (2.5.45) and (2.5.46), gives

$$\begin{aligned}
&\sum_{r=1}^{m_1}\frac{\partial A_{1,r}}{\partial t}\langle M_{1,r},\; M_{1,k}\rangle \;-\; \gamma\sum_{r=1}^{m_1}B_{1,r}\langle M_{1,r},\; M_{1,k}\rangle \\
&= -\sum_{\ell=1}^{J_1}g\Big(\frac{\rho_{1,\ell}-\rho_{1,\ell-1}}{\rho_{1,1}}\Big)\frac{\partial\zeta_{1,\ell-1}}{\partial x}\,a_{1,\ell-1,k} \;+\; \frac{\tau_{sx}}{\rho_{1,1}H_1}M_{1,k}(0) + \widetilde{X}_{1,1}\,a_{1,0,k} \\
&\quad - \frac{\alpha_1}{H_1^2}\sum_{r=1}^{m_1}A_{1,r}\sum_{\ell=1}^{J_1}\Big(\frac{\rho_{1,\ell}}{\rho_{1,1}}\int_{\xi_{1,\ell-1}}^{\xi_{1,\ell}}\mu_{1,\ell}\frac{dM_{1,r}}{d\sigma_1}\frac{dM_{1,k}}{d\sigma_1}d\sigma_1\Big), \qquad k = 1,\cdots,m_1,
\end{aligned} \tag{2.5.47}$$

and

$$\sum_{r=1}^{m_2} \frac{\partial A_{2,r}}{\partial t}\langle M_{2,r},\ M_{2,k}\rangle \ -\ \gamma \sum_{r=1}^{m_2} B_{2,r}\langle M_{2,r},\ M_{2,k}\rangle$$

$$\begin{aligned} = & -\sum_{\ell=1}^{J_1} g\Big(\frac{\rho_{1,\ell}-\rho_{1,\ell-1}}{\rho_{2,1}}\Big)\frac{\partial \zeta_{1,\ell-1}}{\partial x}\, a_{2,0,k} - \sum_{\ell=1}^{J_2} g\Big(\frac{\rho_{2,\ell}-\rho_{2,\ell-1}}{\rho_{2,1}}\Big)\frac{\partial \zeta_{2,\ell-1}}{\partial x}\ a_{2,\ell-1,k} \\ & - \frac{\tau_{bx}}{\rho_{2,1}H_2} M_{2,k}(1) + \widetilde{X}_{2,1}\, a_{2,0,k} \\ & - \frac{\alpha_2}{H_2^2}\sum_{r=1}^{m_2} A_{2,r} \sum_{\ell=1}^{J_2}\Big(\frac{\rho_{2,\ell}}{\rho_{2,1}}\int_{\xi_{2,\ell-1}}^{\xi_{2,\ell}} \mu_{2,\ell}\frac{dM_{2,r}}{d\sigma_2}\frac{dM_{2,k}}{d\sigma_2}d\sigma_2\Big), \qquad k=1,\cdots,m_2. \end{aligned} \tag{2.5.48}$$

The equations for V_1, V_2 can be derived in a similar manner, but the details are omitted for simplicity.

Substituting (2.5.40) and (2.5.41) into (2.4.9), we obtain the equations of continuity for the upper and lower domains

$$\begin{aligned} & \frac{\partial \zeta_{1,j}}{\partial t} + \sum_{r=1}^{m_1} H_1\Big(\frac{\partial A_{1,r}}{\partial x} + \frac{\partial B_{1,r}}{\partial y}\Big)a_{1,j,r} \\ & \qquad + \sum_{r=1}^{m_2} H_2\Big(\frac{\partial A_{2,r}}{\partial x} + \frac{\partial B_{2,r}}{\partial y}\Big)a_{2,0,r} = 0, \qquad j=0,\cdots,J_1-1, \end{aligned} \tag{2.5.49}$$

$$\frac{\partial \zeta_{2,j}}{\partial t} + \sum_{r=1}^{m_2} H_2\Big(\frac{\partial A_{2,r}}{\partial x} + \frac{\partial B_{2,r}}{\partial y}\Big)a_{2,j,r} = 0, \qquad j=0,\cdots,J_2-1. \tag{2.5.50}$$

For the upper domain, Ω_1, the U and V equations can be written in matrix form as

$$\begin{aligned} \mathbf{C}_1\mathbf{A}_1^{\bullet} = \ & \gamma\mathbf{C}_1\mathbf{B}_1 + \frac{\tau_{sx}}{\rho_{1,1}H_1}\mathbf{E}_1^s + \widetilde{X}_{1,1}\mathbf{E}_1^{(1)} - \frac{\alpha_1}{H_1^2}\mathbf{D}_1\mathbf{A}_1, \\ & - \sum_{\ell=1}^{J_1} g\Big(\frac{\rho_{1,\ell}-\rho_{1,\ell-1}}{\rho_{1,1}}\Big)\frac{\partial \zeta_{1,\ell-1}}{\partial x}\mathbf{E}_1^{(\ell)} \end{aligned} \tag{2.5.51}$$

$$\begin{aligned} \mathbf{C}_1\mathbf{B}_1^{\bullet} = & -\gamma\mathbf{C}_1\mathbf{A}_1 + \frac{\tau_{sy}}{\rho_{1,1}H_1}\mathbf{E}_1^s + \widetilde{Y}_{1,1}\mathbf{E}_1^{(1)} - \frac{\alpha_1}{H_1^2}\mathbf{D}_1\mathbf{B}_1 \\ & - \sum_{\ell=1}^{J_1} g\Big(\frac{\rho_{1,\ell}-\rho_{1,\ell-1}}{\rho_{1,1}}\Big)\frac{\partial \zeta_{1,\ell-1}}{\partial y}\mathbf{E}_1^{(\ell)} \end{aligned} \tag{2.5.52}$$

Similarly for the lower domain Ω_2, one obtains

$$\begin{aligned}\mathbf{C}_2\mathbf{A}_2^{\bullet} = \quad & \gamma\mathbf{C}_2\mathbf{B}_2 - \frac{\tau_{bx}}{\rho_{2,1}H_2}\mathbf{E}_2^b + \widetilde{X}_{2,1}\mathbf{E}_2^{(1)} - \frac{\alpha_2}{H_2^2}\mathbf{D}_2\mathbf{A}_2 \\ & - \sum_{\ell=1}^{J_1} g\Big(\frac{\rho_{1,\ell}-\rho_{1,\ell-1}}{\rho_{2,1}}\Big)\frac{\partial\zeta_{1,\ell-1}}{\partial x}\mathbf{E}_2^{(1)} \\ & - \sum_{\ell=1}^{J_2} g\Big(\frac{\rho_{2,\ell}-\rho_{2,\ell-1}}{\rho_{2,1}}\Big)\frac{\partial\zeta_{2,\ell-1}}{\partial x}\mathbf{E}_2^{(\ell)}.\end{aligned} \tag{2.5.53}$$

$$\begin{aligned}\mathbf{C}_2\mathbf{B}_2^{\bullet} = & -\gamma\mathbf{C}_2\mathbf{A}_2 - \frac{\tau_{by}}{\rho_{2,1}H_2}\mathbf{E}_2^b + \widetilde{Y}_{2,1}\mathbf{E}_2^{(1)} - \frac{\alpha_2}{H_2^2}\mathbf{D}_2\mathbf{B}_2 \\ & - \sum_{\ell=1}^{J_1} g\Big(\frac{\rho_{1,\ell}-\rho_{1,\ell-1}}{\rho_{2,1}}\Big)\frac{\partial\zeta_{1,\ell-1}}{\partial y}\mathbf{E}_2^{(1)} \\ & - \sum_{\ell=1}^{J_2} g\Big(\frac{\rho_{2,\ell}-\rho_{2,\ell-1}}{\rho_{2,1}}\Big)\frac{\partial\zeta_{2,\ell-1}}{\partial y}\mathbf{E}_2^{(\ell)},\end{aligned} \tag{2.5.54}$$

The continuity equations can be written in matrix form,

$$\mathbf{Z}_1^{\bullet} = -\sum_{i=1}^{2} H_i\mathbf{E}_i(\mathbf{A}_i' + \mathbf{B}_i'), \tag{2.5.55}$$

$$\mathbf{Z}_2^{\bullet} = -H_2\mathbf{E}_2(\mathbf{A}_2' + \mathbf{B}_2'). \tag{2.5.56}$$

The definition of the matrices appearing in (2.5.51) to (2.5.56) are found from (2.5.21) to (2.5.29) by setting $i = 1, 2$.

Note that for the Galerkin solutions of the domain Ω_1, the boundary conditions imposed at the top and bottom of the domain are all natural conditions and therefore no corrections to the matrix integrals are needed. The bottom boundary conditions for the domain Ω_2 are treated in a way similar to the one domain system. For the case of the no-slip bottom boundary condition the modified $(m_2 - 1)$ th and $(m_2 - 2)$ th basis functions are obtained from (2.5.32) and (2.5.33) by setting $i = 2$. The layer-averaged and domain-averaged horizontal components of current are obtained in (2.5.35) to (2.5.38) by setting $i = 1, 2$.

2.6 Solutions via the use of a Galerkin method applied over the vertical space domain: a basis set of eigenfunctions

This section describes Galerkin solutions in terms of a basis set of eigenfunctions which satisfy a Sturm-Liouville eigenvalue problem resulting from the spectral decomposition of the second-order vertical diffusivity operator. The solution procedure is similar to that described in Section 2.5 although the final set of equations for the coefficients of the eigenfunction expansion is quite different from those of the B-spline expansion. In this section it is assumed that the eigenfunctions have been found by either numerical or analytical means. The details of the construction of these eigenfunctions are described in Chapter 3.

As seen in Section 2.4, it is necessary to introduce a set of weighted scalar products which depend upon the domain structure of the system. For a one domain system, a set of eigenvalues and eigenfunctions spanning the entire depth is defined to represent the solutions of the system, whereas for the two domain system two independent sets of eigenvalues and eigenfunctions spanning upper and lower domains are defined. In contrast to the B-splines, the eigenfunctions belong to a global basis set and their structure is determined by the variation in density and eddy viscosity through the vertical. The formulation of spectral solutions is facilitated by representing the local form of the eigenfunction of the j th layer as

$$f_i(\sigma_i) = f_{i[j]}(\sigma_i), \qquad \text{for} \quad \xi_{i,j-1} \leq \sigma_i \leq \xi_{i,j}, \tag{2.6.1}$$

and the local form of r th eigenfunction of the j th layer as

$$f_{i,r}(\sigma_i) = f_{i,j,r}(\sigma_i), \qquad \text{for} \quad \xi_{i,j-1} \leq \sigma_i \leq \xi_{i,j} \qquad r = 1, 2, \cdots, m_i, \tag{2.6.2}$$

where $i = 0, 1, 2,\ j = 1, \cdots, J_i$. The local forms of eigenfunctions of each layer (often called piecewise eigenfunctions) will be used for clarity of the solution procedure.

Galerkin solutions are sought with respect to the scalar product (2.5.4) for Ω_0, and with respect to (2.5.39) for Ω_i, $i = 1, 2$. The vertical variation of eddy viscosity over each domain is assumed to be given by (2.5.5) and (2.5.42), respectively.

2.6.1 One domain solutions

The two components of horizontal current, U_0 and V_0, are expanded using m_0 depth varying continuous functions, so that

$$U_0(x, y, \sigma_0, t) = \sum_{r=1}^{m_0} A_{0,r}(x, y, t)\, f_{0,r}(\sigma_0)\ , \tag{2.6.3}$$

$$V_0(x, y, \sigma_0, t) = \sum_{r=1}^{m_0} B_{0,r}(x, y, t)\, f_{0,r}(\sigma_0), \tag{2.6.4}$$

where the coefficients $A_{0,r}$ and $B_{0,r}$ are to be determined. Using local forms of the continuous functions, the expressions (2.6.3) and (2.6.4) may be represented as follows:

$$U_{0,j}(x, y, \sigma_0, t) = \sum_{r=1}^{m_0} A_{0,r}(x, y, t)\ f_{0,j,r}(\sigma_0)\ , \qquad \xi_{0,j-1} \le \sigma_0 \le \xi_{0,j}, \tag{2.6.5}$$

$$V_{0,j}(x, y, \sigma_0, t) = \sum_{r=1}^{m_0} B_{0,r}(x, y, t)\ f_{0,j,r}(\sigma_0)\ , \qquad \xi_{0,j-1} \le \sigma_0 \le \xi_{0,j}, \tag{2.6.6}$$

where $j = 1, \cdots, J_i$.

Taking the scalar product (2.5.4) of equation (2.4.5) with $f_{0,j,k}$ gives

$$\begin{aligned} \frac{\partial \langle U_{0,k} \rangle}{\partial t} - \gamma \langle V_{0,k} \rangle = &- \sum_{\ell=1}^{J_0} g\left(\frac{\rho_{0,\ell} - \rho_{0,\ell-1}}{\rho_{0,1}}\right) \frac{\partial \zeta_{0,\ell-1}}{\partial x}\ a_{0,\ell-1,k} \\ &+\ \widetilde{X}_{0,1}\, a_{0,0,k} + I_{0,k}, \end{aligned} \tag{2.6.7}$$

where

$$\langle U_{i,k} \rangle = \langle U_i, f_{i,j,k} \rangle = \sum_{j=1}^{J_i} \left(\frac{\rho_{i,j}}{\rho_{i,1}} \int_{\xi_{i,j-1}}^{\xi_{i,j}} U_{i,j}\, f_{i,j,k}\ d\sigma_i \right)\ , \tag{2.6.8}$$

$$\langle V_{i,k}\rangle = \langle V_i, f_{i,j,k}\rangle = \sum_{j=1}^{J_i}\left(\frac{\rho_{i,j}}{\rho_{i,1}}\int_{\xi_{i,j-1}}^{\xi_{i,j}} V_{i,j}\, f_{i,j,k}\; d\sigma_i\right), \tag{2.6.9}$$

$$a_{i,\ell,k} = \sum_{j=\ell+1}^{J_i}\int_{\xi_{i,j-1}}^{\xi_{i,j}} f_{i,j,k}\; d\sigma_i \;= \int_{\xi_{i,\ell}}^{1} f_{i,k}\; d\sigma_i, \tag{2.6.10}$$

and

$$I_{i,k} = \frac{\alpha_i}{H_i^2}\sum_{j=1}^{J_i}\left\{\frac{\rho_{i,j}}{\rho_{i,1}}\int_{\xi_{i,j-1}}^{\xi_{i,j}}\frac{\partial}{\partial\sigma_i}\left(\mu_{i,j}\frac{\partial U_{i,j}}{\partial\sigma_i}\right) f_{i,j,k}\; d\sigma_i,\right\} \tag{2.6.11}$$

with $i = 0$, $k = 1, \cdots, m_i$.

Integrating (2.6.11) by parts twice yields

$$\begin{aligned} I_{0,k} = \; & -\frac{1}{\rho_{0,1}H_0}\sum_{j=1}^{J_0}\left\{\tau_{zx}(\xi_{0,j})\; f_{0,j,k}(\xi_{0,j}) - \tau_{zx}(\xi_{0,j-1})\; f_{0,j,k}(\xi_{0,j-1})\right\} \\ & - \frac{\alpha_0}{H_0^2}\sum_{j=1}^{J_0}\left[\frac{\rho_{0,j}}{\rho_{0,1}}\left(\mu_{0,j}\frac{df_{0,j,k}}{d\sigma_0}\right)U_{0,j}\right]_{\xi_{0,j-1}}^{\xi_{0,j}} \\ & + \frac{\alpha_0}{H_0^2}\sum_{j=1}^{J_0}\left\{\frac{\rho_{0,j}}{\rho_{0,1}}\int_{\xi_{0,j-1}}^{\xi_{0,j}} U_{0,j}\,\frac{d}{d\sigma_0}\left(\mu_{0,j}\frac{df_{0,j,k}}{d\sigma_0}\right)d\sigma_0\right\}. \end{aligned} \tag{2.6.12}$$

Substituting the sea surface and bottom boundary conditions (2.4.10) and (2.4.12), and using the interfacial conditions (2.4.13) and (2.4.14), gives

$$\begin{aligned} I_{0,k} = & -\frac{\tau_{bx}}{\rho_{0,B}H_0}f_{0,B,k}(1) + \frac{\tau_{sx}}{\rho_{0,1}H_0}f_{0,1,k}(0) \\ & - \frac{\alpha_0}{H_0^2}\left\{\frac{\rho_{0,B}}{\rho_{0,1}}\left(\mu_{0,B}\frac{df_{0,B,k}}{d\sigma_0}\right)_b U_{0,B}(1) - \left(\mu_{0,1}\frac{df_{0,1,k}}{d\sigma_0}\right)_s U_{0,1}(0)\right\} \\ & + \frac{\alpha_0}{H_0^2}\sum_{j=1}^{J_0}\left\{\frac{\rho_{0,j}}{\rho_{0,1}}\int_{\xi_{0,j-1}}^{\xi_{0,j}} U_{0,j}\;\frac{d}{d\sigma_0}\left(\mu_{0,j}\frac{df_{0,j,k}}{d\sigma_0}\right)d\sigma_0\right\}, \end{aligned} \tag{2.6.13}$$

where $k = 1, \cdots, m_0$ and the suffixes s and b in the second row of (2.6.13) denote evaluation at $\sigma_0 = 0$ and 1, respectively.

Substituting the expansions (2.6.5) and (2.6.6) into (2.6.7), using (2.6.8),

(2.6.9) and (2.6.13), yields

$$\begin{aligned}
&\sum_{r=1}^{m_0}\frac{\partial A_{0,r}}{\partial t}\Big\langle f_{0,\ell,r},\ f_{0,\ell,k}\Big\rangle\ -\ \gamma\sum_{r=1}^{m_0}B_{0,r}\Big\langle f_{0,\ell,r},\ f_{0,\ell,k}\Big\rangle \\
&=-\sum_{\ell=1}^{J_0}g\Big(\frac{\rho_{0,\ell}-\rho_{0,\ell-1}}{\rho_{0,1}}\Big)\frac{\partial\zeta_{0,\ell-1}}{\partial x}\ a_{0,\ell-1,k} \\
&\quad-\frac{\tau_{bx}}{\rho_{0,B}H_0}f_{0,B,k}(1)+\frac{\tau_{sx}}{\rho_{0,1}H_0}f_{0,1,k}(0)+\widetilde{X}_{0,1}\,a_{0,0,k} \qquad (2.6.14)\\
&\quad-\frac{\alpha_0}{H_0^2}\sum_{r=1}^{m_0}A_{0,r}\Big\{\frac{\rho_{0,B}}{\rho_{0,1}}\Big(\mu_{0,B}\frac{df_{0,B,k}}{d\sigma_0}\Big)_1 f_{0,B,r}(1)-\Big(\mu_{0,1}\frac{df_{0,1,k}}{d\sigma_0}\Big)_0 f_{0,1,r}(0)\Big\} \\
&\quad+\frac{\alpha_0}{H_0^2}\sum_{r=1}^{m_0}A_{0,r}\sum_{j=1}^{J_0}\Big\{\frac{\rho_{0,j}}{\rho_{0,1}}\int_{\xi_{0,j-1}}^{\xi_{0,j}}f_{0,j,r}\frac{d}{d\sigma_0}\Big(\mu_{0,j}\frac{df_{0,j,k}}{d\sigma_0}\Big)d\sigma_0\Big\},
\end{aligned}$$

where $k=1,\cdots,m_0$.

Up to this point the procedure is essentially the same as that of the basis set of B-spline functions except that the integration by parts is applied twice. Following Heaps (1983), a spectral basis is determined by finding solutions to

$$\frac{d}{d\sigma_0}\Big(\mu_{0,j}\frac{df_{0[j]}}{d\sigma_0}\Big)=-\lambda_0\,f_{0[j]},\qquad j=1,\cdots,J_i, \qquad (2.6.15)$$

subject to separable *limit conditions*

$$\Big(\mu_{0,1}\frac{df_{0[1]}}{d\sigma_0}\Big)_0=\beta_{0,1}f_{0[1]}(0), \qquad (2.6.16)$$

$$\Big(\mu_{0,B}\frac{df_{0[B]}}{d\sigma_0}\Big)_1=\beta_{0,2}f_{0[B]}(1), \qquad (2.6.17)$$

and interfacial conditions

$$\left.\begin{aligned}
f_{0[j]}(\xi_{0,j}) &= f_{0[j+1]}(\xi_{0,j}) \\
\Big(\mu_{0,j}\frac{df_{0[j]}}{d\sigma_0}\Big)_{\xi_{0,j}} &= \frac{\rho_{0,j+1}}{\rho_{0,j}}\Big(\mu_{0,j+1}\frac{df_{0[j+1]}}{d\sigma_0}\Big)_{\xi_{0,j}}
\end{aligned}\right\}\quad j=1,\cdots,J_0-1. \qquad (2.6.18)$$

Equations (2.6.15) to (2.6.18) constitute a multilayered eigenvalue problem, giving a sequence of real-valued eigenvalues and eigenfunctions which have the orthogonality property

$$\langle f_{0,j,r},\ f_{0,j,k}\rangle = \sum_{j=1}^{J_0}\left(\frac{\rho_{0,j}}{\rho_{0,1}}\int_{\xi_{0,j-1}}^{\xi_{0,j}} f_{0,j,r}f_{0,j,k}\ d\sigma_0\right) = 0 \quad \text{for} \quad r \neq k. \tag{2.6.19}$$

Details on the limit conditions of the eigenfunctions will be described in Chapter 3 in conjunction with their numerical determination.

Let $\lambda_{i,k}$ and $f_{i,k}$, $i = 0$, $k = 1, \cdots, m_i$, be a set of eigenvalues and eigenfunctions satisfying the Sturm-Liouville type boundary problem represented by equations (2.6.15) to (2.6.18). Then, (2.6.14) becomes

$$\begin{aligned}\frac{\partial A_{i,k}}{\partial t} = \gamma B_{i,k} - \sum_{\ell=1}^{J_i} g\left(\frac{\rho_{i,\ell}-\rho_{i,\ell-1}}{\rho_{i,1}}\right)\frac{\partial \zeta_{i,\ell-1}}{\partial x}\, a_{i,\ell-1,k}\,\Phi_{i,k} \\ + \widetilde{X}_{i,1}\, a_{i,0,k}\,\Phi_{i,k} - \frac{\alpha_i}{H_i^2}\lambda_{i,k}A_{i,k} + (J^x_{i,k}+K^x_{i,k})\Phi_{i,k},\end{aligned} \tag{2.6.20}$$

where

$$J^x_{i,k} = \frac{\tau_{sx}}{\rho_{i,1}H_i}f_{i,k}(0) - \frac{\tau_{bx}}{\rho_{i,1}H_i}f_{i,k}(1), \tag{2.6.21}$$

$$K^x_{i,k} = \frac{\alpha_i}{H_i^2}\sum_{r=1}^{m_i} A_{i,r}\left\{\beta_{i,1}f_{i,k}(0)f_{i,r}(0) - \rho_{i,B}\rho_{i,1}^{-1}\beta_{i,2}f_{i,k}(1)f_{i,r}(1)\right\}, \tag{2.6.22}$$

$$\Phi_{i,k} = \left\langle f_{i,j,k},\ f_{i,j,k}\right\rangle^{-1} = \left(\sum_{j=1}^{J_i}\frac{\rho_{i,j}}{\rho_{i,1}}\int_{\xi_{i,j-1}}^{\xi_{i,j}} f^2_{i,j,k}\ d\sigma_i\right)^{-1}, \tag{2.6.23}$$

and $i = 0$, $k = 1, \cdots, m_i$.

Similarly,

$$\begin{aligned}\frac{\partial B_{i,k}}{\partial t} = -\gamma A_{i,k} - \sum_{\ell=1}^{J_i} g\left(\frac{\rho_{i,\ell}-\rho_{i,\ell-1}}{\rho_{i,1}}\right)\frac{\partial \zeta_{i,\ell-1}}{\partial y}\, a_{i,\ell-1,k}\,\Phi_{i,k} \\ + \widetilde{Y}_{i,1}\, a_{i,0,k}\,\Phi_{i,k} - \frac{\alpha_i}{H_i^2}\lambda_{i,k}B_{i,k} + (J^y_{i,k}+K^y_{i,k})\Phi_{i,k},\end{aligned} \tag{2.6.24}$$

where

$$J^y_{i,k} = \frac{\tau_{sy}}{\rho_{i,1} H_i} f_{i,k}(0) - \frac{\tau_{by}}{\rho_{i,1} H_i} f_{i,k}(1), \tag{2.6.25}$$

$$K^y_{i,k} = \frac{\alpha_i}{H_i^2} \sum_{r=1}^{m_i} B_{i,r} \left\{ \beta_{i,1} f_{i,k}(0) f_{i,r}(0) - \rho_{i,B} \rho_{i,1}^{-1} \beta_{i,2} f_{i,k}(1) f_{i,r}(1) \right\}, \tag{2.6.26}$$

and $i = 0$, $k = 1, \cdots, m_i$.

Substituting (2.6.5) and (2.6.6) into (2.4.9) gives the continuity equation of the form

$$\frac{\partial \zeta_{i,j}}{\partial t} + H_i \sum_{r=1}^{m_i} \left\{ \frac{\partial A_{i,r}}{\partial x} + \frac{\partial B_{i,r}}{\partial y} \right\} a_{i,j,r} = 0, \tag{2.6.27}$$

where $i = 0$, $j = 0, \cdots, J_i - 1$.

The vertical modes in equations (2.6.20) and (2.6.24) are coupled through the terms for the bottom friction

$$\tau_{bx} = \rho_{i,B} \; k_b \sum_{r=1}^{m_i} A_{i,r} f_{i,r}(1), \tag{2.6.28}$$

$$\tau_{by} = \rho_{i,B} \; k_b \sum_{r=1}^{m_i} B_{i,r} f_{i,r}(1), \tag{2.6.29}$$

and the *stressing* terms $K^x_{i,k}$, $K^y_{i,k}$ which involve $\beta_{0,1}$ and $\beta_{0,2}$. In this case, a matrix inversion is required to solve for the coefficients of the eigenfunction expansion. With $\beta_{0,1} = 0$ and $\beta_{0,2} = \infty$ or $\beta_{0,2} = k_b = 0$, the system of equations becomes uncoupled.

Consider the alternative expansion of the $U_{i,j}$ and $V_{i,j}$ velocities used in a series of works by Heaps, namely,

$$U_{i,j}(x, y, \sigma_i, t) = \sum_{r=1}^{m_i} \widehat{A}_{i,r}(x, y, t) \, \Phi_{i,r} \, f_{i,j,r}(\sigma_i) \quad \text{for} \quad \xi_{i,j-1} \leq \sigma_i \leq \xi_{i,j}, \tag{2.6.30}$$

$$V_{i,j}(x, y, \sigma_i, t) = \sum_{r=1}^{m_i} \widehat{B}_{i,r}(x, y, t) \, \Phi_{i,r} \, f_{i,j,r}(\sigma_i) \quad \text{for} \quad \xi_{i,j-1} \leq \sigma_i \leq \xi_{i,j}. \tag{2.6.31}$$

With the use of the relations

$$A_{i,r} \to \widehat{A}_{i,r}\Phi_{i,r}, \qquad B_{i,r} \to \widehat{B}_{i,r}\Phi_{i,r}, \tag{2.6.32}$$

(2.6.20) and (2.6.24) reduce to

$$\begin{aligned}\frac{\partial \widehat{A}_{i,k}}{\partial t} = \; & \gamma \widehat{B}_{i,k} \; - \sum_{\ell=1}^{J_i} g\left(\frac{\rho_{i,\ell} - \rho_{i,\ell-1}}{\rho_{i,1}}\right)\frac{\partial \zeta_{i,\ell-1}}{\partial x}\, a_{i,\ell-1,k} \\ & + \widetilde{X}_{i,1}\, a_{i,0,k} - \frac{\alpha_i}{H_i^2}\lambda_{i,k}\widehat{A}_{i,k} + (J^x_{i,k} + K^x_{i,k}),\end{aligned} \tag{2.6.33}$$

$$\begin{aligned}\frac{\partial \widehat{B}_{i,k}}{\partial t} = & -\gamma \widehat{A}_{i,k} \; - \sum_{\ell=1}^{J_i} g\left(\frac{\rho_{i,\ell} - \rho_{i,\ell-1}}{\rho_{i,1}}\right)\frac{\partial \zeta_{i,\ell-1}}{\partial y}\, a_{i,\ell-1,k} \\ & + \widetilde{Y}_{i,1}\, a_{i,0,k} - \frac{\alpha_i}{H_i^2}\lambda_{i,k}\widehat{B}_{i,k} + (J^y_{i,k} + K^y_{i,k}),\end{aligned} \tag{2.6.34}$$

where

$$J^x_{i,k} = \frac{\tau_{sx}}{\rho_{i,1}H_i} f_{i,k}(0) - \frac{\tau_{bx}}{\rho_{i,1}H_i} f_{i,k}(1), \tag{2.6.35}$$

$$J^y_{i,k} = \frac{\tau_{sy}}{\rho_{i,1}H_i} f_{i,k}(0) - \frac{\tau_{by}}{\rho_{i,1}H_i} f_{i,k}(1), \tag{2.6.36}$$

$$K^x_{i,k} = \frac{\alpha_i}{H_i^2}\sum_{r=1}^{m_i} \widehat{A}_{i,r}\Phi_{i,r}\left\{\beta_{i,1} f_{i,k}(0) f_{i,r}(0) - \rho_{i,B}\rho_{i,1}^{-1}\beta_{i,2} f_{i,k}(1) f_{i,r}(1)\right\}, \tag{2.6.37}$$

$$K^y_{i,k} = \frac{\alpha_i}{H_i^2}\sum_{r=1}^{m_i} \widehat{B}_{i,r}\Phi_{i,r}\left\{\beta_{i,1} f_{i,k}(0) f_{i,r}(0) - \rho_{i,B}\rho_{i,1}^{-1}\beta_{i,2} f_{i,k}(1) f_{i,r}(1)\right\}, \tag{2.6.38}$$

$$\tau_{bx} = \rho_{i,B} k_b \sum_{r=1}^{m_i} \widehat{A}_{i,r}\Phi_{i,r} f_{i,r}(1), \tag{2.6.39}$$

$$\tau_{by} = \rho_{i,B} k_b \sum_{r=1}^{m_i} \widehat{B}_{i,r}\Phi_{i,r} f_{i,r}(1), \tag{2.6.40}$$

and $i = 0$, $k = 1, \cdots, m_i$.

The continuity equation takes the form

$$\frac{\partial \zeta_{0,j}}{\partial t} + H_0 \sum_{r=1}^{m}\left\{\frac{\partial A_{0,r}}{\partial x} + \frac{\partial B_{0,r}}{\partial y}\right\}\Phi_{0,r}\, a_{0,j,r} = 0, \tag{2.6.41}$$

where $i = 0$, $j = 0, \cdots, J_i - 1$.

In applying the basis set of eigenfunctions in Chapters 4 and 5 we will employ Heaps' formulation. Hence we write (2.6.33) and (2.6.34) here in matrix form as

$$\begin{aligned}
\widehat{\mathbf{A}}_i^{\bullet} = & \ \iota\gamma\widehat{\mathbf{B}}_i - \frac{\alpha_i}{H_i^2}\mathbf{\Lambda}_i\widehat{\mathbf{A}}_i \\
& + \frac{\alpha_i}{H_{i,1}^2}\Big(\beta_{i,1}\mathbf{C}^s - \rho_{i,B}\rho_{i,1}^{-1}\beta_{i,2}\mathbf{C}^b\Big)\widehat{\mathbf{A}}_i + \Big(\frac{\tau_{sx}}{\rho_{i,1}H_i}\mathbf{E}_i^s - \frac{\tau_{bx}}{\rho_{i,1}H_i}\mathbf{E}_i^b\Big) \\
& - \sum_{\ell=1}^{J_i} g\Big(\frac{\rho_{i,\ell} - \rho_{i,\ell-1}}{\rho_{i,1}}\Big)\frac{\partial\zeta_{i,\ell-1}}{\partial x}\mathbf{E}_i^{(\ell)} + \widetilde{X}_{i,1}\mathbf{E}_i^{(1)}, \qquad (2.6.42)
\end{aligned}$$

$$\begin{aligned}
\widehat{\mathbf{B}}_i^{\bullet} = & -\iota\gamma\widehat{\mathbf{A}}_i - \frac{\alpha_i}{H_i^2}\mathbf{\Lambda}_i\widehat{\mathbf{B}}_i \\
& + \frac{\alpha_i}{H_{i,1}^2}\Big(\beta_{i,1}\mathbf{C}^s - \rho_{i,B}\rho_{i,1}^{-1}\beta_{i,2}\mathbf{C}^b\Big)\widehat{\mathbf{B}}_i + \Big(\frac{\tau_{sy}}{\rho_{i,1}H_i}\mathbf{E}_i^s - \frac{\tau_{by}}{\rho_{i,1}H_i}\mathbf{E}_i^b\Big) \\
& - \sum_{\ell=1}^{J_i} g\Big(\frac{\rho_{i,\ell} - \rho_{i,\ell-1}}{\rho_{i,1}}\Big)\frac{\partial\zeta_{i,\ell-1}}{\partial y}\mathbf{E}_i^{(\ell)} + \widetilde{Y}_{i,1}\mathbf{E}_i^{(1)}, \qquad (2.6.43)
\end{aligned}$$

and (2.6.41) becomes

$$\mathbf{Z}_i^{\bullet} + \ H_i\mathbf{E}_i^H\big(\mathbf{A}_i' + \mathbf{B}_i'\big) = 0, \qquad (2.6.44)$$

where $i = 0$. In these equations:

$\widehat{\mathbf{A}}_i$ and $\widehat{\mathbf{B}}_i$ are column vectors of length m_i with kth element

$$\widehat{A}_{i,k} \quad \text{and} \quad \widehat{B}_{i,k}, \ \text{respectively;} \qquad (2.6.45)$$

$\widehat{\mathbf{A}}_i^{\bullet}$ and $\widehat{\mathbf{B}}_i^{\bullet}$ are column vectors of m_i with kth element

$$\frac{\partial\widehat{A}_{i,k}}{\partial t} \quad \text{and} \quad \frac{\partial\widehat{B}_{i,k}}{\partial t}, \ \text{respectively;} \qquad (2.6.46)$$

$\mathbf{Z}_i^{\bullet}$ is a column vector of length m_i with kth element

$$\frac{\partial\zeta_{i,k}}{\partial t}; \qquad (2.6.47)$$

$\widehat{\mathbf{A}}_i'$ and $\widehat{\mathbf{B}}_i'$ are column vectors of length m_i with k th element

$$\frac{\partial \widehat{A}_{i,k}}{\partial x} \quad \text{and} \quad \frac{\partial \widehat{B}_{i,k}}{\partial y}, \text{ respectively;} \tag{2.6.48}$$

$\mathbf{C}^s$ is a matrix of order $m_i \times m_i$ with $(r,\ k)$ th element

$$\Phi_{i,r} f_{i,r}(0) f_{i,k}(0); \tag{2.6.49}$$

$\mathbf{C}^b$ is a matrix of order $m_i \times m_i$ with $(r,\ k)$ th element

$$\Phi_{i,r} f_{i,r}(1) f_{i,k}(1); \tag{2.6.50}$$

$\mathbf{E}_i^H$ is a matrix of order $m_i \times m_i$ with (r, k) th element

$$\Phi_{i,k} \int_{\xi_{i,r-1}}^{1} f_{i,k}\ d\sigma_i; \tag{2.6.51}$$

$\mathbf{E}_i^{(\ell)}$, $\ell = 1, \cdots, J_i$, is a column vector of length m_i with k th element

$$\int_{\xi_{i,\ell-1}}^{1} f_{i,k}\ d\sigma_i; \tag{2.6.52}$$

$\mathbf{E}_i^s$ and $\mathbf{E}_i^b$ are column vectors of length m_i with k th element

$$f_{i,k}(0) \quad \text{and} \quad f_{i,k}(1), \text{ respectively;} \tag{2.6.53}$$

and $\mathbf{\Lambda}$ is a matrix of eigenvalues, that is, with (r, k) th element

$$\Lambda_{i,r,k} = \begin{cases} \lambda_{i,k}, \\ 0 \end{cases}. \tag{2.6.54}$$

Once the coefficients of the eigenfunction expansions are computed from equations (2.6.42), (2.6.43) and (2.6.44), along with the appropriate initial conditions and lateral boundary conditions, the two components of horizontal current at depth σ_0 are obtained from (2.6.30) and (2.6.31), respectively.

The layer-averaged velocities over each layer $\Omega_{i,j}$, with $a_{i,0,r} = 0$, are derived as

$$\overline{U}_{i,j} = \frac{1}{\Delta\xi_{i,j}} \sum_{r=1}^{m_i} \widehat{A}_{i,r}(x,y,t)\, \Phi_{i,r}(a_{i,j-1,r} - a_{i,j,r}), \tag{2.6.55}$$

$$\overline{V}_{i,j} = \frac{1}{\Delta\xi_{i,j}} \sum_{r=1}^{m_i} \widehat{B}_{i,r}(x,y,t)\, \Phi_{i,r}(a_{i,j-1,r} - a_{i,j,r}), \tag{2.6.56}$$

and the domain-averaged velocities for Ω_i are derived as

$$\overline{U}_i(x,y,\sigma_i,t) = \sum_{r=1}^{m_i} \widehat{A}_{i,r}(x,y,t)\, \Phi_{i,r}\, a_{i,0,r}, \tag{2.6.57}$$

$$\overline{V}_i(x,y,\sigma_i,t) = \sum_{r=1}^{m_i} \widehat{B}_{i,r}(x,y,t)\, \Phi_{i,r}\, a_{i,0,r}, \tag{2.6.58}$$

with $i = 0$ and $j = 1, \cdots, J_i$.

2.6.2 Two domain solutions

Expanding the two components of horizontal current in terms of the coefficients $A_{i,r}(x,y,t)$ and $B_{i,r}(x,y,t)$ and eigenfunctions $f_{i,r}(\sigma_i)$ gives

$$U_i(x,y,\sigma_i,t) = \sum_{r=1}^{m_i} A_{i,r}(x,y,t)\, f_{i,r}(\sigma_i), \tag{2.6.59}$$

$$V_i(x,y,\sigma_i,t) = \sum_{r=1}^{m_i} B_{i,r}(x,y,t)\, f_{i,r}(\sigma_i), \tag{2.6.60}$$

where the coefficients $A_{i,r}$ and $B_{i,r}$, $i = 1, 2$, are to be determined. The expressions for $U_{i,j}$ and $V_{i,j}$, using the local forms of eigenfunctions, are

$$U_{i,j}(x,y,\sigma_i,t) = \sum_{r=1}^{m_i} A_{i,r}(x,y,t)\, f_{i,j,r}(\sigma_i), \qquad \xi_{i,j-1} \le \sigma_i \le \xi_{i,j}, \tag{2.6.61}$$

$$V_{i,j}(x,y,\sigma_i,t) = \sum_{r=1}^{m_i} B_{i,r}(x,y,t)\, f_{i,j,r}(\sigma_i), \qquad \xi_{i,j-1} \le \sigma_i \le \xi_{i,j}. \tag{2.6.62}$$

Without going into the details of the derivation, we will work out the final sets of spectral equations. By determining the eigenvalues and eigenfunctions from

$$\frac{d}{d\sigma_i}\left(\mu_{i,j}\frac{df_{i[j]}}{d\sigma_i}\right) = -\lambda_i f_{i[j]}, \qquad i=1,2,\ j=1,\cdots,J_i, \tag{2.6.63}$$

with limit conditions

$$\left.\begin{aligned}\left(\mu_{i,1}\frac{df_{i[1]}}{d\sigma_i}\right)_0 &= \beta_{i,1} f_{i[1]}(0),\\ \left(\mu_{i,B}\frac{df_{i[B]}}{d\sigma_i}\right)_1 &= \beta_{i,2} f_{i[B]}(1),\end{aligned}\right\} \qquad i=1,2, \tag{2.6.64}$$

and interfacial conditions

$$\left.\begin{aligned} f_{i[j]}(\xi_{i,j}) &= f_{i[j+1]}(\xi_{i,j})\\ \left(\mu_{i,j}\frac{df_{i[j]}}{d\sigma_i}\right)_{\xi_{i,j}} &= \frac{\rho_{i,j+1}}{\rho_{i,j}}\left(\mu_{i,j+1}\frac{df_{i,j+1}}{d\sigma_i}\right)_{\xi_{i,j}}\end{aligned}\right\} \quad i=1,2,\ j=1,\cdots,J_i-1, \tag{2.6.65}$$

we then arrive at the equations of the form

$$\begin{aligned}\frac{\partial A_{1,k}}{\partial t} &= \gamma B_{1,k} - (\alpha_1/H_1^2)\lambda_{1,k}A_{1,k} + (J^x_{1,k}+K^x_{1,k})\Phi_{1,k}\\ &\quad - \sum_{\ell=1}^{J_1} g\left(\frac{\rho_{1,\ell}-\rho_{1,\ell-1}}{\rho_{1,1}}\right)\frac{\partial \zeta_{1,\ell-1}}{\partial x}\, a_{1,\ell-1,k}\,\Phi_{1,k} + \widetilde{X}_{1,1}\, a_{1,0,k}\,\Phi_{1,k}, \end{aligned}\tag{2.6.66}$$

$$\begin{aligned}\frac{\partial A_{2,k}}{\partial t} &= \gamma B_{2,k} - (\alpha_2/H_2^2)\lambda_{2,k}A_{2,k} + (J^x_{2,k}+K^x_{2,k})\Phi_{2,k}\\ &\quad - \sum_{\ell=1}^{J_1} g\left(\frac{\rho_{1,\ell}-\rho_{1,\ell-1}}{\rho_{2,1}}\right)\frac{\partial \zeta_{1,\ell-1}}{\partial x}\, a_{2,0,k}\,\Phi_{2,k} + \widetilde{X}_{2,1}\, a_{2,0,k}\,\Phi_{2,k}\\ &\quad - \sum_{\ell=1}^{J_2} g\left(\frac{\rho_{2,\ell}-\rho_{2,\ell-1}}{\rho_{2,1}}\right)\frac{\partial \zeta_{2,\ell-1}}{\partial x}\, a_{2,\ell-1,k}\,\Phi_{2,k}, \end{aligned}\tag{2.6.67}$$

where

$$J^x_{1,k} = \frac{\tau_{sx}}{\rho_{1,1}H_1} f_{1,k}(0), \tag{2.6.68}$$

$$K^x_{1,k} = \frac{\alpha_1}{H_1^2} \sum_{r=1}^{m_1} A_{1,r}\Big(\beta_{1,1} f_{1,k}(0) f_{1,r}(0) - \rho_{1,B}\rho_{1,1}^{-1}\beta_{1,2} f_{1,k}(1) f_{1,r}(1)\Big), \quad (2.6.69)$$

$$J^x_{2,k} = -\frac{\tau_{bx}}{\rho_{2,1} H_2} f_{2,k}(1), \quad (2.6.70)$$

$$K^x_{2,k} = \frac{\alpha_i}{H_2^2} \sum_{r=1}^{m_1} A_{2,r}\Big(\beta_{2,1} f_{2,k}(0) f_{2,r}(0) - \rho_{2,B}\rho_{2,1}^{-1}\beta_{2,2} f_{2,k}(1) f_{2,r}(1)\Big), \quad (2.6.71)$$

with $k = 1, \cdots, m_i$. The terms $\Phi_{1,k}$ and $\Phi_{2,k}$ are found from (2.6.23) by setting $i = 1, 2$. It should be mentioned that choosing values of $\beta_{1,2} = \beta_{2,1} = 0$ is desirable to obtain satisfactory results because stress-free conditions are enforced at the interior domain boundary. For brevity, the corresponding V_i equations are omitted.

Substituting (2.6.61) and (2.6.62) into (2.4.9), we obtain the equations of continuity for the upper and lower domains

$$\frac{\partial \zeta_{1,j}}{\partial t} + \sum_{r=1}^{m_1} H_1\Big(\frac{\partial A_{1,r}}{\partial x} + \frac{\partial B_{1,r}}{\partial y}\Big) a_{1,0,r} + \sum_{r=1}^{m_2} H_2\Big(\frac{\partial A_{2,r}}{\partial x} + \frac{\partial B_{2,r}}{\partial y}\Big) a_{2,0,r} = 0, \quad j = 0, \cdots, J_1 - 1, \quad (2.6.72)$$

$$\frac{\partial \zeta_{2,j}}{\partial t} + \sum_{r=1}^{m_2} H_2\Big(\frac{\partial A_{2,r}}{\partial x} + \frac{\partial B_{2,r}}{\partial y}\Big) a_{2,0,r} = 0, \quad j = 0, \cdots, J_2 - 1. \quad (2.6.73)$$

By expanding the $U_{i,j}$ and $V_{i,j}$ velocities in a form

$$U_{i,j}(x, y, \sigma_i, t) = \sum_{r=1}^{m_i} \widehat{A}_{i,r}(x, y, t)\, \Phi_{i,r}\, f_{i,j,r}(\sigma_i) \quad \text{for} \quad \xi_{i,j-1} \le \sigma_i \le \xi_{i,j}, \quad (2.6.30)$$

$$V_{i,j}(x, y, \sigma_i, t) = \sum_{r=1}^{m_i} \widehat{B}_{i,r}(x, y, t)\, \Phi_{i,r}\, f_{i,j,r}(\sigma_i) \quad \text{for} \quad \xi_{i,j-1} \le \sigma_i \le \xi_{i,j}, \quad (2.6.31)$$

where $i = 0, 1, 2$, we get

$$\frac{\partial \widehat{A}_{1,k}}{\partial t} = \gamma \widehat{B}_{1,k} - (\alpha_1/H_1^2)\lambda_{1,k}\widehat{A}_{1,k} + (J^x_{1,k} + K^x_{1,k})$$

$$- \sum_{\ell=1}^{J_1} g\Big(\frac{\rho_{1,\ell}-\rho_{1,\ell-1}}{\rho_{1,1}}\Big)\frac{\partial\zeta_{1,\ell-1}}{\partial x}\,a_{1,\ell-1,k} + \widetilde{X}_{1,1}\,a_{1,0,k}, \tag{2.6.74}$$

$$\begin{aligned}\frac{\partial \widehat{A}_{2,k}}{\partial t} &= \gamma \widehat{B}_{2,k} - (\alpha_2/H_2^2)\lambda_{2,k}\widehat{A}_{2,k} + (J^x_{2,k}+K^x_{2,k}) \\ &\quad - \sum_{\ell=1}^{J_1} g\Big(\frac{\rho_{1,\ell}-\rho_{1,\ell-1}}{\rho_{2,1}}\Big)\frac{\partial\zeta_{1,\ell-1}}{\partial x}a_{2,0,k} + \widetilde{X}_{2,1}\,a_{2,0,k} \\ &\quad - \sum_{\ell=1}^{J_2} g\Big(\frac{\rho_{2,\ell}-\rho_{2,\ell-1}}{\rho_{2,1}}\Big)\frac{\partial\zeta_{2,\ell-1}}{\partial x}a_{2,\ell-1,k}\,,\end{aligned} \tag{2.6.75}$$

where $k = 1, \cdots, m_i$ and the terms $J^x_{i,k}$ and $K^x_{i,k}$ for Ω_1 and Ω_2 can be found from (2.6.68) to (2.6.71) by replacing $A_{i,r}$ by $\widehat{A}_{i,r}\Phi_{i,r}$.

The continuity equations take the form

$$\begin{aligned}&\frac{\partial\zeta_{1,j}}{\partial t} + \sum_{r=1}^{m_1} H_1\Big(\frac{\partial\widehat{A}_{1,r}}{\partial x}+\frac{\partial\widehat{B}_{1,r}}{\partial y}\Big)\Phi_{1,r}\,a_{1,0,r} \\ &\qquad + \sum_{r=1}^{m_2} H_2\Big(\frac{\partial\widehat{A}_{2,r}}{\partial x}+\frac{\partial\widehat{B}_{2,r}}{\partial y}\Big)\Phi_{2,r}\,a_{2,0,r} = 0, \quad j = 0,\cdots,J_1-1,\end{aligned} \tag{2.6.76}$$

$$\frac{\partial\zeta_{2,j}}{\partial t} + \sum_{r=1}^{m_2} H_2\Big(\frac{\partial\widehat{A}_{2,r}}{\partial x}+\frac{\partial\widehat{B}_{2,r}}{\partial y}\Big)\Phi_{2,r}\,a_{2,0,r} = 0, \quad j = 0,\cdots,J_2-1. \tag{2.6.77}$$

Writing (2.6.74) and (2.6.75) and the V equation of motion in matrix form leads to:

$$\begin{aligned}\widehat{\mathbf{A}}_1^{\bullet} = {}& \iota\gamma\widehat{\mathbf{B}}_1 - \frac{\alpha_1}{H_1^2}\mathbf{\Lambda}_1\widehat{\mathbf{A}}_1 + \frac{\alpha_1}{H_1^2}(\beta_{1,1}\mathbf{C}^s - \rho_{1,B}\rho_{1,1}^{-1}\beta_{1,2}\mathbf{C}^b)\widehat{\mathbf{A}}_1 + \frac{\tau_{sx}}{\rho_{1,1}H_i}\mathbf{E}_1^s \\ & - \sum_{\ell=1}^{J_1} g\Big(\frac{\rho_{1,\ell}-\rho_{1,\ell-1}}{\rho_{1,1}}\Big)\frac{\partial\zeta_{1,\ell-1}}{\partial x}\mathbf{E}_1^{(\ell)} + \widetilde{X}_{1,1}\mathbf{E}_1^{(1)};\end{aligned} \tag{2.6.78}$$

$$\begin{aligned}\widehat{\mathbf{B}}_1^{\bullet} = {}& -\iota\gamma\widehat{\mathbf{A}}_1 - \frac{\alpha_1}{H_1^2}\mathbf{\Lambda}_1\widehat{\mathbf{B}}_1 + \frac{\alpha_1}{H_1^2}(\beta_{1,1}\mathbf{C}^s - \rho_{1,B}\rho_{1,1}^{-1}\mathbf{C}^b)\widehat{\mathbf{B}}_1 + \frac{\tau_{sy}}{\rho_{1,1}H_1}\mathbf{E}_1^s \\ & - \sum_{\ell=1}^{J_1} g\Big(\frac{\rho_{1,\ell}-\rho_{1,\ell-1}}{\rho_{1,1}}\Big)\frac{\partial\zeta_{1,\ell-1}}{\partial y}\mathbf{E}_1^{(\ell)} + \widetilde{Y}_{1,1}\mathbf{E}_1^{(1)};\end{aligned} \tag{2.6.79}$$

$$\widehat{\mathbf{A}}_2^{\bullet} = \iota\gamma\widehat{\mathbf{B}}_2 - \frac{\alpha_2}{H_2^2}\mathbf{\Lambda}_2\widehat{\mathbf{A}}_2 + \frac{\alpha_2}{H_2^2}(\beta_{1,1} - \rho_{2,B}\rho_{2,1}^{-1}\beta_{2,2}\mathbf{C}^b)\widehat{\mathbf{A}}_2 - \frac{\tau_{bx}}{\rho_{2,1}H_2}\mathbf{E}_2^b$$
$$- \sum_{\ell=1}^{J_1} g\Big(\frac{\rho_{1,\ell} - \rho_{1,\ell-1}}{\rho_{2,1}}\Big)\frac{\partial\zeta_{1,\ell-1}}{\partial x}\mathbf{E}_2^{(1)} + \widetilde{X}_{2,1}\mathbf{E}_2^{(1)}$$
$$- \sum_{\ell=1}^{J_2} g\Big(\frac{\rho_{2,\ell} - \rho_{2,\ell-1}}{\rho_{2,1}}\Big)\frac{\partial\zeta_{2,\ell-1}}{\partial x}\mathbf{E}_2^{(\ell)}; \tag{2.6.80}$$

$$\widehat{\mathbf{B}}_2^{\bullet} = -\iota\gamma\widehat{\mathbf{A}}_2 - \frac{\alpha_2}{H_2^2}\mathbf{\Lambda}_2\widehat{\mathbf{B}}_2 + \frac{\alpha_2}{H_2^2}(\beta_{1,1} - \rho_{2,B}\rho_{2,1}^{-1}\beta_{2,2}\mathbf{C}^b)\widehat{\mathbf{B}}_2 - \frac{\tau_{by}}{\rho_{2,1}H_2}\mathbf{E}_2^b$$
$$- \sum_{j=1}^{J_1} g\Big(\frac{\rho_{1,\ell} - \rho_{1,\ell-1}}{\rho_{2,1}}\Big)\frac{\partial\zeta_{1,\ell-1}}{\partial y}\mathbf{E}_2^{(1)} + \widetilde{Y}_{2,2}\mathbf{E}_2^{(1)}$$
$$- \sum_{j=1}^{J_2} g\Big(\frac{\rho_{2,\ell} - \rho_{2,\ell-1}}{\rho_{2,1}}\Big)\frac{\partial\zeta_{2,\ell-1}}{\partial y}\mathbf{E}_2^{(\ell)}. \tag{2.6.81}$$

Equations (2.5.76) and (2.5.77) in matrix form become

$$\mathbf{Z}_1^{\bullet} = -\sum_{i=1}^{2} H_i\mathbf{E}_i^H(\mathbf{A}_i' + \mathbf{B}_i'), \tag{2.6.82}$$
$$\mathbf{Z}_2^{\bullet} = -H_2\mathbf{E}_2^H(\mathbf{A}_2' + \mathbf{B}_2'). \tag{2.6.83}$$

The definitions of the matrices are found from (2.6.45) to (2.6.54) by setting $i = 1, 2$. The layer-averaged and domain-averaged horizontal components of current can be found by setting $i = 1, 2$ in (2.6.55) to (2.6.58).

CHAPTER 3

CONSTRUCTION OF EIGENFUNCTIONS

3.1 Introductory remarks

This chapter is primarily concerned with the description of a method of numerically determining a basis set of eigenfunctions from a Sturm-Liouville boundary value problem which results from the spectral representation of the vertical eddy viscosity operator. The eigenvalue problem is necessarily multilayered in nature and the coefficients of the second-order operator are defined in an arbitrary manner within each layer. The multilayered Sturm-Liouville problem with variable coefficients can be solved by various numerical methods. To remain consistent with the Galerkin procedure employed in Chapter 2, the eigenfunctions are constructed in terms of a basis set of fourth-order B-spline functions which are in turn represented in terms of an expansion of Chebyshev polynomials, and the same weighted scalar products given in (2.5.4) or (2.5.39) are applied. Therefore, the essence of the method described here is the same as that of the mixed numerical-analytical approach developed by Davies (1983c) for homogeneous seas.

The accuracy of the numerical methods is examined with respect to the number of the knots of B-splines and their distribution. The difference in the structure of vertical modes between the one and two domain systems is described. An eigenequation is derived analytically, in order to determine the validity of the numerical approach, for a three-layered piecewise constant eddy viscosity profile (see Appendix I). A method of projecting the coefficients of the B-spline basis set or the known values of current profiles onto those of the eigenfunctions is described.

3.2 A multilayered eigenvalue system

For convenience, we rewrite the Sturm-Liouville equations and associated limit conditions described in Section 2.5 and 2.6. The eigenvalue problem posed in multilayered systems is

$$\frac{d}{d\sigma_i}\left(\mu_{i,j}\frac{df_{i[j]}}{d\sigma_i}\right) = -\lambda_i f_{i[j]}, \qquad (i = 0,1,2,\ j = 1,\cdots,J_i), \tag{3.2.1}$$

subject to boundary conditions

$$\left(\mu_{i,1}\frac{df_{i[1]}}{d\sigma_i}\right) = \beta_{i,1} f_{i[1]}, \qquad \text{at} \qquad \sigma_i = 0, \qquad i = 0,1, \tag{3.2.2}$$

$$\left(\mu_{i,B}\frac{df_{i[B]}}{d\sigma_i}\right) = \beta_{i,2} f_{i[B]}, \qquad \text{at} \qquad \sigma_i = 1, \qquad i = 0,2, \tag{3.2.3}$$

and interfacial conditions

$$\left.\begin{aligned} f_{i[j]}(\xi_{i,j}) &= f_{i[j+1]}(\xi_{i,j}) \\ \left(\mu_{i,j}\frac{df_{i[j]}}{d\sigma_i}\right)_{\xi_{i,j}} &= \frac{\rho_{i,j+1}}{\rho_{i,j}}\left(\mu_{i,j+1}\frac{df_{i[j+1]}}{d\sigma_i}\right)_{\xi_{i,j}} \end{aligned}\right\} \quad i = 0,1,2,\ j = 1,\cdots,J_i-1. \tag{3.2.4}$$

Since the U_i and V_i currents at $\sigma_i = 0$ are in general non-zero, the values of $\beta_{i,1}$, $i = 0,1,2$, are finite; when a no-slip condition is imposed at the sea bed, each of eigenfunctions is required to satisfy the constraint exactly and hence $\beta_{0,2}$, $\beta_{2,2} \to \infty$; the homogeneous Neumann conditions at the interior domain boundaries, $\sigma_1 = 1$ and $\sigma_2 = 0$, restrict values of $\beta_{1,2}$ and $\beta_{2,1}$ to zero. For a linear slip condition one can determine the eigenfunctions such that

$$k_b\, f_{i,j,r} = -\frac{\alpha_i}{H_i}\left(\mu_{i,j}\frac{df_{i,j,r}}{d\sigma_i}\right) \qquad \text{at} \quad \sigma_i = 1, \tag{3.2.5}$$

where $i = 0,2$. This leads to

$$\beta_{i,2} = -k_b\, H_i/\alpha_i \qquad i = 0,2. \tag{3.2.6}$$

This limit condition has been thoroughly discussed by Davies (1987*a*).

The eigenvalue problem is completed by requiring that

$$f_{i,r}(0) = f_{i,1,r}(0) = 1, \tag{3.2.7}$$

where $i = 0, 1, 2$ and $r = 1, \cdots, m_i$.

Appendix I describes some basic properties of the multilayered eigenvalue system. The system of equations (3.2.1) to (3.2.4) and (3.2.7) constitute a self-adjoint eigenvalue problem, giving the orthogonality condition

$$\langle f_{i,j,r}, f_{i,j,k} \rangle = \sum_{j=1}^{J_i} \left(\frac{\rho_{i,j}}{\rho_{i,1}} \int_{\xi_{i,j-1}}^{\xi_{i,j}} f_{i,j,r} f_{i,j,k} \right) d\sigma_i = \begin{cases} \Phi_{i,r}^{-1} & \text{if} \quad r = k, \\ 0 & \text{if} \quad r \neq k, \end{cases} \tag{3.2.8}$$

where $\Phi_{i,r}^{-1}$ is the square of the energy norm and $i = 0, 1, 2$ and $r = 1, \cdots, m_i$.

The eigenvalues of the system (3.2.1) to (3.2.4) and (3.2.7) can be indexed so that

$$\lambda_{i,1} < \lambda_{i,2} < \cdots < \lambda_{i,k} < \cdots, \tag{3.2.9}$$

and, since the set of eigenvalues has no finite point of accumulation, $\lambda_{i,k} \to \infty$ as $k \to \infty$.

Consideration is now given to the expansions such that:

$$\varpi_i = U_i + \iota V_i = \begin{cases} \sum_{r=1}^{m_i} (A_{i,r} + \iota B_{i,r}) f_{i,r} & (3.2.10) \\ \sum_{r=1}^{m_i} (\widehat{A}_{i,r} + \iota \widehat{B}_{i,r}) \Phi_{i,r} f_{i,r} & (3.2.11) \\ \sum_{r=1}^{m_i} (\widehat{A}_{i,r} + \iota \widehat{B}_{i,r}) \widehat{f}_{i,r} & (3.2.12) \end{cases}$$

where $\iota = \sqrt{-1}$ and $f_{i,r}$ in (3.2.10) is normalised by (3.2.7); (3.2.11) is Heaps' spectral expansion given in (2.6.30) and (2.6.31) and $f_{i,r}$ is also normalised by (3.2.7); $\widehat{f}_{i,r}$ in (3.2.12) is normalised by requiring that $\langle \widehat{f}_{i,j,r}, \widehat{f}_{i,j,r} \rangle = \Phi_{i,r}^{-1} = 1$.

Parseval's identity is helpful in understanding the physical implications of these expansions. Multiplying the expansions with their complex conjugates and integrating through the vertical we have, for the expansion (3.2.10):

$$\int_0^1 \varpi_i^2 \, d\sigma_i = \sum_{r=1}^{m_i} (A_{i,r}^2 + B_{i,r}^2) \int_0^1 f_{i,r}^2 \, d\sigma_i \simeq \sum_{r=1}^{m_i} (A_{i,r}^2 + B_{i,r}^2) \Phi_{i,r}^{-1}; \qquad (3.2.13)$$

for the expansions (3.2.11):

$$\int_0^1 \varpi_i^2 \, d\sigma_i = \sum_{r=1}^{m_i} (\widehat{A}_{i,r}^2 + \widehat{B}_{i,r}^2) \Phi_{i,r}^2 \int_0^1 f_{i,r}^2 \, d\sigma_i \simeq \sum_{r=1}^{m_i} (\widehat{A}_{i,r}^2 + \widehat{B}_{i,r}^2) \Phi_{i,r}; \qquad (3.2.14)$$

and for the expansions (3.2.12):

$$\int_0^1 \varpi_i^2 \, d\sigma_i = \sum_{r=1}^{m_i} (\widehat{A}_{i,r}^2 + \widehat{B}_{i,r}^2). \qquad (3.2.15)$$

Hence, in the expansions (3.2.10) and (3.2.11) the value of $\Phi_{i,r}$ is important in determining the contribution of each vertical mode to the depth-integrated kinetic energy at a particular point in the horizontal plane, while in the expansion (3.2.15) the square of each modal coefficient gives the instantaneous contribution. The modal coefficients $A_{i,r} + \iota B_{i,r}$ and $(\widehat{A}_{i,r} + \iota \widehat{B}_{i,r}) \Phi_{i,r}$ in the expansions (3.2.10) and (3.2.11) represent the instantaneous contribution of r th vertical mode to the surface currents. In the expansion of (3.2.12), $(\widehat{A}_{i,r} + \iota \widehat{B}_{i,r}) \widehat{f}_{i,r}(0)$ gives the contribution to the surface current. Following Heaps and Jones (1983, 1985), the expansion (3.2.11) is used in Chapters 4 and 5.

3.3 Numerical determination of eigenfunctions

Eigenvalues and eigenfunctions can be constructed in analytical ways (as exemplified in Heaps and Jones (1983), Jung and Noye (1988)), but the extension of this method to more generalised eddy viscosity profiles becomes complicated. To estimate the set of eigenvalues and eigenfunctions from the resultant transcendental equation such as (A.2.4) may be time-consuming when changes in eddy viscosity profiles are frequently required.

To handle arbitrary variation of the vertical eddy viscosity in a flexible manner, it is therefore necessary to use a numerical method of approximating a set of eigenvalues and corresponding eigenfunctions. The Galerkin method with expansion of fourth-order B-spline functions is used for consistency with the solutions with a basis set of B-spline functions (described in Section 2.5), and the scalar products (2.5.4) and (2.5.39) are naturally used. Alternatively, it may be possible to develop an iteration method based on the Runge-Kutta-Merson method (Furnes, 1983), which may be advantageous over the Galerkin method when the accuracy of the computed eigenvalues and eigenfunctions has to be monitored (Davies and Furnes, 1986). It is apparent that use of the Runge-Kutta-Merson method will be more effective if initial estimates of eigenvalues are made by the Galerkin method.

Taking the scalar product ((2.5.4) for Ω_0 and (2.5.39) for Ω_i, $i = 1, 2$, respectively) of the r th eigenfunction equation (3.2.1), and integrating by parts, using limit conditions (3.2.2) to (3.2.4) and (3.2.7), yields

$$\begin{aligned}\left\langle \mu_{i,j}\frac{df_{i,j,r}}{d\sigma_i}, \frac{df_{i,j,k}}{d\sigma_i}\right\rangle &= \sum_{j=1}^{J_i}\frac{\rho_{i,j}}{\rho_{i,1}}\int_{\xi_{i,j-1}}^{\xi_{i,j}}\left(\mu_{i,j}\frac{df_{i,j,r}}{d\sigma_i}\right)\left(\frac{df_{i,j,k}}{d\sigma_i}\right)d\sigma_i \\ &= -\beta_{0,1} + \beta_{0,2}\rho_{i,B}\rho_{i,1}^{-1}f_{i,r}(1)f_{i,k}(1) + \lambda_{i,k}\left\langle f_{i,j,r}\, f_{i,j,k}\right\rangle,\end{aligned} \tag{3.3.1}$$

where $i = 0, 1, 2$ and $k = 1, \cdots, m_i$.

To compute eigenfunctions efficiently for arbitrary profiles of $\mu_{i,1}$ and $\mu_{i,2}$, the r th eigenfunction is represented in terms of a set of fourth-order B-spline functions $M_{i,\ell}$, $\ell = 1, \cdots, \overline{n}_i$, namely,

$$f_{i,j,q}(\sigma_i) = \sum_{\ell=1}^{\overline{n}_i} L_{i,\ell,q}\, M_{i,\ell}(\sigma_i), \qquad \text{for } \xi_{i,j-1} \le \sigma_i \le \xi_{i,j}, \tag{3.3.2}$$

where $i = 0, 1, 2$, $j = 1, \cdots, J_i$, $q = 1, \cdots, m_i$. In general one must choose $\overline{n}_i$

substantially larger than m_i. In theory, an arbitrary set of basis functions can be chosen from a finite-dimensional subspace belonging to $C^0[0,1]$.

Substitution of the B-spline expansion (3.3.2) into equation (3.3.1) yields the matrix equation

$$\mathbf{L}_i^T \widetilde{\mathbf{D}}_i \mathbf{L}_i = \mathbf{\Lambda}_i \mathbf{L}_i^T \mathbf{C}_i \mathbf{L}_i, \tag{3.3.3}$$

where $i = 0, 1, 2$. In this equation:

$\mathbf{L}_i$ is an $\overline{n}_i \times \overline{n}_i$ matrix with (r,k) th element

$$L_{i,r,k}; \tag{3.3.4}$$

$\mathbf{L}_i^T$ is its transpose;

$\mathbf{\Lambda}$ is a matrix of eigenvalues, that is, with (r,k) th element

$$\Lambda_{i,r,k} = \begin{cases} \lambda_{i,k}, \\ 0 \end{cases} \tag{3.3.5}$$

$\widetilde{\mathbf{D}}_i = \mathbf{D}_i + \widetilde{\mathbf{B}}_i$ and $\mathbf{D}_i$ is a $\overline{n}_i \times \overline{n}_i$ matrix with (r,k) th elements

$$\sum_{j=1}^{J_i} \frac{\rho_{i,j}}{\rho_{i,1}} \int_{\xi_{i,j-1}}^{\xi_{i,j}} \mu_{i,j} \frac{dM_{i,r}}{d\sigma_i} \frac{dM_{i,k}}{d\sigma_i} \, d\sigma_i; \tag{3.3.6}$$

$\widetilde{\mathbf{B}}_i$ is a $\overline{n}_i \times \overline{n}_i$ matrix with (r,k) th elements

$$\beta_{0,1} - \beta_{0,2} \rho_{i,B} \rho_{i,1}^{-1} f_{i,r}(1) f_{i,k}(1); \tag{3.3.7}$$

and $\mathbf{C}_i$ is a $\overline{n}_i \times \overline{n}_i$ matrix with (r,k) th element

$$\sum_{j=1}^{J_i} \frac{\rho_{i,j}}{\rho_{i,1}} \int_{\xi_{i,j-1}}^{\xi_{i,j}} M_{i,r} M_{i,k} \, d\sigma_i \, . \tag{3.3.8}$$

It should be noted that since the solutions of the self-adjoint eigenvalue problem is approximated on a finite-dimensional space, a finite number of eigenvalues are determined.

The matrices $\mathbf{C}$ and $\widetilde{\mathbf{D}}$ are sparse because the B-splines have restricted support. Once the coefficients $L_{i,r,k}$ are defined from (3.3.3), the eigenfunctions are correspondingly defined by (3.3.2) and then all the necessary integrals in (2.6.49) to (2.6.53) can be evaluated. In practice it is expedient to expand the B-spline functions in terms of Chebyshev polynomials. Detailed descriptions of representing B-splines semi-analytically in terms of Chebyshev polynomials can be found in Cox (1972, 1975) and Davies (1977*a*).

3.4 A projection method for estimates of modal composition

The use of a basis set of B-splines has certain computational advantages due mainly to the piecewise nature of the splines, and the existence of high-order derivatives and various invariant properties, but their use provides little physical insight into the structure of the flow field being modelled. In this regard, the basis set of eigenfunctions is very useful, particularly when the vertical structure of eddy viscosity, μ_i, is fixed as given in (2.5.5) or (2.5.42). In a recent study by Davies (1985*b*), the B-spline basis has been used for accuracy while the physical interpretation of the results has been performed in terms of eigenfunctions.

As a way of determining the modal composition of current profiles, Davies (1983*a*) also described a method of projecting the coefficients of the B-spline basis set onto those of the eigenfunctions in the course of developing a Galerkin model for wind induced flows in continuously stratified seas. In this section it will be shown that the transformation relation between the coefficients of B-splines and eigenfunctions is also applicable to a multilayered system. In fact, this projection method can also be applied to other polynomial basis sets which have been widely used in literature.

Let the horizontal component of current $U_{i,j}$ be represented in terms of the

B-spline basis set in the following way:

$$U_{i,j}(x,y,\sigma_i,t) \simeq U_{i,j}^{(B)} = \sum_{r=1}^{Q_i} A_{i,r}(x,y,t)\ M_{i,r}(\sigma_i), \qquad \text{for} \quad \xi_{i,j-1} \le \sigma_i \le \xi_{i,j}, \tag{3.4.1}$$

where $i = 0,1,2,\ j = 1,\cdots,J_i$, and the $A_{i,r}$ are coefficients of the B-spline functions at a particular moment in time and position in space computed using the Galerkin method described in Section 2.5. The equivalent expansion of $U_{i,j}(x,y,\sigma_i,t)$ in terms of the eigenfunctions (3.4.1) may be written as

$$U_{i,j}^{(E)} = \sum_{q=1}^{m_i} \widehat{A}_{i,q}(x,y,t)\ \Phi_{i,q}\ f_{i,q}(\sigma_i), \tag{3.4.2}$$

or in local form

$$U_{i,j}^{(E)} = \sum_{q=1}^{m_i} \widehat{A}_{i,q}(x,y,t)\ \Phi_{i,q}\ f_{i,j,q}(\sigma_i), \quad \text{for} \quad \xi_{i,j-1} \le \sigma_i \le \xi_{i,j}\ , \tag{3.4.3}$$

where $i = 0,1,2,\ j = 1,\cdots,J_i$.

Equating (3.4.1) and (3.4.3) and taking the scalar product (2.5.4) (for the domain Ω_0) or (2.5.39) (for the domain Ω_i, $i = 1,2$), of the resulting equations, with $f_{i,j,k}(\sigma_i)$ yield

$$\widehat{A}_{i,k} = \sum_{j=1}^{J_i} \frac{\rho_{i,j}}{\rho_{i,1}} \int_{\xi_{i,j-1}}^{\xi_{i,j}} U_{i,j}^{(B)}\ f_{i,j,k}\ d\sigma_i \tag{3.4.4}$$

$$= \sum_{j=1}^{J_i} \frac{\rho_{i,j}}{\rho_{i,1}} \int_{\xi_{i,j-1}}^{\xi_{i,j}} \left(\sum_{r=1}^{Q_i} A_{i,r}\, M_{i,r} \right)\ f_{i,j,k}\ d\sigma_i. \tag{3.4.5}$$

In special circumstances, the eigenfunctions may be represented in terms of the B-spline functions used in the method with a basis set of B-splines. Then, substituting (3.3.2) into (3.4.5) gives

$$\widehat{A}_{i,k} = \sum_{r=1}^{Q_i} \sum_{\ell=1}^{Q_i} \left\{ A_{i,r}\, L_{i,\ell,k} \sum_{j=1}^{J_i} \frac{\rho_{i,j}}{\rho_{i,1}} \int_{\xi_{i,j-1}}^{\xi_{i,j}} \left(M_{i,r}\ M_{i,\ell} \right) d\sigma_i \right\}, \tag{3.4.6}$$

where $i = 0,1,2,\ k = 1,\cdots,Q_i$.

Expressing (3.4.6) in matrix form gives

$$\widehat{\mathbf{A}}_i = \mathbf{A}_i \; \mathbf{C}_i \; \mathbf{L}_i \; , \tag{3.4.7}$$

where $\widehat{\mathbf{A}}$ and $\mathbf{A}_i$ are row matrices with k th element $\widehat{A}_{i,k}$ and $A_{i,k}$, respectively. The matrices $\mathbf{L}_i$ and $\mathbf{C}_i$ are given by (3.3.4) and (3.3.8). A similar procedure can be applied to the $V_{i,j}$ component of current.

Consequently, once the coefficients $L_{i,\ell,r}$ have been computed by solving (3.3.3) for a given eddy viscosity profile, the first few coefficients $\widehat{A}_{i,r}$ can be readily computed from the known Q_i values of $A_{i,k}^{(B)}$. The accuracy of the estimated coefficients for each eigenfunction depends upon the accuracy in the U and V components of currents reproduced by the basis set of B-splines functions, as well as that of the numerically determined eigenvalues and eigenfunctions. In general, it is expected that the knot distribution of B-spline functions used to expand eigenfunctions will not coincide with that employed in a Galerkin model with a basis set of B-spline functions. Furthermore, the current profiles may be provided in terms of finite-difference methods or by observations rather than by B-spline functions. In such circumstances, the formula (3.4.4) can be applied by replacing $U_{i,j}^{(B)}$ with the computed or observed values. Errors in the estimated values of modal coefficients depends — regardless of the errors in the given current profiles — upon the accuracy of the numerically determined eigenfunctions and the errors arising in the course of projecting the observed or computed current profiles onto each of vertical modes.

The projection method was used in this thesis for the initialisation of the modal coefficients in calculating a free adjustment of flows in an open sea region (see Chapter 4). Otherwise the coefficients of the vertical modes are determined by directly solving the set of modal equations described in Chapter 2.

3.5 Vertical modes in one and two domain systems

3.5.1 Description of the system to be modelled

Figure 3.1 shows a schematic variation of density and eddy viscosity to be considered in this study. Although the models described in Chapter 2 allow for a multilayered system and the arbitrary variation of eddy viscosity within each layer, the application of models is confined to the two- and three-layered systems. Figure 3.1(a) illustrates how the continuous variation of density is approximated in terms of the three homogeneous layers. In accordance with the three-layered representation of density, the depth variation of eddy viscosity can be prescribed in a piecewise-linear manner as sketched in Figure 3.1(b). In the numerical experiments in Chapters 4 and 5 the eddy viscosity profiles are mostly prescribed in a two-layered or three-layered piecewise constant form (with or without a linear decrease near the sea surface) as shown in Figures 3(c) to (f). The two-layer system consists of the upper surface layer and the lower bottom layer whereas the three-layer system consists of the surface layer, the transition layer, known as the pycnocline, and the bottom layer. The zero-stress condition for the two domain system is imposed at the base of the upper layer for the two-layer system and at the base of the pycnocline for the three-layer system.

To facilitate comparison between the one and two domain systems we use, hereafter, simpler notations for the eddy viscosity, density and layer-averaged velocities, namely

for the two-layered system:

$$\left.\begin{matrix}\rho_{0,1}, N_{0,1}, \overline{U}_{0,1} \\ \rho_{1,1}, N_{1,1}, \overline{U}_{1,1}\end{matrix}\right] \Leftrightarrow \rho_T, N_T, \overline{U}_T,$$
$$\left.\begin{matrix}\rho_{0,2}, N_{0,2}, \overline{U}_{0,2} \\ \rho_{2,1}, N_{2,1}, \overline{U}_{2,1}\end{matrix}\right] \Leftrightarrow \rho_B, N_B, \overline{U}_B; \tag{3.5.1}$$

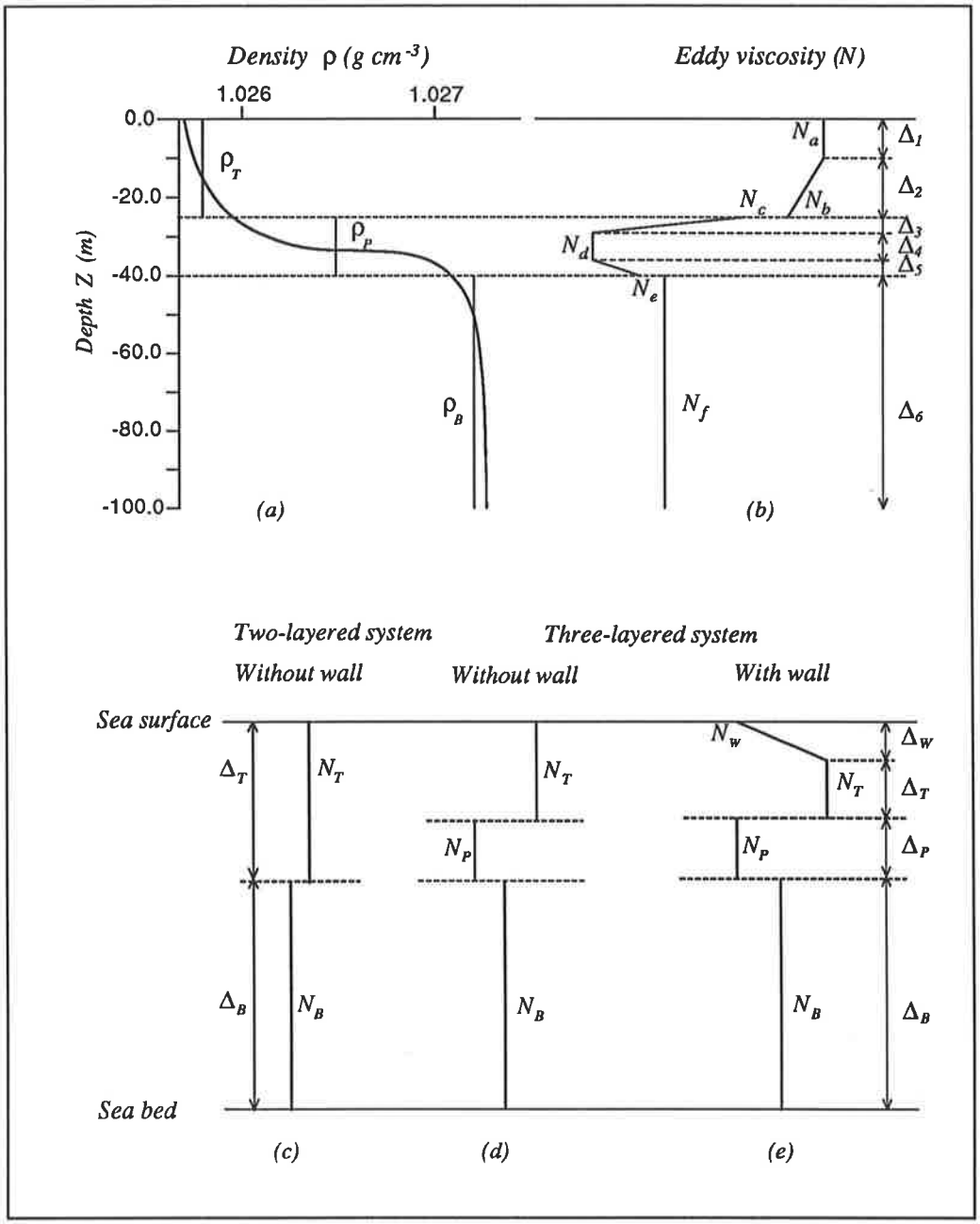

Figure 3.1 A schematic variation of density and eddy viscosity through the vertical.

and for the three-layered system:

$$\left.\begin{matrix}\rho_{0,1}, N_{0,1}, \overline{U}_{0,1} \\ \rho_{1,1}, N_{1,1}, \overline{U}_{1,1}\end{matrix}\right] \Leftrightarrow \rho_T, N_T, \overline{U}_T,$$

$$\left.\begin{matrix}\rho_{0,2}, N_{0,2}, \overline{U}_{0,2} \\ \rho_{1,2}, N_{1,2}, \overline{U}_{1,2}\end{matrix}\right] \Leftrightarrow \rho_P, N_P, \overline{U}_P, \tag{3.5.2}$$

$$\left.\begin{matrix}\rho_{0,3}, N_{0,3}, \overline{U}_{0,3} \\ \rho_{2,1}, N_{2,1}, \overline{U}_{2,1}\end{matrix}\right] \Leftrightarrow \rho_B, N_B, \overline{U}_B.$$

Summarising values of density used in the computations, we take for the two-layered system:

$$\rho_T = 1.0258, \qquad \rho_T = 1.0270\ g\,cm^{-3}; \tag{3.5.3}$$

and for the three-layered system:

$$\rho_T = 1.0258, \qquad \rho_P = 1.0265, \qquad \rho_B = 1.0272\ g\,cm^{-3}. \tag{3.5.4}$$

For wind induced motion in an open sea region the three-layered system is mostly considered. Typical values of the thickness of the surface layer, the pycnocline and the bottom layer used in the computations are:

$$\begin{gathered}\Delta_T = H_i\xi_{i,1} = 25, \quad 60\ m, \\ \Delta_P = H_i(\xi_{i,2} - \xi_{i,1}) = 10, \quad 40\ m, \\ \Delta_T + \Delta_P + \Delta_B = H_0 = H_1 + H_2 = 250\ m.\end{gathered} \tag{3.5.6}$$

In the computations of wind induced motion in a narrow lake we take for the two-layered system:

$$\begin{gathered}\Delta_T = H_i\xi_{i,1} = 40\ m, \\ \Delta_T + \Delta_B = H_0 = H_1 + H_2 = 100\ m;\end{gathered} \tag{3.5.7}$$

and for the three-layered system:

$$\begin{gathered}\Delta_T = H_i\xi_{i,1} = 25\ m, \\ \Delta_P = H_i(\xi_{i,2} - \xi_{i,1}) = 15\ m, \\ \Delta_T + \Delta_P + \Delta_B = H_0 = H_1 + H_2 = 100\ m.\end{gathered} \tag{3.5.8}$$

The values of eddy viscosity in the surface and bottom layers have been tentatively chosen. The eddy viscosity at the surface layer, N_T, ranges from 150 to 1000 $cm^2 s^{-1}$. In calculations with a surface *wall* layer (Figure 3.1(d) and (e)), where a law-of-the-wall is applied by analogy with the atmospheric boundary layer and then the eddy viscosity increases linearly with distance below the free sea surface (Davies, 1985a), the value of N_w was chosen as one fifth of N_T with $\Delta_w = 10\ m$. Under conditions of strong stratification, turbulent motion is suppressed within the pycnocline (Mortimer, 1952). Such a condition of stable stratification has been incorporated by prescribing low values of N_P (Davies, 1982b, 1983a; Heaps and Jones, 1983, 1985). In a recent study by Maas and van Haren (1987) a value of $N_P = 6\ cm^2 s^{-1}$ was chosen within the pycnocline in their three-layered Ekman model. Stratified conditions with $N_P = 10\ cm^2 s^{-1}$ and $\Delta_P = 40\,m$ seem to be unrealistic. Such an extreme condition has been chosen in the interest of demonstrating the influence of the pycnocline upon the vertical structures of the flow field in the one and two domain systems. The eddy viscosity in the bottom layer is assumed uniform throughout the depth and, taking account of the effects of the background turbulence level, two values, $N_P = 100$ and $1000\ cm^2 s^{-1}$, are considered.

3.5.2 Vertical modes

The accuracy of numerically determined eigenfunctions

In order to examine the accuracy of numerically determined eigenfunctions calculations are performed for a three-layered eddy viscosity profile with $N_T = 300$, $N_P = 10$, $N_B = 100\ cm^2 s^{-1}$, $\Delta_T = 25$, $\Delta_P = 15$, $\Delta_B = 60\,m$ and various distributions of knots. The distributions $K1$ and $K3$ are composed of 33 and 50 quasi-uniform interior knots through the vertical, respectively, and the distributions $K2$, $K4$ and $K5$ are composed of 33, 50 and 67 non-uniform interior knot spacings with concentration of knots near the interfaces and within the pycnocline (the number

of interior knot spacings is given by $\overline{m}_i = m_i - n_o + 1$). The exact values of $\lambda_{0,k}$ and $\Phi_{0,k}$ were computed iteratively from the transcendental equation presented in Appendix II. It is apparent from Table 3.1 that increasing the number of B-spline functions gives an improved accuracy in numerically determined eigenvalues and eigenfunctions. It has been revealed in a series of preliminary computations that for a given number of B-spline functions, a high concentration of knots within the pycnocline, particularly at the proximity of the upper surface of the pycnocline, is important in determining eigenfunctions and the associated eigenvalues accurately. When knot spacings are not compressed near the interfaces, *wiggles* appear in the numerically computed eigenfunctions particularly near the bottom of the surface layer. If an insufficient number of B-splines are used along with a uniform distribution of knots, regions of high shear (near the upper and lower surfaces of the pycnocline) are smoothed out. If the knots of B-spline functions are excessively concentrated within certain regions without increasing the total number of knots involved in the calculation, the accuracy of higher eigenvalues and eigenfunctions is rapidly decreased.

In order to accurately compute up to thirty eigenfunctions, distribution $K5$ has been required. In this study about 67 interior knot spacings, with a distribution similar to $K5$ have been generally used for the three-layered one domain system but whenever necessary the total number of knots and their distribution have been adjusted. For the upper domain of the three-layered two domain system about 67 interior knot spacings have been used with high concentration of knots within the pycnocline, while for the lower domain 24 knot spacings (since 10 eigenfunctions are involved in the expansion of the current profile in the bottom layer) are used. For the upper domain of the three-layered two domain system the value of Δ_P/H_1 is very high and hence it is necessary to concentrate considerably more B-spline functions within the pycnocline.

Table 3.1 Eigenvalues computed using a three-layered eddy viscosity distribution shown in Figure 3.1(d) with $\Delta_T = 25$, $\Delta_P = 15$, $\Delta_B = 60\,m$, $N_T = 300$, $N_P = 10$ and $N_T = 100\ cm^2 s^{-1}$, with a no-slip condition for a range of knot distributions

Distribution	K1	K2	K3	K4	K5	Exact
$\overline{m}_i =$	33	33	50	50	67	
r =1	1.076	1.011	1.052	1.008	1.008	1.008
2	6.639	6.356	6.523	6.349	6.349	6.345
3	34.116	30.041	32.613	29.893	29.892	29.819
4	57.120	51.649	54.447	51.542	51.541	51.482
5	117.117	109.123	114.605	108.737	108.734	108.538
10	478.733	415.227	429.679	412.568	412.563	412.389
15	1407.633	1180.577	1138.278	1079.181	1078.798	1076.924
20	2971.537	2283.083	2189.600	1819.659	1817.356	1816.038
25	5174.325	7386.768	3612.439	3045.295	3013.736	3003.123
30	8012.397	30799.402	6044.786	4350.115	4247.103	4228.482
35			9220.318	6478.395	5700.169	5699.498
40			13465.445	11119.358	7907.935	7645.858

Figures 3.2 and 3.3 display the first five vertical modes in one and two domain systems evaluated numerically with $\overline{m}_i = 67$, $i = 0, 1$, and $\overline{m}_2 = 24$, and with a no-slip bottom boundary condition, $\beta_{i,2} = \infty$, $i = 0, 2$, and two linear slip bottom boundary conditions with $\beta_{i,2} = 0$, $\beta_{i,2} = -k_b H_i/\alpha_i$, $i = 0, 2$, for a range of eddy viscosity profiles. The forms of vertical modes are primarily affected by the vertical dependence of the coefficient of the second-order viscosity operator and by the limit conditions used. Note that the domain-averaged value of eddy viscosity, α_i, is not involved in determining the structure of vertical modes. With the use of condition (3.2.5) the value of α_i is taken into account by the value of $\beta_{i,1}$. The role of density on the determination of vertical modes is negligibly small because $\Delta\rho/\rho = O(10^{-3})$. With a very low value of N_P the eigenfunctions show regions of rapid shear at the upper and lower surfaces of the pycnocline. This is due to the requirement $\rho_{i,j}\mu_{i,j}\partial f_{i,j}/\partial\sigma_i = \rho_{i,j+1}\mu_{i,j+1}\partial f_{i,j+1}/\partial\sigma_i$ at each of the

interfaces within the domain.

As a property of eigenfunctions, the r th vertical mode has $r-1$ zeros in the open interval $(0,1)$ for both the slip and no-slip boundary conditions. The zeros of the r th eigenfunction are placed between two consecutive zeros of the $(r-1)$ th eigenfunction. In regions in which values of eddy viscosity are markedly reduced, zeros are concentrated with respect to the rest of the water column. This leads to a rapid change of the modal structure within the pycnocline. An important feature is that, as a consequence of the homogeneous limit conditions, the first eigenvalue is $\lambda_{i,1} = 0$ and the corresponding eigenfunction is $f_{i,1}(\sigma_i) = 1$. It should be noted that local variations of eddy viscosity and density jump have no influence on the first mode. With any other combination of limit conditions at the domain boundaries, for example when a no-slip or stressing condition is enforced at the sea bed, the first vertical mode is no longer independent of vertical eddy viscosity and density.

As a consequence of introducing the zero-stress condition at an interface the water column is divided into two independent domains, Ω_1 and Ω_2. Hence the modal structures of one and two domain systems become dramatically dissimilar to each other. Note that for the two domain system, the region occupied by the pycnocline is represented as significantly increased fractions of the domain compared with that of the one domain system. Hence, the modal structure of the two domain system is very sensitive to local changes in the eddy viscosity profile. Introducing a surface wall layer affects the values of $\lambda_{1,r}$ and $\Phi_{1,r}$ significantly. Changes in the values of $\lambda_{0,k}$ and $\Phi_{0,k}$ were marginal. Under conditions of strong stratification ($N_P << N_T$) the vertical modes in $\Omega_{1,2}$ possess significantly more zeros within the pycnocline compared to those in $\Omega_{0,2}$. In the one domain system, the ratios of eddy viscosity and layer thickness between the three layers determine the modal structures. The modal structures in the domain Ω_1 are determined by

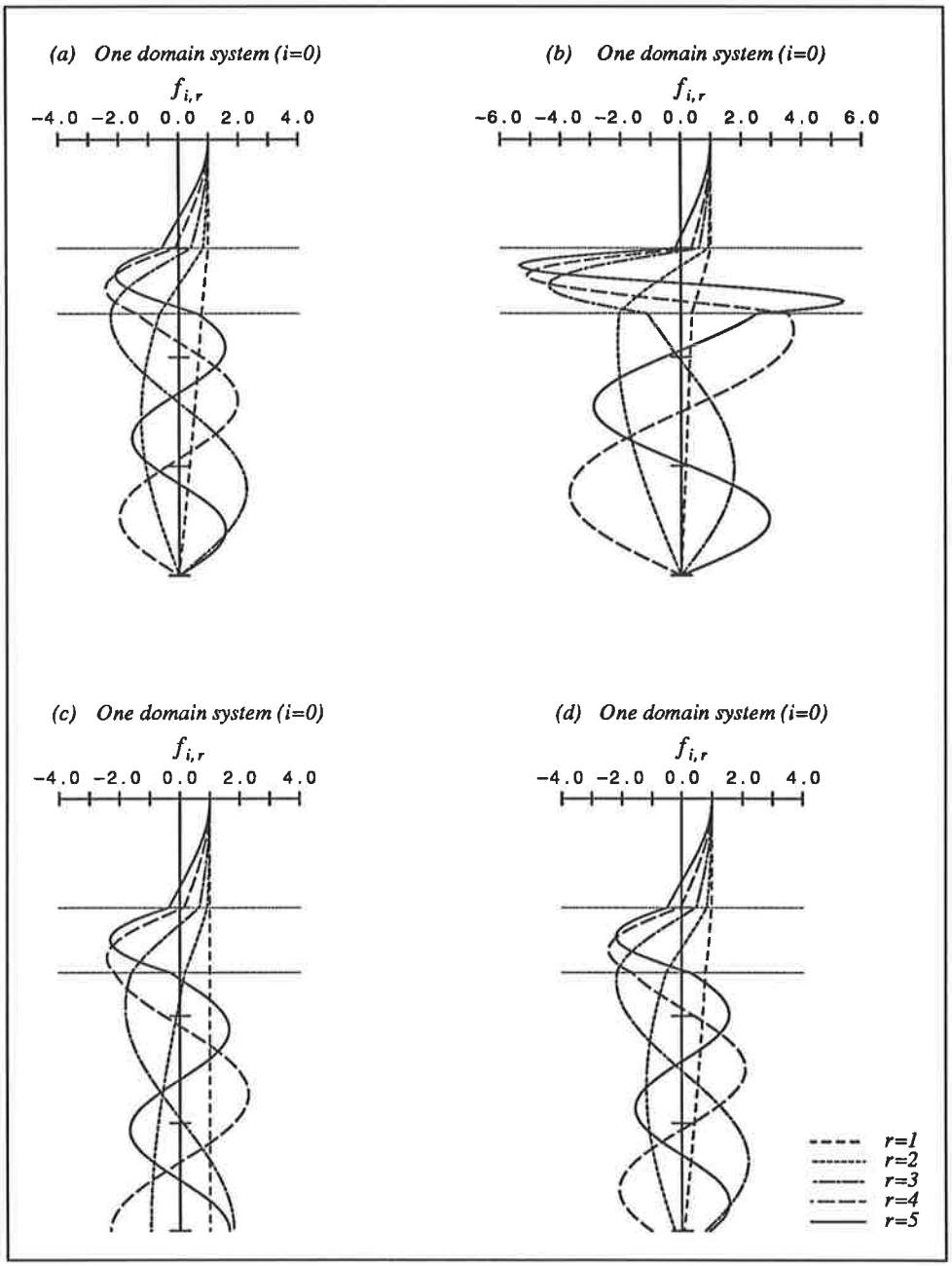

Figure 3.2 The first five vertical modes of the one domain system, obtained using the profile in Figure 3.1(*d*), computed with: Δ_T=25, Δ_P=15, Δ_B=60 m; N_T =300, N_B =100 cm^2s^{-1}; ρ_T=1025.8, 1026.5, 1027.2 $g\,cm^{-3}$; $\beta_{0,1}$=0; and (*a*) N_P =50 cm^2s^{-1} with $\beta_{0,2}$=∞; (*b*) N_P =10 cm^2s^{-1} with $\beta_{0,2}$=∞; (*c*) N_P =50 cm^2s^{-1} with $\beta_{0,2}$=0; (*d*) N_P=50, α_0=142.5 cm^2s^{-1} with $\alpha_0\beta_{0,2}$ =$-k_bH_0$=-0.2 cm^2s^{-1}.

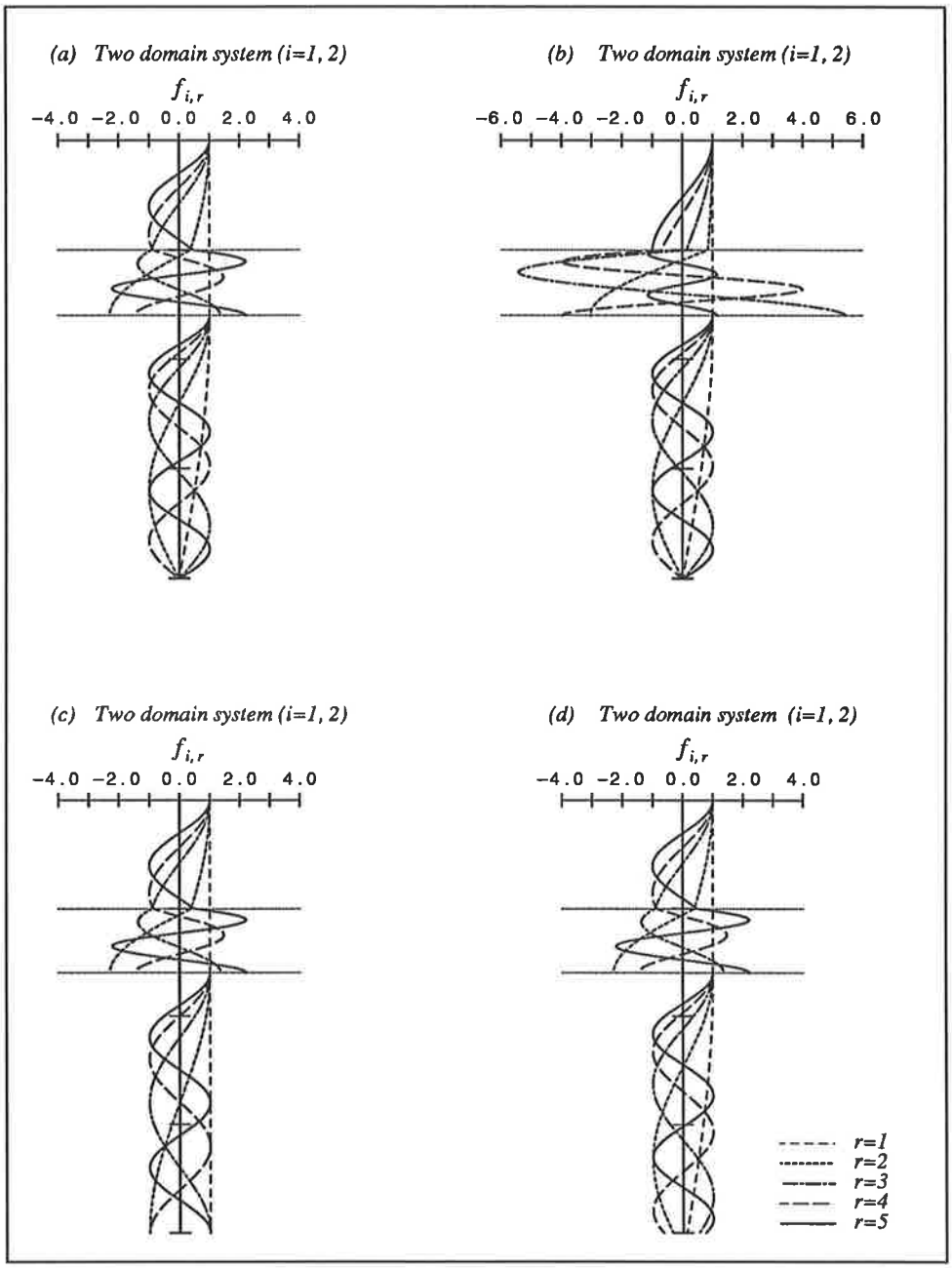

Figure 3.3 The first five vertical modes of the one domain system, obtained using the profile in Figure 3.1(*d*), computed with: Δ_T=25, Δ_P=15, Δ_B=60 m; N_T =300, N_B =100 cm^2s^{-1}; ρ_T=1025.8, 1026.5, 1027.2 $g\,cm^{-3}$; $\beta_{1,1}$=0; and (*a*) N_P =50 cm^2s^{-1} with $\beta_{1,2}$=∞; (*b*) N_P =10 cm^2s^{-1} with $\beta_{1,2}$=∞; (*c*) N_P =50 cm^2s^{-1} with $\beta_{2,2}$=0; (*d*) N_P =50, α_2=100 cm^2s^{-1} with $\alpha_2\beta_{2,2}$ =$-k_bH_2$=-0.12 cm^2s^{-1}.

the ratio of N_T to N_P, and the ratio of Δ_T to Δ_P, and the modal structures in the domain Ω_2 correspond to those with a constant eddy viscosity. For a thorough discussion on the structure of two-layered and three-layered profiles in connection with wind drift current in open sea regions, see Davies (1986).

Table 3.2 and Figure 3.4 show how sensitive the modal structure is to changes in the value of N_P and their functional form within the pycnocline. It is evident that as N_P is increased, while keeping N_T and N_B constant, the region of high shear within the pycnocline is significantly reduced. Particularly, for the two-layered eddy viscosity profile (with $N_P > N_B$) the first five vertical modes show no shear in the transitional layer and their derivatives in the vertical no longer change sign there (Figure 3.4(d)). When the values of piecewise eddy viscosity are joined in a piecewise-linear manner in the vicinity of interface levels, the higher vertical modes tend to show a smooth variation at the interface (Figure 3.4(c)). Comparing Figure 3.4(a) and (c), it is evident that with a small correction to the eddy viscosity profile across the upper surface of the pycnocline ($\Delta_2 = \Delta_3 = 2.5$ m) the modal structure was not significantly different from that of a step-like variation of eddy viscosity, although there is some evidence that higher modes $r \geq 3$ are affected.

The vertical variation of the first five vertical modes, evaluated numerically with $\overline{m}_i = 67$, $i = 0, 1$, and $\overline{m}_2 = 24$, for various ranges of eddy viscosity profiles, are displayed in Figures A.3(a) to A.3(g) in Appendix III (see caption). The modal characteristics of the first five eigenfunctions (involving $\Phi_{i,r}$, $\lambda_{i,r}$, $\alpha_i\lambda_{i,r}$, $a_{i,j,r}$ and $f_i(1)$) computed for the eddy viscosity profiles which will be frequently employed in Chapters 4 and 5 are summarised in Tables A.3(a) to (e) in Appendix III.

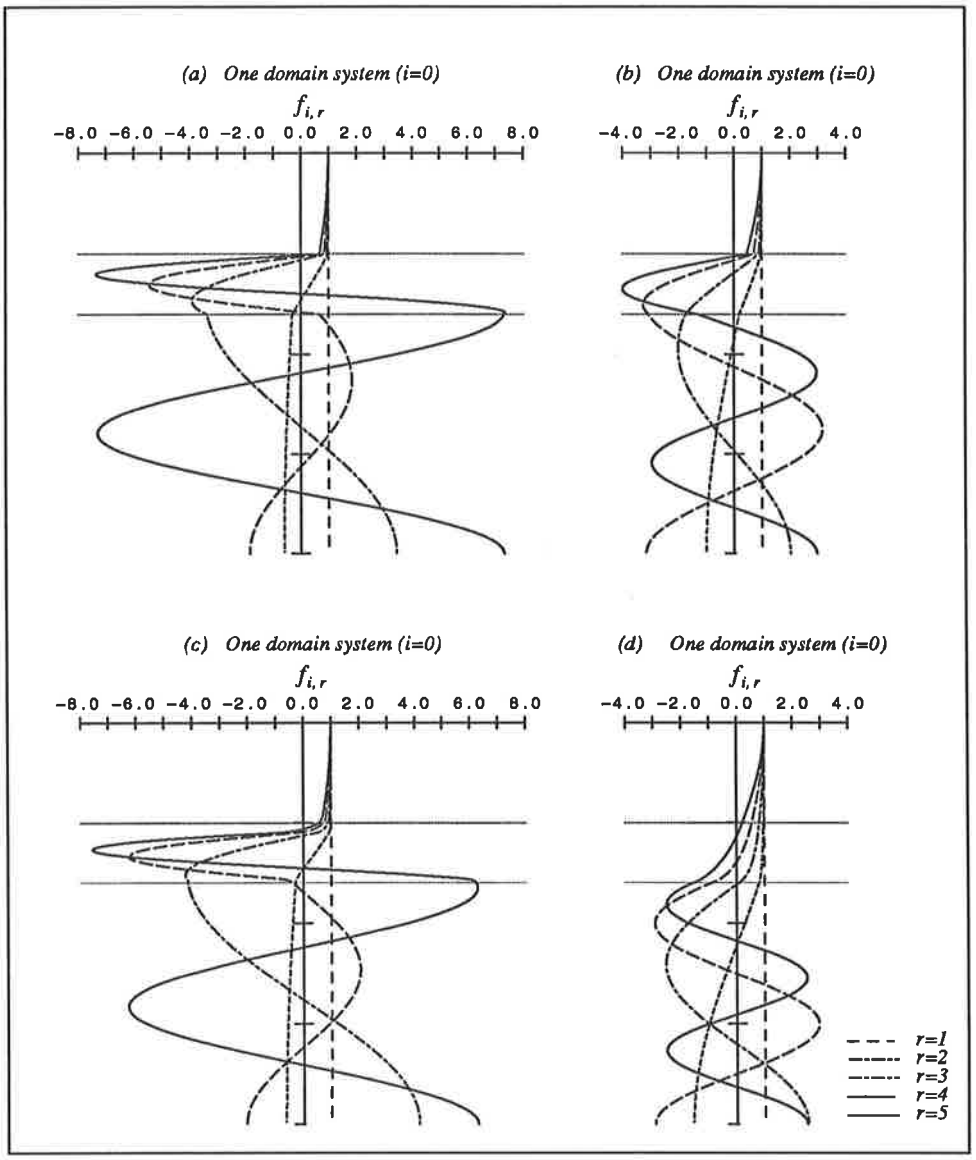

Figure 3.4 The first five vertical modes of the one domain system, obtained using the profile in Figure 3.1(*d*), computed with: ρ_T=1025.8, 1026.5, 1027.2 $g\,cm^{-3}$; $\beta_{0,1}=\beta_{0,2}=0$; and (*a*) Δ_T=25, Δ_P=15, Δ_B=60 m; N_T=1000, N_P=10, N_B=100 $cm^2 s^{-1}$; (*b*) Δ_T=25, Δ_P=15, Δ_B=60 m; N_T=1000, N_P=50, N_B=100 $cm^2 s^{-1}$; (*c*) Δ_1=22.5, Δ_2=2.5, Δ_3=2.5, Δ_4=10, Δ_5=2.5, Δ_6=60 m; N_a=1000, $N_b = N_c$=100, N_d=10, $N_e = N_f$=100 $cm^2 s^{-1}$; (*d*) Δ_T=25, Δ_P=15, Δ_B=60 m; N_T=1000, N_B=100 $cm^2 s^{-1}$, and a linear decrease within the pycnocline with $N_b = N_c = N_T$, $N_e = N_B$.

Table 3.2 Values of $\lambda_{0,k}$ and $\Phi_{0,k}$ for the first seven vertical modes computed for the three-layered eddy viscosity distributions (a), (b), (c) and (d) in Figure 3.4

	(a)		(b)		(c)		(d)	
	$\lambda_{i,r}$	$\Phi_{i,r}$	$\lambda_{i,r}$	$\Phi_{i,r}$	$\lambda_{i,r}$	$\Phi_{i,r}$	$\lambda_{i,r}$	$\Phi_{i,r}$
r =1	0.000	0.999	0.000	0.999	0.000	0.999	0.000	0.999
2	0.953	2.233	1.169	2.159	1.204	2.139	3.141	1.049
3	7.810	0.207	9.011	0.162	9.019	0.153	15.945	0.450
4	16.747	0.294	22.468	0.276	23.678	0.260	40.366	0.343
5	34.747	0.049	40.016	0.058	40.611	0.063	75.584	0.453
6	56.795	0.123	74.497	0.097	77.038	0.075	118.311	0.889
7	81.167	0.032	96.846	0.075	100.843	0.110	163.117	1.388

CHAPTER 4

WIND INDUCED FLOWS IN HORIZONTALLY UNBOUNDED SEAS

4.1 Introductory remarks

This chapter describes, as one of the applications of the models formulated in Chapter 2, the steady state and time-dependent responses of a horizontally unbounded sea subjected to local wind forcing. Steady state calculations are performed by reformulating the system of U and V equations in complex form, whereas the time-dependent calculations are performed on a staggered finite difference grid using the two sets of U and V equations. The sea surface and interfacial gradients are briefly considered in the computations of the steady state current profiles.

There have been extensive numerical experiments conducted by Davies (1985*b*,*c*) and Davies and Furnes (1986) which have led to a description of the overall features of wind induced motion in both homogeneous and stratified open sea regions. Our application is centred, along with the comparison of the one and two domain systems, on the sensitivity of the layered models to changes in the values of the vertical eddy viscosity, particularly within the pycnocline and to changes in the pycnocline thickness. This can serve as a basis for realistic applications in the future. The eigenfunction method is used in a complementary manner to acquire a better understanding of the structure of the flow field.

Although the formulation described in Chapter 2 is based on the multilayered sea, we consider here three-layered one and two domain systems. In the inter-

est of demonstrating the accuracy of the models, the eddy viscosity profiles are prescribed mostly in piecewise constant form. The Coriolis parameter is taken as $\gamma = -0.9178 \times 10^{-4}\ s^{-1}$, representative of Bass Strait at latitude 39° S.

4.2 Steady state solutions

Stratified flows rarely remain stationary, since the time scale of the meteorological events is in general short compared to the time scales necessary to reach a steady state. Nevertheless, to obtain basic ideas on the vertical structure of stratified flows and to verify the models, we start with this simple steady state problem.

Steady flow in an open sea region is composed of the *wind drift current* which is driven by external wind forcing imposed at the sea surface and the *gradient current* which is driven by the combination of the gradients of the sea surface and the interfaces. We note that the hydrodynamic system is linear with multiple components of input functions. Hence, the magnitudes of the U and V components of the pure drift currents are scaled up according to the magnitude of the wind stress. The gradient current is also scaled up according to the combined value of the gravitational forcings.

Using the complex velocity, $\varpi_1 = U_i + \iota V_i$, $\iota = \sqrt{-1}$, the steady state equations of motion in an open sea region can be combined to give

$$\iota\gamma\varpi_{i,j} = \frac{\alpha_i}{H_i^2}\frac{\partial}{\partial\sigma_i}\Big(\mu_{i,j}\frac{\partial\varpi_{i,j}}{\partial\sigma_i}\Big), \tag{4.2.1}$$

where $i = 0$ and $j = 1, 2, 3$ for the three-layered one domain system, and $i = 1, 2$ and $j = 1, 2, 3$ for the three-layered two domain system. The boundary conditions (2.4.10) to (2.4.12) and the interface conditions (2.4.13) to (2.4.17) can be combined in a similar way.

After combining (2.5.18) with (2.5.19), (2.5.51) with (2.5.52) and (2.5.53) with (2.5.54) in complex form, the Galerkin equations for (4.2.1) in terms of a basis set of B-splines take the form

$$(\iota\gamma\mathbf{C}_i + \frac{\alpha_i}{H_i^2}\mathbf{D}_i)\mathbf{W}_i = \mathbf{F}_i + \mathbf{S}_i \tag{4.2.2}$$

where

$$\mathbf{W}_i = \mathbf{A}_i + \iota\mathbf{B}_i \qquad i = 0, 1, 2, \tag{4.2.3}$$

$$\left.\begin{aligned} \mathbf{F}_0 &= (\rho_{0,1}H_0)^{-1}[(\tau_{sx} + \iota\tau_{sy})\mathbf{E}_0^s - (\tau_{bx} + \iota\tau_{by})\mathbf{E}_0^b] \\ \mathbf{F}_1 &= (\rho_{1,1}H_1)^{-1}(\tau_{sx} + \iota\tau_{sy})\mathbf{E}_1^s \\ \mathbf{F}_2 &= -(\rho_{2,1}H_2)^{-1}(\tau_{bx} + \iota\tau_{by})\mathbf{E}_2^b \end{aligned}\right\} \tag{4.2.4}$$

$$\left.\begin{aligned} \mathbf{S}_0 &= -\sum_{\ell=1}^{3} g\Big(\frac{\rho_{0,\ell} - \rho_{0,\ell-1}}{\rho_{0,1}}\Big)\Big(\frac{\partial\zeta_{0,\ell-1}}{\partial x} + \iota\frac{\partial\zeta_{0,\ell-1}}{\partial y}\Big)\mathbf{E}_0^{(\ell)}\,, \\ \mathbf{S}_1 &= -\sum_{\ell=1}^{2} g\Big(\frac{\rho_{1,\ell} - \rho_{1,\ell-1}}{\rho_{1,1}}\Big)\Big(\frac{\partial\zeta_{1,\ell-1}}{\partial x} + \iota\frac{\partial\zeta_{1,\ell-1}}{\partial y}\Big)\mathbf{E}_1^{(\ell)}\,, \\ \mathbf{S}_2 &= -\sum_{\ell=1}^{2} g\Big(\frac{\rho_{1,\ell} - \rho_{1,\ell-1}}{\rho_{2,1}}\Big)\Big(\frac{\partial\zeta_{1,\ell-1}}{\partial x} + \iota\frac{\partial\zeta_{1,\ell-1}}{\partial y}\Big)\mathbf{E}_2^{(1)} \\ &\quad -g\Big(\frac{\rho_{2,1} - \rho_{1,2}}{\rho_{2,1}}\Big)\Big(\frac{\partial\zeta_{2,0}}{\partial x} + \iota\frac{\partial\zeta_{2,0}}{\partial y}\Big)\mathbf{E}_2^{(1)}\,, \end{aligned}\right\} \tag{4.2.5}$$

$$\tau_{bx} + \iota\tau_{by} = \rho_{0,2}k_b \sum_{r=1}^{m_0}(A_{0,r} + \iota B_{0,r})M_{0,r}(1) \qquad \text{for} \quad \Omega_0, \tag{4.2.6}$$

$$\tau_{bx} + \iota\tau_{by} = \rho_{2,1}k_b \sum_{r=1}^{m_2}(A_{2,r} + \iota B_{2,r})M_{2,r}(1) \qquad \text{for} \quad \Omega_2, \tag{4.2.7}$$

The matrices $\mathbf{A}_i$, $\mathbf{B}_i$, $\mathbf{C}_i$, $\mathbf{E}_i^s$, $\mathbf{E}_i^b$ and $\mathbf{E}_i^{(\ell)}$ are given by (2.5.21) to (2.5.25).

Similarly, the spectral equations for (4.2.1), using limit conditions (3.2.2) and (3.2.3) with $\beta_{i,2} = 0$, $i = 0, 1, 2$ and $\beta_{2,1} = 0$, take the form

$$(\iota\gamma + \frac{\alpha_i}{H_i^2}\mathbf{\Lambda}_i)\widehat{\mathbf{W}}_i = \frac{\alpha_i}{H_i^2}\beta_{i,1}\mathbf{C}^s\widehat{\mathbf{W}}_i + \mathbf{F}_i + \mathbf{S}_i, \tag{4.2.8}$$

where

$$\widehat{\mathbf{W}}_i = \widehat{\mathbf{A}}_i + \iota\widehat{\mathbf{B}}_i \qquad i = 0, 1, 2, \tag{4.2.9}$$

$$\tau_{bx} + \iota\tau_{by} = \rho_{0,2} k_b \sum_{r=1}^{m_0} (\widehat{A}_{0,r} + \iota\widehat{B}_{0,r}) \Phi_{0,r} f_{0,r}(1) \qquad \text{for} \quad \Omega_0, \tag{4.2.10}$$

$$\tau_{bx} + \iota\tau_{by} = \rho_{2,1} k_b \sum_{r=1}^{m_2} (\widehat{A}_{2,r} + \iota\widehat{B}_{2,r}) \Phi_{2,r} f_{2,r}(1) \qquad \text{for} \quad \Omega_2, \tag{4.2.11}$$

The matrices $\mathbf{F}_i$ and $\mathbf{S}_i$, $i = 0, 1, 2$, take the same form as those given in (4.2.4) to (4.2.5). The matrices $\widehat{\mathbf{A}}_i$, $\widehat{\mathbf{B}}_i$, $\mathbf{C}_i$, $\mathbf{E}_i^s$, $\mathbf{E}_i^b$ $\mathbf{E}_i^{(\ell)}$ and $\mathbf{\Lambda}_i$ are given by (2.6.45), (2.6.49) and (2.6.51) to (2.6.54).

The vertical modes in equation (4.2.8) are coupled through the terms for bottom friction and stressing at the sea surface. If the bottom friction term is neglected in equations (4.2.10) and (4.2.11) and the homogeneous Neumann limit conditions ($\beta_{i,1} = 0$, $i = 0, 1$) are used, it is possible to write down the spectral solutions of steady drift current as

$$\widehat{A}_{i,1} + \iota\widehat{B}_{i,1} = -\frac{\iota F_i}{\gamma}\,, \tag{4.2.12}$$

$$\widehat{A}_{i,k} + \iota\widehat{B}_{i,k} = (\widehat{A}_{i,1} + \iota\widehat{B}_{i,1})\Big[1 - \frac{\iota\alpha_i}{\gamma H_i^2}\lambda_{i,k}\Big]^{-1} \qquad \text{for} \quad k \geq 2, \tag{4.2.13}$$

where $i = 0, 1$. Note that the value of the first modal coefficient is independent of the density variation and the eddy viscosity profile (although the contribution of $\widehat{A}_{i,1}$ and $\widehat{B}_{i,1}$ to current profiles may be slightly altered by the density variation because of the factor $\Phi_{i,1}$) and, if the wind stress is prescribed in the U-direction, the first vertical mode contributes only to motion in the V-direction. Once the coefficient of the first vertical mode is determined, the coefficients of the higher modes can be successively determined by (4.2.13). The spectral solutions of steady gradient current can be readily written in explicit form.

Figure 4.1 illustrates how body forcings including sea surface and interfacial gradients act in the one and two domain systems. Since the gradients are pre-

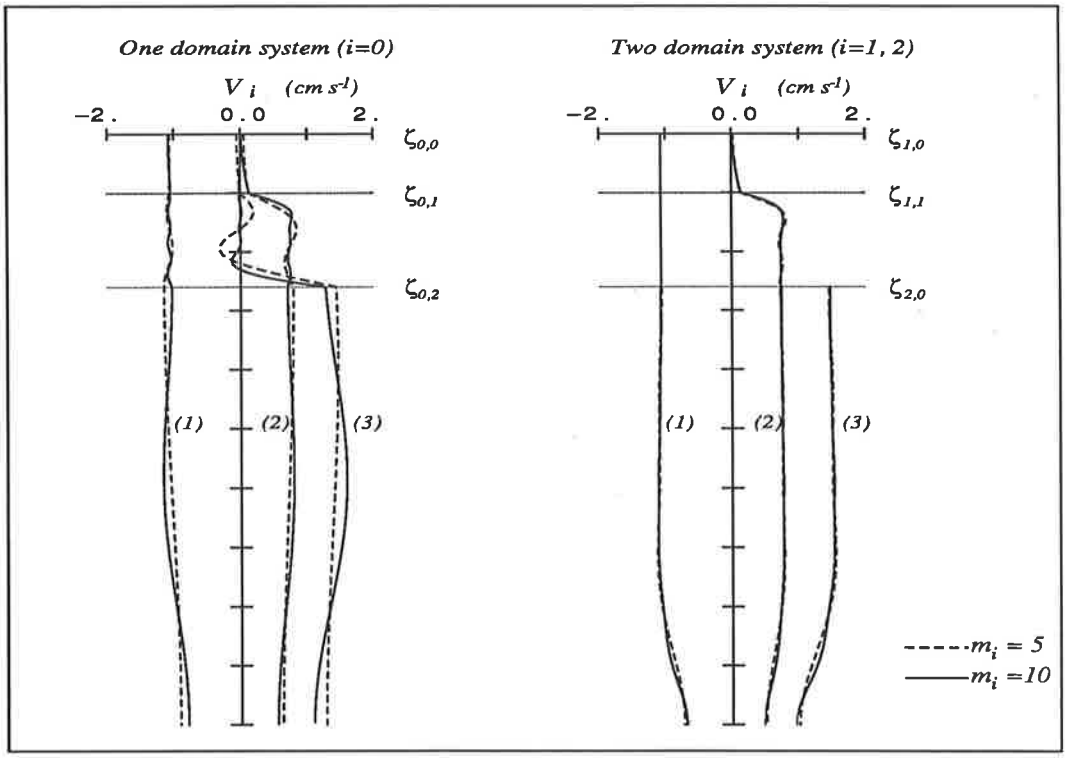

Figure 4.1 Steady velocity profiles, obtained using the profile in Figure 3.1(*d*), in three-layered one and two domain systems computed using a basis set of eigenfunctions, with: Δ_T=25, Δ_P=40, Δ_B=185m; N_T=150, N_P=10, N_B=1000 $cm^2 s^{-1}$; ρ_T=1025.8, ρ_P=1026.5, ρ_B=1027.2 $g\,cm^{-3}$, k_b=0.2 $cm\,s^{-1}$; $\partial\zeta_{i,0}/\partial y = \partial\zeta_{i,1}/\partial y = \partial\zeta_{i,2}/\partial y = 0$; and (1) $\partial\zeta_{i,0}/\partial x = 1.0\times10^{-7}$; (2) $\partial\zeta_{i,1}/\partial x = -1.0\times10^{-4}$; (3) $\partial\zeta_{i,2}/\partial x = -2.0\times10^{-4}$.

scribed only in the x-direction, the dominant part of the current is the V component developed by rotational effects. The magnitude of the gradients have been chosen arbitrarily while the gradient of the free sea surface has been chosen as $O(10^{-3})$ of that of the interfacial gradients, to take into account the proportionate density excess $\Delta\rho_{i,j}/\rho_{i,1}$. It is apparent from Figure 4.1 that, since free sea surface and interfacial gradients act as body forces, the current profile is formed throughout the water column in the one domain system. However, in the two domain system there is no mechanism which enables one to determine the velocity in the upper domain using the gradients $\zeta_{1,2}$. In a bounded region, since the external

and internal gradients will be constrained by the continuity equation (2.4.9), the upper and lower domains will interact with each other and the current velocity will be formed in the upper domain. The current profiles in the two domain system are almost noise-free compared with those of the one domain system and that the convergence of the eigenfunction expansion is very fast. In this study the current profiles in the bottom layer are computed using 10 eigenfunctions.

It can be seen that the presence of the pycnocline little affects the current profiles induced by $\zeta_{0,1}$, which means the gradient of the free sea surface is associated with barotropic flow. The bottom layer is predominantly composed of a geostrophic core, showing nearly constant current profiles except for the near-bottom layer. For the two domain system the depth variations of U_2 and V_2 are allowed only in the presence of bottom friction or when using a no-slip bottom boundary condition. The current profile of the two domain system is in general discontinuous at the interior domain boundary.

We now consider the influence of the pycnocline upon the vertical profile of wind drift current. It is evident from Figure 4.2 that the current profiles in stratified conditions are characterised by the presence of high shears within the pycnocline particularly in the proximity of the surface layer and, as N_P is reduced a rapid reversal of the vertical velocity gradient occurs within the pycnocline. As in the case of the vertical modes, the continuity requirements of the shear stresses force the velocity to change abruptly at $z = -H_i\xi_{i,j}$, the degree of the velocity change depending upon the ratio $\rho_{i,j}\mu_{i,j}/(\rho_{i,j+1}\mu_{i,j+1})$. The shear within the surface layer is sustained predominantly in the U component of the current which is parallel with the direction of the wind stress at the sea surface.

When the value of N_P is decreased and the thickness of the pycnocline is increased, the current profiles of the one and two domain systems agree qualitatively. This is to be expected because the presence of such stratified condi-

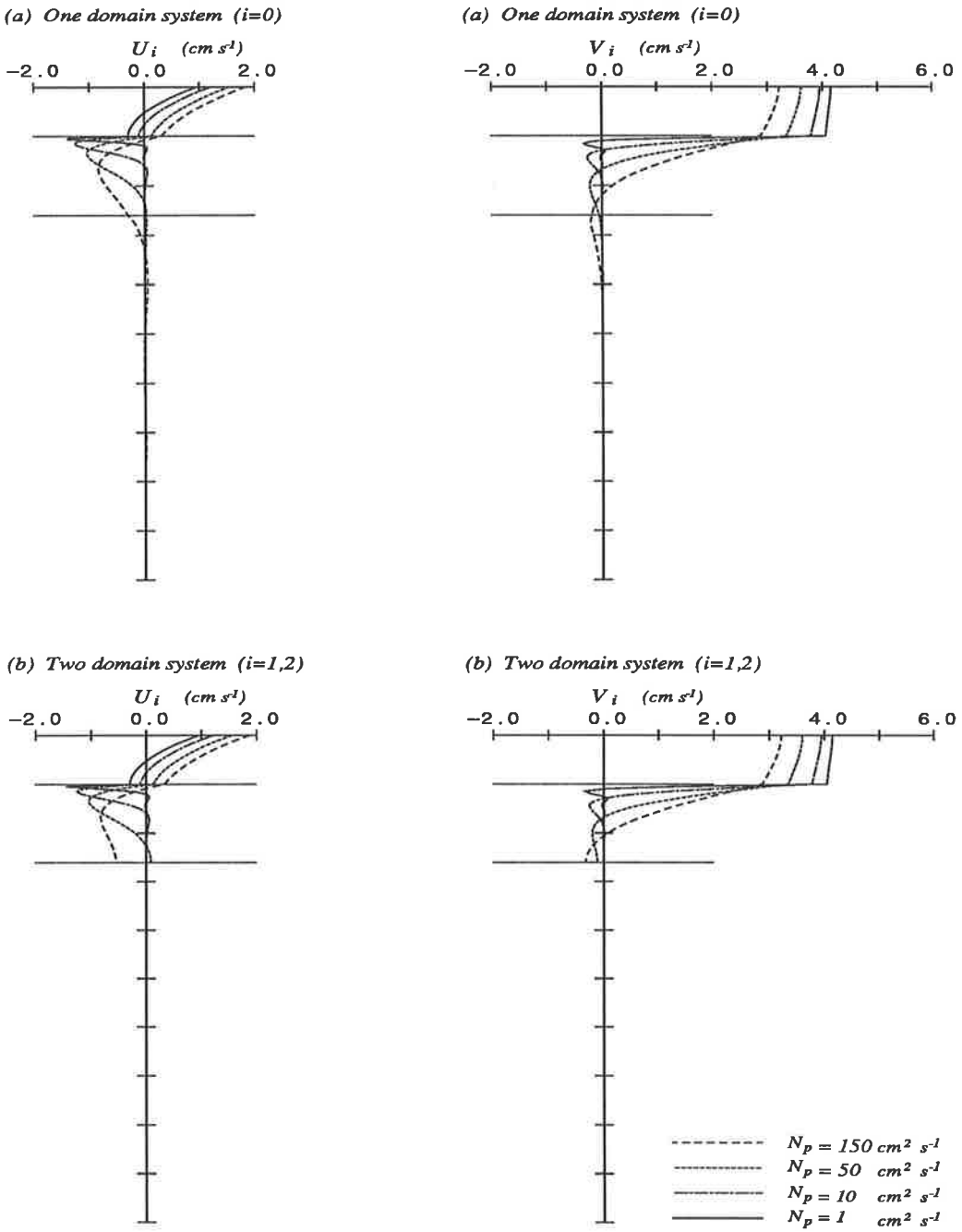

Figure 4.2 Steady velocity profiles of the U and V components of wind drift current, obtained using the profile in Figure 3.1(d), in one and two domain systems computed using a basis set of B-splines, with: Δ_T=25m; ρ_T=1025.8, ρ_P=1026.5 $g\,cm^{-3}$, and for Ω_0, ρ_B=1027.2 $g\,cm^{-3}$, k_b=0.2 $cm\,s^{-1}$; and (a) Δ_P=40, Δ_B=185 m; N_T =1000, N_B=100 cm^2s^{-1}; (b) Δ_P=40 m; N_T =1000 cm^2s^{-1}; (c) Δ_P=40, Δ_B=185 m; N_T=150, N_B=100 cm^2s^{-1}; (d) Δ_P=10, Δ_B=215 m; N_T=1000, N_B=100 cm^2s^{-1}.

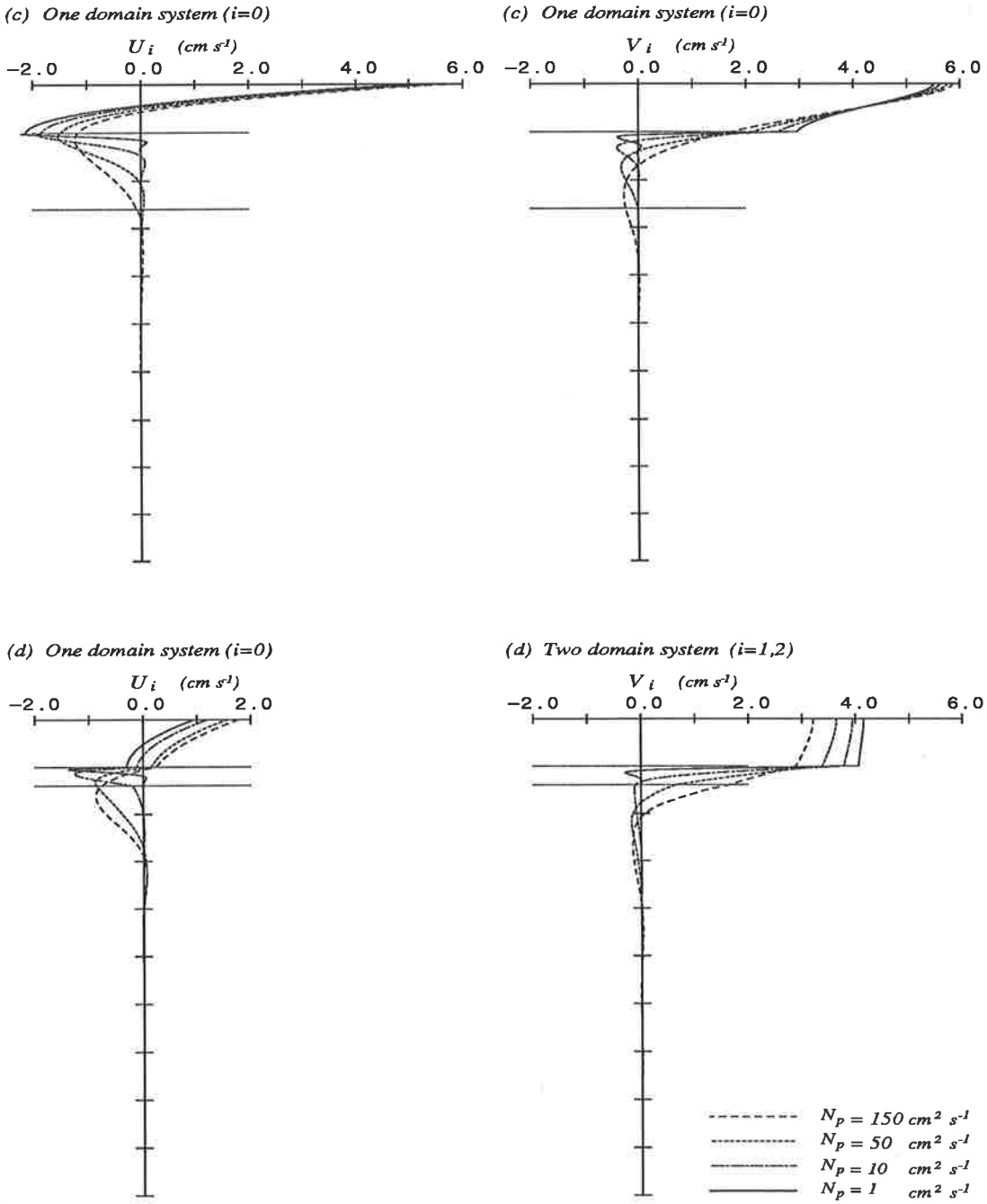

Figure 4.2 Cont'd.

tions significantly affects the depth of frictional influence. The downward flux of the wind shear vanishes effectively below a depth $\widetilde{D}_E$ ($\widetilde{D}_E = D_E/2$ where $D_E = \pi(2\overline{N}/|\gamma|)^{1/2}$ is the Ekman depth and $\overline{N}$ is a suitably averaged value of the vertical eddy viscosity over the depth (Weber, 1981)). When $\widetilde{D}_E$ is larger than Δ_T, one would expect that the vertical structure of the current in the two domain system would be considerably different from that in the one domain system. In determining the Ekman depth, it is important to take into account the eddy viscosity within the pycnocline and the pycnocline thickness, particularly when the mixed layer depth is smaller than the depth of frictional influence computed using N_T (Davies, 1986). An obvious consequence of imposing the stress-free conditions at the base of the pycnocline is that the maximum penetration scale of the wind momentum is limited to H_1. We may choose the base of the surface layer as a lower limit for the steady wind drift currents. In that case, as indicated in Figure 4.2, the presence of a high shear within the pycnocline has to be somehow reflected in the dynamic balance in order to realistically represent the current within the surface layer.

Figure 4.3 shows the angles of the surface wind drift current in the one and two domain systems computed using a basis set of B-spline functions, with various stratification conditions (see Figure caption). The angle measured counterclockwise from the positive x-axis is given by

$$\theta = \arctan(V_i(0)/U_i(0)). \tag{4.2.14}$$

It has been shown by Davies (1986) that, under conditions of strong stratification and a shallow mixed layer depth, the magnitude of the surface current and the angle are primarily determined by the values of Δ_T and Δ_P. It is then to be expected that when N_P is low and Δ_P is high, the difference in the angles of the surface current between the one and two domain systems will be insignificant. The angle of the surface current in the two domain system gradually deviates

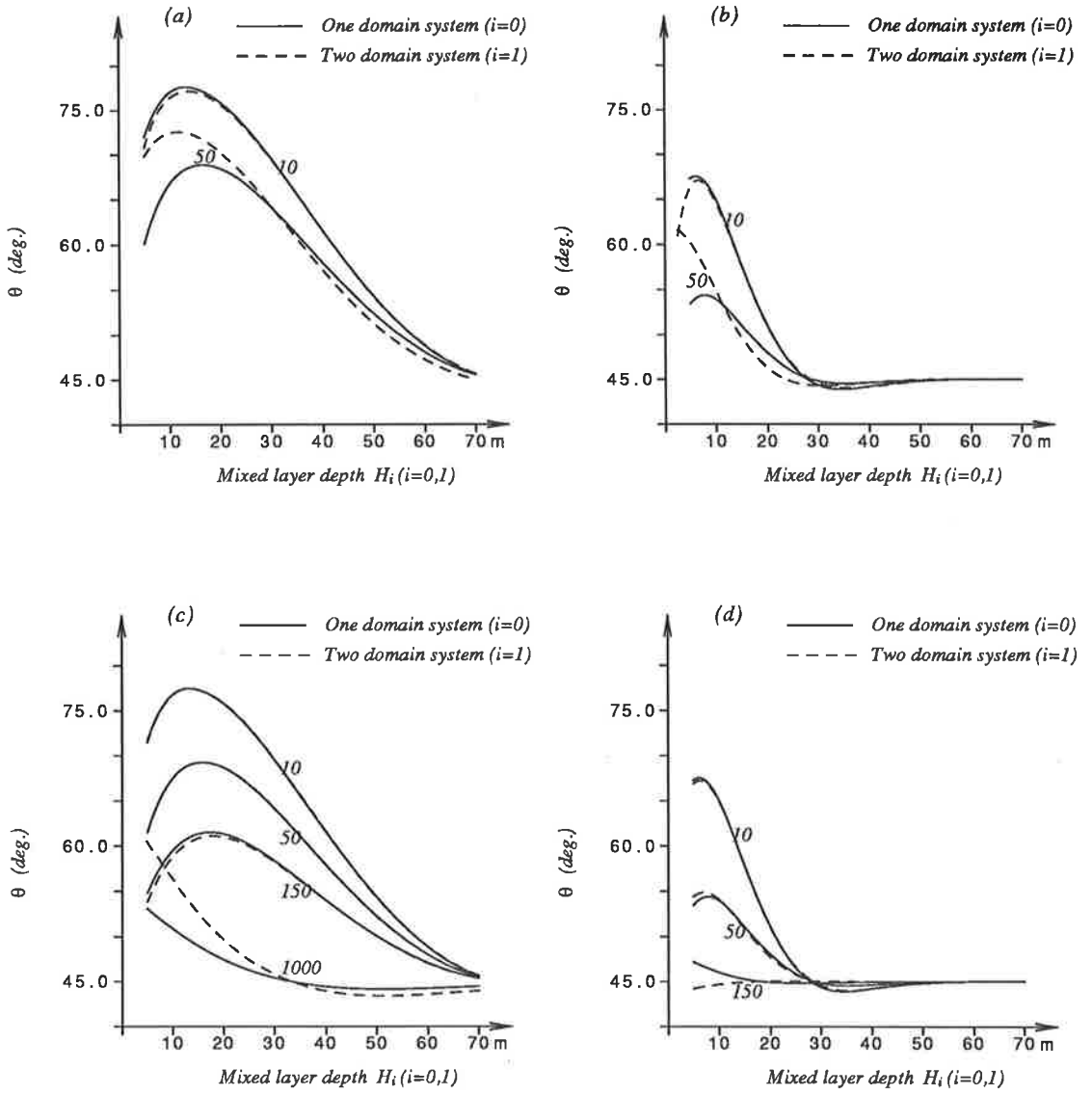

Figure 4.3 Angle θ of steady state wind drift surface currents, obtained using the profile in Figure 3.1(d), in three-layered one and two domain systems computed using a basis set of B-spline functions, with: ρ_T=1025.8, ρ_P=1026.5 $g\,cm^{-3}$, and, for Ω_0, ρ_B=1027.2 $g\,cm^{-3}$, N_B=100 $cm^2 s^{-1}$, H_0= 250 m, k_b=0.0 $cm\,s^{-1}$; and (a) Δ_P=10 m; N_T =1000 and N_P=10, 50 $cm^2 s^{-1}$; (b) Δ_P=10 m; N_T =150 and N_P=10, 50 $cm^2 s^{-1}$; (c) Δ_P=40 m; N_T =1000 and N_P=10, 50, 150, 1000 $cm^2 s^{-1}$; (d) Δ_P=40 m; N_T =150 and N_P=10, 50, 150 $cm^2 s^{-1}$.

from that in the one domain system as the surface layer depth is reduced and the eddy viscosity within the pycnocline is increased. When a stress-free condition is enforced at the base of the surface layer and the surface layer depth is very shallow, the surface current will tend to deflect 90° to the left of the wind direction. It is evident that as the value of Δ_T is increased, the surface current approaches the value computed using the classical Ekman theory (45° to the left of the wind direction in the Southern Hemisphere). If a no-slip condition is imposed at the base of the shallow surface layer, the surface current tends to be aligned with the wind direction.

Convergence of the eigenfunction expansion

We now consider the depth variation of steady current profiles computed using a basis set of eigenfunctions. It is evident from Figure 4.4 that the Gibbs overshoots arise below the point where the high shear occurs. A large number of eigenfunctions have to be used in order to remove the oscillations (particularly in the current profile for the x-direction which is parallel to the wind stress) and to improve the convergence of the surface velocity. It has been revealed in a series of computations that prescribing the eddy viscosity smoothly across the interface is not much help in suppressing the oscillations unless the eddy viscosity profile is substantially smoothed out across the interface. However, there is a certain physical situation in which these oscillations can be significantly suppressed without increasing the number of eigenfunctions and without smoothing the form of eigenfunctions locally. In regions where strong tidal currents are present, it is necessary to increase the value of the eddy viscosity at the bottom layer to the value comparable with that at the surface layer. In this case, as shown in Figure 4.4(b), the Gibbs overshoots are significantly reduced except within the pycnocline.

When a finite number of continuous functions are used, nonphysical oscilla-

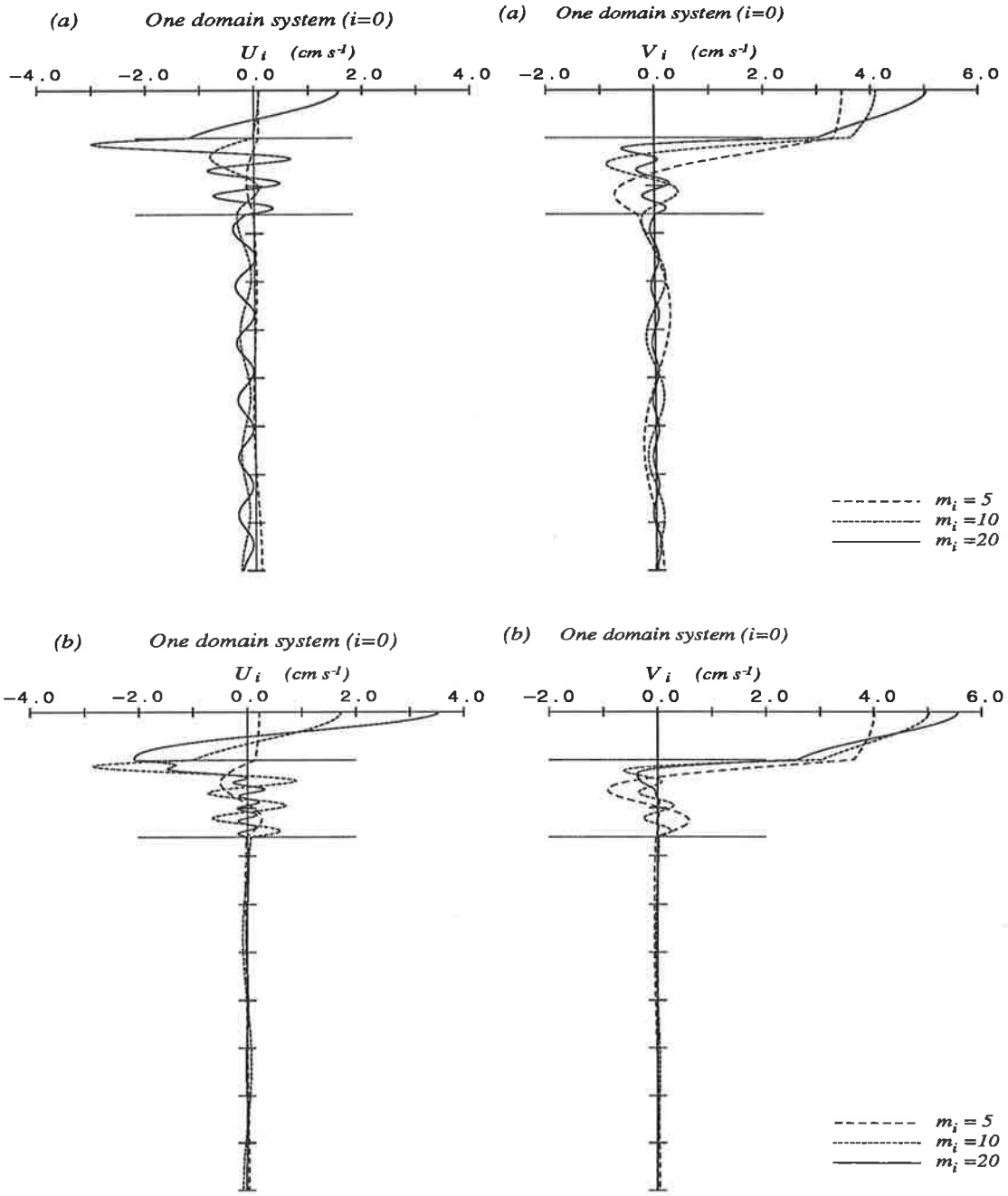

Figure 4.4 Steady velocity profiles of the U and V components of wind drift current, obtained using the profile in Figure 3.1(d), in one domain systems computed using a basis set of eigenfunctions, with: Δ_T=25, Δ_P=40, Δ_B=185 m; N_T =150, N_P=10 $cm^2 s^{-1}$; k_b=0.2 $cm\,s^{-1}$; ρ_T=1025.8, ρ_P=1026.5, ρ_B=1027.2 $g\,cm^{-3}$; $\beta_{0,1}$ =$\beta_{0,2}$=0; and (a) N_B=50 $cm^2 s^{-1}$; (b) N_B=1000 $cm^2 s^{-1}$.

tions are produced with overshoots whenever a discontinuous change in solutions arises and in such cases the Galerkin solution behaves like the solution found by using a low-order finite difference method (Canuto, 1987). It is known that Chebyshev polynomials are also susceptible to the Gibbs phenomenon in the presence of internal discontinuities (Gottlieb and Orszag, 1977). We note that the discontinuity of the eigenfunctions itself is not a source of the Gibbs overshoots. It has been found that with a small number of eigenfunctions the compatibility between the form of the first few eigenfunctions and the current profiles within the pycnocline is an important factor determining whether the nonphysical oscillations arise or not.

We now briefly examine the influence of using a non-zero stress limit condition at the sea surface on the convergence of the surface current and U, V current profiles. It is evident from Figure 4.5 that the value of $\beta_{i,1}$ significantly affects the convergence of the surface current. For a negative value of $\beta_{i,1}$ the form of the eigenfunctions is such that the derivative of each eigenfunction with respect to the depth coordinates (namely, $-df_i/d\sigma_i$) at the sea surface is a positive constant. Consequently both of the U and V surface currents are overestimated and, since the external stress is applied only in the U-direction, the V surface current shows a lack of convergence, producing a kink in the profile near the sea surface. There is some evidence that nonphysical oscillations arise in the V current profile, while the U current profile is almost free of oscillations. When a positive value of $\beta_{i,1}$ is used, the U and V components of current near the sea surface reveal a reversal in the vertical velocity gradient. In this case the form of the eigenfunctions is such that the derivative of each eigenfunction with respect to depth coordinates at the sea surface is a negative constant, whereas the gradient of the U current near the sea surface are non-negative. By using this expansion, the U and V surface currents are significantly underestimated. There is also some evidence that nonphysical oscillations appear in the U current profile. As the value of

$\beta_{i,1}$ approaches an optimum value and as the number of eigenfunctions used is increased, the oscillation is suppressed. Davies and Owen (1979) have shown that the surface current can be reproduced accurately by using Chebyshev and Legendre polynomials particularly in wind induced currents. It should be noted that by using the limit condition (3.2.2) at the sea surface all of the eigenfunctions have the same value for the vertical gradient at the sea surface, whereas the components in both the Chebyshev or Legendre polynomial expansions have in general different vertical gradients at the sea surface.

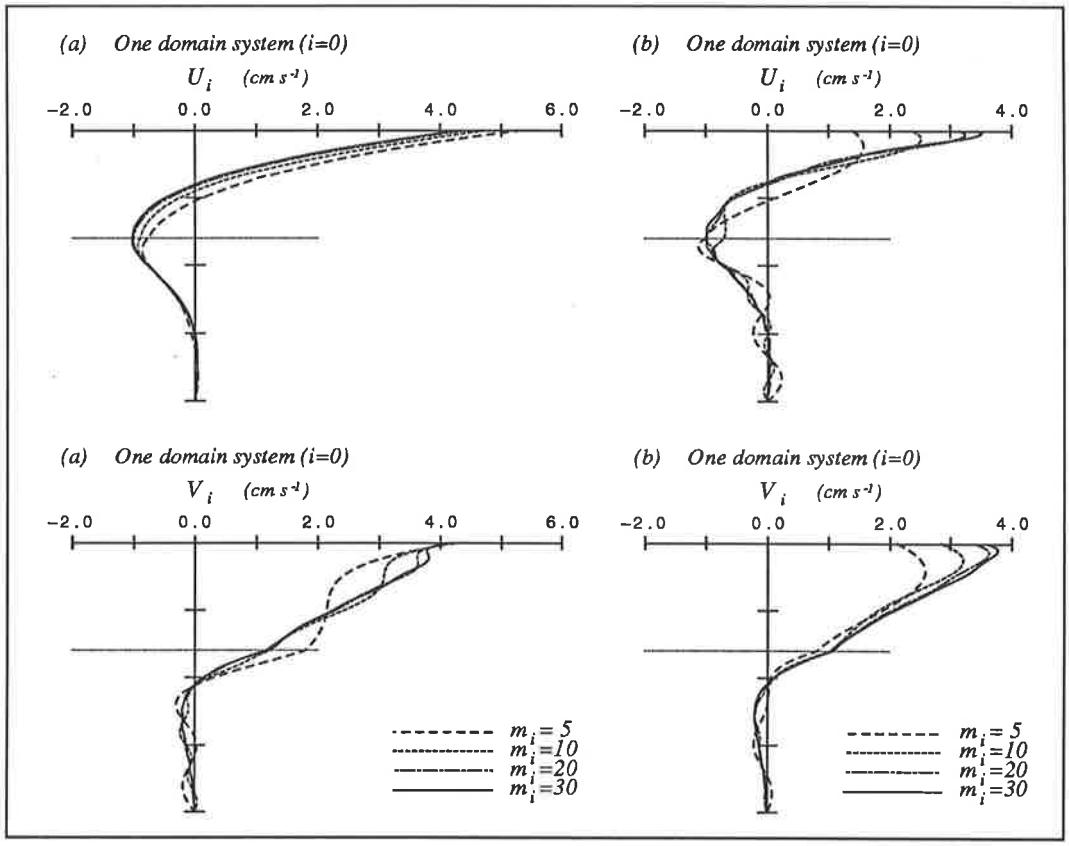

Figure 4.5 Steady velocity profiles of the U and V components of wind drift current, obtained using the profile in Figure 3.1(c), in the one domain system computed using a basis set of eigenfunctions, with an increasing number of m_0. A no-slip condition ($\beta_{0,2}=\infty$) is used at the sea bed with: Δ_T=40, Δ_B=60 m; N_T =300, N_B=100, α_0=180 cm^2s^{-1}; ρ_T=1025.8, 1027.0 $g\,cm^{-3}$; and (a) $\alpha_0\beta_{0,1}$=−0.125 cm^2s^{-1}; (b) $\alpha_0\beta_{0,1}$=0.125 cm^2s^{-1}.

4.3 Time-dependent wind induced motion

4.3.1 Description of the model

This section is concerned with the application of the Galerkin models to wind drift currents in two and three-layered horizontally unbounded seas following the onset of a suddenly applied spatially homogeneous wind stress. The layered structures and the vertical eddy viscosity are assumed to be independent of the horizontal coordinates. Surface and interfacial displacements are all suppressed. The thickness of each layer is kept constant with respect to time, although in practice the wind action causes the pycnocline to become diffused as the mixed-layer depth is reduced. Under these conditions, the pertinent equations of motion for the time dependent wind drift currents in open sea regions may be written as follows:

$$\frac{\partial U_{i,j}}{\partial t} - \gamma U_{i,j} = \frac{\alpha_i}{H_i^2}\frac{\partial}{\partial \sigma_i}\left(\mu_{i,j}\frac{\partial U_{i,j}}{\partial \sigma_i}\right), \tag{4.3.1}$$

$$\frac{\partial V_{i,j}}{\partial t} + \gamma V_{i,j} = \frac{\alpha_i}{H_i^2}\frac{\partial}{\partial \sigma_i}\left(\mu_{i,j}\frac{\partial V_{i,j}}{\partial \sigma_i}\right), \tag{4.3.2}$$

where $i = 0, j = 1, 2, 3$ for the three-layered one domain system, and $i = 1, j = 1, 2$ for the upper domain of the three-layered two domain system. Since the wind shear is not transmitted downwards across the interior domain boundary, the lower domain Ω_2 will remain at rest. Hence the two domain system here can be viewed as an open sea region of depth H_1 which is composed of the surface layer and the pycnocline. The velocity shear at the base level of the upper domain may be introduced as a driving force for the lower domain— this will be described later.

The numerical solutions of (4.3.1) and (4.3.2) are generated from a quiescent state of motion described by a zero initial velocity field, namely,

$$U_i = V_i = 0 \qquad \text{at} \quad t = 0. \tag{4.3.3}$$

Calculations of a transient free motion subjected to a non-zero initial velocity field will be described at the end of this chapter.

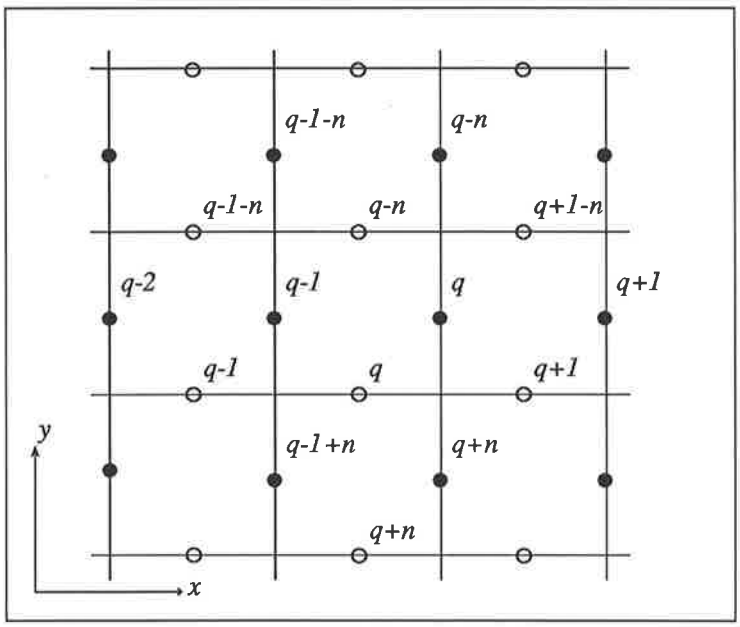

Figure 4.6 A staggered finite difference grid for the rectangular x–y plane showing the locations of $U_{i,q}$ and $V_{i,q}$ and neighboring grid points; • = a U_i-point (also A_i and $\widehat{A}_i$); o = a V_i-point (also B_i and $\widehat{B}_i$); n represents the number of computational grid points in a row; calculations are preformed using $q = 5$ and $n = 3$.

The surface wind stress is suddenly applied at $t = 0$ in the following form:

$$H(t)\ \tau_{sx} \quad \text{for a step-function wind stress,} \tag{4.3.4}$$

$$(H(t) - H(t - T_1))\tau_{sx} \quad \text{for a constant wind pulse with a duration } T_1, \tag{4.3.5}$$

where $H(t)$ is the Heavyside function and $\tau_{sx} = 1\ dyne\ cm^{-2}$.

The model developed is designed to use the staggered finite difference grid system, shown in Figure 4.6, in anticipation of its application to a realistic system. Hence, in numerical computations, the two variables U_i and V_i are used rather than the single variable $W_i = U_i + \iota V_i$.

Modal interpretations of the wind drift currents are performed using complex notation.

4.3.2 Integration with respect to time

A basis set of B-spline functions

The solutions of time-dependent wind drift current in the one and two domain systems are derived from (2.5.18) and (2.5.19), and (2.5.51) and (2.5.52), respectively, by omitting the gradients of the free sea surface and the interfaces, the atmospheric pressure and the direct tide-generating forces. Their finite difference representation can be written in the form

$$\mathbf{C}_i^+ \mathbf{A}_i\Big|_q^{t+\Delta t} = \mathbf{C}^- \mathbf{A}_i\Big|_q^t + \Delta t\gamma \mathbf{B}_i\Big|_q^t + \Delta t \mathbf{F}_{i,x}\Big|_q^t \,, \tag{4.3.6}$$

$$\mathbf{C}_i^+ \mathbf{B}_i\Big|_q^{t+\Delta t} = \mathbf{C}^- \mathbf{B}_i\Big|_q^t - \Delta t\gamma \mathbf{A}_i\Big|_q^t + \Delta t \mathbf{F}_{i,y}\Big|_q^t \,, \tag{4.3.7}$$

where $i = 0, 1, 2$ and

$$\mathbf{C}_i^+ = \mathbf{C}_i + \frac{\Delta t}{2}\frac{\alpha_i}{H_i^2}\mathbf{D}_i \,, \tag{4.3.8}$$

$$\mathbf{C}_i^- = \mathbf{C}_i - \frac{\Delta t}{2}\frac{\alpha_i}{H_i^2}\mathbf{D}_i \,, \tag{4.3.9}$$

$$\tau_{bx} = \rho_{0,2} k_b \sum_{r=1}^{m_0} A_{0,r}\Big|_q^t M_{0,r}(1), \qquad \text{for} \quad \Omega_0, \tag{4.3.10}$$

$$\tau_{bx} = \rho_{2,1} k_b \sum_{r=1}^{m_2} A_{2,r}\Big|_q^t M_{2,r}(1), \qquad \text{for} \quad \Omega_2, \tag{4.3.11}$$

The matrices $\mathbf{A}_i$, $\mathbf{B}_i$, $\mathbf{C}_i$, $\mathbf{D}_i$, $\mathbf{E}_i^s$ and $\mathbf{E}_i^b$ are given by (2.5.21) to (2.5.26), and the matrices $\mathbf{F}_{i,x}$ and $\mathbf{F}_{i,y}$ are the real and imaginary parts of $\mathbf{F}_i$ in (4.2.6), respectively.

Integration on the staggered grid system leads to the introduction of periodic boundary conditions. Calculations are performed at the qth point where the conditions

$$A_i\big|_q^t = A_i\big|_{q-1}^t = A_i\big|_{q-1+n}^t = A_i\big|_{q+n}^t, \tag{4.3.12}$$

$$B_i\big|_q^t = B_i\big|_{q+1}^t = B_i\big|_{q+1-n}^t = B_i\big|_{q-n}^t \tag{4.3.13}$$

are satisfied for all t.

The size of the time steps Δt can be chosen in a flexible manner since the propagation of the fast-moving surface waves is suppressed. The CFL condition is no longer a restriction. However, to ensure high accuracy of solutions a time step of 9 seconds has been chosen. When the water depth is taken as being constant, the inversion of the matrices on the left-hand sides in (4.3.6) and (4.3.7) is required only once before marching on in time.

A basis set of eigenfunctions

All solutions, computed hereafter using a basis set of eigenfunctions, are based on Heaps' formulation. We can write down the finite difference representation of (2.6.42), (2.6.43), (2.6.78) to (2.6.81) with $\beta_{i,2} = 0$, $i = 0, 1, 2$, and $\beta_{1,2} = \beta_{2,1} = 0$, omitting the gradients of the free sea surface, the interfaces, the atmospheric pressure and the direct tide-generating forces, as follows:

$$\mathbf{C}_i^+ \, \widehat{\mathbf{A}}_i\big|_q^{t+\Delta t} = \mathbf{C}_i^- \, \widehat{\mathbf{A}}_i\big|_q^t + \Delta t \gamma \widehat{\mathbf{B}}_i\big|_q^t + \Delta t \mathbf{F}_{i,x}\big|_q^t \, , \tag{4.3.14}$$

$$\mathbf{C}_i^+ \, \widehat{\mathbf{B}}_i\big|_q^{t+\Delta t} = \mathbf{C}_i^- \, \widehat{\mathbf{B}}_i\big|_q^t - \Delta t \gamma \widehat{\mathbf{A}}_i\big|_q^t + \Delta t \mathbf{F}_{i,y}\big|_q^t \, , \tag{4.3.15}$$

with

$$\mathbf{C}_i^+ = \mathbf{I} + \frac{\Delta t}{2} \frac{\alpha_i}{H_i^2} \mathbf{\Lambda}_i - \frac{\Delta t \alpha_i}{2 H_i^2} \beta_{i,1} \mathbf{C}^s \, , \tag{4.3.16}$$

$$\mathbf{C}_i^- = \mathbf{I} - \frac{\Delta t}{2} \frac{\alpha_i}{H_i^2} \mathbf{\Lambda}_i + \frac{\Delta t \alpha_i}{2 H_i^2} \beta_{i,1} \mathbf{C}^s \, , \tag{4.3.17}$$

where $i = 0$ and 1 for the one and two domain systems, respectively, $\mathbf{I}$ is the unit matrix and

$$\tau_{bx} = \rho_{0,2} k_b \sum_{r=1}^{m_0} \widehat{A}_{0,r}\Big|_q^t \Phi_{0,r} f_{0,r}(1), \qquad \text{for} \quad \Omega_0, \tag{4.3.19}$$

$$\tau_{bx} = \rho_{2,1} k_b \sum_{r=1}^{m_2} \widehat{A}_{2,r}\Big|_q^t \Phi_{2,r} f_{2,r}(1), \qquad \text{for} \quad \Omega_2, \tag{4.3.20}$$

The matrices $\mathbf{F}_i$, $i = 0, 1, 2$, take the same form as those given in (4.2.6) to (4.2.7). The matrices $\widehat{\mathbf{A}}_i$, $\widehat{\mathbf{B}}_i$, $\mathbf{C}_i$, $\mathbf{E}_i^s$, $\mathbf{E}_i^b$, $\mathbf{E}_i^{(\ell)}$ and $\mathbf{\Lambda}_i$ are given by (2.6.45), (2.6.49) and (2.6.51) to (2.6.54). The periodic boundary conditions are given by replacing $A_{i,r}$ and $B_{i,r}$ with $\widehat{A}_{i,r}$ and $\widehat{B}_{i,r}$ in (4.3.12) and (4.3.13), respectively.

If the basis set is constructed with $\beta_{i,1} = 0$, $i = 0, 1$, $\mathbf{C}_i^+$ and $\mathbf{C}_i^-$ in equations (4.3.16) and (4.3.17) become diagonal matrices. The equations of the modal coefficients are then uncoupled except through the bottom frictional term allowing the finite difference representation of (4.3.16) and (4.3.17) to be simplified to

$$\begin{aligned}\Big(1 + \frac{\Delta t}{2}\frac{\alpha_i}{H_i^2}\lambda_{i,k}\Big)\widehat{A}_{i,k}\Big|_q^{t+\Delta t} = &\Big(1 - \frac{\Delta t}{2}\frac{\alpha_i}{H_i^2}\lambda_{i,k}\Big)\widehat{A}_{i,k}\Big|_q^{t+\Delta t} \\ &+\Delta t\gamma\widehat{B}_{i,k}\Big|_q^t + \Delta t f_{i,k}(1)(\rho_{i,1}H_i)^{-1}(\tau_{sx} - \tau_{bx}) ,\end{aligned} \tag{4.3.21}$$

$$\begin{aligned}\Big(1 + \frac{\Delta t}{2}\frac{\alpha_i}{H_i^2}\lambda_{i,k}\Big)\widehat{B}_{i,k}\Big|_q^{t+\Delta t} = &\Big(1 - \frac{\Delta t}{2}\frac{\alpha_i}{H_i^2}\lambda_{i,k}\Big)\widehat{B}_{i,k}\Big|_q^{t+\Delta t} \\ &-\Delta t\gamma\widehat{A}_{i,k}\Big|_q^t + \Delta t f_{i,k}(1)(\rho_{i,1}H_i)^{-1}(\tau_{sy} - \tau_{by})\end{aligned} \tag{4.3.22}$$

where $i = 0$ and 1 for the one and two domain systems, respectively.

Before considering the solution of the wind induced motion, we briefly examine the rate of convergence of the surface current computed using the eigenfunction expansion. It is apparent from Figure 4.7 that the V component of the surface current (denoted by V_s) converges rapidly and that use of ten vertical modes produce excellent accuracy. However, the rate of convergence of the U component of the surface current (denoted by U_s) is unsatisfactorily slow. This is because the

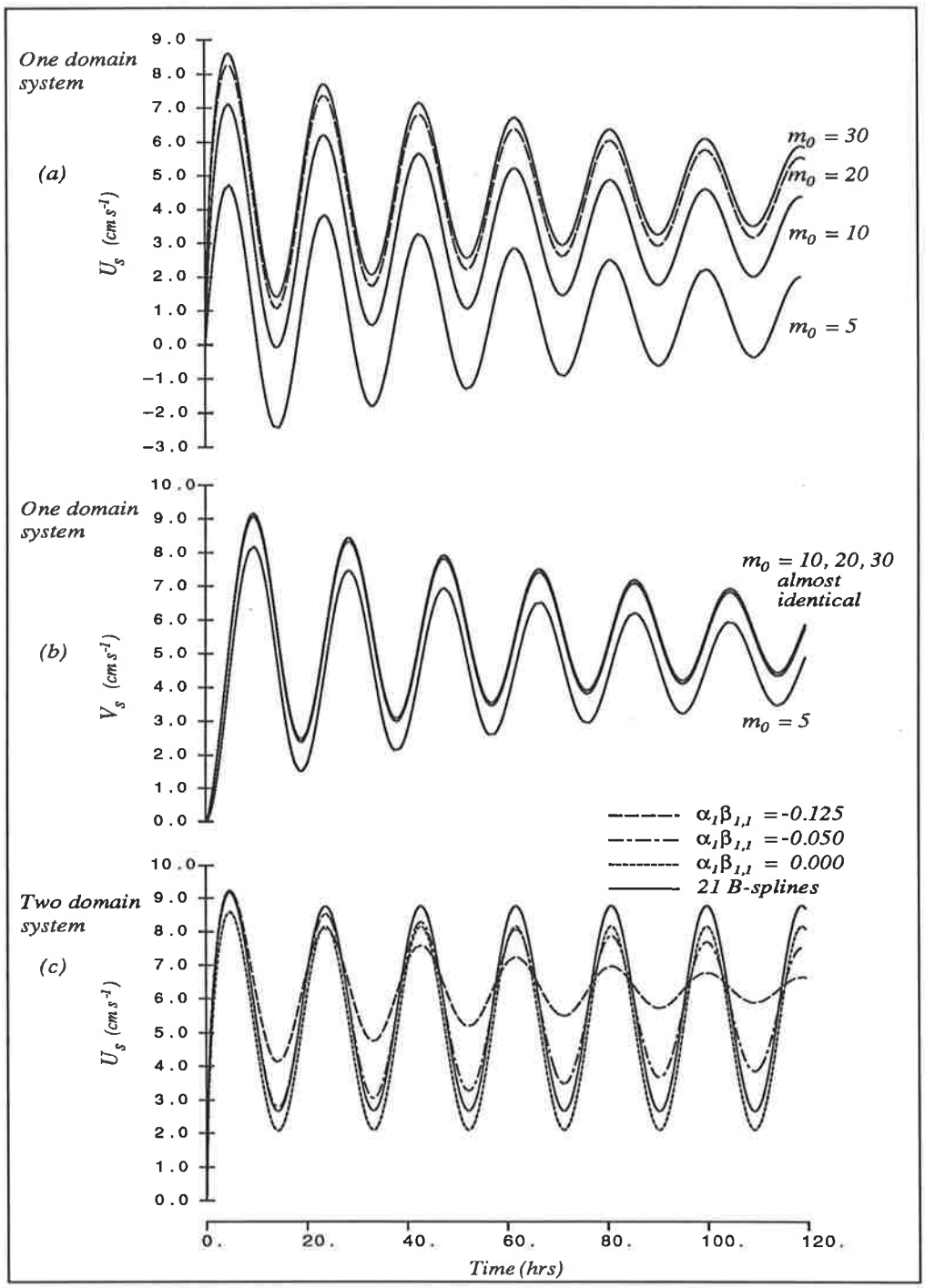

Figure 4.7 Time variations of the wind drift surface currents, obtained using the profile in Figure 3.1(*d*), computed using a basis set of eigenfunctions, with: Δ_T=25, Δ_P=10 *m*; N_T =150, cm^2s^{-1}; ρ_T=1025.8, ρ_P=1026.5 $g\,cm^{-3}$, and for Ω_0, ρ_B=1027.2 $g\,cm^{-3}$, Δ_B=215 *m*, N_B=1000 cm^2s^{-1}, k_b=0.2 $cm\,s^{-1}$; and (*a*), (*b*) N_P =10 cm^2s^{-1}; $\beta_{0,1}$= $\beta_{0,2}$=0.0, with an increasing number of m_0; (*c*) N_P =50, $\alpha_1 \simeq$121.4 cm^2s^{-1} with various values of $\alpha_1\beta_{1,1}$ shown in the key and with 21 *B*-spline functions.

stress τ_{sx} computed with a finite number of eigenfunctions cannot be the same as the value applied externally (Davies and Owen, 1979).

By using an optimum value of $\beta_{i,1}$ we can improve the convergence of the V component of the horizontal current near the surface. This point was discussed in Section 4.1. However, since a system of coupled equations has to be solved with respect to time (as a consequence of introducing the $\beta_{i,1}$ term), the computational effort is rapidly increased as the number of vertical modes is increased. Furthermore, the $\beta_{i,1}$ term effectively acts as a damping term and hence is not suited to the reproduction of temporally quasi-periodic motion (Figure 4.7(c)).

It is evident from Figures 4.8(a) and (b) that, as a consequence of the Gibbs phenomenon, nonphysical oscillations appear in the U component of the current profile in which wind stress is applied. When N_B is increased from 100 to 1000 $cm^2\ s^{-1}$, as noted in the calculation of the steady state profile, the oscillations are significantly reduced except within the pycnocline. Increasing m_i from 10 to 20 is not helpful in suppressing the oscillations. A large number of eigenfunctions have to be used to smooth out the oscillations unless a *cosmetic filter* is applied. In regions where strong tidal currents are omnipresent, it is necessary to increase the vertical variation of the eddy viscosity at the bottom layer to a value comparable to that at the surface layer. Heaps and Jones (1985) have chosen values $N_T = 300\ cm^2\ s^{-1}$ and $N_B = 1000\ cm^2\ s^{-1}$ in applying a three-layered spectral model to a shelf with a depth ranging in the cross-shelf direction from 50 to 300 m. Although it was not explicitly mentioned in their paper, it is conceivable that the reason behind this choice of eddy viscosity was to take into account the tidally-induced background turbulence and at the same time to suppress the Gibbs overshoots.

In a series of preliminary computations it has been found that, despite the slow convergence near the sea surface and the Gibbs overshoots particularly within the pycnocline, the layer-mean values of current were computed accurately, even with

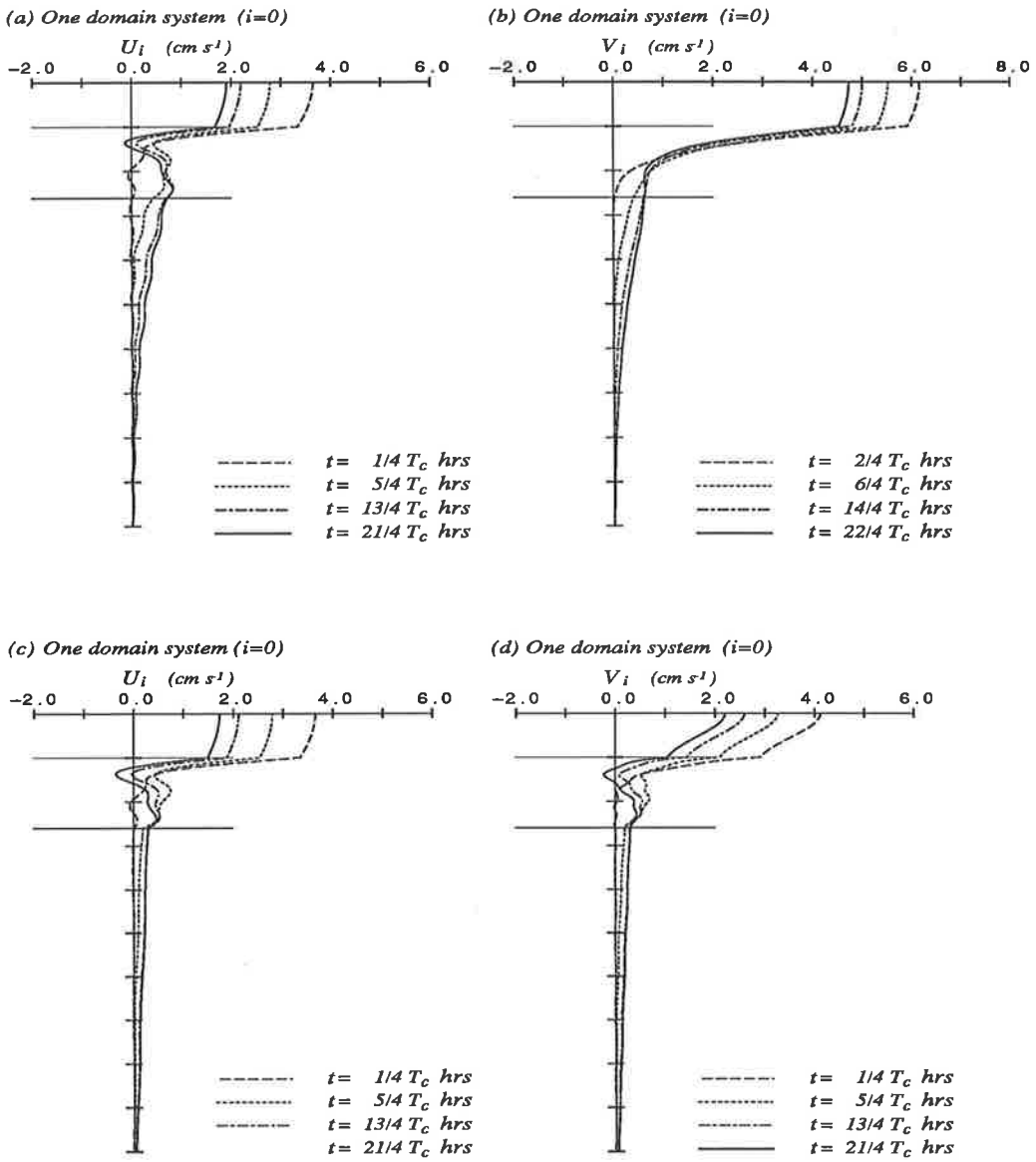

Figure 4.8 Velocity profiles of U and V components of wind drift current, obtained using the profile in Figure 3.1(d), at various time steps computed using a basis set of eigenfunctions, with: Δ_T=25, Δ_P=40, Δ_B=185 m; N_T =1000, N_P=10 $cm^2 s^{-1}$; ρ_T=1025.8, ρ_P=1026.5, ρ_B=1027.2 $g\,cm^{-3}$; k_b=0.2 $cm\,s^{-1}$; $\beta'_{0,1}=\beta_{0,2}=0$; and ($a$),($b$) N_B=100 $cm^2 s^{-1}$ with m_i=10; (c) N_B=1000 $cm^2 s^{-1}$ with m_i=10; (d) N_B=1000 $cm^2 s^{-1}$ with m_i=20.

only five vertical modes. From this point forward, in calculations with a basis set of eigenfunctions, 20 vertical modes along with homogeneous Neumann limit conditions will be used.

4.3.3 Results

To examine the time variation of surface currents in the one and two domain systems and their sensitivity in particular to changes in N_P, wind drift surface currents induced by the step-function wind stress are computed for 120 hrs using a basis set of B-spline functions. Three values of the eddy viscosity N_P are considered, these being $N_P = 10$, 50 and 150 $cm^2 s^{-1}$. Figure 4.9 shows the sensitivity of the U component of the surface current to changes in N_P in the one domain (Figures 4.9(a), (b) and (c)) and two domain systems (Figures 4.9(d) and (d)). It is evident that wind drift surface currents are characterised by an oscillation of inertial period $T_c = 2\pi/\gamma \simeq 18.2$ hrs. The inertial oscillations are in fact formed throughout the water column and the U and V components of the oscillations are 90° out of phase with each other. It is apparent from Figures 4.9(a) to (c) that in the one domain system the values of N_P and Δ_P are important in determining the rate of damping of the inertial oscillations in the surface currents. When N_P is increased and Δ_P is decreased the wind momentum can more rapidly penetrate to the bottom layer. This leads to an enhanced initial damping of the surface current. Also the rate of damping of the surface current is substantially influenced by the surface mixed layer depth. It is evident that with $\Delta_T = 25\,m$ the surface current at $t = T_c/4$ hrs is already affected by the eddy viscosity within the pycnocline. When Δ_T is increased to $60\,m$, the presence of the pycnocline has little effect on the surface current at $t = T_c/4$ hrs. After the initial stage of development the amplitude of the inertial motion decays gradually as the wind momentum diffuses downward out of the surface layer. Over the 120 hrs, the U and V surface components of the surface current continue to decay. Consequently,

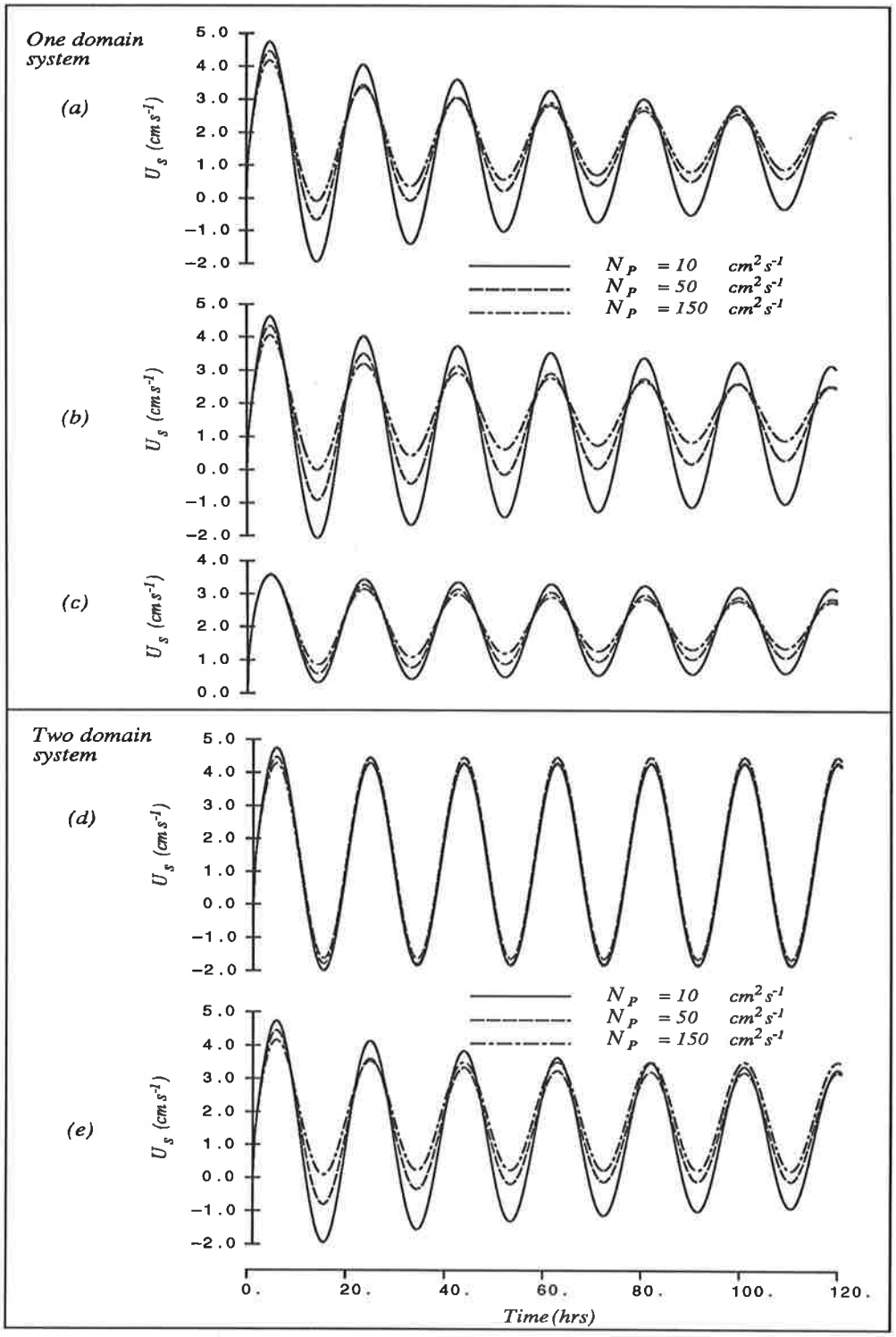

Figure 4.9 Time variation of the U component of wind drift surface current, obtained using the profile in Figure 3.1(d), computed using a basis set of B-spline functions, with: ρ_T=1025.8, ρ_P=1026.5 $g\,cm^{-3}$, and for Ω_0, ρ_B=1027.2 $g\,cm^{-3}$, N_B=100 cm^2s^{-1}, k_b=0.2 $cm\,s^{-1}$; and (a) Δ_T=25, Δ_P=10, Δ_B=215 m; (b) Δ_T=25, Δ_P=40, Δ_B=185 m; (c) Δ_T=60, Δ_P=40, Δ_B=150 m; (d) Δ_T=25, Δ_P=10 m; (d) Δ_T=25, Δ_P=40 m.

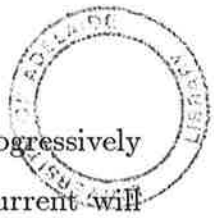

the U and V components of the current in the bottom layer increase progressively over the first few inertial periods. The initial decay of the surface current will last until the system reaches a steady state. It is apparent that, as the value of N_P is increased from 10 to 150 cm^2s^{-1}, the damping of the surface current is significantly enhanced. For details on the wind induced inertial oscillation of the one domain system, see Davies (1985*b*, *c*).

Comparing Figure 4.9(d) with Figures 4.9(a) to (c), it can be seen that with $\Delta_T = 25$ and $\Delta_P = 10\,m$ the quasi-steady inertial oscillations appear almost immediately after the wind stress is suddenly applied at $t = 0$. In the two domain system the maximum penetration depth of wind's energy is constrained to H_1. Consequently, a quasi-steady state is reached rapidly and, in the absence of frictional damping at the base of the domain boundary, the surface currents will exhibit almost pure inertial oscillations. When the value of Δ_P is increased from 10 to $40\,m$ the initial decay of the inertial motion is apparently shown with $N_P = 10$ cm^2s^{-1} and the time variation of the surface current in the two domain system becomes comparable with that of the one domain system (Figure 4.9(d)). This is because the wind energy of the surface layer diffuses downwards very slowly and, in such circumstances, imposing a stress-free condition at the base of the two domain boundary has little influence on the surface current over a couple of inertial periods.

The most interesting fact, as indicated in Figure 4.9(d), is that the inertial motion of the two domain system is undamped and the amplitude of the inertial oscillation is not affected by the depth variation of the eddy viscosity. The presence of this undamped mode has been previously noted by Nomitsu (1933) and Gonella (1971*a*), and recently its physical nature has been discussed by Davies (1985*b*, 1986). Later we will analyse this undamped mode in deriving a transient solution with expansion of *characteristic modes* of the system. To illustrate the

non-dissipative behaviour of the inertial motion in the two domain system, calculations are performed in both one and two domain systems using a constant wind pulse of duration T_1. The time variation of the U and V components of the surface current are displayed as hodographs in Figure 4.10. It is apparent that the inertial motion of the one domain system converges gradually to a steady state value (in the presence of a non-zero bottom friction), which is zero for the wind stress of finite duration, whereas the inertial motion of the two domain system oscillates around zero with a quasi-steady amplitude.

To gain a better understanding of the non-dissipative component of inertial motion, we have derived a transient solution for the wind induced motion in a two-layered open sea subjected to a step-function wind stress. Appendix IV describes the details of the derivation with linear slip and stress-free bottom boundary conditions. Here we write down the non-dissipative part of the transient solutions derived using the stress-free conditions at the base of the domain boundary. The solution is given by

$$\varpi_1{}^{(a)} = U_1^{(a)} + \iota V_1^{(a)} = e^{-\iota\gamma t}\frac{\iota\tau_1}{H_1\gamma}\left[\xi_{1,1} - (\rho_{1,2}/\rho_{1,1})(\xi_{1,1}-1)\right]^{-1}, \quad (4.3.23)$$

where $\tau_1 = \tau_{sx}/\rho_{1,1}$. Since $\rho_{1,2}/\rho_{1,1} \simeq 1$, the above reduces to

$$\varpi_1{}^{(a)} = e^{-\iota\gamma t}\frac{\iota\tau_1}{H_1\gamma}. \quad (4.3.24)$$

Note that this non-dissipative inertial motion is barotropic in nature and hence can be explained in terms of the time behaviour of the first vertical mode determined using homogeneous Neumann limit conditions. An interpretation in terms of vertical modes will be given later. As $H_1 \to \infty$, the value of $\varpi_1^{(a)}$ at each level goes to zero. However, as noted by Gonella (1971*a*), the inertial oscillation of the domain-integrated transport $H_1(\overline{U}_1 + \iota\overline{V}_1)$ will persist indefinitely. It is common practice to find a steady state numerical solution using an asymptotic time marching method. It is evident that for the case of finite depth, the U and

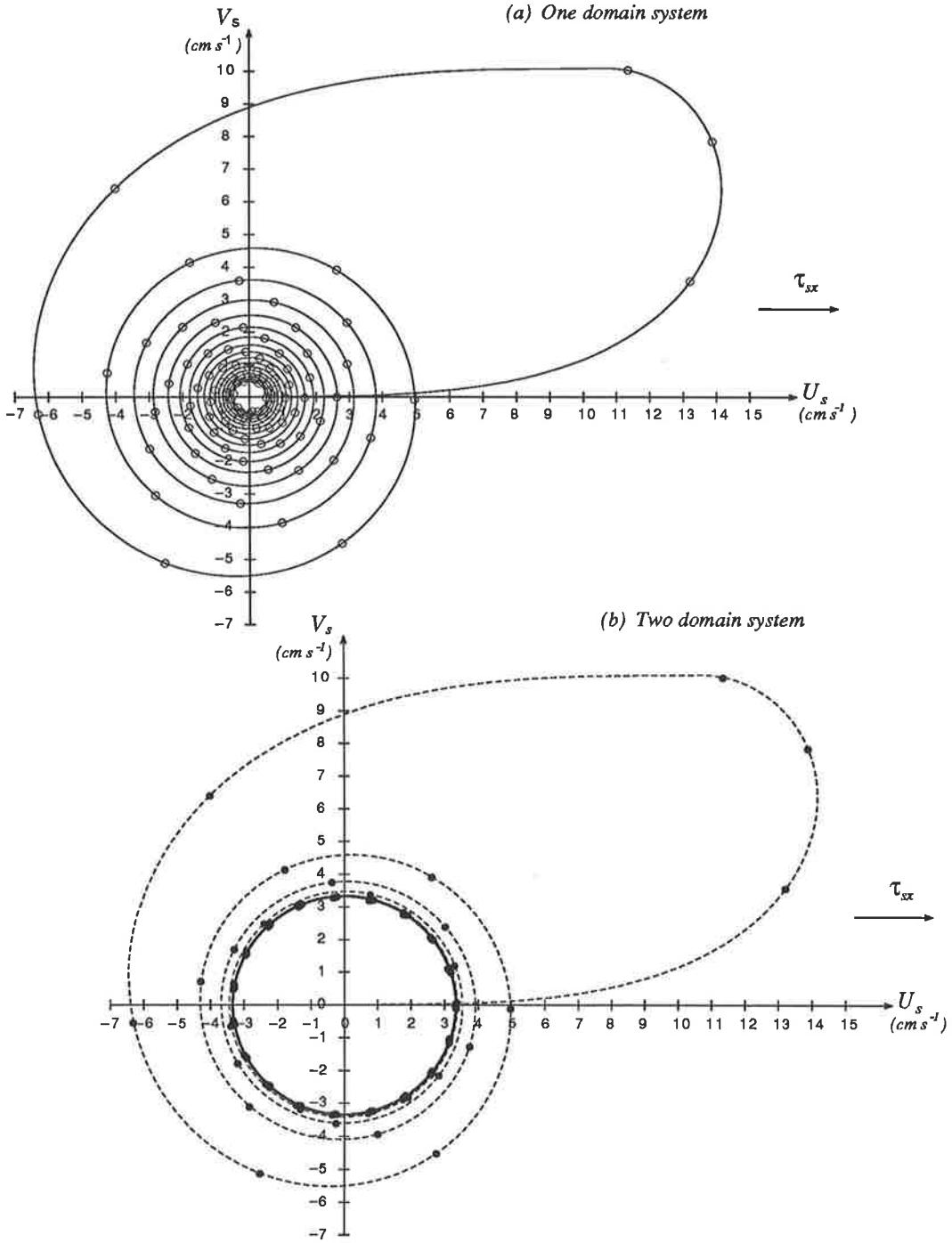

Figure 4.10 Hodographs of U_s and V_s (o and • denote three-hourly values in one and two domain systems, respectively) induced by a constant wind pulse with duration $T_1=T_c/4$ *hrs*, computed using a basis set of B-spline functions, obtained with the profile in Figure 3.1(*e*), with: $\Delta_W=10$, $\Delta_T=20$, $\Delta_P=10\,m$; $\rho_T=1025.8$, $\rho_P = 1026.5\ g\,cm^{-3}$; and (*a*) $\rho_B = 1027.2\ g\,cm^{-3}$; $k_b=0.2\ cm\,s^{-1}$; $\Delta_B=185\,m$; $N_W=30$, $N_T=150$, $N_P=50$, $N_B=1000\ cm^2s^{-1}$; (*b*) $N_W=30$, $N_T=150$, $N_P=50\ cm^2s^{-1}$.

V components of current in the two domain system computed using the marching method will never reach a steady state value.

The mixed layer depth Δ_T is of importance in determining the initial development of the inertial motion. It is apparent from Figure 4.11 that as the surface mixed layer depth is reduced, the surface current is significantly enhanced. This is to be expected since in stratified conditions the wind's energy in the surface layer is effectively capped by the pycnocline underneath. Furthermore, the deepening of the mixed layer depth is not reflected in the model and, consequently, the magnitude of the surface current is overestimated. This point has been shown by Davies (1985*c*) using a three-dimensional finite difference model. Under conditions of strong stratification ($N_P = 10\, cm^2 s^{-1}$) and the deep mixed layer depth ($\Delta_T = 60\, m$) the U and V components of the surface current of the two domain system are in good agreement with those of the one domain system, whereas under conditions of weak stratification and shallow mixed layer depth ($\Delta_T = 10\, m$), the surface currents of the two systems start to deviate from each other from about $t = T_c/4$ onwards.

We observe from Figure 4.12(a) that with $\Delta_P = 40\, m$ and $N_P = 10\ cm^2 s^{-1}$ the penetration of the wind's energy to the bottom layer is apparently retarded. In this case a high shear region is maintained at the top of the pycnocline. Under conditions of weaker stratification ($N_P = 50\ cm^2 s^{-1}$) with pycnocline thickness $\Delta_P = 10\, m$, the high shear region is significantly reduced and, on a time scale of about half of the inertial period, a considerable amount of wind energy is transmitted to the bottom layer (Figure 4.12(b)). For the one domain system a reversal of the velocity gradient can take place within the pycnocline under conditions of strong stratification ($N_P = 10\ cm^2 s^{-1}$) and with pycnocline thickness $\Delta_P = 40\ m$, whereas the gradient of the profile in the two domain system undergoes no such reversal. Decreasing N_T to 150 $cm^2 s^{-1}$ significantly enhances the shear within

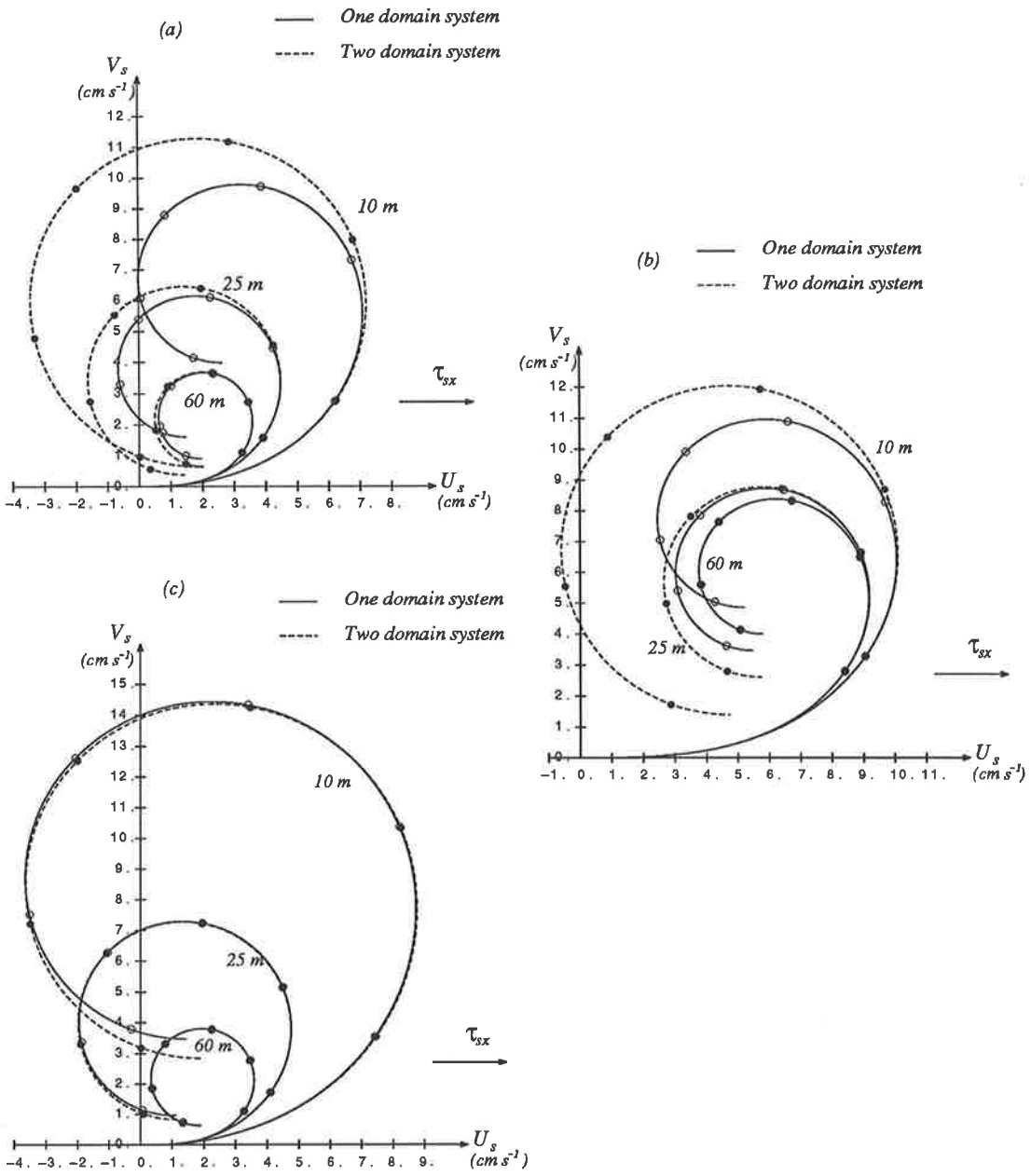

Figure 4.11 Initial development of the surface current, obtained using the profile in Figure 3.1(*d*), in three-layered one and two domain systems, computed using a basis set of *B*-spline functions, with: Δ_P=10 *m*, ρ_T=1025.8, ρ_P=1026.5 $g\,cm^{-3}$, and ,for Ω_0, ρ_B=1027.2 $g\,cm^{-3}$, H_0=250 *m*; N_B=100 $cm^2 s^{-1}$ and k_b=0.0 $cm\,s^{-1}$; and (*a*) N_T =1000, N_P=50 $cm^2 s^{-1}$; (*b*) N_T =150, N_P=50 $cm^2 s^{-1}$; (*c*) N_T =1000, N_P=10. $cm^2 s^{-1}$.

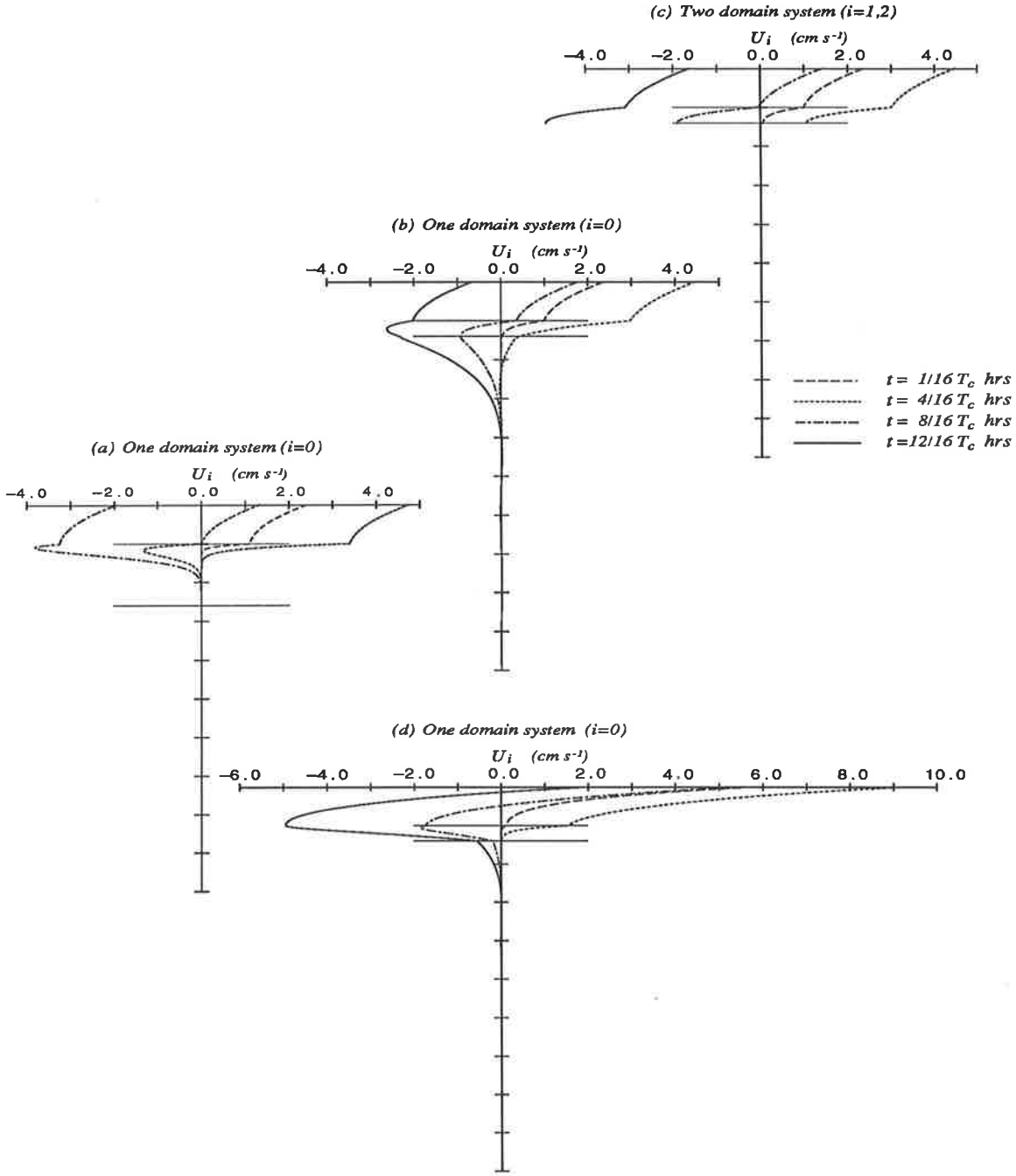

Figure 4.12 Velocity profiles of the U component of wind drift current (obtained using the profile in Figure 3.1(d)) at t=1/16, 4/16, 8/16 and 12/16 hrs, computed using a basis set of B-spline functions with: Δ_T=25 m; ρ_T=1025.8, ρ_P=1026.5 $g\,cm^{-3}$, and, for Ω_0, ρ_B=1027.2 $g\,cm^{-3}$, k_b=0.2 $cm\,s^{-1}$; and (a) Δ_P=40, Δ_B=185 m; N_T =1000, N_P=10, N_B=100 cm^2s^{-1}; (b) Δ_P=10, Δ_B=215 m; N_T =1000, N_P=50, N_B=100 cm^2s^{-1}; (c) Δ_P=10, Δ_B=215 m; N_T =1000, N_P=50 cm^2s^{-1}; (d) Δ_P=10, Δ_B=215 m; N_T =150, N_P=10, N_B=100 cm^2s^{-1}.

the surface layer and, in this example, a reversal of the velocity gradient occurs at the upper surface of the pycnocline.

The present approach enables one to introduce a surface wall layer in a discontinuous manner. Although results are not explicitly presented in this thesis, it was noted that the surface currents intensified greatly when a step-like surface wall boundary layer was introduced in the eddy viscosity profile.

We now consider the time variation of the horizontal components of current induced by a constant wind pulse of finite duration. The duration of the winds and the changes in wind direction play crucial roles in determining whether inertial oscillations will be enhanced or suppressed (Veronis and Stommel, 1956; Pollard, 1970). Let the horizontal velocities at σ_i computed with the step-function wind stress and the general time-varying wind stress be denoted by $\varpi^{(u)}$ and $\varpi^{(p)}$, respectively. The principle of superposition in the linear input-output system (Heaps, 1966; Forristall *et al.*, 1977; Forristall, 1980) then gives:

$$\varpi^{(p)}(\sigma_i,t)= \int_0^t \tau_{sx}(\tau)\frac{\partial \varpi^{(u)}}{\partial t}(t-\tau,\sigma_i)\,d\tau. \tag{4.3.25}$$

For a constant wind pulse of duration T_1, (4.3.25) reduces to

$$\varpi_i^{(p)} = \varpi_i^{(u)}(t,\sigma_i), \qquad 0 \le t \le T_1, \tag{4.3.26}$$

$$\varpi_i^{(p)} = \varpi_i^{(u)}(t,\sigma_i) - \varpi_i^{(u)}(t-T_1,\sigma_i), \qquad t > T_1. \tag{4.3.27}$$

We note in (4.3.26) and (4.3.27) that current induced by the constant wind pulse is composed of the two step-function responses. The first part is the time response following the onset of the step-function wind stress τ_{sx} at $t = 0$ and the second part is the time response following the onset of the step-function $-\tau_{sx}$ at $t = T_1$ *hrs*. Consequently, the energy contained in the inertial motion is critically dependent upon the phase difference between the two time responses.

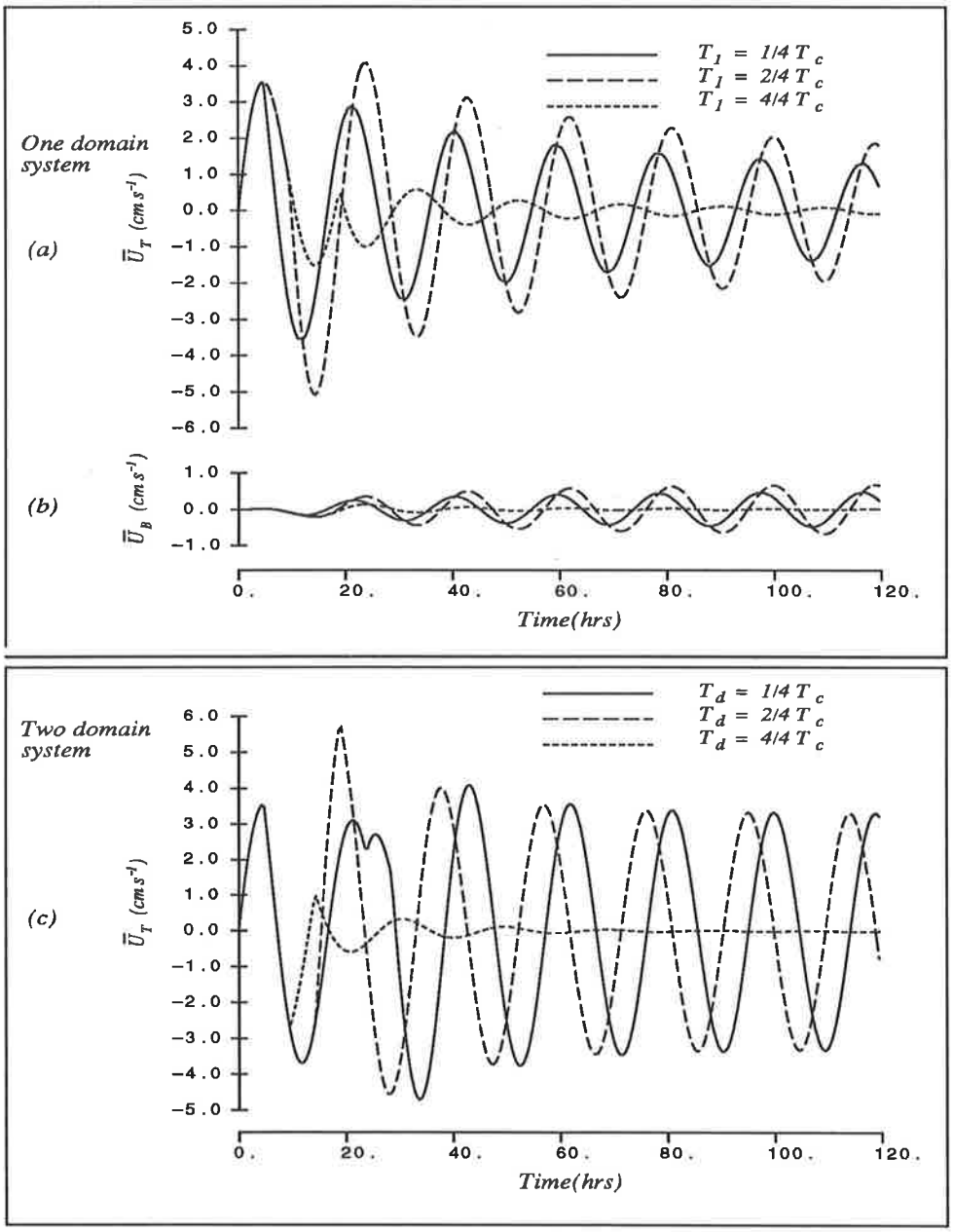

Figure 4.13 Time variation of $\overline{U}_T$, $\overline{U}_P$ and $\overline{U}_B$ (obtained using the profile in Figure 3.1(d)) computed using a basis set of B-spline functions, with: Δ_T=25, Δ_P=40 m, ρ_T=1025.8, ρ_P=1026.5 $g\,cm^{-3}$; and (a),(b) Δ_B=185 m; k_b=0.2 $cm\,s^{-1}$; ρ_B=1027.2 $g\,cm^{-3}$; N_T=1000, N_P=50, N_B=100 $cm^2 s^{-1}$ with a wind pulse of duration $T_1 = T_c/4$, $T_c/2$, and T_c hrs; (c) N_T=1000, N_P=50 $cm^2 s^{-1}$ with a constant wind pulse of duration $T_1 = T_c/2$ hrs followed by a second wind pulse of duration $T_1 = T_c/2$ hrs with intervals $T_d = T_c/4$, $T_c/2$, and T_c hrs.

Figure 4.13 illustrates the influence of the duration of the wind forcing on the time variation of $\overline{U}_i$. We can see from Figures 4.13(a) and (b) that the inertial oscillations intensify with $T_1 = T_c/2$ hrs, whereas a large proportion of the inertial energy in the U component of the current is removed at all depths with $T_1 = T_c$ hrs. The frequency of the wind pulses can also enhance and suppress the inertial response. When the first wind pulse is followed by the second wind pulse with time lag $T_c/2$ hrs, the inertial oscillation intensifies and the value of the second peak is larger than that of the first one (Figure 4.13(c)). In these computations, since the wind's energy is supplied for a finite period, the steady state solution is zero, hence the current oscillates inertially around zero after the wind stops.

Figure 4.14 depicts the vertical velocity profiles computed with a constant wind pulse of duration $T_c/4$ hrs. Comparing the profile at $t = T_c/4$ hrs with those at following time steps, it is apparent that after the wind action stops, the inertial energy within the surface layer diffuses downwards and consequently, the shear within the pycnocline is significantly reduced as time progresses. In the absence of external stresses the shear cannot be maintained within the surface mixed layer. The variation of the velocity profile through the pycnocline is almost linear. The wind's energy diffuses from the surface layer to the bottom layer over a couple of inertial periods until the rotational forcing and the internal friction limit the penetration. It is evident that when N_P is increased from 100 to 1000 $cm^2 s^{-1}$, the wind momentum penetrates to greater depths. It is also noticeable from Figure 4.14(d) that after the first two inertial periods the current profiles become almost uniform throughout the domain. This is due to the fact that once the wind stress is removed, the contribution of the higher modes to the current profiles decays exponentially with respect to time but the first vertical mode, which is barotropic in nature, is undamped. This point will be discussed more thoroughly later.

The numerical results given by Mellor and Durbin (1975) should be noted

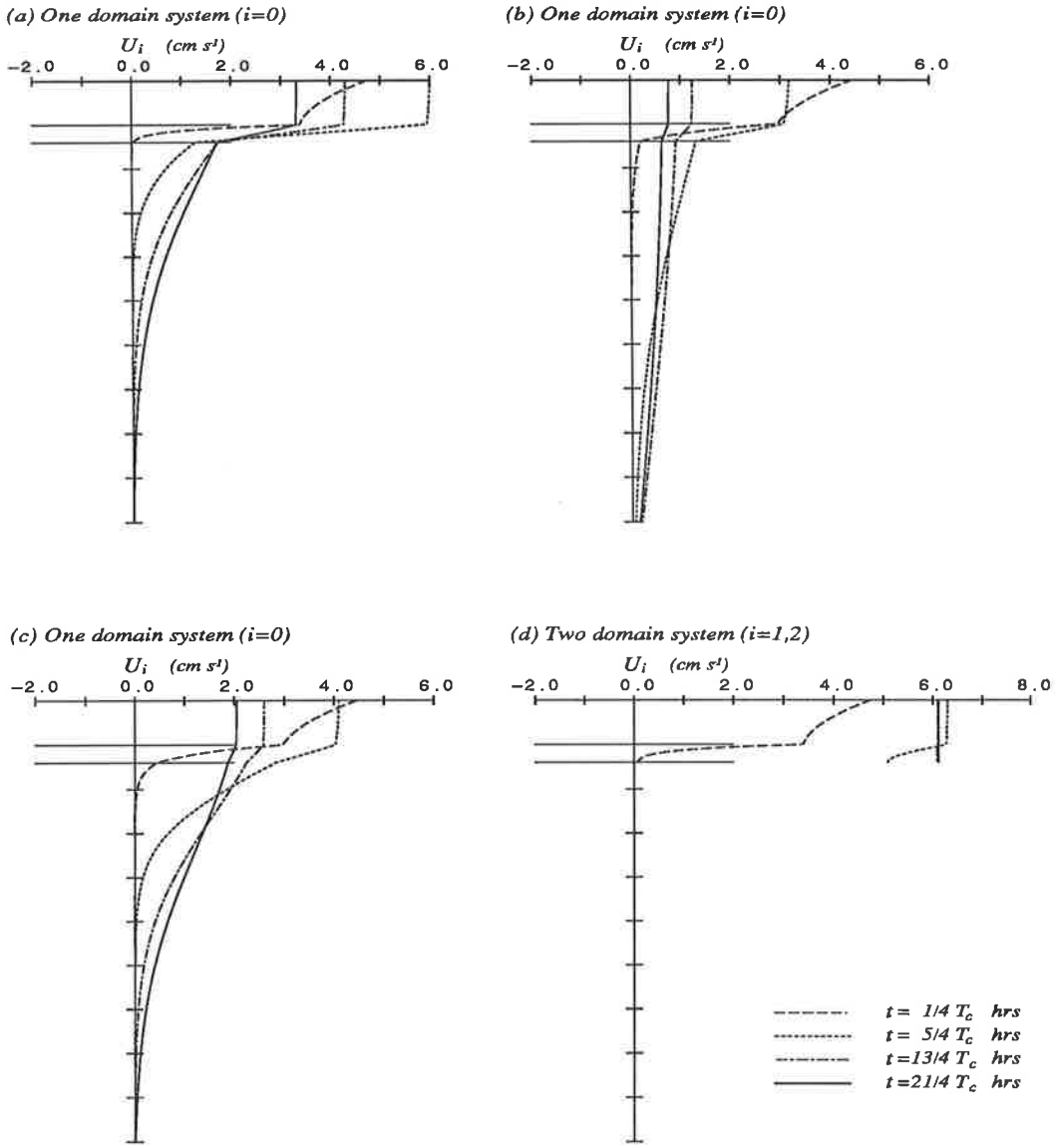

Figure 4.14 The U velocity profiles (obtained using the profile in Figure 3.1(d)) at t=1/4T_c, 5/4T_c, 9/4T_c and 17/4T_c hrs, induced by a wind pulse of duration T_1=1/2T_c hrs. Computed using a basis set of B-spline functions, with: Δ_T=25, Δ_P=10 cm^2s^{-1}; ρ_T=1025.8, ρ_P=1026.5 $g\,cm^{-3}$, and for Ω_0, Δ_B=215 m, ρ_B=1027.2 $g\,cm^{-3}$, k_b=0.2 $cm\,s^{-1}$; and (a) N_P=10, N_B=100 cm^2s^{-1}; (b) N_P=10, N_B=1000 cm^2s^{-1}; (c) N_P=50, N_B=100 cm^2s^{-1}; (d) N_P=10 cm^2s^{-1}.

at this stage. Their model, based on the second level turbulence closure scheme, predicted that when the wind stops no further deepening of the mixed layer occurs. Given a wind of finite duration, their results support the layered model which assumes the existence of the well-formed time-invariant layered structure *a priori*.

The time variation of modal coefficients

In what follows, we describe a modal solution for the transient wind drift current in an open sea region induced by a suddenly applied wind stress at $t = 0$. Although our concern is centred on the excitation of the undamped free motion in the two domain system, solutions are derived for a more general system. The two-layered one domain system with non-zero linear bottom friction is considered with a non-zero arbitrary initial velocity field and with $\beta_{i,1} = \beta_{i,2} = 0$ being used to construct a basis set of eigenfunctions. The two domain system may be recovered by setting $i = 1$ and $k_b = 0$. To analyse the input-output relation of the linear system, we use complex notation.

Defining the complex velocity $\varpi_{i,j}(t,\sigma_i) = U_{i,j}(t,\sigma_i) + \iota V_{i,j}(t,\sigma_i)$, we write equations (4.3.1) and (4.3.2) in complex form:

$$\frac{\partial \varpi_{i,j}}{\partial t} + \iota\gamma\varpi_{i,j} = \frac{\alpha_i}{H_i^2}\frac{\partial}{\partial \sigma_i}\Big(\mu_{i,j}\frac{\partial \varpi_{i,j}}{\partial \sigma_i}\Big) \quad \text{for} \quad \xi_{i,j-1} \le \sigma_i \le \xi_{i,j}, \quad (4.3.28)$$

where $i = 0$ and $j = 1, 2$.

We seek a solution in a truncated series of the form

$$\varpi_{i,j} = \sum_{r=1}^{m_i} \widehat{\varpi}_i \, \Phi_{i,r} f_{i,j,r}(\sigma_i) \quad \text{for} \quad \xi_{i,j-1} \le \sigma_i \le \xi_{i,j}, \quad (4.3.29)$$

subject to the boundary conditions

$$-\frac{\alpha_i}{H_i}\Big(\mu_{i,1}\frac{\partial \varpi_i}{\partial \sigma_i}\Big) = \frac{\tau_{sx}}{\rho_{i,1}} \quad \text{at} \quad \sigma_i = 0, \quad (4.3.30)$$

$$-\frac{\alpha_i}{H_i}\Big(\mu_{i,B}\frac{\partial \varpi_i}{\partial \sigma_i}\Big) = k_b\varpi_i \quad \text{at} \quad \sigma_i = 1, \quad (4.3.31)$$

and the non-zero initial condition

$$\varpi_{i,j} = \varpi_{i,j}(0), \tag{4.3.32}$$

where $i = 0$ and $j = 1, 2$.

After taking the scalar product (2.5.4) of (4.3.28) with $f_{i,j,k}$ we apply integration by parts twice. Then, using (3.2.2) and (3.2.3) with $\beta_{i,1} = \beta_{i,2} = 0$, and (4.3.30) and (4.3.31), the resulting equation takes the form

$$\Big\langle \frac{\partial \varpi_{i,j}}{\partial t} + \iota \varpi_{i,j} \ , \ f_{i,j,k} \Big\rangle - \Big\langle \varpi_{i,j} \ , \ \frac{\alpha_i}{H_i^2} \frac{d}{d\sigma_i}\Big(\mu_{i,j} \frac{df_{i,j,k}}{d\sigma_i}\Big) \Big\rangle$$
$$- \tau_{sx}(\rho_{i,1} H_i)^{-1} f_{i,k}(0) + (\rho_{i,2} k_b)(\rho_{i,1} H_i)^{-1} \varpi_{i,2}(1) f_{i,k}(1) = 0, \tag{4.3.33}$$

where $i = 0$ and $k = 1, \cdots, m_0$.

Let $f_{i,r}$, $i = 0$, $r = 1, \cdots, m_i$, be a basis set of eigenfunctions (with a local form $f_{i,j,r}$) determined from the equation

$$\frac{d}{d\sigma_i}\Big(\mu_{i,j} \frac{df_{i[j]}}{d\sigma_i}\Big) = -\lambda_i f_{i[j]} \tag{3.2.1}$$

subject to the limit conditions (3.2.2) and (3.2.3) with $\beta_{i,1} = \beta_{i,2} = 0$. Substituting (4.3.32) into (4.3.33), and using the orthogonality condition (3.2.8) of the eigenfunctions

$$\sum_{j=1}^{J_i} \Big(\frac{\rho_{i,j}}{\rho_{i,1}} \int_{\xi_{i,j-1}}^{\xi_{i,j}} f_{i,j,r} f_{i,j,k} \Big) d\sigma_i = \begin{cases} \Phi_{i,k}^{-1} & \text{if} \quad r = k, \\ 0 & \text{if} \quad r \neq k, \end{cases} \tag{3.2.8}$$

we obtain

$$\frac{\partial \widehat{\varpi}_{i,k}}{\partial t} = -\big(\iota\gamma + \lambda_{i,k}\alpha_i/H_i^2\big)\widehat{\varpi}_{i,k} + \tau_{sx}(\rho_{i,1}H_i)^{-1} f_{i,k}(0)$$
$$- (\rho_{i,2}k_b)(\rho_{i,1}H_i)^{-1}\Big(\sum_{r=1}^{m_i} \widehat{\varpi}_{i,r}\Phi_{i,r}\, f_{i,r}(1)\Big) f_{i,k}(1), \tag{4.3.34}$$

where $\widehat{\varpi}_{i,k} = \widehat{A}_{i,k} + \iota\widehat{B}_{i,k}$, $k = 1, \cdots, m_i$. Note that all the vertical modes are coupled through the bottom friction term.

Writing (4.3.34) in matrix form we have

$$\widehat{\mathbf{w}}_i^{\bullet} = \mathbf{\Gamma}\widehat{\mathbf{w}}_i + \mathbf{F}_{x,i}, \tag{4.3.35}$$

where:

$\widehat{\mathbf{w}}_i^{\bullet}$ is a column vector of length m_i with k th element

$$\frac{d\widehat{\varpi}_{i,k}}{dt}; \tag{4.3.36}$$

$\widehat{\mathbf{w}}_i$ is a column vector of length m_i with k th element

$$\widehat{\varpi}_{i,k}; \tag{4.3.37}$$

$\mathbf{F}_{i,x}$ is a column vector of length m_i with k th element

$$\tau_{sx}(\rho_{i,1}H_i)^{-1} f_{i,k}(0) = \tau_{sx}(\rho_{i,1}H_i)^{-1} = F_k; \tag{4.3.38}$$

$\mathbf{\Gamma}$ is a $m_i \times m_i$ square matrix with (r,k) th element

$$\Gamma_{r,k} = -(\iota\gamma + \lambda_{i,k}\alpha_i/H_i^2)\delta_{rk} - (\rho_{i,2}k_b)(\rho_{i,1}H_i)^{-1} f_{i,r}(1) f_{i,k}(1)\Phi_{i,k}; \tag{4.3.39}$$

and δ_{rk} is the Kronecker symbol.

Equation (4.3.35) is often encountered in the analysis of standard input–output systems and techniques for obtaining its solution are extensively discussed in many text books (for example, Zadeh and Desoer, 1963). For completeness, we write down the essential steps of the solution procedure. Let $\mathbf{e}_r$ be the r th normalised eigenvector (often called the state vector) satisfying

$$\mathbf{\Gamma}\ \mathbf{e}_r = \epsilon_r \mathbf{e}_r, \tag{4.3.40}$$

in which ϵ_r is the associated r th eigenvalue. If $\mathbf{\Gamma}$ has m_i distinct eigenvalues, (4.3.35) admits a representation of the form

$$\widehat{\mathbf{w}}_i = \sum_{r=1}^{m_i} c_r(t)\ \mathbf{e}_r. \tag{4.3.41}$$

Substituting (4.3.40) and (4.3.41) into (4.3.35), we get

$$\sum_{r=1}^{m_i} \frac{dc_r}{dt}\mathbf{e}_r = \mathbf{\Gamma}\left[\sum_{r=1}^{m_i} c_r\mathbf{e}_r\right] + \mathbf{F}_{i,x} \tag{4.3.42}$$

$$= \sum_{r=1}^{m_i} c_r\epsilon_r\mathbf{e}_r + \mathbf{F}_{i,x}. \tag{4.3.43}$$

Let the j th component of $\mathbf{e}_r$ be denoted by $e_{r,j}$. Taking a complex scalar product of $\mathbf{e}_r$ and $\mathbf{e}_k$ such that

$$< \mathbf{e}_r, \mathbf{e}_k >= \sum_{j=1}^{m_i} e_{r,j}\ e^*_{k,j} = \delta_{rk}, \tag{4.3.44}$$

we obtain

$$\frac{dc_k}{dt} = c_k\epsilon_k + F^{(e)}_k, \tag{4.3.45}$$

where

$$F^{(e)}_k =< \mathbf{F}_{i,x}\ , \mathbf{e}_k >= \sum_{j=1}^{m_i} F_j\ e^*_{k,j}\ , \tag{4.3.46}$$

and $k = 1, \cdots, m_i$.

Projecting the initial velocity field (4.3.32) onto each mode defines a column vector $\widehat{\mathbf{w}}_i(0)$ of length m_i with k th element

$$\widehat{\varpi}_{i,k}(0) = \sum_{j=1}^{J_i} \frac{\rho_{i,j}}{\rho_{i,1}} \int_{\xi_{i,j-1}}^{\xi_{i,j}} \varpi_{i,j}(0)\ f_{i,j,k}\ d\sigma_i. \tag{4.3.47}$$

Expanding $\widehat{\mathbf{w}}_i(0)$ in terms of $\mathbf{e}_r$, $r = 1, \cdots, m_i$, and taking a complex scalar product with $\mathbf{e}_k$, we have

$$< \widehat{\mathbf{w}}(0), \mathbf{e}_k >= \sum_{j=1}^{m_i} \widehat{\varpi}_{i,j}(0)\ e^*_{k,j} = c_k(0). \tag{4.3.48}$$

By the convolution theorem, the solution of (4.3.45) subject to the initial condition (4.3.48), is given by

$$c_k(t) = \exp\{\epsilon_k t\} \left[c_k(0) + \int_0^t \exp\{-\epsilon_k \tau\} F_k^{(e)}(\tau) d\tau\right], \tag{4.3.49}$$

where $k = 1, \cdots, m_i$. Hence, from (4.3.41), we get

$$\widehat{\mathbf{w}}_i(t) = \sum_{r=1}^{m_i} \exp\{\epsilon_r t\}\ \mathbf{e}_r \left[c_r(0) + \int_0^t \exp\{-\epsilon_r \tau\} F_r^{(e)}(\tau) d\tau\right]. \tag{4.3.50}$$

With a zero-stress condition, $k_b = 0$, or with a no-slip bottom condition (by the requirement $f_{i,k}(1) = 0$ for all k), the $m_i \times m_i$ square matrix $\mathbf{\Gamma}$ has zero values for all off-diagonal elements; its eigenvectors $\mathbf{e}_r$ have all zero components except for the r th, which is unity. It follows then that

$$c_k(t) = \widehat{\varpi}_{i,k}(t) = \exp\{\tilde{\epsilon}_k t\} \left[c_k(0) + \int_0^t \exp\{-\tilde{\epsilon}_k \tau\} F_k^{(e)} d\tau\right], \tag{4.3.51}$$

where

$$\tilde{\epsilon}_k = \Gamma_{r,r} = -\left(\iota\gamma + \lambda_{i,k}\alpha_i / H_{i,k}^2\right), \tag{4.3.52}$$

$$F_k^{(e)} = F_k = \tau_{sx}(\rho_{i,1} H_i)^{-1}, \tag{4.3.53}$$

and $r = 1, \cdots, m_i$. Note that the number of vertical modes determines the number of components of eigenvectors and in the absence of bottom friction each characteristic mode carries the information on each vertical mode. In this solution the wind stress can vary arbitrarily with respect to time. For an idealised form of wind stress, for example a sinusoidal or step-function wind stress, (4.3.51) can be integrated analytically. Davies (1987*b*) derived solutions similar to (4.3.51) with $c_k(0) = 0$ and using a no-slip condition at the sea bed.

Figures 4.15(a) to (d) illustrate the time variation of the vertical modes in one and two domain systems induced by a step-function wind stress. All the characteristic modes are excited by the step-function wind stress and each *excitation*

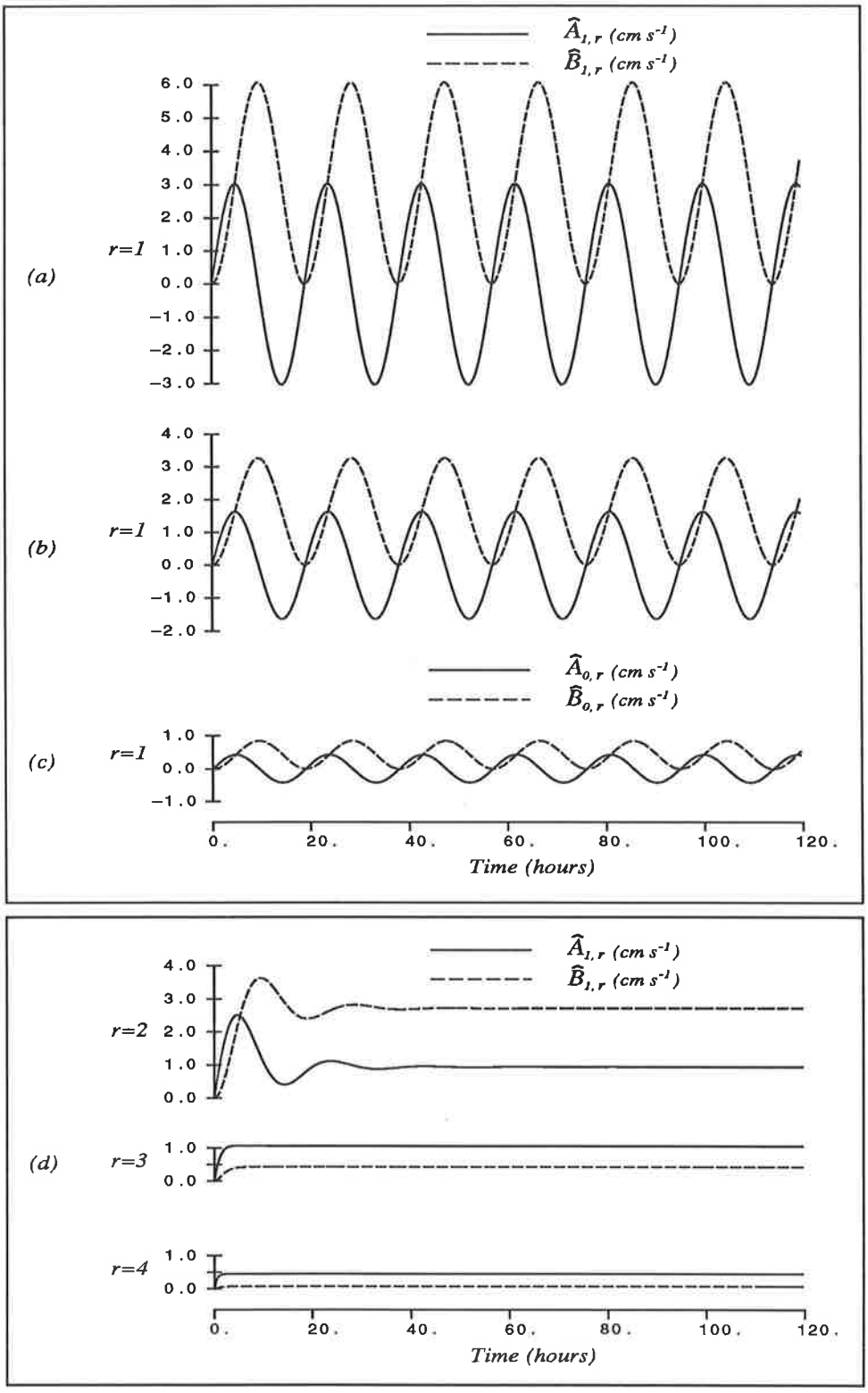

Figure 4.15 (Caption on next page).

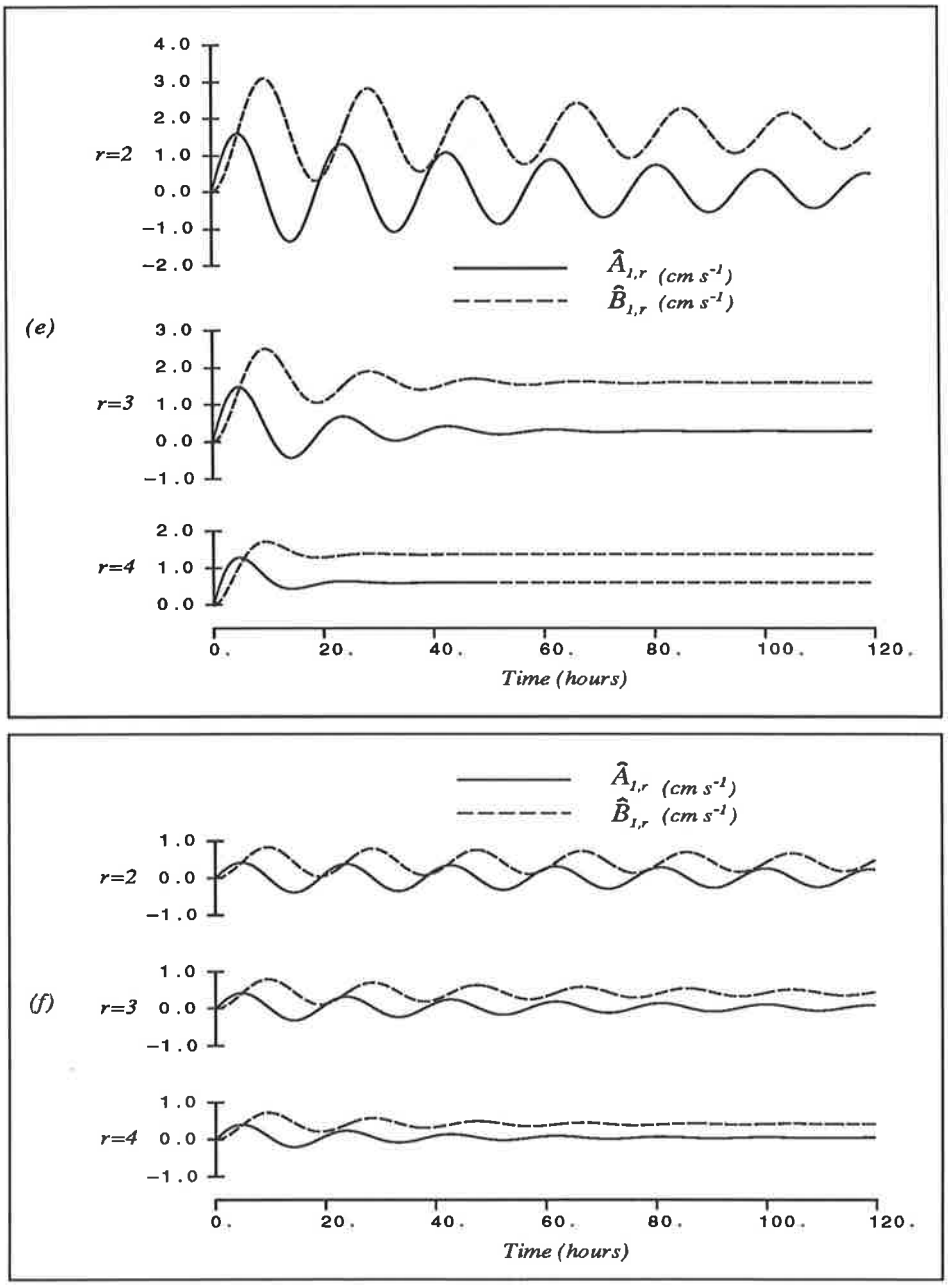

Figure 4.15 Time variation of the various vertical modes, obtained using the profile in Figure 3.1(d), induced by a step-function wind stress. A stress-free condition (k_b=0.0 $cm\,s^{-1}$) is imposed at the base of the domain with: Δ_T=25m; ρ_T=1025.8, ρ_P=1026.5 $g\,cm^{-3}$, and for Ω_0, ρ_B=1027.2 $g\,cm^{-3}$; N_T=1000, N_P=10 cm^2s^{-1}; and (a) Δ_P=10m; (b) Δ_P=40m; (c) Δ_P=10, Δ_B=215m with N_B=100 cm^2s^{-1}; (d) as in (a); (e) as in (b); (f) as in (c).

can be defined by $F_k^{(e)} = \tau_{sx}(\rho_{i,1}H_i)^{-1}$ in (4.3.53). Physically, the excitation of higher modes is necessary to represent the localised variation of the wind drift current at the initial stage (Davies, 1985*b*). In the absence of bottom friction, the rates of decay of the modal coefficients in both systems are entirely determined by the real part of $\tilde{\epsilon}_k$, that is, $\alpha_i\lambda_{i,k}/H_i^2$ in (4.3.52). It should be stressed that the depth of the one domain system ($H_0 = 250\,m$) is sufficiently large and hence the influence of the bottom friction upon the decay of the inertial oscillations is in fact insignificant. Since the eigenvalues $\lambda_{i,r}$ are an increasing sequence of real numbers, the initial damping of the higher modes will be faster than that of the lower modes (see Figures 4.15(*d*) to (*e*)). Consequently, for the wind stress of finite duration the barotropic mode will dominate in the current profiles as time progresses (see Figure 4.14). The difference in the initial damping of the higher vertical modes between the one and two domain systems is in part attributable to the difference in the values of α_i.

It is apparent from Figures 4.15(*a*) to (*c*) that the first mode is undamped in the absence of bottom friction. If the water initially at rest is subjected to the step-function wind stress at $t = 0$, then from (4.3.51) to (4.3.53), and noting that $\lambda_{i,1} = 0$, we have

$$c_1 = \widehat{A}_{i,1} + \iota\widehat{B}_{i,1} = -\frac{\iota\tau_1}{H_i\gamma}\left(1 - e^{-\iota\gamma t}\right). \tag{4.3.54}$$

Note that the first part of (4.3.54) is the steady state solution which is identical to (4.2.12) and the second is the nondissipative oscillatory solution. The first vertical mode plays an important role with regards to the net transport. Noting that $\Phi_{i,1} \simeq 1$ and that $a_{i,0,r} = \int_0^1 f_{i,r}d\sigma_i \simeq 0$ for all $r \geq 2$, we have

$$H_i\int_0^1 (U_i + \iota V_i)\,d\sigma_i \simeq H_i(\widehat{A}_{i,1} + \iota\widehat{B}_{i,1}) = -\frac{\iota\tau_1}{\gamma}\left(1 - e^{-\iota\gamma t}\right). \tag{4.3.55}$$

Thus the first vertical mode will serve to give rise to a net transport irrespective of the depth variation of the eddy viscosity. As $H_i \to \infty$, the first vertical modes $\widehat{A}_{i,1}$ and $\widehat{B}_{i,1}$ will go to zero. However, the transport will persist indefinitely.

The non-zero value of $F_k^{(e)}$ implies that all characteristic modes will be excited independently of each other, and since the eigenvalues ϵ_k, $k = 1, \cdots, m_i$, are distinct and their real parts are negative, the modes will converge to steady state values at different rates. One would expect that the time behaviour of the vertical modes would be significantly different from that of those for the zero-stress condition as the values of $(k_b/H_i) f_{0,k}(1) f_{0,r}(1) \Phi_{0,k}$ in (4.3.39) were increased, thereby reducing the diagonal dominance in $\mathbf{\Gamma}$. The effect of bottom friction on the vertical modes will be referred to in the next section.

Effects of introducing frictional dissipation for the two domain system

The simple linear slab model developed by Pollard and Millard (1970) has been successfully used on many occasions to reproduce major features of inertial oscillations observed in the surface mixed layer (for example, see Kundu, 1976; Daddio *et al.*, 1978). A linear two-layered model for the local generation of inertial motion, extending the linear slab model, is described here which allows for the diffusion of the wind's energy downwards through the pycnocline and in the horizontal directions.

To remain consistent with the representation of the bottom friction, we assume that the downward flux of the wind's energy to the bottom layer is a linear function of the velocity at the base of the pycnocline; that is, we pose

$$-\frac{\alpha_1}{H_1}\left(\mu_{1,1}\frac{\partial U_{1,1}}{\partial \sigma_1}\right) = \frac{\tau_{dx}}{\rho_{1,1}}, \qquad -\frac{\alpha_1}{H_1}\left(\mu_{1,1}\frac{\partial V_{1,1}}{\partial \sigma_1}\right) = \frac{\tau_{dy}}{\rho_{1,1}}, \tag{4.3.56}$$

$$\tau_{dx} = \rho_{1,2}\, k_d\, U_{i,d}, \qquad \tau_{dy} = \rho_{1,2}\, k_d\, V_{i,d}, \tag{4.3.57}$$

where k_d is the linear frictional coefficient, and $U_{i,d}$ and $V_{i,d}$ are the velocities at $\sigma_1 = 1$. The system is then composed of the surface mixed layer and the pycnocline, with bottom friction imposed at the base of the domain boundary.

Essentially, we consider a two-layered one domain system of depth H_1 with a linear slip bottom boundary condition.

The horizontal diffusion of the inertial energy can be represented in a way similar to the Pollard-Millard linear slab model which is written as

$$\frac{\partial \overline{U}_T}{\partial t} - \gamma \overline{V}_T = F_T - k_m \overline{U}_T, \tag{4.3.58}$$

$$\frac{\partial \overline{V}_T}{\partial t} + \gamma \overline{U}_T = G_T - k_m \overline{V}_T, \tag{4.3.59}$$

where

$$F_T = \frac{\tau_{sx}}{\rho_{1,1}\Delta_T}, \qquad G_T = \frac{\tau_{sy}}{\rho_{1,1}\Delta_T}. \tag{4.3.60}$$

The parameter k_m represents the damping of the inertial oscillations in the surface mixed layer.

On introducing horizontal diffusion terms (related to the U_i and V_i components of the current at each level) into equations (4.3.1) and (4.3.2), we have

$$\frac{\partial U_{i,j}}{\partial t} - \gamma V_{i,j} = -k_h U_{i,j} + \frac{\alpha_i}{H_i^2}\frac{\partial}{\partial \sigma_i}\Big(\mu_{i,j}\frac{\partial U_{i,j}}{\partial \sigma_i}\Big), \tag{4.3.61}$$

$$\frac{\partial V_{i,j}}{\partial t} + \gamma U_{i,j} = -k_h V_{i,j} + \frac{\alpha_i}{H_i^2}\frac{\partial}{\partial \sigma_i}\Big(\mu_{i,j}\frac{\partial V_{i,j}}{\partial \sigma_i}\Big), \tag{4.3.62}$$

where $i = 1$, $j = 1, 2$. This formulation is motivated in part by the analytical model given by Hopkins (1974) in which the diffusion terms $k_h U_i$ and $k_h V_i$ are introduced primarily to control the indefinite growth of the alongshore component of the geostrophic velocities induced by a steady wind. These equations can be used either with a zero-stress condition or with the frictional condition (4.3.56). It is obvious that the removal of inertial energy from the surface mixed layer can be calibrated through the adjustment of the frictional parameters k_d and/or k_h.

We can expect from previous results that the influence of the changes in k_d upon the decay of the inertial oscillations in the surface layer is closely related

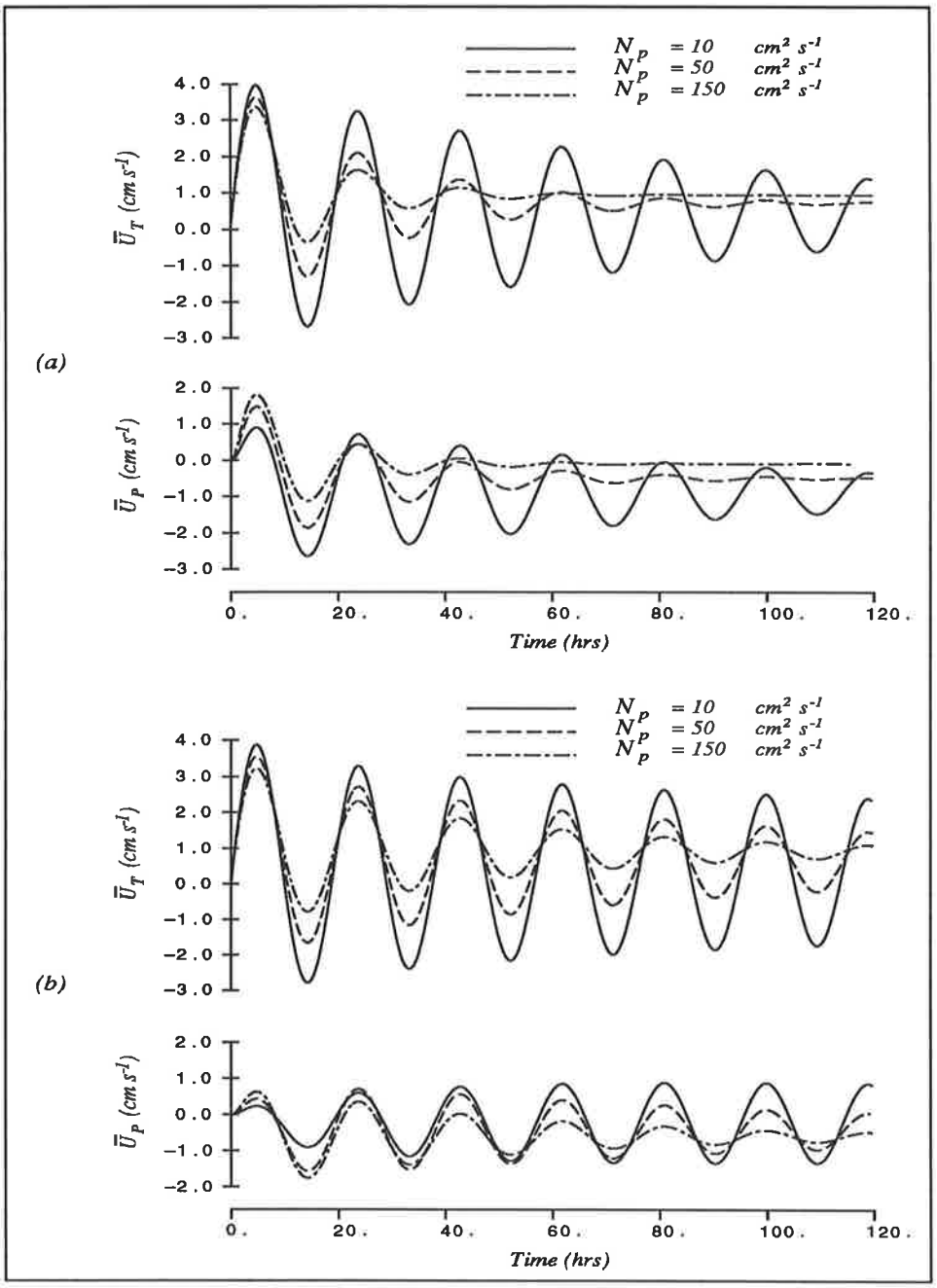

Figure 4.16 Time variation of $\overline{U}_T$ and $\overline{U}_P$, obtained using the profile in Figure 3.1(*d*), computed with frictional dissipation imposed at the base of the pycnocline. A basis set of *B*-spline functions was used with: k_d=0.1 cms^{-1}; Δ_T=25*m*; ρ_T=1025.8, ρ_P=1026.5 $g\,cm^{-3}$; N_T =1000, N_P =10 $cm^2 s^{-1}$; and (*a*) Δ_P=10*m*; (*b*) Δ_P=40*m*.

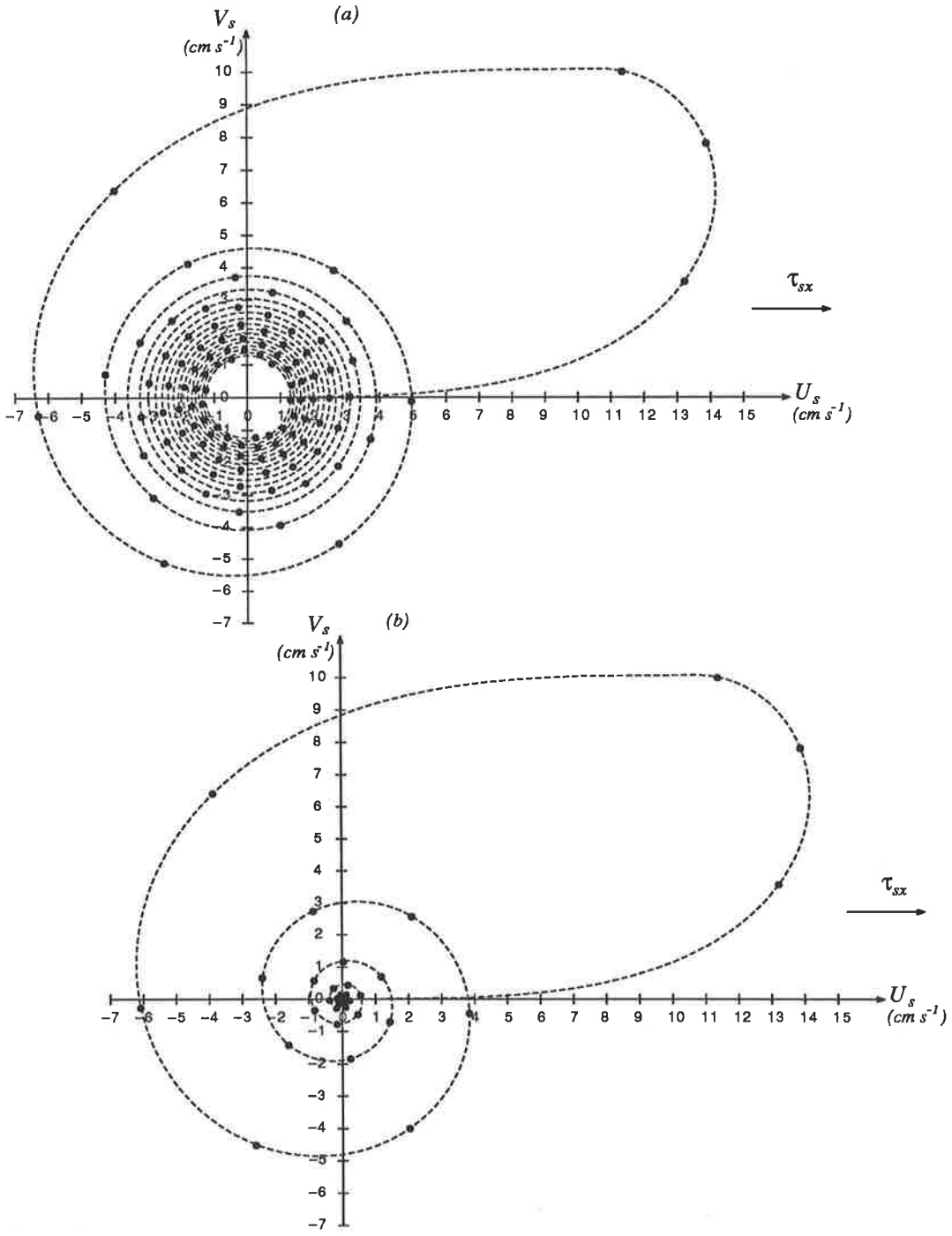

Figure 4.17 Hodographs of U_s and V_s (with • denoting three-hourly values) induced by a constant wind pulse with a duration of $T_1=T_c/4$, computed with frictional dissipation imposed at the base of the pycnocline. A basis set of B-spline functions was used (with the profile in Figure 3.1(e)) with: $\Delta_W=10$, $\Delta_T=20$, $\Delta_P=10m$; $\rho_T=1025.8$, $\rho_P = 1026.5\ g\,cm^{-3}$; $N_W=30$, $N_T=150$, $N_P=50\ cm^2 s^{-1}$; and (a) $k_d=0.01\ cm\,s^{-1}$; (b) $k_d=1.0\ cm\,s^{-1}$.

to the conditions of stratification. For convenience, we present the time variation of $\overline{U}_T$ and $\overline{U}_P$ computed with $k_d = 0.1\ cm\,s^{-1}$ for the values of $N_P = 10$, 50 and 150 $cm^2 s^{-1}$ and $\Delta_P = 10$ and $40\,m$ (Figure 4.16). Comparing Figure 4.16 with Figures 4.9(a) to (c), we can see that the time variation resembles those of the one domain system. The major difference is that in the one domain system the damping of the inertial oscillations within the surface layer is affected by the eddy viscosity at the bottom layer along with the parameters N_P, Δ_T and Δ_P, while in this two-layered model the time behaviour of the inertial oscillations in the surface layer are independent of the conditions in the bottom layer. In the one domain system the surface current is influenced by the mean value of the eddy viscosity through the water column, and its depth variation (Davies, 1985c). The present model provides as an improvement to the Pollard-Millard model detailed information on the vertical structure of the inertial oscillations. We note that with $\Delta_P = 40\ m$, $N_P = 10\ cm^2 s^{-1}$, the layer-mean velocity $\overline{U}_P$ increases progressively over the 120 hrs while the damping of $\overline{U}_T$ continues. Figure 4.17 displays as time hodograms the sensitivity of the damping of the surface current to the value of k_d.

We now consider the time variation of the modal coefficients in the presence of frictional dissipation at the base of the two domain system. Figures 4.18(a) and 4.18(c) depict the time dependence of the first four modal coefficients computed using $k_d = 0.1\ cm\,s^{-1}$, for $\Delta_P = 10$ and 40 m. For the purpose of comparison, the time variation of the third and fourth vertical modes computed using a stress-free condition with $\Delta_P = 40\,m$ is also plotted in Figure 4.18(b). It is evident from these figures that the frictional dissipation damps the first vertical mode. The decay rate of the first vertical mode computed with $\Delta_P = 40\ m$ is significantly slower than that computed with $\Delta_P = 10\ m$. This is expected because the downward flux of inertial energy is represented by the U and V components of current at the base of the pycnocline.

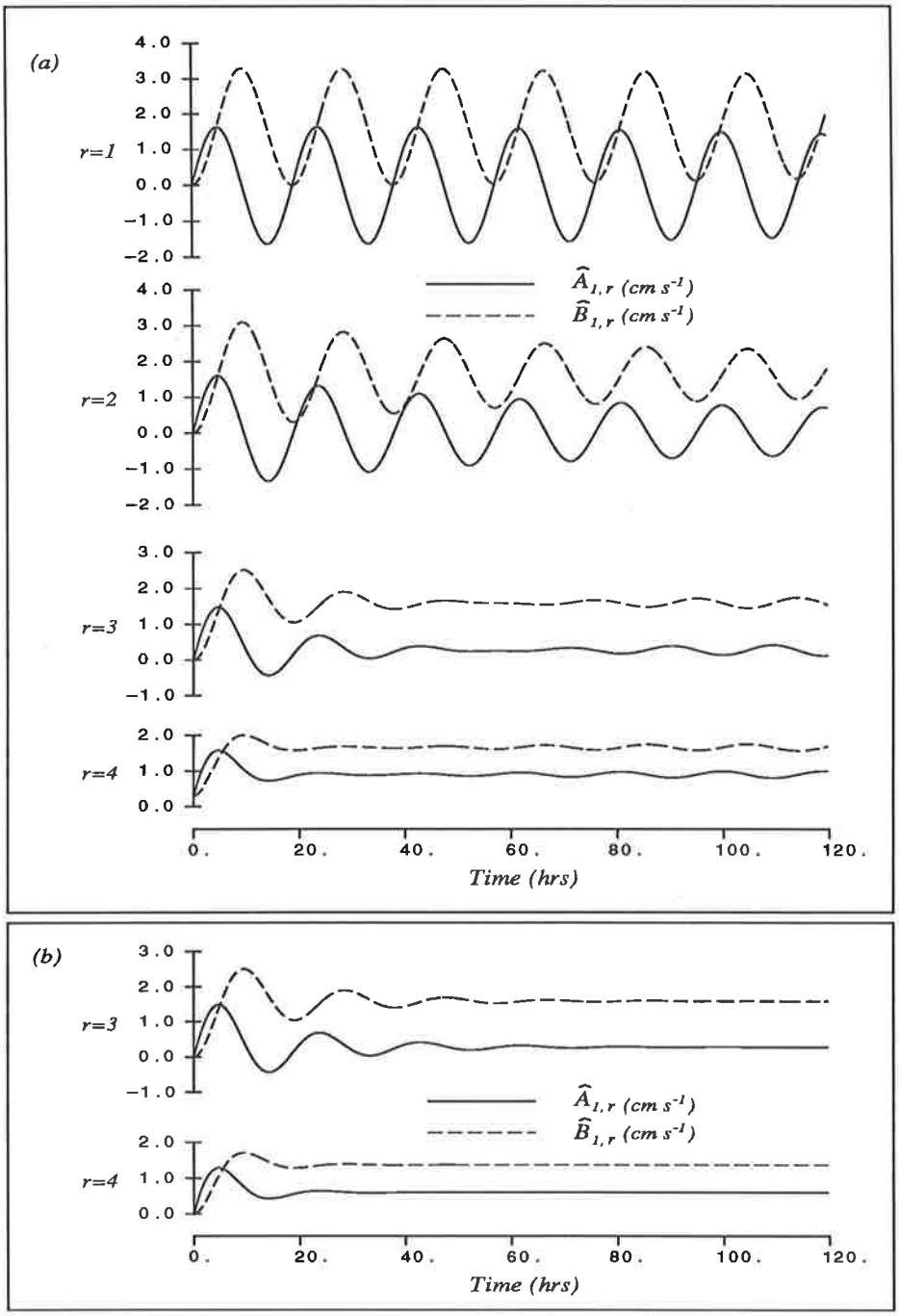

Figure 4.18 Time variation of the various vertical modes, obtained using the profile in Figure 3.1(d), with frictional dissipation imposed at the base of the pycnocline. A step-function wind stress was used with: Δ_T=25 m; ρ_T=1025.8, ρ_P=1026.5 $g\,cm^{-3}$; N_T=1000, N_P=10 $cm^2\,s^{-1}$; $\beta_{1,1}=\beta_{1,2}=0$; and ($a$) Δ_P=40 m; k_d=0.1 $cm\,s^{-1}$; (b) for comparison purpose, Δ_P=40 m; k_d=0.0$cm\,s^{-1}$; (c) Δ_P=10 m, k_d=0.1 $cm\,s^{-1}$.

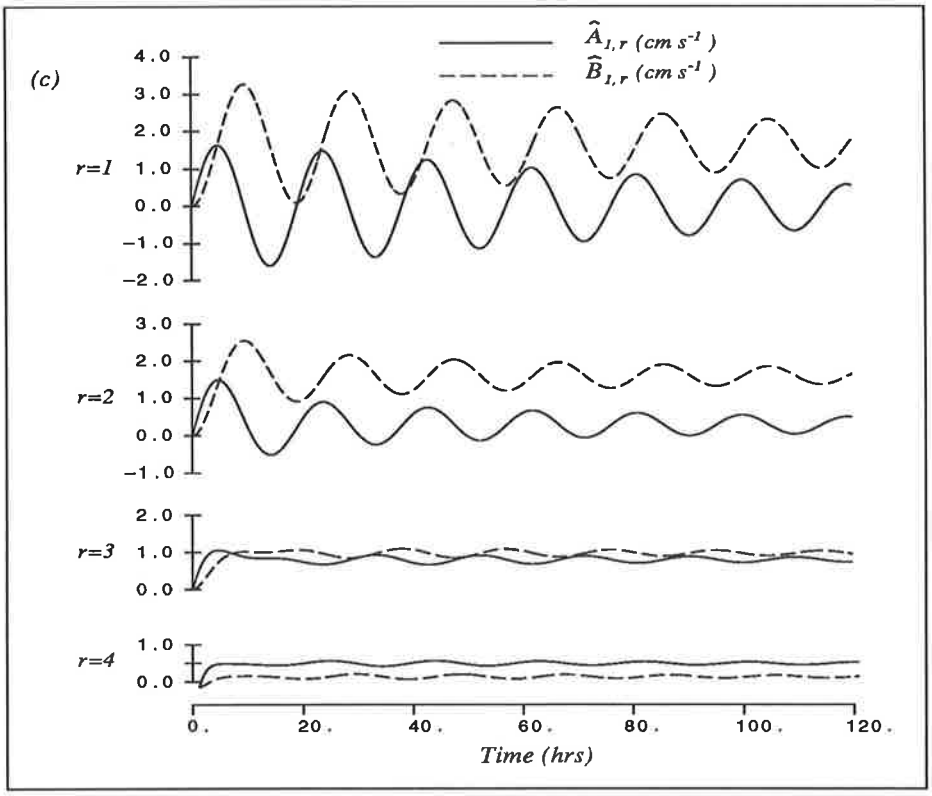

Figure 4.18 Cont'd.

The interesting fact is that when the value of k_d is zero, the coefficients of the higher vertical modes attain a steady state more rapidly than when the value of k_d is non-zero. This point has been discussed in detail by Davies (1985*b*) for a homogeneous sea. Initially, all the vertical modes are excited by the step-function wind stress. When a zero-stress condition is enforced at the base of the domain, the coefficients of the vertical modes are damped exponentially by the internal friction term $\alpha_i \lambda_{i,k} / H_i^2 \widehat{W}_{i,k}$. Consequently the higher modes converge to the steady state value faster than the lower modes. Since the modal equations are uncoupled, no interaction arise between the vertical modes (see (4.3.51)). When the stress at the base of the domain is non-zero, the initial decay of each vertical mode is determined by the frictional dissipation imposed at the base of the domain boundary and by the internal friction. Note that in this case the modal equations

are coupled. Since the friction term at the base of the pycnocline is given by

$$\begin{aligned}\tau_{dx} &= \rho_{1,2}\, k_d\, U_{i,d} = \rho_{1,2} k_d \sum_{r=1}^{m_1} \widehat{A}_{1,r} \Phi_{1,r} f_{1,r}(1), \\ \tau_{dy} &= \rho_{1,2}\, k_d\, V_{i,d} = \rho_{1,2} k_d \sum_{r=1}^{m_1} \widehat{B}_{1,r} \Phi_{1,r} f_{1,r}(1),\end{aligned} \tag{4.3.63}$$

where $\Phi_{1,r}$ is strictly positive and $f_{1,r}(1)$ changes sign as r increases, the inertial oscillations locked in the first few modal coefficients (in these examples, mainly the first and second modes) will give rise to periodic changes in the bottom stress, through the interaction between the vertical modes, thus producing time dependent fluctuations of the higher vertical modes. The oscillations in $\widehat{A}_{1,3}$ and $\widehat{A}_{1,4}$ shown in Figures 4.18(a) and (c) are due to such interaction. It is apparent that the time dependent fluctuations of the higher vertical modes become pronounced when the off-diagonal terms of $\mathbf{\Gamma}$ in (4.3.39) are substantially increased. Note that the characteristic modes determined by the linear summation of the vertical modes do not interact each other (see (4.3.49)). In the case of $N_P = 10\ cm^2 s^{-1}$ and $\Delta_P = 40\, m$, the rate of penetration of the wind's momentum slows within the pycnocline, causing the contribution of the bottom friction to increase gradually. Consequently, the contribution of the time dependent fluctuation of the bottom stress to the coefficients of the higher vertical modes is noticeable after a couple of inertial periods (Figure 4.18(a)).

The influence of k_h upon the rate of damping of the inertial oscillations within the surface layer and the pycnocline is depicted in Figure 4.19. It is apparent that the horizontal dissipation term damps the first vertical mode. In contrast to the case of k_d, the presence of the horizontal dissipation term does not complicate the time response of the individual vertical modes. This is because no interaction between the vertical modes arises through the horizontal dissipation term.

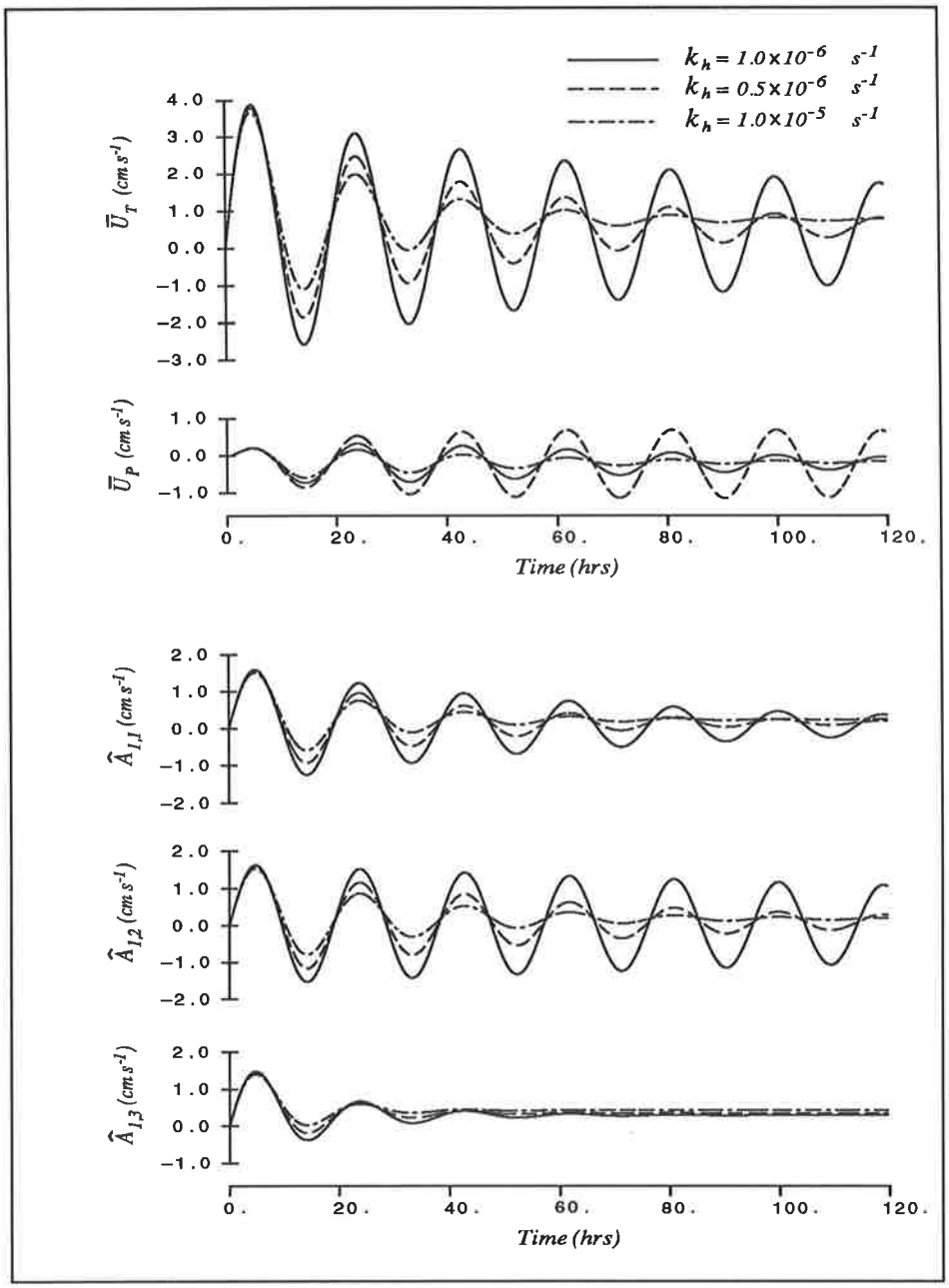

Figure 4.19 Time variation of $\overline{U}_T$ and $\overline{U}_P$ and the first three vertical modes in domain Ω_1, obtained using the profile in Figure 3.1(*d*), computed with horizontal dissipation. A step-function wind stress was used with: k_h=1.0×10^{-6}, 0.5×10^{-6} and 1.0×10^{-5} s^{-1}; Δ_T=25, Δ_P=40m; ρ_T=1025.8, ρ_P=1026.5 $g\,cm^{-3}$; N_T =1000 and N_P =50 $cm^2 s^{-1}$.

We may write equations (4.3.61) and (4.3.62) in complex form as follows:

$$\frac{\partial \varpi_{i,j}}{\partial t} + \iota\gamma\varpi_{i,j} = -k_h\varpi_{i,j} + \frac{\alpha_1}{H_1^2}\frac{\partial}{\partial \sigma_i}\Big(\mu_{i,j}\frac{\partial \varpi_{i,j}}{\partial \sigma_i}\Big). \tag{4.3.64}$$

By replacing $\iota\gamma + \alpha_1\lambda_{1,k}/H_1^2$ with $\iota\gamma + k_h + \alpha_1\lambda_{1,k}/H_1^2$ in (4.3.52), one can obtain solutions of (4.3.64) subject to the initial condition (4.3.32) and the boundary conditions (4.3.56) and (4.3.57). For convenience, we list the solutions in the absence of the frictional dissipation at the base of the pycnocline:

$$c_k(t) = \widehat{\varpi}_{i,k}(t) = \exp\{\tilde{\epsilon}_k t\}\ \Big[c_k(0) + \int_0^t \exp\{-\tilde{\epsilon}_k\tau\}F_k^{(e)}d\tau\Big], \tag{4.3.51}$$

where

$$\tilde{\epsilon}_k = -\big(\iota\gamma + k_h + \lambda_{i,k}\alpha_i/H_{i,k}^2\big), \tag{4.3.65}$$

$$F_k^{(e)} = F_k = \tau_{sx}(\rho_{i,1}H_i)^{-1}, \tag{4.3.53}$$

and $i = 1$, $r = 1, \cdots, m_i$. With the introduction of the horizontal dissipation term the real part of the characteristic modes is changed. This leads to an enhanced damping of the inertial oscillations.

In realistic applications, due to the uncertainty of the values of k_b and k_h, the present model has to be calibrated to fit the observed inertial motions. There are certain advantages of using the present model over the Pollard-Millard model in which the single factor k_m is used to represent the decay of the inertial motion in the surface layer. It would be expected that the time response of the Pollard-Millard model might be sensitive to the value of k_m. In the present two-layer model, the pycnocline acts as an *energy absorber* to control the downward flux of the wind shear. Consequently, the dependence of the time response to the value k_d will be lessened, particularly in conditions of strong stratification and deep pycnocline depth. An important point is that since an arbitrary eddy viscosity profile is allowed within each layer, any local information on the conditions of stratification can be incorporated in a flexible manner. If the horizontal extent of

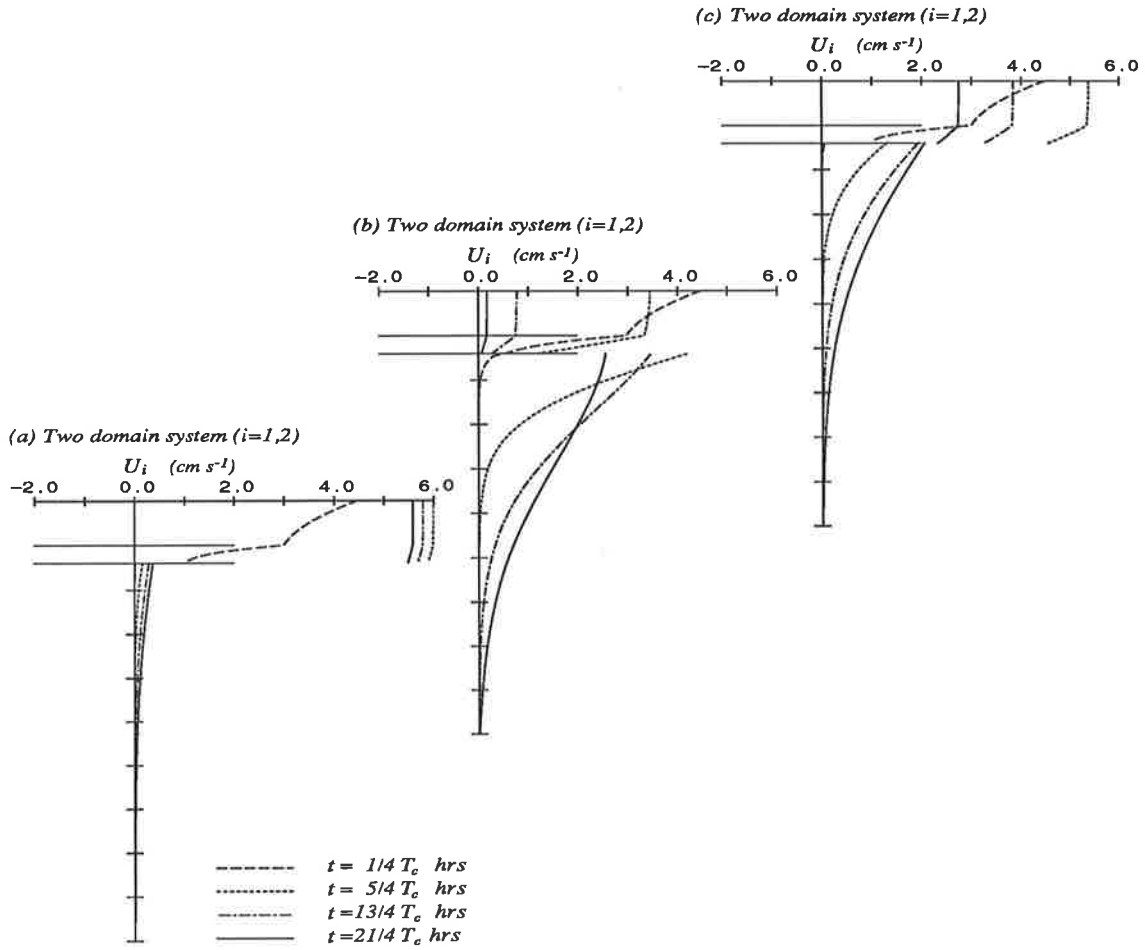

Figure 4.20 The U velocity profiles at t=1/4T_c, t=5/4T_c, 13/4T_c and 21/4T_c *hrs*, obtained using the profile in Figure 3.1(*d*), computed with a constant wind pulse of duration $T_c/4$ *hrs*. The stress components given by equation (4.3.57) are introduced at the base of the pycnocline which are in turn used as forcings for the bottom layer. A basis set of B-spline functions are used with: Δ_T=25, Δ_P=10, Δ_B=215 m; N_T =1000, N_P =50, N_B =100 $cm^2 s^{-1}$; ρ_T=1025.8, ρ_P=1026.5, ρ_B=1027.2 $g\,cm^{-3}$; and (*a*) k_d=0.001 $cm\,s^{-1}$; (*b*) k_d=0.01 $cm\,s^{-1}$; (*c*) k_d=0.1 $cm\,s^{-1}$.

the wind field is known, the horizontal dissipation of the wind's momentum can be calibrated reasonably well by changing k_h. Furthermore, continuous profiles of the horizontal components of current over the domain can be obtained in the present model at the expense of slightly increased computational effort (compared with the Pollard-Millard model).

We refer to Figure 4.20. When a uniform wind forcing is applied in a horizontally unbounded open sea region, no motion can arise in the bottom layer of the two domain system. Under the assumptions that the bottom layer is sufficiently deep and that the magnitudes of the horizontal components of the current there are small, the frictional dissipation computed with the velocity at the base of the upper domain can be used as a driving force for the bottom layer in a way similar to that in the two-layered steady state model of Welander (1968). However, it should be noted that in this case no feed-back mechanism from the lower domain to the upper domain is taken into account. Figure 4.20 illustrates the current profiles in the bottom layer driven by the interfacial shear $\tau_{dx} + \iota\tau_{dy}$ and their sensitivity to the value of k_d.

A transient free motion with a non-zero initial condition

To conclude this chapter, we consider the transient free motion of an open sea started by the given initial velocity field. All external stresses are removed throughout the computation. This system has been considered by Gonella (1971*a*) in a homogeneous sea with a constant eddy viscosity. Using the present numerical approach we can prescribe arbitrary variations of the initial velocity and eddy viscosity profiles.

For simplicity we consider the initial velocity field as follows:

$$U_i(\sigma_i, 0) = 10\ cm\, s^{-1} \quad 0 \leq \sigma_i \leq \xi_{i,1}, \tag{4.3.66}$$

$$U_i(\sigma_i, 0) = 0 \quad \text{for} \quad \xi_{i,1} < \sigma_i \leq 1, \tag{4.3.67}$$

$$V_i(\sigma_i, 0) = 0 \quad \text{throughout the domain} \tag{4.3.68}$$

where $i = 0, 1$. For the non-zero initial value problem it is necessary to initialise the expansion coefficients. In finite difference methods such an initialisation is straightforward.

Calculations are performed using a basis set of eigenfunctions. Projecting the initial velocity field onto the the vertical modes gives

$$\widehat{A}_{i,k}(0) = \Big\langle U_{i,j}(0),\ f_{i,j,k} \Big\rangle, \qquad \widehat{B}_{i,k}(0) = 0 \tag{4.3.69}$$

where $i = 0, 1$ and $k = 1, \cdots, m_i$. For an arbitrary form of the initial velocity field, $\widehat{A}_{i,k}$ in (4.3.69) can be evaluated using numerical quadrature. Substituting conditions (4.3.66) to (4.3.68) into (4.3.69) gives

$$\widehat{A}_{i,k}(0) = 10 \int_0^{\xi_{i,1}} f_{i,j,k}\ d\sigma_i = 10\ (a_{i,0,k} - a_{i,1,k}), \tag{4.3.70}$$

where $i = 0, 1$ and $k = 1, \cdots, m_i$. If the initial velocity field is computed by reconstituting the estimated coefficients of the vertical modes, nonphysical oscillations arise below the surface layer because of the presence of the discontinuity in the initial velocity field. However, immediately after the start, the current profiles become free of the oscillations.

For convenience, we list again the transient solution (4.3.51) for this initial value problem without the wind stress terms, namely

$$c_k(t) \ = \widehat{\varpi}_{i,k}(t) = \exp\{\tilde{\epsilon}_k t\}\ c_k(0), \tag{4.3.71}$$

where

$$< \widehat{\mathbf{w}}_i(0), \mathbf{e}_k > = \sum_{j=1}^{m_i} \widehat{\varpi}_{i,j}(0)\ e^*_{k,j} = c_k(0), \tag{4.3.48}$$

$$\tilde{\epsilon}_k \ = \Gamma_{r,r} = -\big(\iota\gamma + \lambda_{i,k}\alpha_i / H^2_{i,k}\big), \tag{4.3.52}$$

and $i = 0, 1$, $k = 1, \cdots, m_i$. Note that each characteristic mode will be excited selectively depending upon the initial condition.

Figure 4.21 depicts the time variation of the first four vertical modes in the one domain system computed with $N_P = 10\ cm^2 s^{-1}$ and the two second vertical modes in the two domain system computed with $N_P = 10$ and $150\ cm^2 s^{-1}$. It

is apparent from these figures that the inertial oscillations will dominate the time response of the surface currents and layer-mean velocities of the free motion. The velocity at each level approaches zero as $t \rightarrow \infty$, either in the presence of bottom friction or in an infinitely deep sea. With the initial conditions (4.3.66) to (4.3.68) all the vertical modes are excited and, since $f_{i,1}(\sigma_i) = 1$, the magnitude of $\widehat{A}_{i,1}$ is given by $10\Delta_T/H_i \; cm\, s^{-1}$. In the absence of bottom friction the first vertical mode is undamped whereas the higher modes decay at different rates due to the presence of internal friction. Note that the inertial oscillations of the second vertical mode in the one domain system decay very slowly. In the two domain system the internal friction is increased significantly because of the reduced depth . Furthermore, since the region occupied by the pycnocline is a significant fraction of the domain, the value of $\alpha_{1,1}$ plays an important role in determining the rate of damping of the second vertical mode.

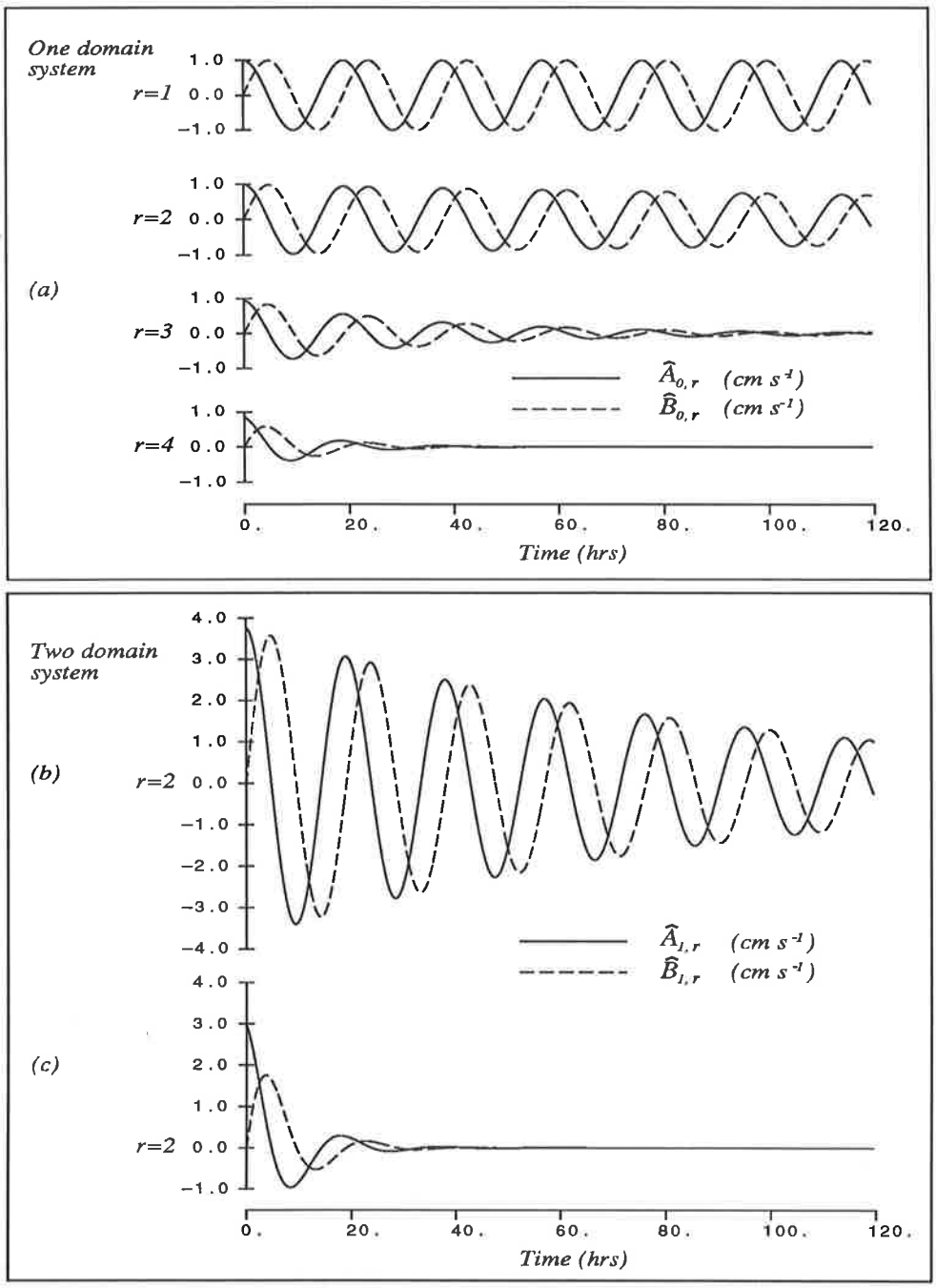

Figure 4.21 Time variation of various modal coefficients computed with the initial conditions (4.3.66) to (4.3.68). Stress-free conditions are imposed at the upper and lower domain boundaries with: Δ_T=25, Δ_P=40 m; ρ_T=1025.8, ρ_P=1026.5 $g\,cm^{-3}$; $\beta_{i,1}=\beta_{i,2}=0, i=0,1$; and for Ω_0, ρ_B=1027.2 $g\,cm^{-3}$, Δ_B=185 m; and (*a*) N_T =150, N_P=10, N_B=1000 $cm^2 s^{-1}$; (*b*) N_T =150, N_P=10 $cm^2 s^{-1}$; (*c*) N_T =150, N_P=150 $cm^2 s^{-1}$.

CHAPTER 5

WIND INDUCED MOTION IN NARROW FLAT-BOTTOMED LAKES

5.1 Introductory Remarks

This chapter is concerned with the application of the layered models described in Chapter 2 to wind induced motion in elongated two and three-layered lakes of finite length and uniform depth. It is assumed that the longitudinal axis of the lake is parallel to the x-axis and that mean values of the layer thickness are independent of time and the x-coordinate. Since the system is bounded, the gradients of the free surface and the interfaces participate in the dynamic balance but the Coriolis parameter, which played a central role in determining the wind induced inertial motion in an open sea region, is omitted. The direct tide-generating forces and the effect of the atmospheric pressure gradient are also neglected. Thus, the system of governing equations can be written as follows:

$$\frac{\partial U_{i,j}}{\partial t} = -\sum_{\ell=1}^{j} g\Big(\frac{\rho_{i,\ell}-\rho_{i,\ell-1}}{\rho_{i,j}}\Big)\frac{\partial \zeta_{i,\ell-1}}{\partial x} + \frac{\alpha_i}{H_i^2}\frac{\partial}{\partial \sigma_i}\Big(\mu_{i,j}\frac{\partial U_{i,j}}{\partial \sigma_i}\Big), \quad i=0, j=1,2,3;\ i=1, j=1,2, \tag{5.1.1}$$

$$\frac{\partial U_{i,j}}{\partial t} = -\sum_{\ell=1}^{2} g\Big(\frac{\rho_{1,\ell}-\rho_{1,\ell-1}}{\rho_{i,j}}\Big)\frac{\partial \zeta_{1,\ell-1}}{\partial x} - g\Big(\frac{\rho_{i,j}-\rho_{1,2}}{\rho_{i,j}}\Big)\frac{\partial \zeta_{i,j-1}}{\partial x} + \frac{\alpha_i}{H_i^2}\frac{\partial}{\partial \sigma_i}\Big(\mu_{i,j}\frac{\partial U_{i,j}}{\partial \sigma_i}\Big), \quad i=2,\ j=1, \tag{5.1.2}$$

$$\frac{\partial \zeta_{i,j-1}}{\partial t} - \frac{\partial \zeta_{i,j}}{\partial t} + H_i\frac{\partial}{\partial x}\Big(\int_{\xi_{i,j}}^{\xi_{i,j-1}} U_{i,j}\ d\sigma_i\Big) = 0, \quad i=0,1,\ j=1,2, \tag{5.1.3}$$

$$\frac{\partial \zeta_{i,j-1}}{\partial t} + H_i\frac{\partial}{\partial x}\Big(\int_{\xi_{i,j}}^{\xi_{i,j-1}} U_{i,j}\ d\sigma_i\Big) = 0, \quad i=0, j=3;\ i=2, j=1. \tag{5.1.4}$$

Our primary concerns in this chapter will be with calculating the time response of interfacial displacements in the two and three-layered systems, extending Heaps' two-layer two domain model numerically, and investigating the sensitivity of the interfacial displacements to the eddy viscosity (particularly to N_P) and to the density distribution. The dimension of the idealised x–z model is chosen to be the same as that considered by Davies (1983*a*).

Calculations are in the main performed using a basis set of B-splines over 60 *hrs*, with a step-function wind stress of 1 $dyne\,cm^{-2}$ which is instantaneously applied at $t = 0$ uniformly over the horizontal domain. The assumption that the wind stress is constant over the basin is reasonable for a small lake, because the characteristic length scales of the meteorological events are much larger than those of the lake.

When we examine the sensitivity of the interfacial displacements to changes in the density of the layers, $\rho_{i,1}(= \rho_T)$ and $\rho_{i,2}(= \rho_P)$ will be varied for the two and three-layered systems, respectively.

5.2 Finite difference form of the Galerkin equations

The staggered finite difference grid in the x-direction is shown in Figure 5.1. The displacements of the free surface and the interfaces $\zeta_{i,j}$ are evaluated at points indicated by a "•" symbol. Each of the coefficients of the B-splines and of the eigenfunctions for the current velocity $A_{i,r}$, is evaluated at the points marked by a "+" symbol. The left and right land boundaries are located at $x = 0$ and L, respectively. The points for $\zeta_{i,j}$ are numbered from left to right, assuming that there is one extra point just outside each end of the model region. Such a labelling is implemented keeping in mind the incorporation of horizontal diffusion and non-linear advection terms in future applications. The depth of water, the thickness of the layers, and the wind stress are defined at the points for $\zeta_{i,j}$ although their spa-

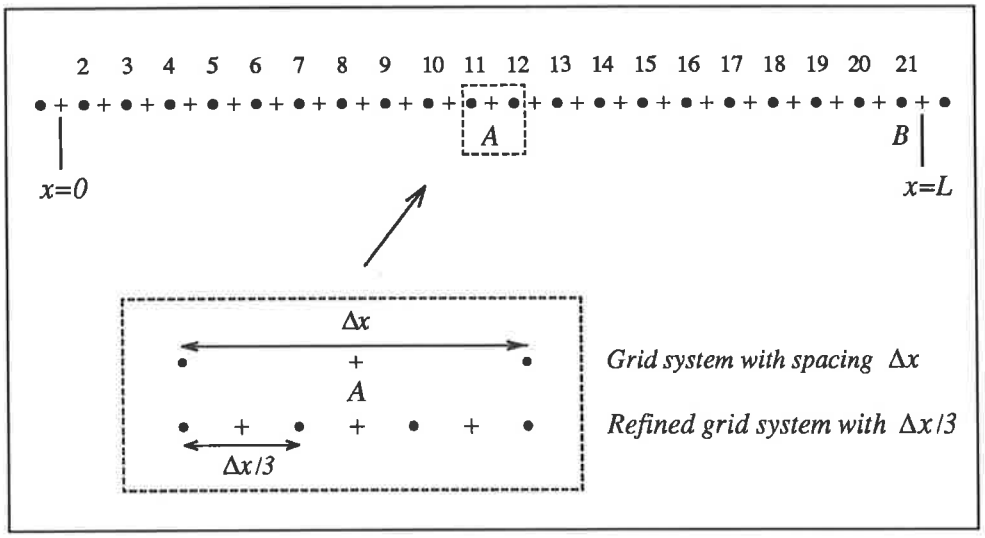

Figure 5.1 A staggered finite difference grid for the x-direction in which • indicates a u_i-point (also $A_{i,r}$ or $\widehat{A}_{i,r}$, $r = 1, \cdots, m_i$) and + indicates a $\zeta_{i,j}$-point.

tial variation is not considered in these computations. The coarse grid system has a grid spacing of $\Delta x = 475\,m$. The finer grid system, which has a spacing of one third of the coarse grid, is used to illustrate the improved accuracy in reproducing the internal displacements for the two domain system.

A basis set of B-splines

Along a horizontal closed boundary of general form in the x–y plane, the normal component of the current vanishes for all $t \geq 0$, thus

$$A_{i,r} \cos\psi + B_{i,r} \sin\psi = 0, \qquad i = 0, 1, 2,\ r = 1, \cdots, m_i, \tag{5.2.1}$$

where ψ is the inclination of the normal to the x-axis. For the narrow lake considered here, $\psi = 0$, so the boundary conditions imposed at the closed ends $x = 0$ and $x = L$ are

$$A_{i,r}(x,t) = 0 \quad \text{for } t \geq 0, \qquad i = 0, 1, 2,\ r = 1, \cdots, m_i. \tag{5.2.2}$$

The simulation starts with the body of water at rest, that is, the velocity field, the free surface and the internal displacements at $t = 0$ are all assumed to be zero. Thus,

$$\begin{aligned} A_{i,r}(x,0) &= 0, \qquad i = 0,1,2,\ r = 1,\cdots,m_i, \\ \zeta_{i,j}(x,0) &= 0, \qquad i = 0,1,2,\ j = 1,\cdots,J_i, \end{aligned} \tag{5.2.3}$$

for all x.

Under the narrow lake approximation, the matrix equations (2.5.18), (2.5.20), (2.5.51), (2.5.53), (2.5.55) and (2.5.56) simplify to one-dimensional form and are approximated using central differencing for the spatial derivatives and a forward approximation for the time derivative on the grid shown in Figure 5.1. The Galerkin solutions of (5.1.1) and (5.1.2) are expressed, neglecting the effects of the atmospheric pressure gradients and the direct tide-generating forces, in the form

$$\mathbf{C}_i^+ \, \mathbf{A}_i\big|_q^{t+\Delta t} = \mathbf{C}_i^- \, \mathbf{A}_i\big|_q^{t} + \Delta t \mathbf{F}_{i,x} \ + (\Delta t/\Delta x)\mathbf{S}_{i,x} \ , \qquad i = 0,1,2, \tag{5.2.4}$$

where

$$\left.\begin{aligned} \mathbf{C}_i^+ &= \mathbf{C}_i + \frac{\Delta t}{2}\frac{\alpha_i}{H_i^2}\mathbf{D}_i \\ \mathbf{C}_i^- &= \mathbf{C}_i - \frac{\Delta t}{2}\frac{\alpha_i}{H_i^2}\mathbf{D}_i \end{aligned}\right\} \qquad i = 0,1,2, \tag{5.2.5}$$

$$\left.\begin{aligned} \mathbf{F}_{0,x} &= (\rho_{0,1}H_0)^{-1}(\tau_{sx}\mathbf{E}_0^s - \tau_{bx}\mathbf{E}_0^b) \\ \mathbf{F}_{1,x} &= (\rho_{1,1}H_1)^{-1}\tau_{sx}\mathbf{E}_1^s \\ \mathbf{F}_{2,x} &= -(\rho_{2,1}H_2)^{-1}\tau_{bx}\mathbf{E}_2^b \end{aligned}\right\} \tag{5.2.6}$$

$$\left.\begin{aligned} \mathbf{S}_{0,x} &= -\sum_{\ell=1}^{3} g\Big(\frac{\rho_{i,\ell}-\rho_{i,\ell-1}}{\rho_{i,1}}\Big)\Big[\zeta_{i,\ell-1}\big|_{q+1}^{t+\Delta t} - \zeta_{i,\ell-1}\big|_q^{t+\Delta t}\Big]\mathbf{E}_i^{(\ell)} \\ \mathbf{S}_{1,x} &= -\sum_{\ell=1}^{2} g\Big(\frac{\rho_{i,\ell}-\rho_{i,\ell-1}}{\rho_{i,1}}\Big)\Big[\zeta_{i,\ell-1}\big|_{q+1}^{t+\Delta t} - \zeta_{i,\ell-1}\big|_q^{t+\Delta t}\Big]\mathbf{E}_i^{(\ell)} \\ \mathbf{S}_{2,x} &= -\sum_{\ell=1}^{2} g\Big(\frac{\rho_{1,\ell}-\rho_{1,\ell-1}}{\rho_{2,1}}\Big)\Big[\zeta_{1,\ell-1}\big|_{q+1}^{t+\Delta t} - \zeta_{1,\ell-1}\big|_q^{t+\Delta t}\Big]\mathbf{E}_2^{(1)} \\ &\quad -g\Big(\frac{\rho_{2,1}-\rho_{1,2}}{\rho_{2,1}}\Big)\Big[\zeta_{2,0}\big|_{q+1}^{t+\Delta t} - \zeta_{2,0}\big|_q^{t+\Delta t}\Big]\mathbf{E}_2^{(1)} \end{aligned}\right\} \tag{5.2.7}$$

$$\tau_{bx} = \rho_{0,2} k_b \sum_{r=1}^{m_0} A_{0,r}\Big|_q^t M_{0,r}(1), \qquad \text{for} \quad \Omega_0, \tag{5.2.8}$$

$$\tau_{bx} = \rho_{2,1} k_b \sum_{r=1}^{m_2} A_{2,r}\Big|_q^t M_{2,r}(1), \qquad \text{for} \quad \Omega_2, \tag{5.2.9}$$

The continuity equation is expressed in the form

$$\mathbf{Z}_i\Big|_q^{t+\Delta t} = \mathbf{Z}_i\Big|_q^t - H_i\,(\Delta t/\Delta x)\mathbf{E}_i\Big[\mathbf{A}_i\Big|_q^t - \mathbf{A}_i\Big|_{q-1}^t\Big]\ , \tag{5.2.10}$$

where $i = 0, 1, 2$. The matrix $\mathbf{Z}_i$ is a column vector of length J_i (3 for Ω_0; 2 for Ω_1; 1 for Ω_2) with k th element $\zeta_{i,k-1}$. The other matrices are given by (2.5.21) to (2.5.26).

The coefficients of the B-splines for the horizontal current $A_{i,r}$, $r = 1, \cdots, m_i$, and the displacements $\zeta_{i,j}$ involving the free surface and the internal interfaces are then calculated as time progresses. The explicit marching scheme given in equations (5.2.4) and (5.2.10) is basically equivalent to that described by Davies (1980*a*) except that in the two domain system the procedures are applied to both the upper and lower domains. The CFL condition $\Delta x/\sqrt{2gh}$, restricts the time step to $\Delta t = 9$ *sec* and 3 *sec* for the coarse and fine grids, respectively. It would be necessary to employ a time and/or space-splitting technique for internal modes in a manner similar to that described by Heaps and Jones (1983), in order to reduce the computational effort required when the method is applied to a horizontally two-dimensional fine grid system.

A basis set of eigenfunctions

Heaps' expansion given by (2.6.30) is employed with the homogeneous limit conditions, $\beta_{0,1} = \beta_{0,2} = 0$.

Boundary and initial conditions are obtained by replacing $A_{i,r}$ in (5.2.2) and (5.2.3) with $\widehat{A}_{i,r}$. At the closed ends we have

$$\left.\begin{aligned}\widehat{A}_{i,r}(0,t) &= 0\\ \widehat{A}_{i,r}(L,t) &= 0\end{aligned}\right\} \qquad i=0,1,2,\ r=1,\cdots,m_i, \tag{5.2.11}$$

for all $t>0$, with the initial conditions for the displacements and velocities being

$$\begin{aligned}\widehat{A}_{i,r}(x,0) &= 0, \qquad i=0,1,2,\ r=1,\cdots,m_i,\\ \zeta_{i,j}(x,0) &= 0, \qquad i=0,1,2,\ j=1,\cdots,J_i,\end{aligned} \tag{5.2.12}$$

for all x.

The spectral solution of (5.1.1) and (5.1.2) is expressed in the form

$$\begin{aligned}\Big[1+\frac{\Delta t}{2}\frac{\alpha_i}{H_i^2}\lambda_{i,k}\Big]\widehat{A}_{i,k}\Big|_q^{t+\Delta t} =& \Big[1-\frac{\Delta t}{2}\frac{\alpha_i}{H_i^2}\lambda_{i,k}\Big]\widehat{A}_{i,k}\Big|_q^{t}\\ &+\Delta t F_{i,x}+(\Delta t/\Delta x)S_{i,x},\end{aligned} \tag{5.2.13}$$

where $i=0,1,2$ and

$$\left.\begin{aligned}F_{0,x} &= (\rho_{0,1}H_0)^{-1}(\tau_{sx}-f_{i,k}(1)\tau_{bx})\\ F_{1,x} &= (\rho_{1,1}H_1)^{-1}\tau_{sx}\\ F_{2,x} &= -f_{2,k}(1)(\rho_{2,1}H_2)^{-1}\tau_{bx}\end{aligned}\right\} \tag{5.2.14}$$

$$\left.\begin{aligned}S_{0,x} &= -\sum_{\ell=1}^{3} g\Big(\frac{\rho_{0,\ell}-\rho_{0,\ell-1}}{\rho_{0,1}}\Big)\Big[\zeta_{0,\ell-1}\Big|_{q+1}^{t+\Delta t}-\zeta_{0,\ell-1}\Big|_q^{t+\Delta t}\Big]a_{0,\ell-1,k}\\ S_{1,x} &= -\sum_{\ell=1}^{2} g\Big(\frac{\rho_{1,\ell}-\rho_{1,\ell-1}}{\rho_{1,1}}\Big)\Big[\zeta_{1,\ell-1}\Big|_{q+1}^{t+\Delta t}-\zeta_{1,\ell-1}\Big|_q^{t+\Delta t}\Big]a_{1,\ell-1,k}\\ S_{2,x} &= -\sum_{\ell=1}^{2} g\Big(\frac{\rho_{1,\ell}-\rho_{1,\ell-1}}{\rho_{2,1}}\Big)\Big[\zeta_{1,\ell-1}\Big|_{q+1}^{t+\Delta t}-\zeta_{1,\ell-1}\Big|_q^{t+\Delta t}\Big]a_{2,0,k}\\ &\quad -g\Big(\frac{\rho_{2,1}-\rho_{1,2}}{\rho_{2,1}}\Big)\Big[\zeta_{2,0}\Big|_{q+1}^{t+\Delta t}-\zeta_{2,0}\Big|_q^{t+\Delta t}\Big]a_{2,0,k}\end{aligned}\right\} \tag{5.2.15}$$

$$\tau_{bx}=\rho_{0,2}k_b\sum_{r=1}^{m_0}\widehat{A}_{0,r}\Big|_q^t\Phi_{0,r}f_{0,r}(1), \qquad \text{for} \quad \Omega_0, \tag{5.2.16}$$

$$\tau_{bx}=\rho_{2,1}k_b\sum_{r=1}^{m_2}\widehat{A}_{2,r}\Big|_q^t\Phi_{2,r}f_{2,r}(1), \qquad \text{for} \quad \Omega_2, \tag{5.2.17}$$

The continuity equation is expressed in the form:

$$\mathbf{Z}_i\big|_q^{t+\Delta t} = \mathbf{Z}_i\big|_q^t - H_i\ (\Delta t/\Delta x)\ \mathbf{E}_i^H \left[\mathbf{A}_i\big|_q^t - \mathbf{A}_i\big|_{q-1}^t\right] , \qquad (5.2.18)$$

where $i = 0, 1, 2$. The matrices in (5.2.18) are given by (2.6.45) and (2.6.51).

5.3 Results

Figures 5.2 and 5.3 depict the time variation of the interfacial displacements in the two and three-layered systems computed with various combinations of the eddy viscosity and the coefficients of the linear bottom friction. Referring to the two-layered system (Figure 5.2), calculations have been performed on the coarse grid system for the one domain system and on both the coarse and fine grid systems for the two domain system, using a basis set of B-spline functions. The eddy viscosity in the upper layer was fixed at $N_T = 300\ cm^2 s^{-1}$ while values of $k_b = 0.0$, 0.1 and 1.0 $cm\, s^{-1}$ were applied with $N_B = 100\ cm^2 s^{-1}$. For comparison purposes, the time variations of the interfacial displacements computed with $k_b = 1.0\ cm\, s^{-1}$ and $N_B = 1000\ cm^2 s^{-1}$ are plotted together. The internal motion induced by a step-function wind stress exhibits oscillations which are associated with the internal seiche period of the basin (Heaps, 1966; Davies, 1983*a*) and which have a period of about 12 *hrs*. The interface at the right half of the basin is displaced downwards under the wind action, while the free surface is displaced upwards. We exclude from our consideration the time variation of the free surface which is associated with the short-period surface seiche motion. It is apparent from Figures 5.2(*a*) and (*b*) that the damping of the internal seiche motion is increased as values of k_b and N_B are increased. Although the results are not explicitly presented, the plot of the interface displacements computed using a no-slip condition with $N_B = 100$ $cm^2 s^{-1}$ was not significantly different from that computed with $N_B = 100\ cm^2 s^{-1}$ and $k_b = 1.0\ cm\, s^{-1}$. The most striking fact is that there is significant difference in the rate of damping of the internal seiche motion between the one and two

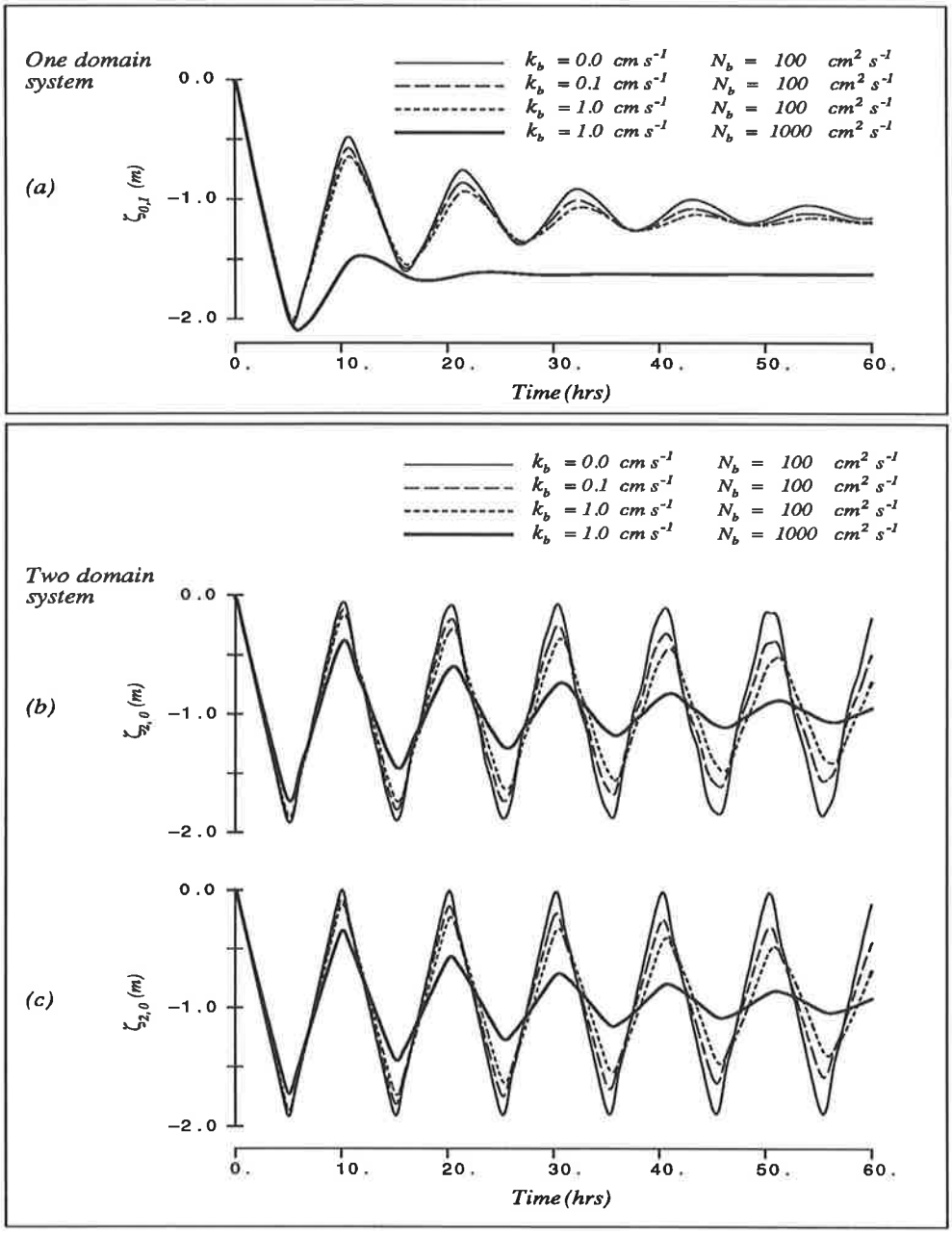

Figure 5.2 Time variation of interfacial displacements (at corner point B in Figure 5.1) in two-layered one and two domain systems, obtained using the profile in Figure 3.1(*c*), computed using a basis set of *B*-splines, with: Δ_T=40, Δ_B=60 *m*; ρ_T=1025.8, ρ_B=1027.0 *g cm*$^{-3}$; N_T=300 *cm*^{2}*s*$^{-1}$, with various values of k_b and N_B shown in the key; and (*a*), (*b*) on a coarse grid with Δx = 1425 *m*; (*c*) on a finer grid with Δx=475 *m*.

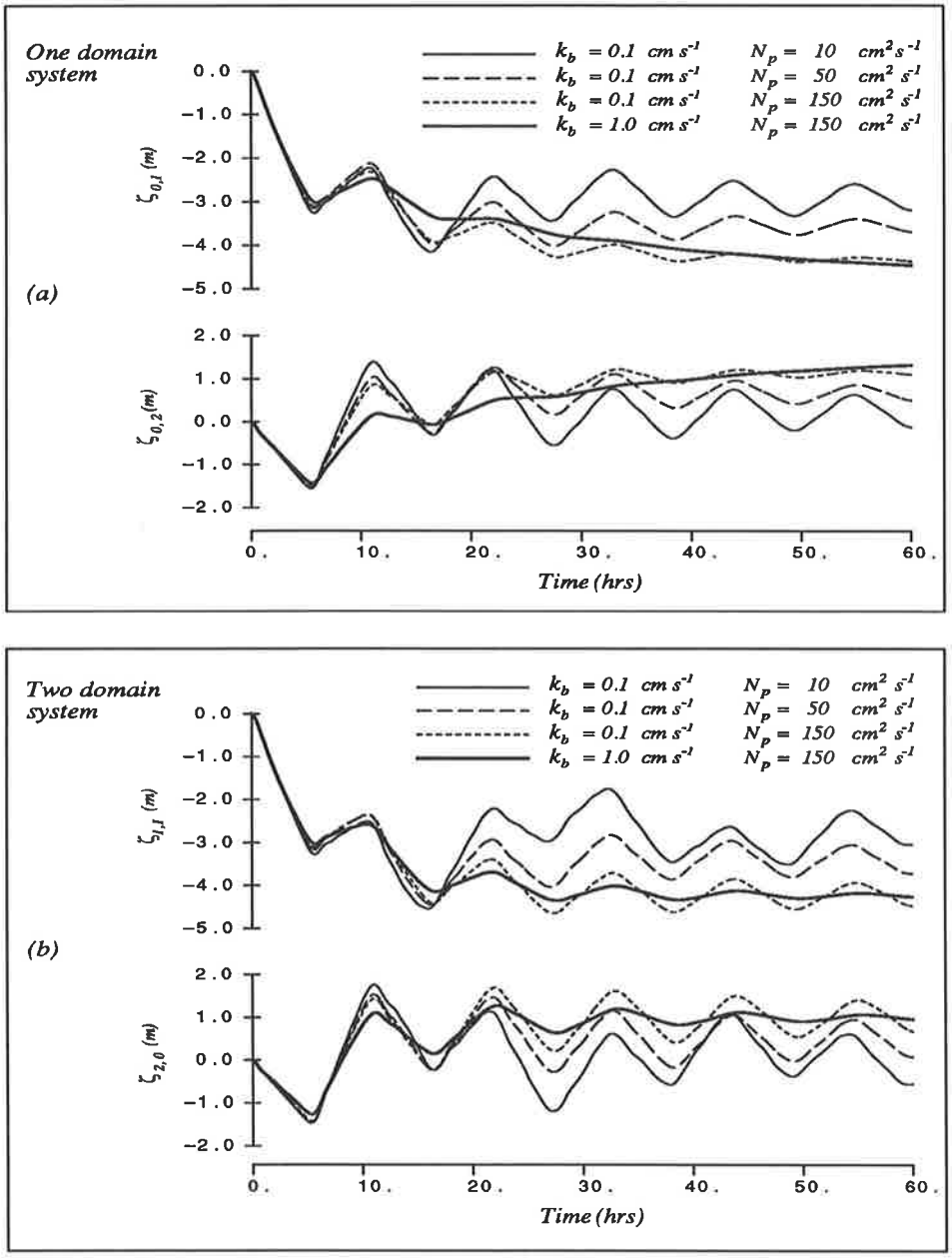

Figure 5.3 Time variation of interfacial displacements (at corner point B in Figure 5.1) in a three-layered one and two domain systems, obtained using the profile in Figure 3.1(d), computed using a basis set of B-splines. A coarse grid with $\Delta x = 1425\,m$ was used with N_T=300 $cm^2 s^{-1}$, with: Δ_T=25, Δ_P=15, Δ_B=60 m; ρ_T=1025.8, ρ_P=1026.5, 1027.2 $g\,cm^{-3}$; N_T=300, N_B=100 $cm^2 s^{-1}$, various values of k_b and N_P shown in the key.

domain systems. The internal seiche motion in the two domain system is damped much more slowly than in the one domain system. The time variation of the one domain system computed using $N_B = 100\ cm^2 s^{-1}$ and $k_b = 0.0\ cm\, s^{-1}$ is in fact comparable with that of the two domain system computed with $N_B = 1000\ cm^2 s^{-1}$ and $k_b = 1.0\ cm\, s^{-1}$. Preliminary computations have revealed that with $N_B = 100\ cm^2 s^{-1}$ and $k_b = 0.2\ cm\, s^{-1}$ the interface $\zeta_{1,1}$ oscillates even at $t = 300\ hrs$ with an amplitude of about 5.0 cm, whereas the interface $\zeta_{0,1}$ remains at a quasi-steady value after about $t = 80\ hrs$. We can note that with $N_B = 1000\ cm^2 s^{-1}$ and $k_b = 1.0\ cm\, s^{-1}$, the one domain system is heavily damped, almost preventing the development of the internal seiche motion. Using a two-layered two domain model, Heaps (1966) has predicted a critical value of the coefficient of linear bottom friction (related to the mean-velocity at the bottom layer) beyond which the development of an internal seiche motion is prevented. It is evident that the critical value of the bottom frictional coefficient of the one domain system will be significantly lower than that of the two domain system. We also note that in a highly dissipative situation with $N_B = 1000\ cm^2 s^{-1}$ and $k_b = 1.0\ cm\, s^{-1}$ the mean value of $\zeta_{0,1}$ is significantly lowered, whereas the mean value of $\zeta_{1,1}$ remains unaffected. In the absence of the interfacial stress the steady state velocities in the bottom layer (apart from the possible presence of the undamped mode) are all zero and the gradients of the free surface and the interface are given by Heaps (1984), namely

$$\frac{\partial \zeta_{i,0}}{\partial x} = \frac{\tau_{sx}}{\rho_T g \Delta_T}, \tag{5.3.1}$$

$$\frac{\partial \zeta_{i,1}}{\partial x} = -\frac{\rho_T}{\rho_B - \rho_T}\frac{\partial \zeta_{i,0}}{\partial x} = -\frac{1}{\rho_B - \rho_T}\frac{\tau_{sx}}{g\Delta_T}. \tag{5.3.2}$$

Integrating (5.3.1) and (5.3.2), satisfying the constraints of continuity of volume, that is, $\int_0^L \zeta_{1,0}\, d\sigma_1 = \int_0^L \zeta_{2,0}\, d\sigma_2 = 0$ gives

$$\zeta_{1,0} = [\rho_T g \Delta_T]^{-1}(2x - L)\tau_{sx}, \tag{5.3.3}$$

$$\zeta_{2,0} = -\left[(\rho_B - \rho_T)g\Delta_T\right]^{-1}\tau_{sx}(2x - L). \tag{5.3.4}$$

Thus, in the two domain system the eddy viscosity in the bottom layer and the coefficient of bottom friction do not influence the mean displacement of $\zeta_{i,1}$.

The presence of spatial truncation errors is apparent in the solutions for the two domain system computed on a coarse grid system (Figure 5.2(b)). The effect of numerical truncation is not noticeable in the one domain system because of the strong damping. Increasing the spatial resolution by one third reproduces the saw-tooth behaviour of $\zeta_{i,1}$ accurately.

In the case of the three-layered system, calculations have been performed on the coarse grid system for both one and two domain systems using the eddy viscosity profile shown in Figure 3.1(d). As in calculations for the two-layered system, a basis set of B-spline functions was again used. Figure 5.3 shows the time variations of the two interfacial displacements at corner point B (shown in Figure 5.1) computed with N_T fixed at 300 cm^2s^{-1}, N_B at 100 cm^2s^{-1} and N_P taking a range of values, namely N_P = 10, 50 and 150 cm^2s^{-1}. For comparison purposes the time variations of the two interfacial displacements computed with $N_T = 300$, $N_P = 150$, $N_B = 1000$ cm^2s^{-1} and $k_b = 1.0$ $cm\,s^{-1}$ are also shown. It is evident on comparing Figure 5.3 with Figure 5.2 that the time variation of the internal seiche motion in the three-layered system is complicated compared with that of the two-layered system. A scenario on the time-dependent circulation pattern has been described in detail by Davies (1983a). In contrast to the two-layered system, the time behaviour of the interfacial displacements in the one domain system is very similar to that of the two domain system although a difference in the rate of decay of the internal seiche motion is apparent. For the three-layered system, the internal seiche motions in both the one and two domain systems are damped in the absence of bottom friction. This point will be discussed in more detail later. It is apparent that the mean displacement of the interfaces is sensitive to

change in the value of N_P and, as the value of N_P is decreased from 150 to 10 $cm^2 s^{-1}$, the downward displacement of $\zeta_{i,1}$ and the upward displacement of $\zeta_{i,2}$ are both enhanced. We note that in contrast to the two-layered system the mean displacements in both one and two domain systems computed with $N_B = 1000$ $cm^2 s^{-1}$ and $k_b = 1.0$ $cm\, s^{-1}$ are comparable with each other.

To understand why the internal seiche motions of the one and two domain systems decay at considerably different rates each other in two-layered conditions (when N_P is high), a series of calculations have been performed on a coarse grid using a basis set of eigenfunctions, with an increasing number of m_i. It is apparent from Figure 5.4 that in the one domain system the contribution to the internal seiche motion comes from the second mode $\widehat{A}_{0,2}$, whereas in the two domain system the contribution to the internal seiche motion comes from $\widehat{A}_{1,1}$ and $\widehat{A}_{2,1}$. The contribution of the higher modes is mainly associated with the mean displacement of the interfaces. In the one domain system the largest contribution to the mean displacement of the interfaces comes from $\widehat{A}_{0,3}$, which is concurrently responsible for the return-flow within the pycnocline and for the smooth variation of the current at the bottom layer (Davies, 1983*a*). Under conditions of strong stratification ($N_P = 10$ $cm^2 s^{-1}$), the modes up to $r = 4$ contribute significantly. With $N_P = 150$ $cm^2 s^{-1}$, the fifth mode also significantly contributes to the mean displacement. In the two domain system the mean displacement of interfaces is attributable to the second mode $\widehat{A}_{1,2}$. Highly dissipative conditions such as $N_B = 1000$ $cm^2 s^{-1}$ and $k_b = 1.0$ $cm\, s^{-1}$, the internal seiche motion does not develop. In this case the vertical modes $\widehat{A}_{0,2}$ and $\widehat{A}_{1,1}$ directly contribute to the mean displacements of $\zeta_{i,1}$, $i = 0, 1$.

From these results it is evident that the damping of the internal seiche motion in the one domain system is predominantly determined by the rate at which $\widehat{A}_{0,2}$ decays. In the two domain system the time behaviour of the internal seiche motion

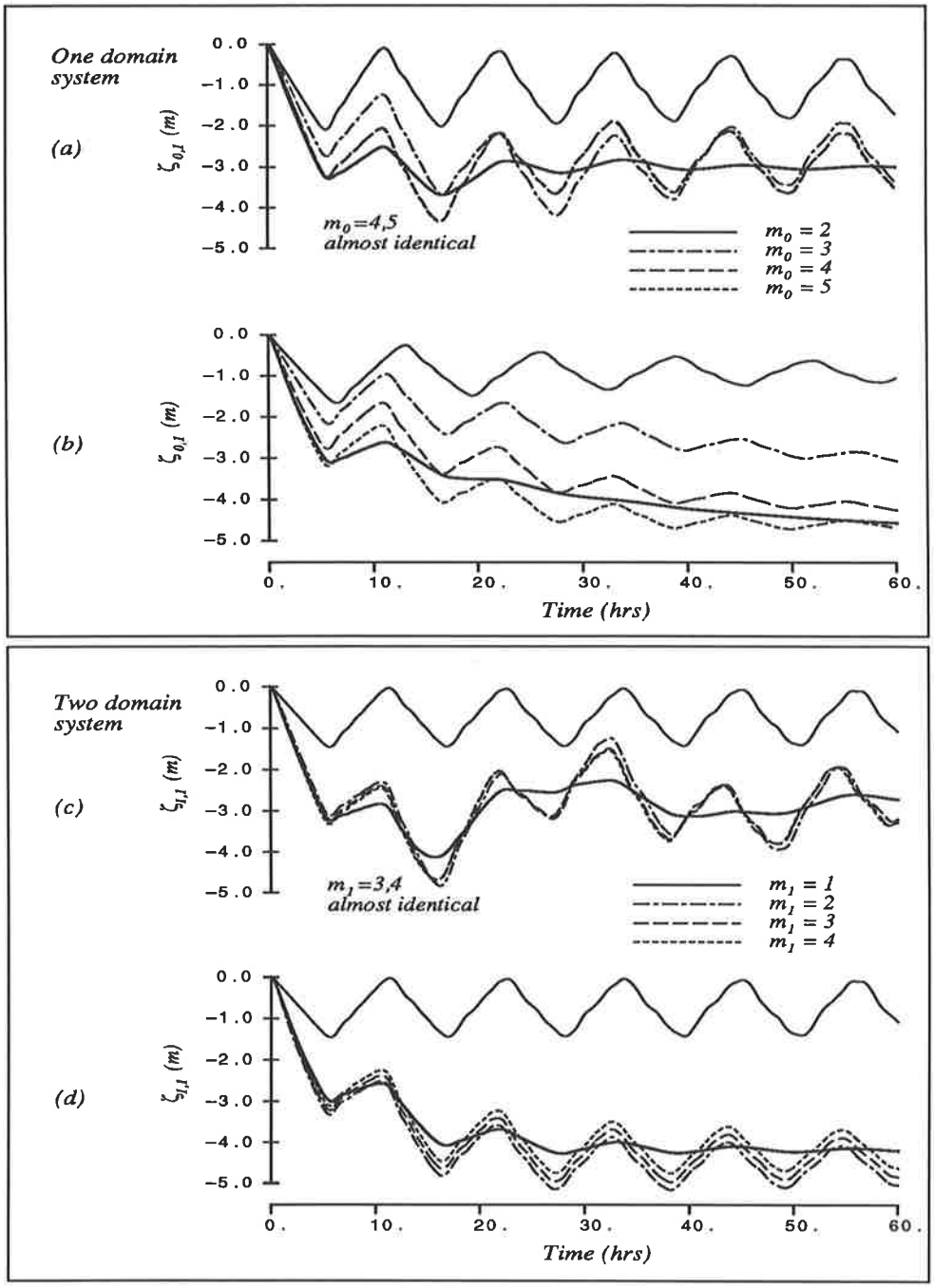

Figure 5.4 Time variation of (at corner point B in Figure 5.1) of three-layered systems, obtained using the profile in Figure 3.1(*d*), computed with an increasing number of m_i. A coarse grid with $\Delta x = 1425\,m$ was used with: Δ_T=25, Δ_P=15, Δ_B=60 m; ρ_T=1025.8, ρ_P=1026.5, 1027.2 $g\,cm^{-3}$; N_T=300 $cm^2 s^{-1}$; and (*a*) N_P=10 $cm^2 s^{-1}$, k_b=0.0 $cm\,s^{-1}$, the thick solid line denoting calculation with N_B=1000 $cm^2 s^{-1}$, k_b=1.0 $cm\,s^{-1}$ and m_0=4; (*b*) as in (a) but with N_P=150 $cm^2 s^{-1}$; (c) as in (a) but with k_b=0.0 $cm\,s^{-1}$, m_2=1, the thick solid line denoting calculation with N_B=1000 $cm^2 s^{-1}$, k_b=1.0 $cm\,s^{-1}$ and m_1=m_2=4; (*d*) as in (c) but with N_P=150 $cm^2 s^{-1}$.

is represented by the first vertical modes $\widehat{A}_{1,1}$ and $\widehat{A}_{2,1}$. This explains why even though each vertical mode experiences significantly greater internal damping in the two domain system (due to the reduced depth), the internal seiche motion decays more rapidly in the one domain system. In the absence of bottom friction the difference in the rates of damping of the internal seiche motions between the one and two domain systems is determined by the factor $\alpha_0\lambda_{0,2}/H_0^2$ (because the eigenvalue of the two first vertical modes of the two domain system are both zero). It is evident from Table 5.1 that for given values of the depth and layer thicknesses, decreasing the value of N_P significantly reduces the damping of the second mode. Consequently, the internal seiche motion of the three-layered one domain system decays significantly more slowly than in the two-layered one domain system. Note that the internal seiche motion of the three-layered one domain system computed with $N_P = 10\ cm^2s^{-1}$ (shown in Figure 5.3(a)) is comparable with that of the three-layered two domain system computed with $N_P = 50\ cm^2s^{-1}$ (shown in Figure 5.3(b)).

Table 5.1 Values of $\alpha_i\lambda_{i,2}/H_i^2$ computed for various combinations of N_P, N_B and H_i with $\Delta_T = 25$, $\Delta_P = 15\,m$

	$N_T=$	300 cm^2s^{-1}	300 cm^2s^{-1}	300 cm^2s^{-1}	300 cm^2s^{-1}
	$N_P=$	10 cm^2s^{-1}	50 cm^2s^{-1}	150 cm^2s^{-1}	300 cm^2s^{-1}
$N_B=$	100 cm^2s^{-1}				
	H_0=250m	0.126×10^{-5}	0.155×10^{-5}	0.159×10^{-5}	0.160×10^{-5}
	H_0=100m	0.294×10^{-5}	0.846×10^{-5}	1.120×10^{-5}	1.203×10^{-5}
N_B=	1000 cm^2s^{-1}				
	H_0=250m	0.241×10^{-5}	0.888×10^{-5}	1.349×10^{-5}	1.475×10^{-5}
	H_0=100m	0.333×10^{-5}	1.500×10^{-5}	3.543×10^{-5}	5.274×10^{-5}
$N_B=$	30 cm^2s^{-1}				
	H_0=250m	0.045×10^{-5}	0.048×10^{-5}	0.048×10^{-5}	0.048×10^{-5}
	H_0=100m	0.212×10^{-5}	0.347×10^{-5}	0.377×10^{-5}	0.384×10^{-5}

Spigel and Imberger (1980) have shown how to estimate an e-folding decay

time for the internal seiche motion in a two-layered system on the assumption that the energy of the internal seiche motion is dissipated by the bottom friction. We note that such an assumption is invalid for the one domain system whenever the internal seiche motion is damped predominantly by the internal friction. It appears that their semi-theoretical argument is suitable for explaining the decay of the internal seiche motion in the two-layered two domain system in the presence of bottom friction.

From Figure 5.5, it is apparent that the time variation of the layer-mean velocities also exhibits oscillations of the internal seiche period particularly at the surface and bottom layers, and that the influence of the change in N_P upon the decay of the oscillations is similar to that of the interfacial displacements. In the one domain system the damping of the oscillations in the surface and bottom layers is significantly increased as the value of N_P is increased, while in the two domain system the damping of the oscillations is increased marginally. We note that the oscillations at the surface layer and at the pycnocline each show a phase difference of 180° with the oscillation at the bottom layer and with $N_P = 10\ cm^2 s^{-1}$, the time variation similar to that for a square-wave appears within the pycnocline. The square wave-like variation of $\overline{U}_P$ is due to the presence of a modulation, with a period about three times larger than that of the internal seiche motion, superimposed on the periodic internal seiche motion. Comparing Figure 5.5 with Figures 5.3 and 5.4, we note that the period of the modulation is roughly the same time that the interface takes to reach the equilibrium level. The decay of the modulation is significantly slower in the two domain system compared with that in the one domain system. The layer-mean velocities tend to converge to zero as time goes by, which indicates the formation of a steady cell-like circulation within each layer. In a steady state the flow field is composed of the wind driven clockwise circulation in the surface layer, the anticlockwise circulation within the pycnocline and the clockwise circulation in the bottom layer (Davies, 1983*a*).

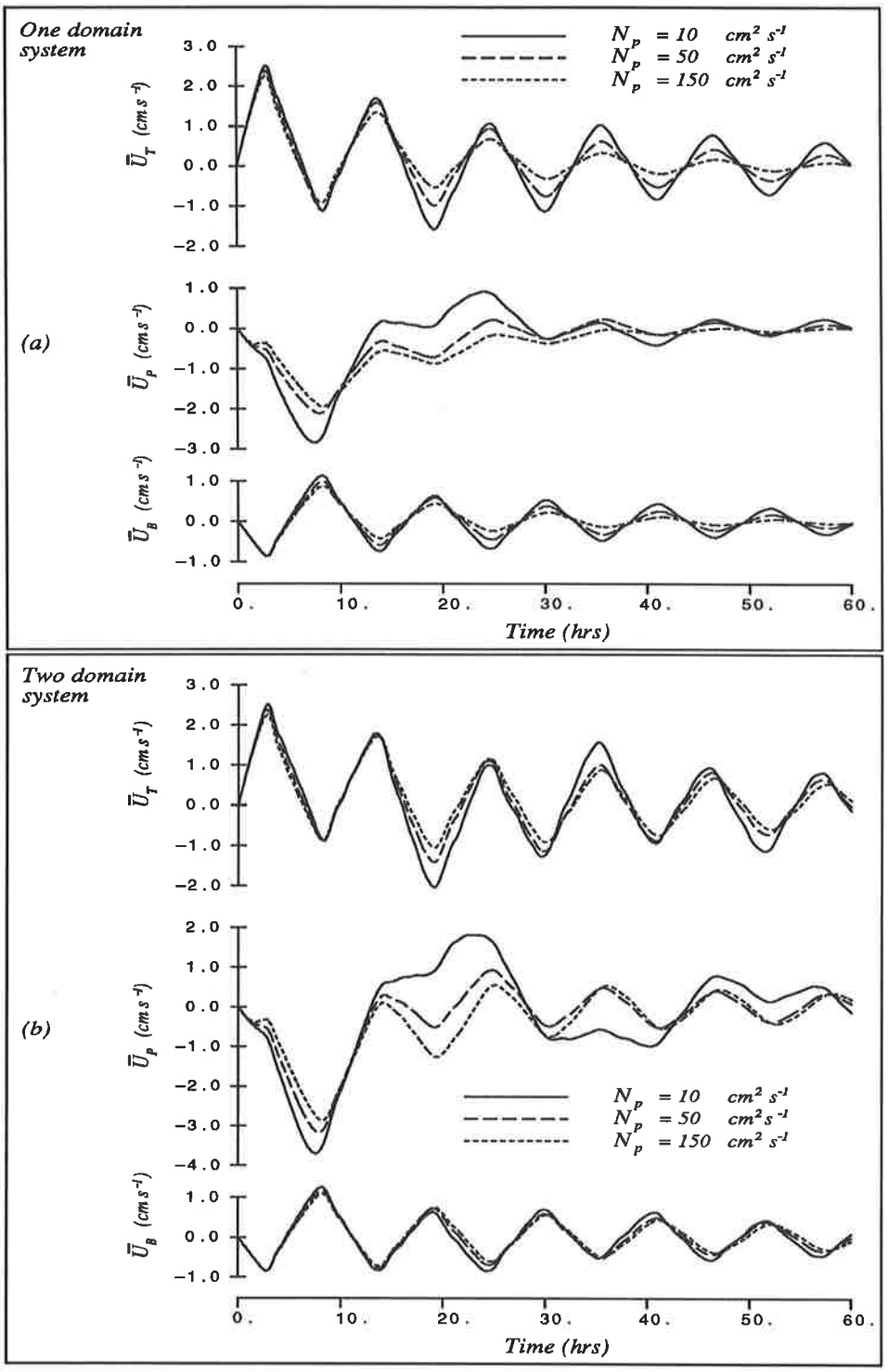

Figure 5.5 Time variation of $\overline{U}_T$, $\overline{U}_P$ and $\overline{U}_B$ (at center point A in Figure 5.1) of three-layered one and two domain systems, obtained using the profile in Figure 3.1(*d*), computed using a basis set of *B*-splines. A coarse grid with $\Delta x = 1425\,m$ was used with: Δ_T=25, Δ_P=15, Δ_B=60 m; ρ_T=1025.8, ρ_P=1026.5, ρ_B=1027.2 $g\,cm^{-3}$; N_T=300, N_B=100 $cm^2 s^{-1}$ and k_b=0.2 $cm\,s^{-1}$.

Without presenting detailed results, we briefly comment on the sensitivity of the interfacial displacements and of the layer-mean velocity within the pycnocline to changes in the value of N_T in the three-layered systems. Calculations (computed using $N_P = 10\ cm^2 s^{-1}$ with the layer thickness and depth variation of the density used in Figure 5.5) showed that increasing N_T from 150 to 1000 $cm^2 s^{-1}$ reduced the mean values of the downward displacement of $\zeta_{0,1}$ and the upward displacement of $\zeta_{0,2}$ by approximately $50\,cm$ in both one and two domain systems. The effect of changing N_T upon the decay of the internal seiche motion is relatively small unless the ratio of the surface layer thickness to total depth is substantially increased or the value of N_T is extremely large. Decreasing N_T initially enhances the layer-mean velocity within the pycnocline. However, calculations with $N_T = 150\ cm^2 s^{-1}$ showed that after the interface reaches its equilibrium level the effect of changing N_T upon the layer-mean velocities becomes insignificant.

Figure 5.6 shows the current profiles computed using a basis set of B-spline functions at $t = 2.82$, 8.28 and 19.56 hrs. At $t = 2.82\ hrs$ the mean current velocity at the surface layer is at its maximum in the direction of the wind stress. At $t = 8.28\ hrs$ the mean current velocities at the pycnocline intensify to a maximum in the direction opposite to the wind stress and this maximum occurs at $t = 19.56$ hrs for the mean current velocity at the surface layer (see Figure 5.5). It is noticeable that at the pycnocline of the one domain system, a conspicuous return flow of jet-like nature appears at $t = 8.28\ hrs$. In the two domain system the return flow does not show a jet-like behaviour because it is not frictionally retarded at the base of the pycnocline. It has been revealed in a series of computations that the layer-mean velocities within the pycnocline are comparatively insensitive to the value of N_T, although current profiles show much more sensitivity to changes in the value of N_T (compare Figure 5.6(c) and (d)).

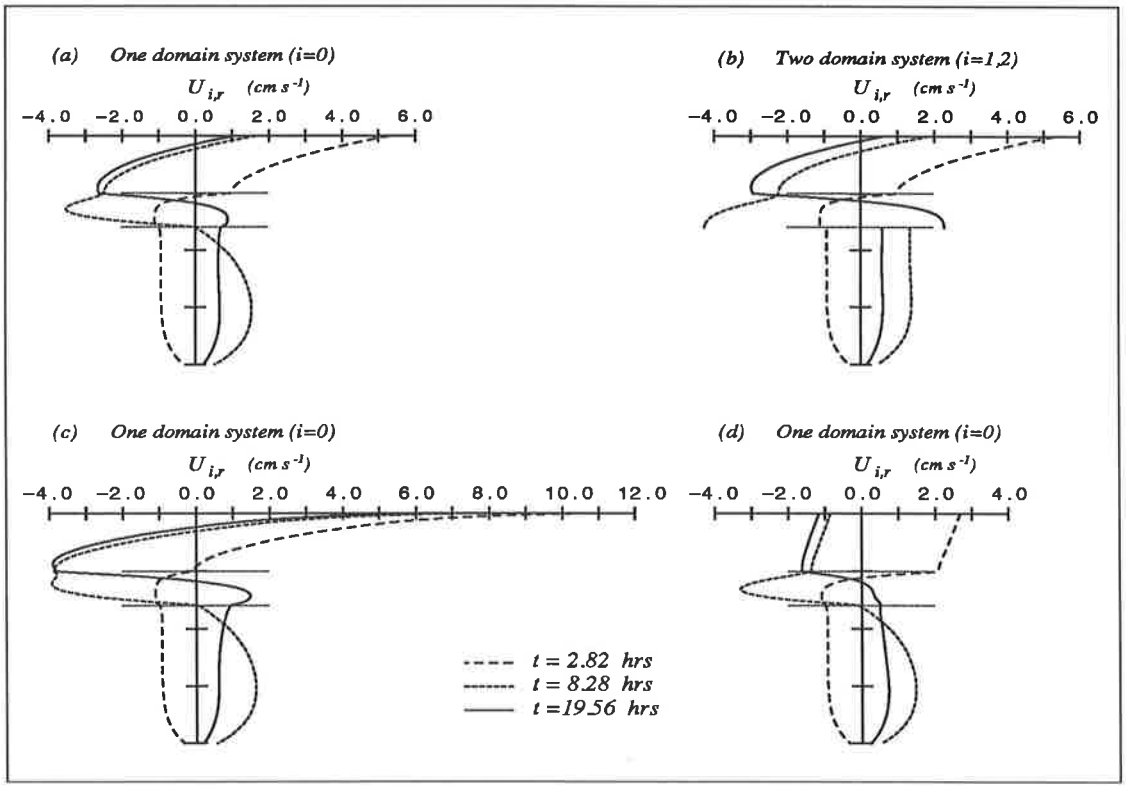

Figure 5.6 Vertical profiles at t=2.82, 8.28 and 19.56 *hrs* (at centre point A in Figure 5.1) of three-layered one and two domain systems, obtained using the profile in Figure 3.1(d), computed using a basis set of B-splines. A coarse grid with $\Delta x = 1425\,m$, is used with Δ_T=25, Δ_P=15, Δ_B=60 m; ρ_T=1025.8, ρ_P=1026.5, ρ_B=1027.2 $g\,cm^{-3}$; and (a) N_T=300, N_P=50, N_B=100 $cm^2 s^{-1}$ with m_0=18; (b), N_T=300, N_P=50, N_B=100 $cm^2 s^{-1}$ with m_1=15 and m_2=6; (c) N_T=150, N_P=10, N_B=100 $cm^2 s^{-1}$ with m_0=18; (d) N_T=1000, N_P=10, N_B=100 $cm^2 s^{-1}$, with m_0=18.

The current profiles shown in Figure 5.7 are computed using a basis set of eigenfunctions with $m_i = 5$ and 20. It is evident that nonphysical oscillations appear in the two domain system when a small number of eigenfunctions is used. In contrast to the two domain system, solutions of the one domain system do not exhibit oscillations even with $m_0 = 5$. With a small number of eigenfunctions, the compatibility between the form of the first few eigenfunctions and the current profiles within the pycnocline, rather than the discontinuity of the eigenfunctions, is critical in determining whether Gibbs phenomena arise. With a value of $\beta_{i,1} = 0$,

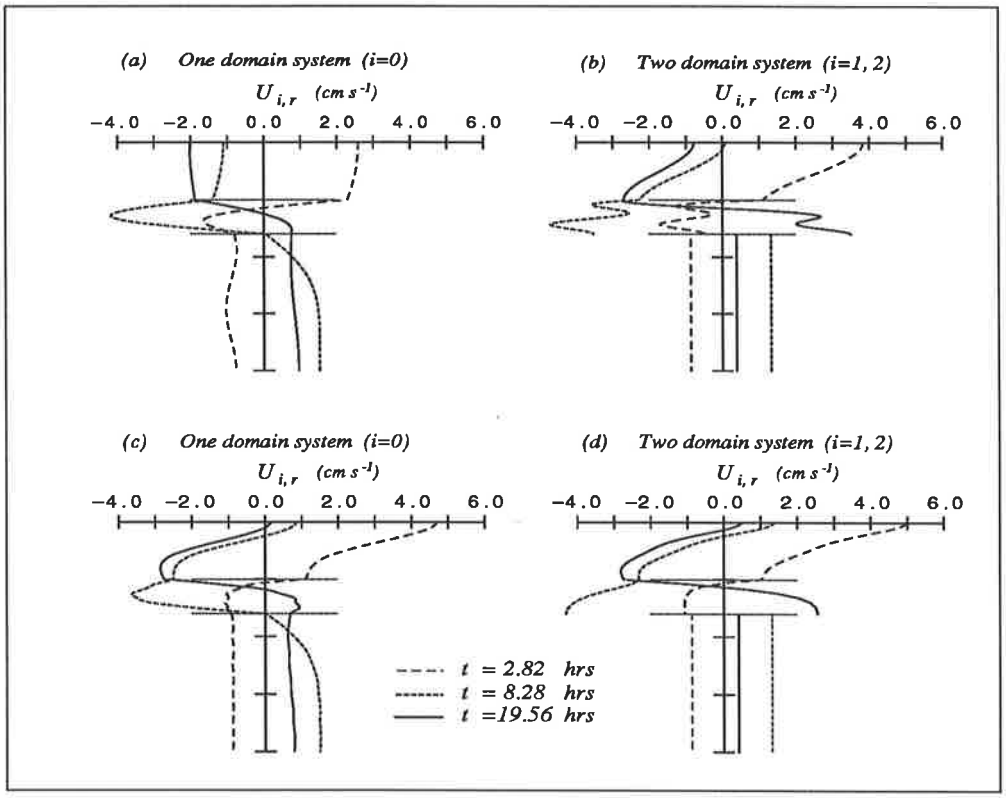

Figure 5.7 Vertical profiles at t=2.82, 8.28 and 19.56 *hrs* (at centre point A in Figure 5.1) of three-layered one and two domain systems, obtained using the profile in Figure 3.1(*d*), computed using a basis set of eigenfunctions. A coarse grid with $\Delta x = 1425\,m$, is used with: Δ_T=25, Δ_P=15, Δ_B=60 m; ρ_T=1025.8, ρ_P=1026.5; ρ_B=1027.2 $g\,cm^{-3}$; N_B=100 $cm^2 s^{-1}$; k_b=0.0 $cm\,s^{-1}$; and (*a*) N_T=300, N_P=10 $cm^2 s^{-1}$ with m_0=5; (*b*) N_T=300, N_P=50 $cm^2 s^{-1}$ with m_1=5 and m_2=1; (*c*) as in (*a*) but with m_0=20; (*d*) as in (*b*) but with m_1=20.

as noted in Chapter 4, the surface current is significantly underestimated. However, a set of preliminary calculations have revealed that the layer-mean velocities were reproduced accurately. Furthermore, the presence of Gibbs overshoots was not a serious problem as far as the accuracy of the layer-mean velocities is concerned. In the current profile computed using a basis set of B-spline functions (Figure 5.6), there was no evidence of spurious oscillations unless the number of B-splines is dramatically reduced and the knots of B-spline functions are poorly-

distributed.

We now consider the time variations of the first few vertical modes at the centre point B shown in Figure 5.1. A series of calculations were performed on a coarse grid system with $k_b = 0.0$ and $1.0\ cm\ s^{-1}$. The eddy viscosity at the surface layer N_T was fixed at 300 $cm^2 s^{-1}$, and N_B at 100 $cm^2 s^{-1}$, while N_P took two values, namely 150 and 10 $cm^2 s^{-1}$. It is evident that reducing N_P complicates the time variations of the first few vertical modes particularly in the two domain system. Preliminary computations showed that the time variation of the modal coefficients in the two-layered one domain system ($N_T = 300$, $N_B = 100\ cm^2 s^{-1}$ with $\Delta_T = 40$, $\Delta_B = 60\ m$) was not much different from Figure 5.8(a). The time behaviour of the modal coefficients in the two-layered two domain system was very similar to that in open sea regions described in Chapter 4.

From Figure 5.8 we note that decreasing the value of N_P greatly increases the contribution of the vertical modes $\widehat{A}_{0,3}$, $\widehat{A}_{0,4}$ in the one domain system, and $\widehat{A}_{1,2}$, $\widehat{A}_{1,3}$ in the two domain system, which are associated with the growth of the return flow (compare these figures with Figure 5.5). This point has also been noted by Davies (1983a). It is again evident that the internal seiche motion with a period of approximately 12 hrs is primarily associated with $\widehat{A}_{0,2}$ in the one domain system and with $\widehat{A}_{1,1}$ and $\widehat{A}_{2,1}$ in the two domain system. One would imagine that the time behaviour of the first two vertical modes in the two domain system ($\widehat{A}_{1,1}$ and $\widehat{A}_{2,1}$) is similar, as a whole, to that of the second mode in the one domain system. Furthermore, the time variations of $\widehat{A}_{1,2}$ and $\widehat{A}_{1,3}$ resemble those of $\widehat{A}_{0,3}$ and $\widehat{A}_{0,4}$, respectively. We note that $\widehat{A}_{0,5}$ and $\widehat{A}_{0,6}$ are significantly affected by the bottom friction. For the two domain system the effect of the bottom friction is gradually reduced as the mode number is increased. Although results are not plotted here, the first vertical modes $\widehat{A}_{2,1}$ and $\widehat{A}_{1,1}$ were 180° out of phase with each other and the magnitude of $\widehat{A}_{2,1}$ was approximately equal to $-(H_1/H_2)\widehat{A}_{1,1}$. In the bottom

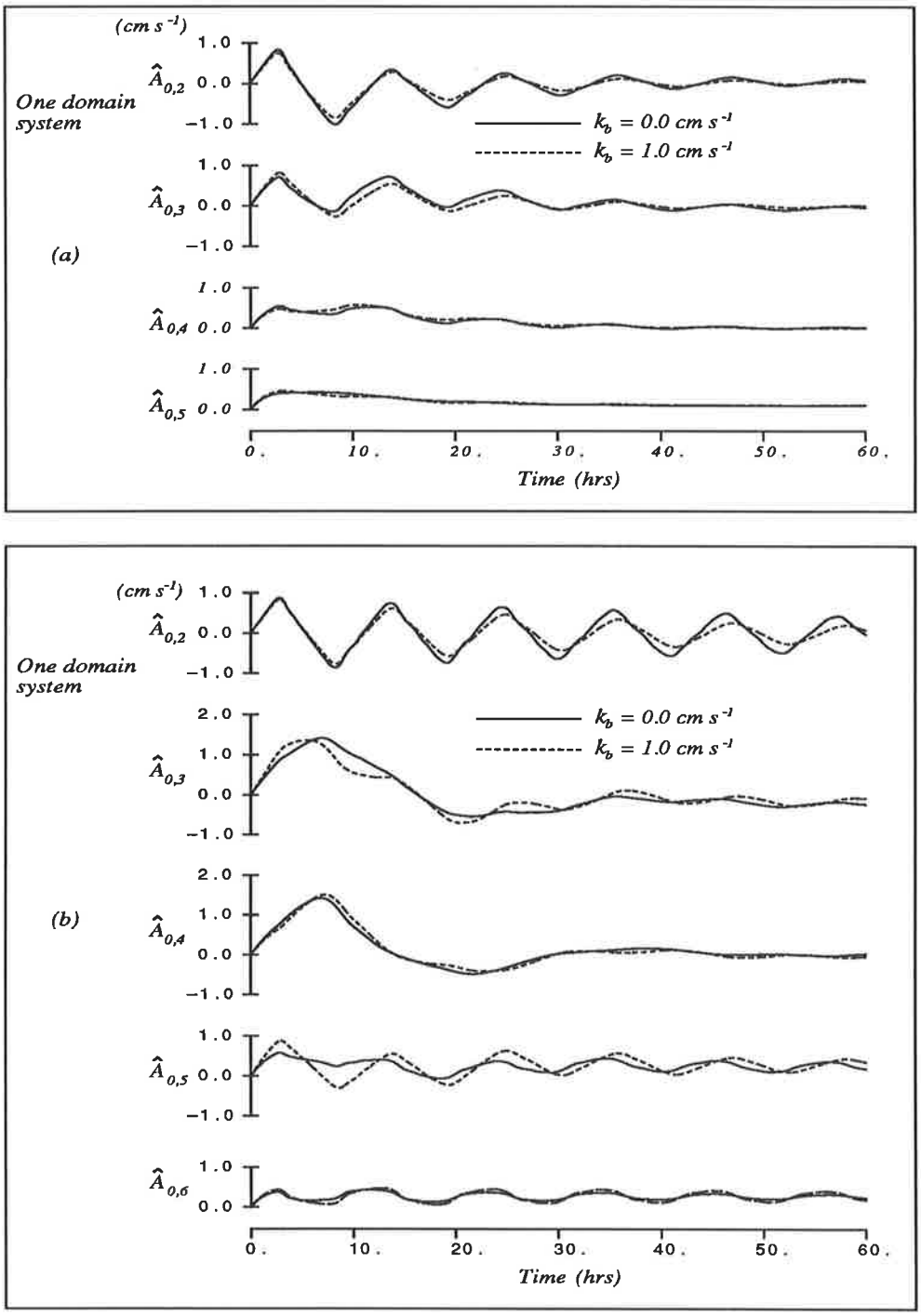

Figure 5.8 Time variations of the various vertical modes (at centre point A in Figure 5.1) induced by a step-function wind stress. A coarse grid with Δx=1425m was used with: Δ_T=25, Δ_P=15, Δ_B=60 m; ρ_T=1025.8, ρ_P=1026.5, ρ_B=1027.2 $g\,cm^{-3}$; $\beta_{0,1} = \beta_{0,2}$ =0; N_T =300, N_B =100 $cm^2 s^{-1}$; and $(a),(c)$ N_P =150 $cm^2 s^{-1}$; $(b),(d)$ N_P =10 $cm^2 s^{-1}$.

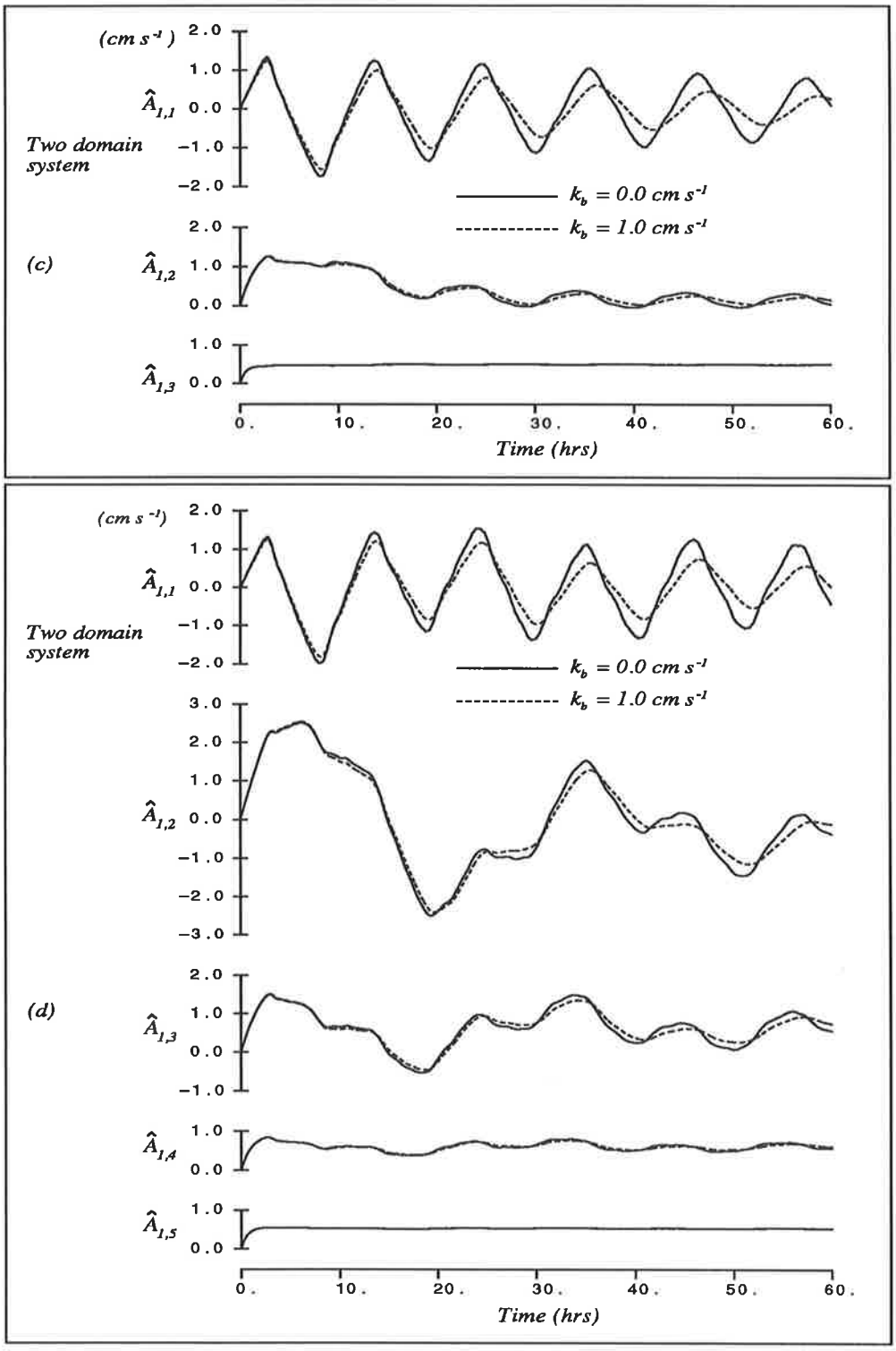

Figure 5.8 Cont'd.

layer of the two domain system the imposition of zero bottom friction excites the first vertical mode only, producing the uniform profile throughout the domain (see Figure 5.7). In the upper domain all vertical modes are excited, thereby producing the depth variation of the current.

In the following, the excitation of the free modes is analysed for a two-layer two domain system. Assuming that the water, initially at rest, is subjected to a wind stress of the form

$$\tau_{sx} = H(t)\tau_n \sin\Big(\frac{n\pi x}{L}\Big), \tag{5.3.5}$$

then the corresponding expressions for the free surface, the interface and the U component of the current satisfying the lateral boundary condition (5.2.3), may be written as

$$\zeta_{1,0} = Z_{1,0}\cos\big(\frac{n\pi x}{L}\big), \quad \zeta_{2,0} = Z_{2,0}\cos\big(\frac{n\pi x}{L}\big), \tag{5.3.6}$$

$$U_{1,1} = \widehat{U}_{1,1}\sin\big(\frac{n\pi x}{L}\big), \quad U_{2,1} = \widehat{U}_{2,1}\sin\big(\frac{n\pi x}{L}\big). \tag{5.3.7}$$

A linear slip condition of the following form is enforced at $\sigma_2 = 1$:

$$-\frac{\alpha_2\mu_{2,1}}{H_2}\frac{\partial U_{2,1}}{\partial\sigma_2} = \tilde{k}_b\overline{U}_B, \tag{5.3.8}$$

where the coefficient $\tilde{k}_b$ is in general different from k_b.

Substituting (5.3.5) to (5.3.7) into (5.1.1) to (5.1.4) yields

$$\frac{\partial\widehat{U}_{1,1}}{\partial t} = \frac{n\pi g}{L}Z_{1,0} + \frac{\alpha_1\mu_{1,1}}{H_1^2}\frac{\partial^2\widehat{U}_{1,1}}{\partial\sigma_1^2}, \tag{5.3.9}$$

$$\frac{n\pi H_1}{L}\int_0^1 \widehat{U}_{1,1}d\sigma_1 + \frac{dZ_{1,0}}{dt} - \frac{dZ_{2,0}}{dt} = 0, \tag{5.3.10}$$

$$\frac{\partial\widehat{U}_{2,1}}{\partial t} = \frac{n\pi g}{L}\frac{\rho_{1,1}}{\rho_{2,1}}Z_{1,0} + \frac{n\pi g}{L}\Big(1-\frac{\rho_{1,1}}{\rho_{2,1}}\Big)Z_{2,0} + \frac{\alpha_2\mu_{2,1}}{H_2^2}\frac{\partial^2\widehat{U}_{2,1}}{\partial\sigma_2^2}, \tag{5.3.11}$$

$$\frac{n\pi H_2}{L}\int_0^1 \widehat{U}_{2,1}d\sigma_2 + \frac{dZ_{2,0}}{dt} = 0. \tag{5.3.12}$$

Expanding $\widehat{U}_{i,1}$ in terms of the coefficients $\widehat{A}_{i,1}(t)$ and the eigenfunctions $f_{i,r}(\sigma_i)$ gives

$$\widehat{U}_i(\sigma_i,t)=\sum_{r=1}^{m_i}\widehat{A}_{i,r}(t)\Phi_{i,r}f_{i,r}(\sigma_i), \tag{5.3.13}$$

where the coefficients $\widehat{A}_{i,r}$, $i=1,2$, are to be determined. With the use of homogeneous limit conditions the spectral formulation of (5.3.9) to (5.3.12) becomes

$$\frac{d\widehat{A}_{1,k}}{dt}=\frac{n\pi g}{L}Z_{1,0}\,a_{1,0,k}+\frac{\tau_n}{\rho_{1,1}H_1}-\lambda_{1,k}\frac{\alpha_1}{H_1^2}\widehat{A}_{1,k}, \tag{5.3.14}$$

$$\frac{n\pi H_1}{L}\widehat{A}_{1,1}+\frac{dZ_{1,0}}{dt}-\frac{dZ_{2,0}}{dt}=0, \tag{5.3.15}$$

where $k=1,\cdots,m_1$, and

$$\begin{aligned}\frac{d\widehat{A}_{2,k}}{dt}=&-\lambda_{2,k}\frac{\alpha_2}{H_2^2}\widehat{A}_{2,k}-\tilde{k}_b\widehat{A}_{2,1}\\&+\frac{n\pi g}{L}\Big(\frac{\rho_{1,1}}{\rho_{2,1}}\Big)Z_{1,0}\,a_{2,0,k}+\frac{n\pi g}{L}\Big(1-\frac{\rho_{1,1}}{\rho_{2,1}}\Big)Z_{2,0}\,a_{2,0,k},\end{aligned} \tag{5.3.16}$$

$$\frac{n\pi H_2}{L}\widehat{A}_{2,1}+\frac{dZ_{2,0}}{dt}=0, \tag{5.3.17}$$

where $k=1,\cdots,m_2$. The presence of internal friction ensures the damping of the higher vertical modes in both the upper and lower domains, hence we consider the first vertical mode only. The linear system described by equations (5.3.14) to (5.3.17) admits the matrix representation

$$\widehat{\mathbf{W}}^{\bullet}=\mathbf{\Gamma}\widehat{\mathbf{W}}+\mathbf{F}, \tag{5.3.18}$$

where

$$\mathbf{\Gamma}=\begin{pmatrix}0&0&-H_1\frac{n\pi}{L}&-H_2\frac{n\pi}{L}\\0&0&0&-H_2\frac{n\pi}{L}\\g\frac{n\pi}{L}&0&0&0\\g\frac{\rho_{1,1}}{\rho_{2,1}}\frac{n\pi}{L}&g\Big(1-\frac{\rho_{1,1}}{\rho_{2,1}}\Big)\frac{n\pi}{L}&0&-\tilde{k}_b\end{pmatrix}, \tag{5.3.19}$$

$$\widehat{\mathbf{W}}^{\bullet} = \begin{pmatrix} \frac{dZ_{1,0}}{dt} \\ \frac{dZ_{2,0}}{dt} \\ \frac{d\widehat{A}_{1,1}}{dt} \\ \frac{d\widehat{A}_{2,1}}{dt} \end{pmatrix}, \qquad \widehat{\mathbf{W}} = \begin{pmatrix} Z_{1,0} \\ Z_{2,0} \\ \widehat{A}_{1,1} \\ \widehat{A}_{2,1} \end{pmatrix}, \qquad \mathbf{F} = \begin{pmatrix} 0 \\ 0 \\ \tau_n(\rho_{1,1}H_{1,1})^{-1} \\ 0 \end{pmatrix}. \tag{5.3.20}$$

As seen in Chapter 4, the excitation of the undamped free modes will depend upon the nature of the eigenvalues of $\mathbf{\Gamma}$. If the real parts of eigenvalues are all positive, then all of the excited modes will converge to steady state values.

The eigenvalues ϵ are found from the characteristic equation, $det(\mathbf{\Gamma} - \epsilon\mathbf{I}) = 0$. Considering the case $\tilde{k}_b = 0$; the characteristic equation is

$$\begin{aligned} &det(\mathbf{\Gamma} - \epsilon\mathbf{I}) \\ &\quad = \epsilon^4 + \frac{gn^2\pi^2}{L^2}(H_1 + H_2)\epsilon^2 + g^2H_1H_2\Big(1 - \frac{\rho_{1,1}}{\rho_{2,1}}\Big)\frac{n^4\pi^4}{L^4} \\ &\quad = (\epsilon^2 + \kappa_1^2)(\epsilon^2 + \kappa_2^2) = 0 \end{aligned} \tag{5.3.21}$$

where

$$\left.\begin{matrix} k_1^2 \\ k_2^2 \end{matrix}\right\} = \frac{1}{2}\Big(\frac{n\pi}{L}\Big)^2 g\Big\{(H_1 + H_2) \pm [(H_1 + H_2)^2 - 4H_1H_2(1 - \frac{\rho_{1,1}}{\rho_{2,1}})]^{1/2}\Big\}. \tag{5.3.22}$$

The presence of the undamped motion is then obvious. Note that these solutions are equivalent to simple poles when the Laplace transform is applied (Heaps, 1966, p.51). Since $(1 - \rho_{1,1}/\rho_{2,1})$ is very small, it follows that, to a first approximation,

$$T_1 = \frac{2L}{n}\big[g(H_1 + H_2)\big]^{-1/2}, \qquad T_2 = \frac{2L}{n}\Big[g\frac{\rho_{2,1} - \rho_{1,1}}{\rho_{2,1}}\frac{H_1H_2}{H_1 + H_2}\Big]^{-1/2}, \tag{5.3.23}$$

which are the periods of the surface and internal seiches, respectively, driven by τ_n (Heaps, 1966). The eigenvalues of the characteristic modes for a non-zero value of $\tilde{k}_b$ can be found from Heaps (1966).

The one domain system can be analysed in a similar way. For simplicity, consider the homogeneous system with $\tilde{k}_b = 0$. Again spectral solutions of the system admits the matrix representation

$$\widehat{\mathbf{W}}^{\bullet} = \mathbf{\Gamma}\widehat{\mathbf{W}} + \mathbf{F}, \tag{5.3.24}$$

where

$$\mathbf{\Gamma} = \begin{pmatrix} 0 & -H_0 \frac{n\pi}{L} \\ g\frac{n\pi}{L} & 0 \end{pmatrix}, \tag{5.3.25}$$

and

$$\widehat{\mathbf{W}}^{\bullet} = \begin{pmatrix} \frac{dZ_{0,1}}{dt} \\ \frac{d\widehat{A}_{0,1}}{dt} \end{pmatrix}, \quad \widehat{\mathbf{W}} = \begin{pmatrix} Z_{0,1} \\ \widehat{A}_{0,1} \end{pmatrix}, \quad \mathbf{F} = \begin{pmatrix} 0 \\ \tau_n(\rho_{0,1}H_{0,1})^{-1} \end{pmatrix}. \tag{5.3.26}$$

Since the characteristic values are purely imaginary, namely

$$\epsilon_0 = \pm\iota(gH_0)^{1/2}\left(\frac{n\pi}{L}\right), \tag{5.3.27}$$

the first vertical mode is undamped.

The analysis of the three-layer system is much more complicated and is not described here. However, we note that the presence of the undamped mode depends upon whether or not the first vertical mode is coupled with the higher modes through the equation of continuity. If they are coupled, then the internal friction for the higher modes damps the first vertical mode. In general, the contribution of the higher vertical modes in the equation of continuity is comparatively small, that is, $|a_{1,0,r}| << |a_{1,0,1}|$ for all $r > 1$. Therefore the first two vertical modes ($\widehat{A}_{1,1}$ and $\widehat{A}_{2,1}$) exhibit weakly-decaying oscillations. For similar reasons the first vertical mode of the three-layered one domain system is damped in the absence of bottom friction.

To conclude this chapter and, at the same time, to present the results of a final set of numerical experiments in this thesis, the influence of the changes in density

upon the interfacial displacements in the three-layered system is considered. In layered models the continuous depth variation of the density field is represented by a stack of discrete homogeneous layers. It is well-known that such an approximation can produce considerable errors in determining interfacial displacements (up to 10 % according to Davies (1982*b*)) unless a large number of layers is used. Due to this shortcoming, layered models have to be calibrated in real applications, by modifying the density and/or the thickness of the layers.

Figure 5.9 shows how sensitive the damping of the interfacial displacements is to the variation in density. In the calculations of the two-layered systems, $\rho_{i,1}$ is taken as 1025.8, 1026.1 and 1026.3 $g\,cm^{-3}$, and $\rho_{i,2}$ is fixed at 1027.0 $g\,cm^{-3}$, whereas in the calculations for the three-layered systems, $\rho_{i,2}$ is taken as 1026.3, 1026.5 and 1026.7 $g\,cm^{-3}$, while $\rho_{i,1}$ and $\rho_{i,3}$ are fixed at 1025.8 and 1027.2 $g\,cm^{-3}$, respectively. It is evident that the phase and amplitude of the internal seiche motion are significantly affected by the changes in density. Given the two-layered system (Figures 5.9(*a*) and (*b*)), we note that increasing $\rho_{i,2}$ from 1025.8 to 1026.3 $g\,cm^{-3}$ (and so reducing the difference in density between the upper and lower layers) gives rise to an increase in the wavelength and the amplitude of the internal seiche motion. The mean values of the interfacial displacements are also affected in both systems but in different ways: for the one domain system the peaks of the maxima and minima are displaced downwards, whereas for the two domain system the peaks of the minima are displaced downwards while the peaks of the maxima remain almost at the same level. Calculations using the three-layered system also exhibit changes in the wavelength and amplitude of the internal seiche motion. With the change of $\rho_{i,2}$ in the three-layered system, changes in the mean value of $\zeta_{i,1}$ were particularly significant. The principle effect of decreasing $\rho_{i,2}$ from 1.0267 to 1.0263 $g\,cm^{-3}$ (and hence reducing the difference in the density between the surface layer and the pycnocline) is the increase of the downward displacement of the mean value of $\zeta_{i,1}$. With $N_P = 10\ cm^2 s^{-1}$, the

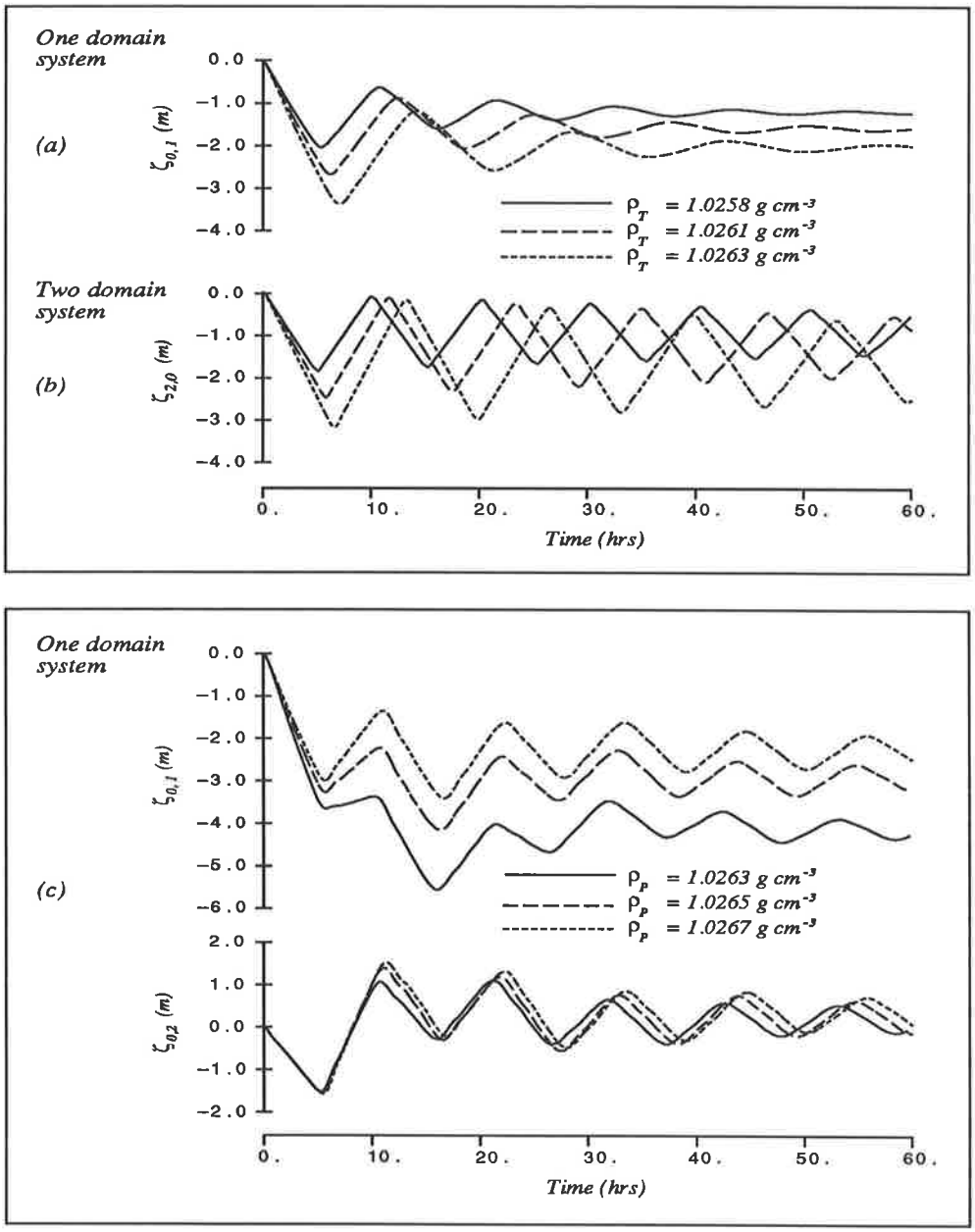

Figure 5.9 Time variation of interfacial displacements (at corner point B in Figure 5.1) of three-layered one and two domain systems computed using a basis set of B-splines. Computed om a finer grid with Δx=475 m, with: k_b=0.2 $cm\,s^{-1}$, and $(a)(b)$ Δ_T=40, Δ_B=60 m; N_T =300, N_B =100 $cm^2 s^{-1}$; ρ_T=1025.8, ρ_T=1026.1, ρ_T=1026.3 and ρ_B=1027.0 $g\,cm^{-3}$ with the profile in Figure 3.1(c). Computed on a coarse grid with Δx=1425 m, with k_b=0.2 $cm\,s^{-1}$; (c) Δ_T=25, Δ_P=15, Δ_B=60 m; N_T =300, N_P =10, N_B =100 $cm^2 s^{-1}$; ρ_T=1025.8, ρ_B=1027.2 and ρ_P=1026.3, 1026.5, 1026.7 $g\,cm^{-3}$ with the profile Figure 3.1(d); (d) as in (c) but with N_P =150; (e) as in (c).

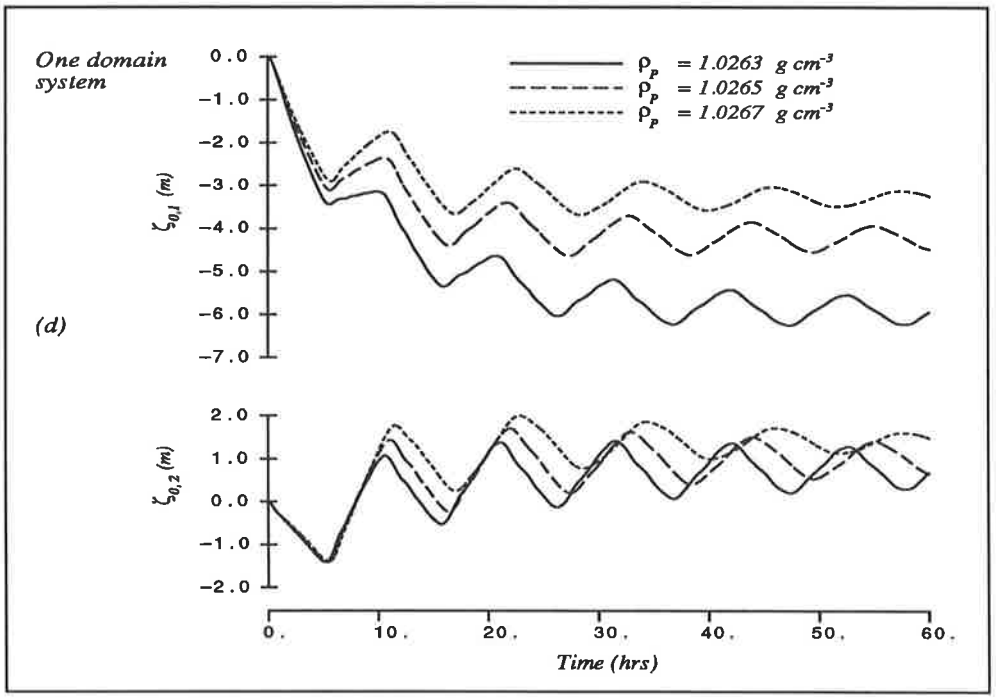

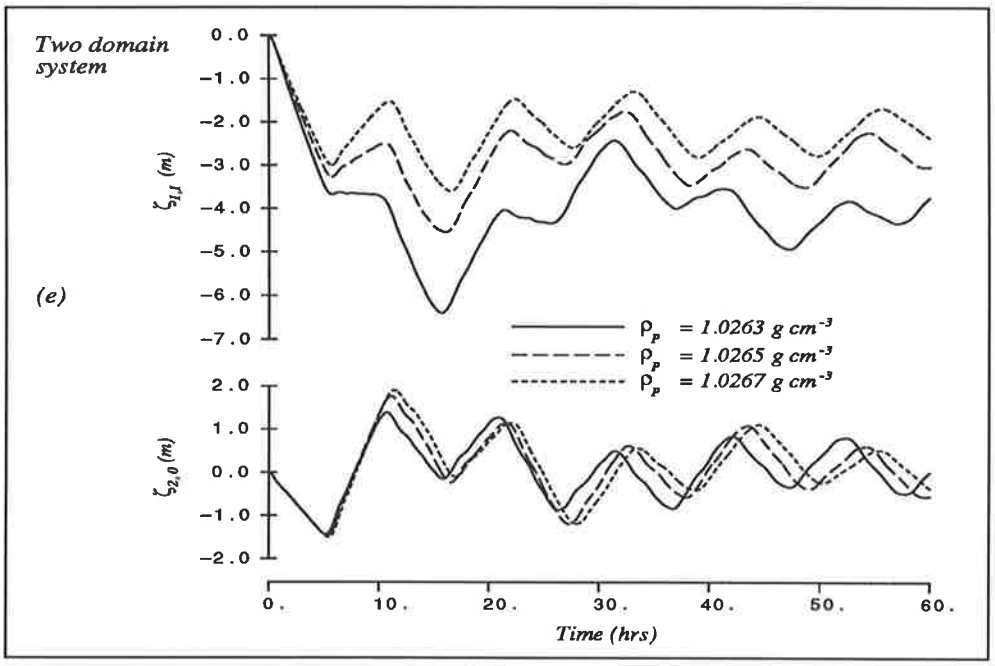

Figure 5.9 Cont'd.

lower surface of the pycnocline was significantly less affected in both one and two domain systems. However, as the value of N_P is increased to 150 $cm^2 s^{-1}$ the effect of the density variations upon the mean displacement of $\zeta_{2,0}$ becomes apparent (Figure 5.9(d)). The effects of density variations upon the interfacial displacements of the three-layered two domain system are quite similar to those of the one domain system but as the value of $\rho_{1,2}$ is reduced, a modulation seems to appear in the time variation of $\zeta_{1,1}$ (Figure 5.9(d)).

In calculations using a Galerkin model accounting for a continuously stratified sea, Davies (1982b) showed that the jet-like return flow within the pycnocline is developed primarily due to the reduction of the eddy viscosity there. The sensitivity of the layered model to the depth variation of the density leads to a slightly different interpretation. Figure 5.10 indicates that in layered models the intensity of the return flow can be significantly enhanced by the density variation particularly when the value of N_P is low (Figure 5.10(a)). As the value of N_P is increased from 10 to 150 $cm^2 s^{-1}$, the intensity of the return flow is substantially reduced (Figure 5.10(b)). Although results are not plotted here, the use of a stress-free condition at the base of the pycnocline further enhances the transport through the return flow. However, as seen in Figure 5.6 the return flow in the two domain system does not take a jet-like form. Calculations also show that as the return flow within the pycnocline intensifies the oscillations of the current at the surface layer are enhanced, whilst the magnitude of the layer-mean velocity in the bottom layer is not affected much by the change in ρ_P.

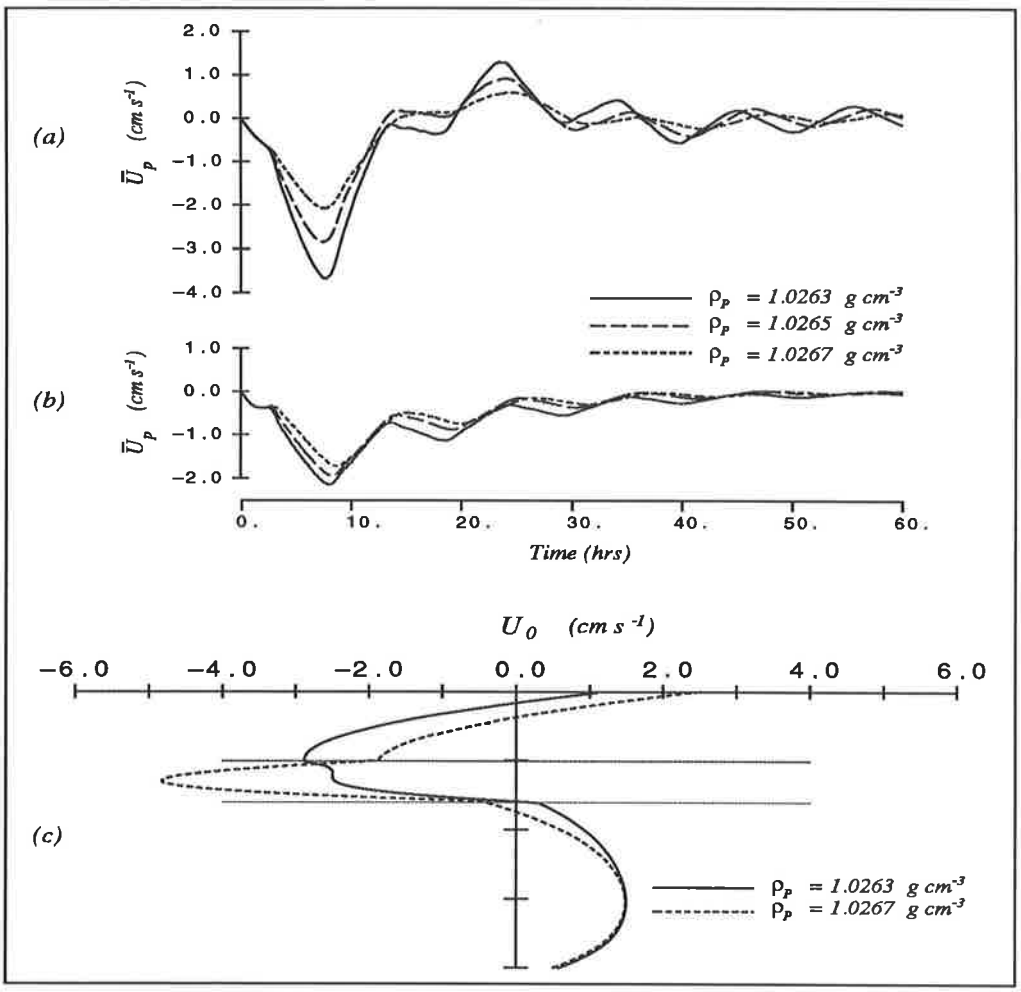

Figure 5.10 Time variation of $\overline{U}_P$ (at centre point A in Figure 5.1) and vertical variations of current at t=8.28 *hrs* (at corner point B in Figure 5.1) in a three-layered one domain system (with the profile in Figure 3.1(*d*)) computed using a basis set of B-splines. A coarse grid with $\Delta x = 1425\,m$ was used with: Δ_T=25, Δ_P=15, Δ_B=60 m; N_T=300, N_B=100 $cm^2 s^{-1}$; k_b=0.2 $cm\,s^{-1}$; ρ_T=1025.8, ρ_B=1027.2 $g\,cm^{-3}$; and (*a*) N_P=10 $cm^2 s^{-1}$ and ρ_P=1026.3, 1026.5, 1026.7 $g\,cm^{-3}$; (*b*) as in (*a*) but with N_P=150 $cm^2 s^{-1}$; (*c*) as (*a*) but with N_P=10 $cm^2 s^{-1}$ and ρ_P=1026.3, 1026.7 $g\,cm^{-3}$.

CHAPTER 6

CONCLUSION

A series of calculations for idealised situations involving wind induced flows in stably stratified waters has been performed to obtain an understanding of the vertical structures of these flows. The models used were layered and included a Galerkin-finite element model with a basis set of B-spline functions and a Galerkin-spectral model with a basis set of numerically determined eigenfunctions. It was found that the Galerkin-finite element model accurately portrays the vertical structure of wind-induced motion in stably stratified flows, while the Galerkin-spectral model efficiently portrays the physics of the motion. Interactive use of these two methods will be of great use in improving insight into stratified flows when a well-formed layered system can be assumed and the vertical structure of eddy viscosity is time-invariant.

The models can cope with arbitrary variation of the vertical eddy viscosity within each layer and, in theory, the vertical eddy viscosity profile with any form of discontinuities can be prescribed at *any* level of the water column. Obviously, increased flexibilty of the model in incorporating local variation of eddy viscosity has advantages over analytical approaches such as in Heaps and Jones (1983, 1985). The model can allow for the effects of a wall boundary layer near the sea surface, smooth variation of eddy viscosity across the interfaces and the boundary layer near the sea bed. Furthermore, a calibration of the numerical model, which involves changing the eddy viscosity and thickness of the surface layer and the pycnocline, can be done in a flexible manner. Such calibration is inevitable

in practice, due to the uncertainty in choosing input parameters and dividing a hydrodynamic system into a finite number of homogeneous layers.

Attention was directed at comparing two interfacial conditions, the first being the continuity of horizontal current and shear stresses, and the second being the stress-free condition imposed tentatively at the base of the pycnocline which retards the downward penetration of wind energy. The assumption of a stress-free condition at the base of the pycnocline diversifies the dynamic response of wind-induced flows and through a series of experiments their use was found to be very encouraging in strongly stratified cases. The upper domain is driven by wind shear and body forces and the lower domain is essentially driven by body forces, although in a bounded region the two domains are coupled through the kinematic constraint of the velocity field. For realisation of the full potential of the stress-free interface condition, a set of numerical experiments is needed in two-dimensional basins in which the water body experiences rotational effects and lateral boundary constraints. In an open sea region a nondissipative free mode is excited in the absence of the bottom friction. In a stratified lake of finite length the excitation of a nondissipative free mode depends upon whether the nondissipative mode is coupled with the higher modes or not. The imposition of a stress-free bottom boundary condition in a two-layered two domain system excites the free mode. With the basis set of eigenfunctions, we have identified that contribution to the internal seiche motion in a stratified channel predominantly comes from the second vertical mode. In the two domain system the two first vertical modes act as a whole like the second mode of the one domain system.

The rate of convergence of the spectral method depends upon whether nonphysical oscillations arise as a consequence of the Gibbs phenomenon. It is known that classical continuous functions such as trigonometric functions, Chebyshev and Legendre polynomials, are all susceptible to internal discontinuity (Gottlieb and

Orszag, 1977). However, the cause of nonphysical oscillations is slightly different here because the eigenfunctions are discontinuously defined through a modal matching technique. We note that the presence of high-level background turbulence activity of tidal origin at the bottom layer is helpful in suppressing the Gibbs phenomenon. The compatibility of external boundary conditions and limit conditions for basis functions is also of importance in determining whether oscillations will be produced. The basis set of B-spline functions was accurate in reproducing surface currents and the high shear of the current within the pycnocline. By concentrating knots across the interfaces and high shear regions the rapid variation of the current profiles was accurately reproduced without any spurious numerical oscillations.

A two-layered model has been proposed for the study of the local generation of inertial motion driven by a local wind stress. As a major feature, the model incorporates the downward flux of wind energy through the base of the pycnocline and horizontal dissipation. The inertial motion in the surface layer can be modelled and calibrated in a realistic manner, taking into account local information available on stratification. The pycnocline acts as an energy absorber in controlling the damping of inertial motion along with the coefficients of horizontal dissipation and bottom friction. Results obtained in the study, such as the sensitivity of wind induced motion to changing the values of eddy viscosity, particularly within the pycnocline, the pycnocline thickness and the coefficients of interfacial friction, will serve as a valuable basis for realistic applications in the future.

Follow-up research will include modeling wind induced flows in two-dimensional horizontal or vertical planes in the presence of lateral boundaries and/or with non-uniform bottom topography. To solve fully three-dimensional equations a time-splitting and/or space-splitting technique (Heaps and Jones, 1983) may be required to reduce computational effort. Application to Bass Strait, as an ex-

tension of the previous studies based on depth-integrated homogeneous models (Fandry, 1982) and a three-dimensional finite difference model (Arnold and Noye, 1986), is particularly envisaged for the study of wind circulation during the period of summer stratification. Finally, the methodology used in this thesis can be applied to a wide range of problems including thermal exchanges between the soil and atmosphere and groundwater flows.

BIBLIOGRAPHY

Abbott, M.B., J.Aa. Bertelsen, A. Kej and I.R. Warren, 1975: Systems modeling of stratified fluids. In: *Symposium on modelling techniques*, **1**, *Proceedings of the 2nd Annual Symposium of Waterways, Harbors and Coastal Engineering Division*, *pp.* 605–624, published Am. Soc. Civil Engrs.

Abramowitz, M. and I.A. Stegun, 1970: *Handbook of mathematical functions.* Dover Publ. Inc., New York.

Arnold, R.J. and B.J. Noye, 1986: Open boundary conditions for a tidal and storm surge model of Bass Strait. In: *Computational Techniques and Applications: CTAC 85*, J. Noye and R.L. May (editors), *pp.* 503–518, North-Holland.

Axelsson, O. and V.A. Barker, 1984: *Finite element solution of boundary value problems: Theory and computation.* Academic press, 432 *p.*

Bennett, J.R., 1977: A three-dimensional model of Lake Ontario's summer circulation. I. Comparison with observations. *J. Phys. Oceanogr.*. **7**, 591–601.

Blumburg, A. and G.L. Mellor, 1980: A coastal ocean numerical model. In: *Mathematical modelling of estuarine physics*, J. Sündermann and K.-P. Holz (editors), *pp* 203–219, Springer-Verlag (Lecture Notes on Coastal and Estuarine Studies **1**).

Canuto, C., 1987: Topics in spectral methods for hyperbolic equations. In: *Partial differential equations of hyperbolic type and applications*, G. Geymonat (editor), *pp.* 1–32, World Scientific Publishing Co., Singapore.

Cheng, R.T., T.M. Powell and T.M. Dillon, 1976: Numerical models of wind-driven circulation in lakes, *Appl. Math. Modelling*, **1**, 141–159.

Clarke, D.J., 1974: Three-dimensional storm surge computations. *Geophys. J. R. astr. Soc.*, **39**, 195–199.

Cooper, C. K. and B. Pearce, 1977: A three-dimensional numerical model to calculate currents in coastal waters utilizing a depth varying vertical eddy viscosity. *Ralph M. Parsons Laboratory for Water Resources and Hydrodynamics*, Massachusetts Institute of Technology, Technical Report **226**, 147 *p.*

Cox, M.G., 1972: The numerical evaluation of B-splines. *J. Inst. Maths. Applics.*, **10**, 134–149.

Cox, M.G., 1975: An algorithm for spline interpolation. *J. Inst. Maths. Applics.*, **15**, 95–108.

Csanady, G.T., 1968: Motions in a model Great Lake due to a suddenly imposed wind. *J. Geophys. Res.*, **73**, 6435–6447.

Daddio, E., Wm J. Wiseman, Jr and S.P. Murray, 1978: Inertial currents over the inner shelf near 30°*N*. *J. Phys. Oceanogr.*, **8**, 728–733.

D'Alessio, A., P.L. De Angelis, A. Murli and M.A. Pirozzi, 1983: Numerical models for the simulation of currents in Naples gulf. *Mathematics and Computers in Simulation*, **25**, 436–451.

Davies, A.M., 1977*a*: A numerical investigation of errors arising in applying the Galerkin method to the solution of nonlinear partial differential equations. *Comp. Meth. Appl. Mech. Eng.*, **11**, 341–350.

Davies, A.M., 1977*b*: The numerical solution of the three-dimensional hydrodynamic equations using a *B*-spline representation of the vertical current profile. In: *Bottom Turbulence, Proceedings of the 8th Liege Colloquium on Ocean Hydrodynamics*, J.C.J. Nihoul (editor), *pp.* 1–25, published Elsevier Oceanography Series **19**.

Davies, A.M., 1977*c*: Three-dimensional model with depth-varying eddy viscosity. In: *Bottom Turbulence, Proceedings of the 8th Liege Colloquium on Ocean Hydrodynamics*, J.C.J. Nihoul (editor), *pp.* 27–48, published Elsevier Oceanography Series **19**.

Davies, A.M., 1978*a*: Application of the Galerkin method to the solution of Burgers' equation. *Comp. Meth. Appl. Mech. Eng.*, **14**, 305–321.

Davies, A.M., 1978*b*: The use of the Galerkin method with a basis set of *B*-splines for the solution of one-dimensional primitive equations. *J. Comp. Phys*, **27**, 123–137.

Davies, A.M., 1980*a*: On formulating a three-dimensional hydrodynamic sea model with an arbitrary variation of vertical eddy viscosity. *Comp. Meth. Appl. Mech. Eng.*, **22**, 187–211.

Davies, A.M., 1980*b*: Application of the Galerkin method to the formulation of a three-dimensional non-linear hydrodynamic sea model. *Appl. Math. Modelling*, **4**, 245–2561.

Davies, A.M, 1980*c*: Application of numerical models to the computation of the wind-induced circulation of the North Sea during JONSDAP'76. *Meteor*

Forsch.-Ergebnisse, **22**, 53–68.

Davies, A.M., 1981*a*: Three-dimensional hydrodynamic numerical models. Part 1. A homogeneous ocean-shelf model. Part 2. A stratified model of the northern North sea. In: *Proceedings of symposium on the Norwegian Coastal Currents*, held Geilo, Norway, Sep 1980, R. Saetre and M. Mork (editors), published Bergen University, 370–426 *p.*

Davies, A.M., 1981*b*: Three-dimensional modelling of surges. In: *Flood due to high winds and tides*, D.H. Peregrine (editor), *pp.* 45–74, Academic press, London.

Davies, A.M., 1982*a*: Formulating a three-dimensional hydrodynamic sea model using a mixed Galerkin-Finite difference method. In: *Proceedings of the 4th Int. Conf. on Finite elements in water resources*, held Hannover, 1982, K.-P. Holz. *et al.* (editors), *pp.* 5-27 to 5-41, Springer-Verlag.

Davies, A.M., 1982*b*: On computing the three-dimensional flow in a stratified sea using the Galerkin method, *Appl. Math. Modelling*, **6**, 347–362.

Davies, A.M., 1983*a*: Numerical modelling of stratified flow: a spectral approach. *Cont. Shelf Res.*, **2**, 275–300.

Davies, A.M., 1983*b*: Application of a Galerkin-eigenfunction method to computing currents in homogeneous and stratified seas. In: *Numerical Methods for Fluid Dynamics*, K.W. Morton and M.J. Bains (editors), *pp.* 287–301, Academic Press, London.

Davies, A.M., 1983*c*: Formulation of a linear three-dimensional hydrodynamic sea model using a Galerkin-eigenfunction method. *Int. J. Numer. Meth. Fluids*, **3**, 33–60.

Davies, A.M., 1985*a*: On determining the profile of steady wind induced currents. *Appl. Math. Modelling*, **9**, 409–418.

Davies, A.M., 1985*b*: A three dimensional modal model of wind induced flow in a sea region. *Prog. Oceanogr.*, **15**, 71–128.

Davies, A.M., 1985*c*: Application of a sigma coordinate sea model to the calculation of wind-induced currents. *Cont. Shelf Res.*, **4**, 389–423.

Davies, A.M., 1986: Application of a spectral model to the calculation of wind drift currents in an idealised stratified sea. *Cont. Shelf Res.*, **5**, 579–610.

Davies, A.M., 1987*a*: Spectral models in continental shelf sea oceanography. In: Three-dimensional coastal ocean models, N.S. Heaps (editor), *pp.* 71–106,

published Am. Geophys. Union (Coastal and Estuarine Sciences **4**).

Davies, A.M., 1987*b*: On extracting current profiles from vertically integrated numerical models. In: *Proceedings of JONSMOD'86* held Delft, 1986, P.P.G. Dyke (editor), *Coastal Engineering*, **11**, 445–477.

Davies, A.M. and G.K. Furnes, 1980: Observed and computed M_2 tidal currents in the North Sea. *J. Phys. Oceanogr.*, **10**, 237–257.

Davies, A.M. and G.K. Furnes, 1986: On the determination of vertical structure functions for time-dependent flow problems. *Tellus*, **38A**, 462–477.

Davies, A.M. and I.D. James, 1983: Three-dimensional Galerkin-Spectral sea models of the North Sea and German Bight. In: *Proceedings of International Symposium on North Sea Dynamics*, Hamburg, 1981, J. Sündermann and W. Lenz (editors), *pp.* 85–94, Springer-Verlag.

Davies, A.M. and A. Owen, 1979: Three-dimensional numerical sea model using the Galerkin method with a polynomial basis set. *Appl. Math. Modelling*, **3**, 421–428.

Davies, A.M. and C.V. Stephens, 1983: Comparison of the finite difference and Galerkin methods as applied to the solution of the hydrodynamic equations. *Appl. Math. Modelling*, **7**, 226–240.

De Boor, C., 1978: A practical guide to splines, Springer-Verlag (Applied Mathematical Sciences **27**), 392*p*.

Desai, C.S. and L.D. Johnson, 1973: Evaluation of some numerical schemes for consolidation. *Int. J. Num. Methods Eng.*, **7**, 243–254.

Fandry, C.B., 1982: A numerical model of the wind-driven transient motion in Bass Strait. *J. Geophys. Res.*, **87**, 499–517.

Fandry, C.B., 1983: Model for the three-dimensional structure of wind-driven and tidal circulation in Bass Strait. *Aust. J. Mar. Freshw. Res.*, **34**, 121–141.

Fletcher, C.A.J., 1984: Computational Galerkin Methods. Springer-Verlag, 309*p*.

Forristall, G.Z., R.C. Hamilton and V.J. Cardone, 1977: Continental shelf currents in tropical storm Delia: Observations and theory. *J. Phys. Oceanogr.*, **7**, 532–546.

Forristall, G.Z., 1980: A two-layer model for Hurricane-driven currents on an irregular grid. *J. Phys. Oceanogr.*, **10**, 1417–1438.

Furnes, G.K., 1983: A three-dimensional numerical sea model with eddy viscosity

varying piecewise linearly in the vertical. *Cont. Shelf Res.*, **2**, 231–241.

Furnes, G.K. and M. Mork, 1987: Formulation of a continuously stratified sea model with three-dimensional representation of the upper layer. In: JONSMOD'86, P.P.G. Dyke (editor), *Coastal Eng.*, **11**, 415–444.

Garder, A. and W.H. Raymond, 1974: Galerkin approximations to vertical temperature profiles across the earth's surface. *Monthly Weather Rev.*, **102**, 426–432.

Gonella, J. 1971*a*: A local study of inertial oscillations in the upper layers of the ocean. *Deep-Sea Res.*, **18**, 775–788.

Gonella, J., 1971*b*: The drift current from observations made on the Bouée Laboratoire. *Cah. Océanogr.*, **23**, 19–33

Gordon, R.B., 1982: Wind-driven circulation in Narrangansett Bay. Ph.D Dissertation, University of Rhode Island, Kingston, 166 *p.*

Gottlieb, D. and S.A. Orszag, 1977: Numerical analysis of spectral methods: theory and application. *NSF-CBMS Monogr.*, **26**, Soc. Ind. and Appl. Math., Philadelphia.

Heaps, N.S., 1966: Wind effects on the water in a narrow two-layered lake. *Phil. Trans. R. Soc. London*, **259**, 393–416.

Heaps, N.S., 1972: On the numerical solution of the three-dimensional hydrodynamical equations for tides and storm surges. *Mém. Soc. r. Sci. Liège, Ser* 6, **2**, 143–180.

Heaps, N.S., 1973: Three-dimensional numerical model of the Irish Sea. *Geophys. J. R. astr. Soc.*, **35**, 99–120.

Heaps, N.S., 1974: Development of a three-dimensional numerical model of the Irish Sea. *Rapp. P. -v. Réun. Cons. int. Explor. Mer.*, **167**, 147–162.

Heaps, N.S. and J.E. Jones, 1975: Storm surge computations for the Irish Sea using a three-dimensional numerical model. *Mém. Soc. r. Sci. Liège, Ser* 6, **7**, 289–333.

Heaps, N.S. and J.E. Jones, 1977: Density currents in the Irish Sea. *Geophys. J. R. astr. Soc.*, **51**, 393–429.

Heaps, N.S., 1981: Three-dimensional model for tides and surges with vertical eddy viscosity prescribed in two layers — I. Mathematical formulation. *Geophys. J. R. astr. Soc.*, **64**, 291–302.

Heaps, N.S. and J.E. Jones, 1981: Three-dimensional model for tides and surges

with vertical eddy viscosity prescribed in two layers — II. Irish Sea with bed friction layer. *Geophys. J. R. astr. Soc.*, **64**, 303–320.

Heaps, N.S.,1983: Development of a three-layered spectral model for the motion of a stratified shelf sea. I. Basic equations. In: *Physical Oceanography of coastal and shelf seas*, B. Johns (editor), *pp.* 387–400, Elsevier (Oceanography Series **35**).

Heaps, N.S. and J. E. Jones, 1983: Development of a three-layered spectral model for the motion of a stratified shelf sea. II. Experiments with a rectangular basin representing the Celtic Sea. In: *Physical Oceanography of coastal and shelf seas*, B. Johns (editor), *pp.* 401–465, Elsevier (Oceanography Series **35**).

Heaps, N.S. 1984: Vertical structure of current in homogeneous and stratified water. In: *Hydrodynamics of lakes*, K. Hutter (editor), *pp.* 153–207, Springer-Verlag (CIMS Lecture No. 286).

Heaps, N.S. and J.E. Jones, 1985: A three-layered spectral model with application to wind-induced motion in the presence of stratification and a bottom slope. *Cont. Shelf Res.*, **4**, 279-319.

Higgins, J.R., 1977: Completeness and basis properties of sets of special functions. Cambridge University Press (Cambridge tracts in mathematics, **72**), 134 *p.*

Hopkins, T.S, 1974: On time dependent wind induced motions, *Rapp. P. -v. Reún. Cons. int. Explor. Mer.*, **167**, 21–36.

Hutter, K., 1984: Fundamental equations and approximations. In: *Hydrodynamics of lakes*, K. Hutter (editor), *pp.* 1-33, Springer-Verlag, (CIMS Lecture No. 286).

Javandel, I. and P.A. Witherspoon, 1969: A method of analyzing transient fluid flow in multilayered aquifers. *Water Resour. Res.*, **5**, 856–869.

Johns, B., 1979: The modelling of tidal flow in a channel using a turbulence energy closure scheme. *J. Phys. Oceanogr.*, **8**, 1042–1049.

Johns, B., P.C. Sinha, S.K. DuBe, U.C. Mohanty and A.D. Rao, 1983: Simulation of storm surges using a three-dimensional numerical model: An application to the 1977 Andhra cyclone. *Q. J. Roy. Meteorol. Soc.*, **109**, 211–224.

Jung, K., P. Bills, M. Stevens and J. Noye, 1987: Comparison of finite difference and Galerkin methods in modelling depth-dependent tidal flow in channels. In: *Numerical Modelling: Applications to Marine Systems, Proceedings of the workshop on the Numerical Modelling of Marine Systems* held at the University

of Adelaide, 1986, J. Noye (editor), *pp.* 123-143, North-Holland (Mathematics studies **145**).

Jung, K. and J. Noye, 1988: A spectral method of determining depth variations of currents in a two-layer stratified sea. In: *Computational Techniques and Applications: CTAC 87*, J. Noye (editor), *pp.* 333–346, North-Holland.

Koutitas, C., 1978: Numerical solution of the complete equations for nearly horizontal flows. *Adv. Water Resour.*, **1**, 213–217.

Koutitas, C. and B. O'Connor, 1980*a*: Modeling three-dimensional wind-induced flows. *J. Hydraul. Div. of Am. Soc. Civil Engrs.*, **106** (HY11), 1843–1865.

Koutitas, C. and B. O'Connor, 1980*b*: *Finite-element fractional step solution of the 3-D coastal circulation model.* In: *Proceedings of the 3rd International Conference on Finite Elements in Water Resources*, S.Y. Wang *et al.* (editors), *pp.* 5.64 to 5.71, CML Publications, Computational Mechanics Centre, Southampton.

Kundu, P.K., 1976: An analysis of inertial oscillations observed near Oregon coast. *J. Phys. Oceanogr*, **6**, 879–893.

Laible, J.P., 1980: Finite element analysis of depth varying flow in lakes and coastal regions. In: *Proceedings of the 3rd International Conference on Finite Elements in Water Resources*, S.Y. Wang *et al.* (editors), *pp.* 5-72 to 5-91, CML Publications, Computational Mechanics Centre, Southampton.

Laible, J.P., 1982: Formulating layered and semi-analytic finite element flow programs with variable eddy viscosity. In: *Proceedings of the 4th International Conference on Finite Elements in Water Resources*, K.-P. Holz *et al.* (editors), *pp.* 5-79 to 5-90, Springer-Verlag/Computational Mechanics Centre, Southampton.

Lattès, R., 1969: Methods of resolution for selected boundary problems in mathematical physics. *Gordon and Breach Science Publishers*, New York, 190 *p.*

Leendertse, J.J., R.C. Alexander and S.-K. Liu, 1973: A three-dimensional model for estuaries and coastal seas: Volume I. Principles of computation. **R-1417-OWRR**, The Rand Corporation, Santa Monica.

Leendertse, J.J. and Liu, S.K., 1977: A three-dimensional model for estuaries and coastal seas: Volume IV. Turbulent energy computation. **R-2187-OWRT**, The Rand Corporation, Santa Monica.

Liu, S-K, and J.J. Leendertse, 1978: Multidimensional numerical modeling of

estuaries and coastal seas. *Advances in Hydroscience*, **11**, 95–164.

Liggett, J.A., 1969: Unsteady circulation in shallow homogeneous lakes. *J. Hydraul. Div. of Am. Soc. Civil Engrs.*, **95** (HY4), 1273–1288.

Liggett, J.A. and K.K. Lee, 1971: Properties of circulation in stratified lakes. *J. Hydraul. Div. of Am. Soc. Civil Engrs.*, **97** (HY1), 15-29.

Lynch, D.R. and F.E. Wener, 1987: Three-dimensional hydrodynamics on finite elements. Part I: linearized harmonic model. *Int. J. Num. Meth. Fluids*, **7**, 871–909.

Maas, L.R.M and J.J.M. van Haren, 1987: Observations on the vertical structure of tidal and inertial currents in the central North Sea. *J. Mar. Res.*, **45**, 293–318.

McCreary, J.P., 1981: A linear stratified ocean model of the equatorial undercurrent. *Phil. Trans. Roy. Soc. London*, **A298**, 603–635.

Mcnider, R.T. and J.J. O'Brien, 1973: A multi-layer transient model of coastal upwelling. *J. Phys. Oceanogr.*, **3**, 258–273.

Mellor, G. L. and P.A. Durbin, 1975: The structure and dynamics of the ocean mixed layer. *J. Phys. Oceanogr.*, **5**, 718–728.

Mortimer, C.H., 1952: Water-movements in lakes during summer stratification; evidence from the distribution of temperature in Windmere. *Phil. Trans. Roy. Soc. London*, **B236**, 355–404.

Nihoul, J.C.J., 1977: Three-dimensional model of tides and storm surges in a shallow well-mixed continental sea. *Dyn. Atmos. Ocean*, **2**, 29-47.

Nomitsu, T., 1933: A theory of the rising stage of drift current in the ocean. II. the case of no bottom friction. *Mem. Coll. Sci. Kyoto Imperial University*, **A16**, 275–287.

Noye, B.J., R.L. May and M.D. Teubner, 1981: Three-dimensional numerical model of tides in Spencer Gulf. *Ocean Management*, **6**, 137–147.

Noye, B.J. and M. Stevens, 1987: Three-dimensional numerical model of tides, In: Three-dimensional coastal ocean models, N.S. Heaps (editor), *pp.* 41–69, published Am. Geophys. Union (Coastal and Estuarine Sciences **4**).

O'Brien, J.J. and H.E. Hulburt, 1972: A numerical model of coastal upwelling. *J. Phys. Oceanogr.*, **2**, 14–26.

Owen, A., 1980: A three-dimensional model of the Bristol Channel. *J. Phys.*

Oceanogr., **10**, 1290-1302.

Pearce, B.R. and C.K. Cooper, 1981: Numerical circulation model for wind induced flow. *J. Hydraul. Div. of Am. Soc. Civil Engrs.*, **107** (HY3), 285–302.

Phillips, N.A., 1957: A coordinate system having some special advantages for numerical forecasting. *J. Meteor.*, **14**, 184–185.

Pollard, R.T. ,1970: On the generation by wind of inertial waves in the ocean. *Deep-Sea Res.*, **17**, 795–812.

Pollard, R.T. and R.C. Millard, Jr., 1970: Comparison between observed and simulated wind-generated inertial oscillations. *Deep-Sea Res.*, **17**, 813–821.

Proctor, R., 1987: A three-dimensional numerical model of the eastern Irish sea. In: *Numerical Modelling: Applications to Marine Systems, Proceedings of the workshop on the Numerical Modelling of Marine Systems* held at the University of Adelaide, 1986, J. Noye (editor), *pp.* 25–45, North-Holland (Mathematics studies **145**).

Prenter, P.M., 1975: Splines and variational methods. John Wiley and Sons, 323 *p.*

Preller, R.H., 1986: A numerical model study of the Alboran Sea gyre. *Prog. Oceanogr.*, **16**, 113–146.

Simons, T.J., 1973: Development of three-dimensional numerical models of the Great Lakes. *Science Series* **12**, Canada Center for Inland waters, Burlington, Ontario.

Simons, T.J., 1980: Circulation models of lakes and inland seas. *Can. Bull. Fish. Aquat.* **SCI 203**, Department of Fisheries and Oceans, Ottawa, 146 *p.*

Sheng, Y.P. and H.L. Butler, 1982: Modeling coastal currents and sediment transport. *Proceedings of the 18th Conference on Coastal Engineering* held Capetown, Nov 1982, *pp.* 267–288, published Am. Soc. Civil Engrs.

Spigel, R.H. and J. Imberger, 1980: The classification of mixed-layer dynamics in lakes of small to medium size. *J. Physical Oceanogr.*, **10**, 1104–1121.

Stevens, G.P., 1976: Dynamics of a fluid subject to thermal and gravity diffusion. In: *Proceedings of the 1976 International Conference on Finite Element methods in Engineering*, held at the University of Adelaide, 1976, Y.K. Cheung and S.G. Hutton (editors), *pp.* 17.1 to 17.16, published the University of Adelaide.

Van Foreest, D. and G.B., Brundrit, 1982: A two-mode numerical model with

applications to coastal upwelling. *Prog. Oceanogr.*, **11**, 329–392.

Veronis, G. and H. Stommel, 1956: The action of variable wind stresses on a stratified ocean. *J. Mar. Res.*, **15**, 43–75.

Wang, J.D. and J.J. Connor, 1975: Mathematical modeling of near coastal circulation. *Ralph M. Parsons Laboratory for Water Resources and Hydrodynamics*, Massachusetts Institute of Technology, Technical Report No. 200., 272*p*.

Weber, J.E., 1981: Ekman currents and mixing due to surface gravity waves. *J. Phys. Oceanogr.*, **11**, 1431–1435.

Welander, P., 1957: Wind action on a shallow sea: Some generalization of Ekman's theory. *Tellus*, **9**, 45–52.

Welander, P., 1968: Wind-driven circulation in one- and two-layer oceans of variable depth. *Tellus*, **20**, 1–15.

Wolf, J., 1983: A comparison of a semi-implicit with an explicit scheme in a three-dimensional hydrodynamic model. *Cont. Shelf Res.*, **2**, 215–229.

Yampol'skii, A.D. 1966: The dependence of the velocity of a drift current on the spectrum of the tangential wind stress. *Atm. and Oceanic Phys.*, **2**, 729–732.

Zadeh, L.A. and C.A. Desoer, 1963: Linear system theory: the state space approach. *McGraw-Hill*, 628*p*.

APPENDIX I

Some basic properties of the multilayered self-adjoint eigenvalue problem given in Chapter 3 are presented. Let $\lambda_{i,r}$ and $\lambda_{i,k}$ be two distinct eigenvalues determined from (3.2.1) to (3.2.4) and let $f_{i,j,r}$ and $f_{i,j,k}$ be the corresponding solutions in $\Omega_{i,j}$. Without loss of generality, $i = 0$ is assumed. Thus, for $\Omega_{0,j}$

$$\frac{d}{d\sigma_0}\Big(\mu_{0,j}\frac{df_{0,j,r}}{d\sigma_0}\Big) + \lambda_{0,r} f_{0,j,r} = 0, \tag{A.1.1}$$

$$\frac{d}{d\sigma_0}\Big(\mu_{0,j}\frac{df_{0,j,k}}{d\sigma_0}\Big) + \lambda_{0,k} f_{0,j,k} = 0, \tag{A.1.2}$$

where $j = 1, \cdots, m_0$. Taking the scalar products defined by (2.5.4) of (A.1.1) and (A.1.2) with $f_{0,j,k}$, $f_{0,j,r}$, respectively, and subtracting the two resultant equations gives

$$\begin{aligned}
&(\lambda_{0,r} - \lambda_{0,k}) \sum_{j=1}^{J_0} \frac{\rho_{0,j}}{\rho_{0,1}} \int_{\xi_{0,j-1}}^{\xi_{0,j}} f_{0,j,r}\, f_{0,j,k}\, d\sigma_0 \\
&= \sum_{j=1}^{J_0} \frac{\rho_{0,j}}{\rho_{0,1}} \Big\{ \int_{\xi_{0,j-1}}^{\xi_{0,j}} f_{0,j,k} \frac{d}{d\sigma_0}\Big(\mu_{0,j}\frac{df_{0,j,r}}{d\sigma_0}\Big) - f_{0,j,r}\frac{d}{d\sigma_0}\Big(\mu_{0,j}\frac{df_{0,j,k}}{d\sigma_0}\Big) \Big\}\, d\sigma_0 \,.
\end{aligned} \tag{A.1.3}$$

Substituting conditions (3.2.2) and (3.2.3) into the right-hand side of (A.1.3) yields

$$\begin{aligned}
&(\lambda_{0,r} - \lambda_{0,k}) \sum_{j=1}^{J_0} \frac{\rho_{0,j}}{\rho_{0,1}} \int_{\xi_{0,j-1}}^{\xi_{0,j}} f_{0,j,r}\, f_{0,j,k}\, d\sigma_0 \\
&= -\beta_{0,1}(f_{0,1,r}(0) f_{0,1,k}(0) - f_{0,1,k}(0) f_{0,1,r}(0)) \\
&\quad + \beta_{0,2}(f_{0,B,r}(1) f_{0,B,k}(1) - f_{0,B,k}(1) f_{0,B,r}(1)) = 0.
\end{aligned} \tag{A.1.4}$$

Since $\lambda_{0,r} \neq \lambda_{0,k}$, it follows that the eigenfunctions are orthogonal with respect to

$$\sum_{j=1}^{J_0} \frac{\rho_{0,j}}{\rho_{0,1}} \int_{\xi_{0,j-1}}^{\xi_{0,j}} f_{0,j,r}\, f_{0,j,k}\, d\sigma_0 = 0. \tag{A.1.5}$$

It can be readily shown that all eigenvalues are real. Suppose the eigenvalue is complex, say $\lambda = \lambda^{(R)} + \iota\lambda^{(I)}$, where $\lambda_0^{(I)} \neq 0$. Then, for $\Omega_{0,j}$,

$$\frac{d}{d\sigma_0}\left(\mu_{0,j}\frac{df_{0,j,r}^{(R)}}{d\sigma_0}\right) + \lambda_0^{(R)} f_{0,j,r}^{(R)} - \lambda_i^{(I)} f_{0,j,r}^{(I)} = 0, \tag{A.1.6}$$

$$\frac{d}{d\sigma_0}\left(\mu_{0,j}\frac{df_{0,j,r}^{(I)}}{d\sigma_0}\right) + \lambda_0^{(R)} f_{0,j,r}^{(I)} + \lambda_0^{(I)} f_{0,j,r}^{(R)} = 0, \tag{A.1.7}$$

where $j = 1, \cdots, m_0$. Taking the scalar product (2.5.4), with $f_{0,j,r}^{(I)}$ in (A.1.6) and with $f_{0,j,r}^{(R)}$ in (A.1.7), and then subtracting the two resultant equations yields

$$\begin{aligned}
&\lambda_i^{(I)} \sum_{j=1}^{J_0} \frac{\rho_{0,j}}{\rho_{0,1}} \int_{\xi_{0,j-1}}^{\xi_{0,j}} \left[(f_{0,j,r}^{(R)})^2 + (f_{0,j,r}^{(I)})^2\right] d\sigma_0 \\
&= \sum_{j=1}^{J_0} \frac{\rho_{0,j}}{\rho_{0,1}} \int_{\xi_{0,j-1}}^{\xi_{0,j}} \left[f_{0,j,r}^{(R)} \frac{d}{d\sigma_0}\left(\mu_{0,j}\frac{df_{0,j,r}^{(I)}}{d\sigma_0}\right) - f_{0,j,r}^{(I)} \frac{d}{d\sigma_0}\left(\mu_{0,j}\frac{df_{0,j,r}^{(R)}}{d\sigma_0}\right)\right] d\sigma_0.
\end{aligned} \tag{A.1.8}$$

Integrating by parts, and using:

$$\left(\mu_{0,j}\frac{df_{0,1,r}^{(R)}}{d\sigma_0}\right) = \beta_{0,1} f_{0,1,r}^{(R)}, \quad \text{at} \quad \sigma_0 = 0, \tag{A.1.9}$$

$$\left(\mu_{0,j}\frac{df_{0,1,r}^{(I)}}{d\sigma_0}\right) = \beta_{0,1} f_{0,1,r}^{(I)}, \quad \text{at} \quad \sigma_0 = 0, \tag{A.1.10}$$

$$\left(\mu_{0,j}\frac{df_{0,B,r}^{(R)}}{d\sigma_0}\right) = \beta_{0,2} f_{0,B,r}^{(R)}, \quad \text{at} \quad \sigma_0 = 1, \tag{A.1.11}$$

$$\left(\mu_{0,j}\frac{df_{0,B,r}^{(I)}}{d\sigma_0}\right) = \beta_{0,2} f_{0,B,r}^{(I)}, \quad \text{at} \quad \sigma_0 = 1, \tag{A.1.12}$$

we have

$$\lambda_0^{(I)} \sum_{j=1}^{J_0} \left[(f_{0,j,r}^{(R)})^2 + (f_{0,j,r}^{(I)})^2\right] d\sigma_0 = 0. \tag{A.1.13}$$

However, this is impossible and so it follows that $\lambda_0^{(I)} = 0$ and the eigenvalues are real.

For $\beta_{0,1} \geq 0$ and $\beta_{0,2} \leq 0$ the system has only non-negative eigenvalues. Taking the scalar product (2.5.4) of (3.2.1) with $f_{0,j,r}$, yields

$$\sum_{j=1}^{J_0} \frac{\rho_{0,j}}{\rho_{0,1}} \int_{\xi_{0,j-1}}^{\xi_{0,j}} f_{0,j,r} \frac{d}{d\sigma_0}\Big(\mu_{0,j} \frac{df_{0,j,r}}{d\sigma_0}\Big) d\sigma_0 = -\lambda_0 \sum_{j=1}^{J_0} \frac{\rho_{0,j}}{\rho_{0,1}} \int_{\xi_{0,j-1}}^{\xi_{0,j}} f_{0,j,r}^2 \, d\sigma_0, \tag{A.1.14}$$

where $r = 1, \cdots, m_0$.

By integrating the left hand side of (A.1.14) by parts and by using the limit conditions in (3.2.2) and (3.2.3), we have

$$\begin{aligned} &\sum_{j=1}^{J_0} \frac{\rho_{0,j}}{\rho_{0,1}} \int_{\xi_{0,j-1}}^{\xi_{0,j}} f_{0,j,r} \frac{d}{d\sigma_0}\Big(\mu_{0,j} \frac{df_{0,j,r}}{d\sigma_0}\Big) d\sigma_0 \\ &\quad = -\big(\beta_{0,1} f_{0,1,r}^2(0) - \beta_{0,2} f_{0,B,r}^2(1)\big) - \sum_{j=1}^{J_0} \frac{\rho_{0,j}}{\rho_{0,1}} \int_{\xi_{0,j-1}}^{\xi_{0,j}} \mu_{0,j} \Big(\frac{df_{0,j,r}}{d\sigma_0}\Big)^2 d\sigma_0. \end{aligned} \tag{A.1.15}$$

Then, it follows with $\beta_{0,1} \geq 0$, $\beta_{0,2} \leq 0$ that

$$\sum_{j=1}^{J_0} \frac{\rho_{0,j}}{\rho_{0,1}} \int_{0,j-1}^{\xi_{0,j}} f_{0,j,r} \frac{d}{d\sigma_0}\Big(\mu_{0,j} \frac{df_{0,j,r}}{d\sigma_0}\Big) d\sigma_0 \leq 0, \tag{A.1.16}$$

and hence from (A.1.14)

$$-\lambda_0 \sum_{j=1}^{J_0} \frac{\rho_{0,j}}{\rho_{0,1}} \int_{\xi_{0,j-1}}^{\xi_{0,j}} f_{0,j,r}^2 \, d\sigma_0 \leq 0, \tag{A.1.17}$$

which implies that $\lambda_0 \geq 0$.

APPENDIX II

An eigenequation in a three-layered one domain system is presented for the piecewise constant eddy viscosity profile given as

$$\mu_{0,1} = \mu_T, \qquad 0 \le \sigma_0 \le \xi_{0,1}, \tag{A.2.1}$$

$$\mu_{0,2} = \mu_p, \quad \xi_{0,1} \le \sigma_0 \le \xi_{0,2}, \tag{A.2.2}$$

$$\mu_{0,3} = \mu_b, \quad \xi_{0,2} \le \sigma_0 \le 1. \tag{A.2.3}$$

With $\beta_{0,1} = 0$, $\beta_{0,2} = \infty$, the eigenequation takes the form

$$\begin{aligned} &\cos\{\omega\xi_{0,1}\}\cos\{\Theta_1\omega(\xi_{0,1}-\xi_{0,2})\}\cos\{\Theta_2\omega(1-\xi_{0,2})\} \\ &+R_1^{-1}\sin\{\omega\xi_{0,1}\}\sin\{\Theta_1\omega(\xi_{0,1}-\xi_{0,2})\}\sin\{\Theta_2\omega(1-\xi_{0,2})\} \\ &+R_2^{-1}\cos\{\omega\xi_{0,1}\}\sin\{\Theta_1\omega(\xi_{0,1}-\xi_{0,2})\}\sin\{\Theta_2\omega(1-\xi_{0,2})\} \\ &-(R_1R_2)^{-1}\sin\{\omega\xi_{0,1}\}\cos\{\Theta_1\omega(\xi_{0,1}-\xi_{0,2})\}\sin\{\Theta_2\omega(1-\xi_{0,2})\} = 0, \end{aligned} \tag{A.2.4}$$

where

$$\Theta_1 = (\mu_T/\mu_p)^{1/2}, \tag{A.2.5}$$

$$\Theta_2 = (\mu_T/\mu_b)^{1/2}, \tag{A.2.6}$$

$$R_1 = (\rho_P/\rho_T)(\mu_P/\mu_T)\Theta_1 = (\rho_P/\rho_T)\Theta_1^{-1}, \tag{A.2.7}$$

$$R_2 = (\rho_B/\rho_P)(\mu_B/\mu_P)(\Theta_2/\Theta_1) = (\rho_B/\rho_P)(\Theta_2/\Theta_1)^{-1}, \tag{A.2.8}$$

$$\rho_T = \rho_{0,1}, \quad \rho_P = \rho_{0,2}, \quad \rho_B = \rho_{0,3}. \tag{A.2.9}$$

The eigenvalues are given by

$$\lambda_0 = \omega^2\mu_T. \tag{A.2.10}$$

APPENDIX III

Figures A.3(a) – (g) Vertical variations the first five vertical modes computed numerically using various eddy viscosity profiles

Tables A.3(a) – (e) Values of $a_{i,j,r}$, $f_{i,r}(1)$, α_i, $\lambda_{i,r}$ and $\Phi_{i,r}$ computed using various eddy viscosity profiles

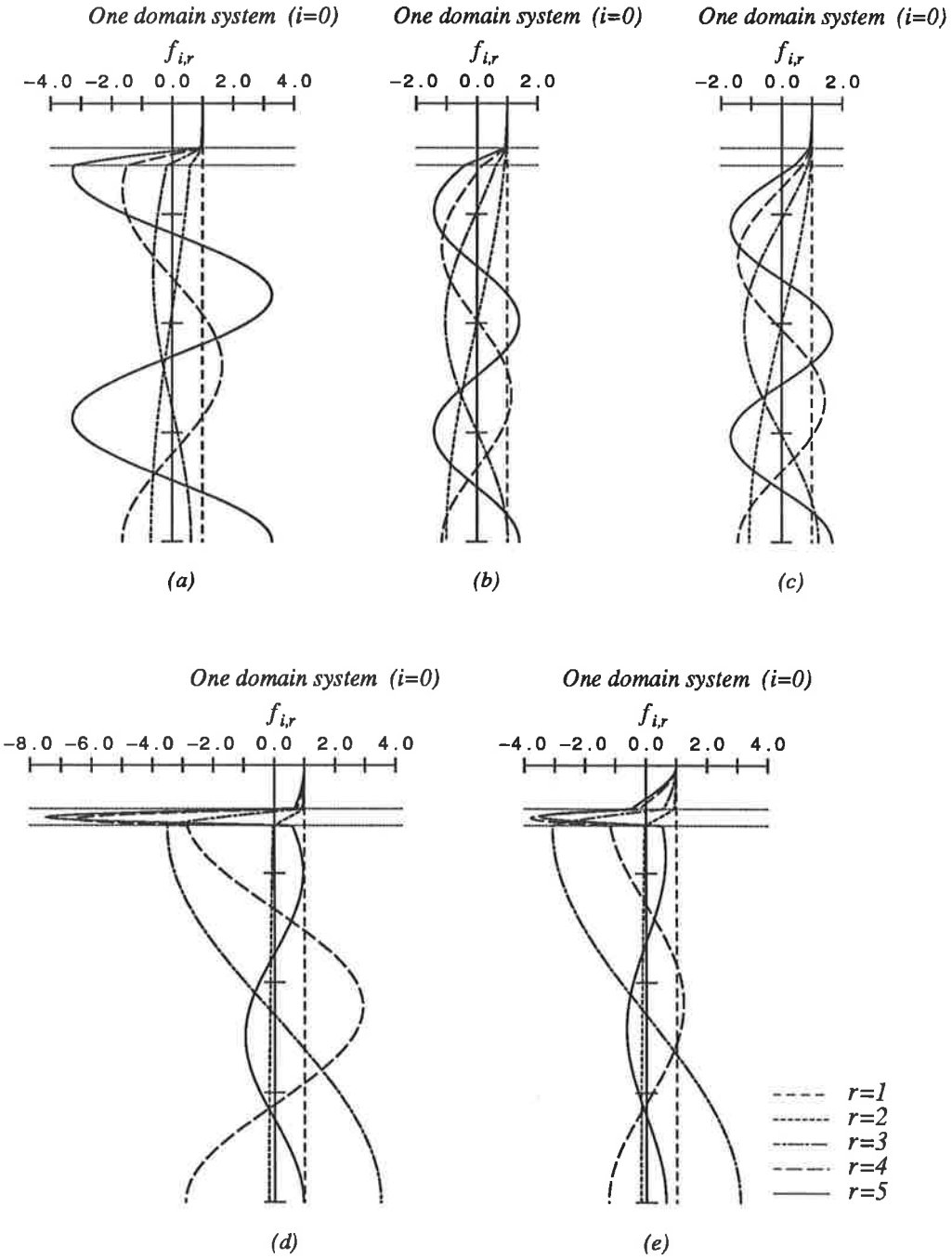

Figure A.3(a) Vertical variations of the first five vertical modes of the one domain system, obtained using the profile in Figure 3.1(d), with: Δ_T=25, Δ_P=10, Δ_B=215 m; ρ_T=1025.8, ρ_P=1026.5, ρ_B=1027.2 $g\,cm^{-3}$; $\beta_{0,1}$= $\beta_{0,2}$=0; and (a) N_T =1000, N_P=10, N_B=100 cm^2s^{-1}; (b) N_T =1000, N_P=50, N_B=100; (c) N_T =1000, N_P=150, N_B=100 cm^2s^{-1}; (d) N_T =1000, N_P=10, N_B=1000 cm^2s^{-1}; (e) N_T =150, N_P=10, N_B=1000 cm^2s^{-1}.

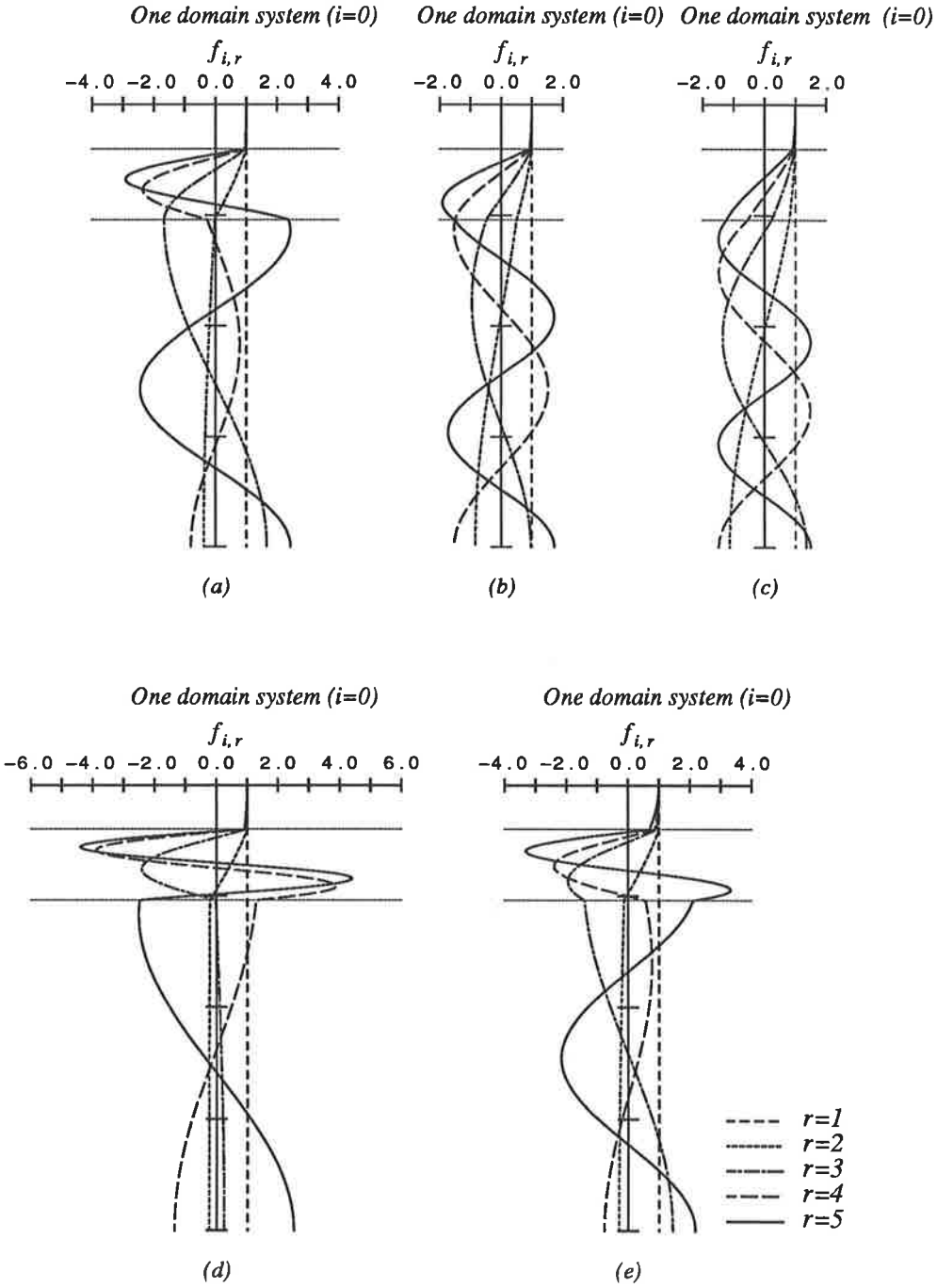

Figure A.3(b) Vertical variations of the first five vertical modes of the one domain system, obtained using the profile in Figure 3.1(d), with: Δ_T=25, Δ_P=40, Δ_B=185 m; ρ_T=1025.8, ρ_P=1026.5, ρ_B=1027.2 $g\,cm^{-3}$; $\beta_{0,1}$= $\beta_{0,2}$=0; and (a) N_T =1000, N_P=10, N_B=100 cm^2s^{-1}; (b) N_T =1000, N_P=50, N_B=100; (c) N_T =1000, N_P=150, N_B=100 cm^2s^{-1}; (d) N_T =1000, N_P=10, N_B=1000 cm^2s^{-1}; (e) N_T =150, N_P=10, N_B=1000 cm^2s^{-1}.

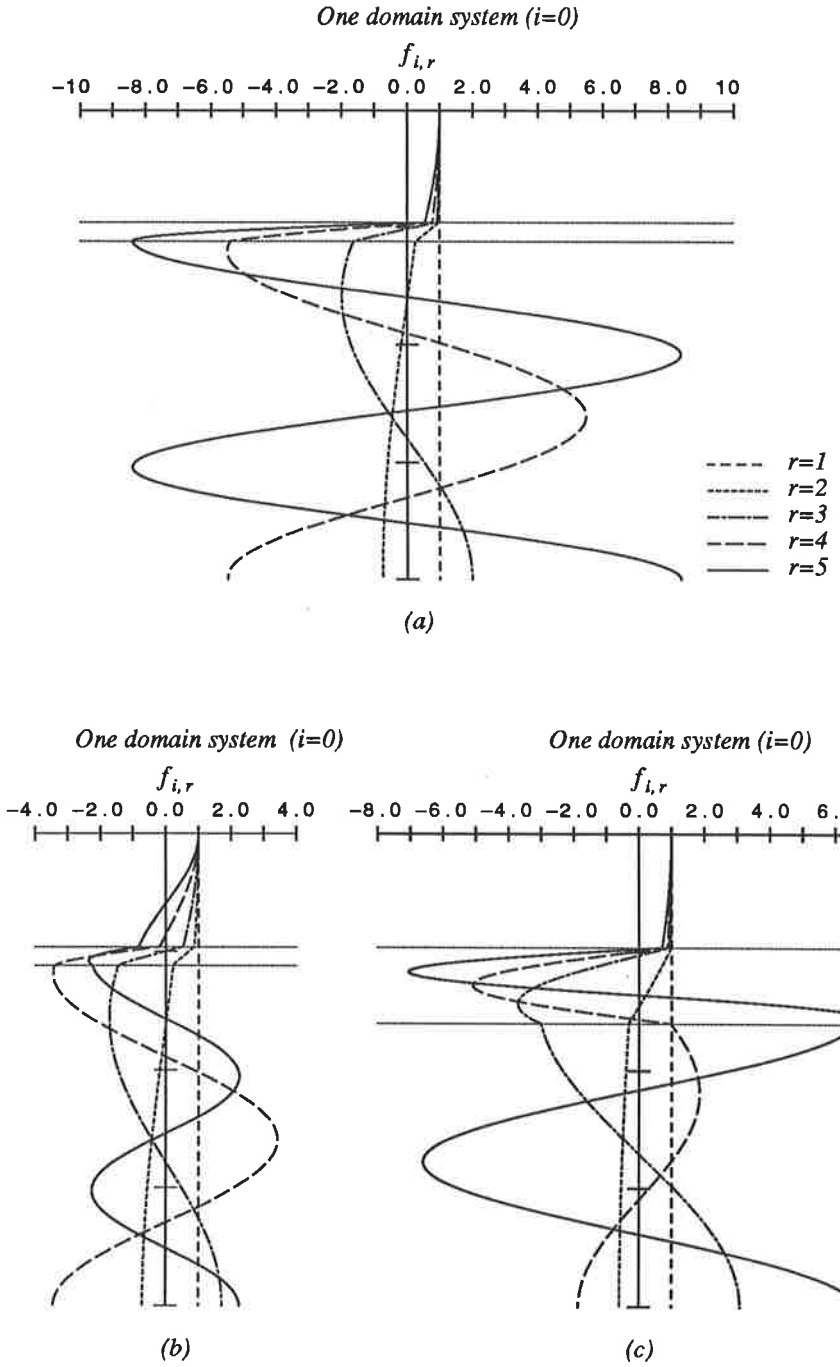

Figure A.3(*c*) Vertical variations of the first five vertical modes of the one domain system, obtained using the profile in Figure 3.1(*d*), with: Δ_T=60 *m*; ρ_T=1025.8, ρ_P=1026.5, ρ_B=1027.2 $g\,cm^{-3}$; $\beta_{0,1}$= $\beta_{0,2}$=0; N_P=10, N_B=100 $cm^2 s^{-1}$; and (*a*) Δ_P=10, Δ_B=180 *m*; N_T =1000 $cm^2 s^{-1}$; (*b*) Δ_P=10, Δ_B=180 *m*; N_T =150 $cm^2 s^{-1}$; (*c*) Δ_P=40, Δ_B=150 *m*; N_T =1000 $cm^2 s^{-1}$.

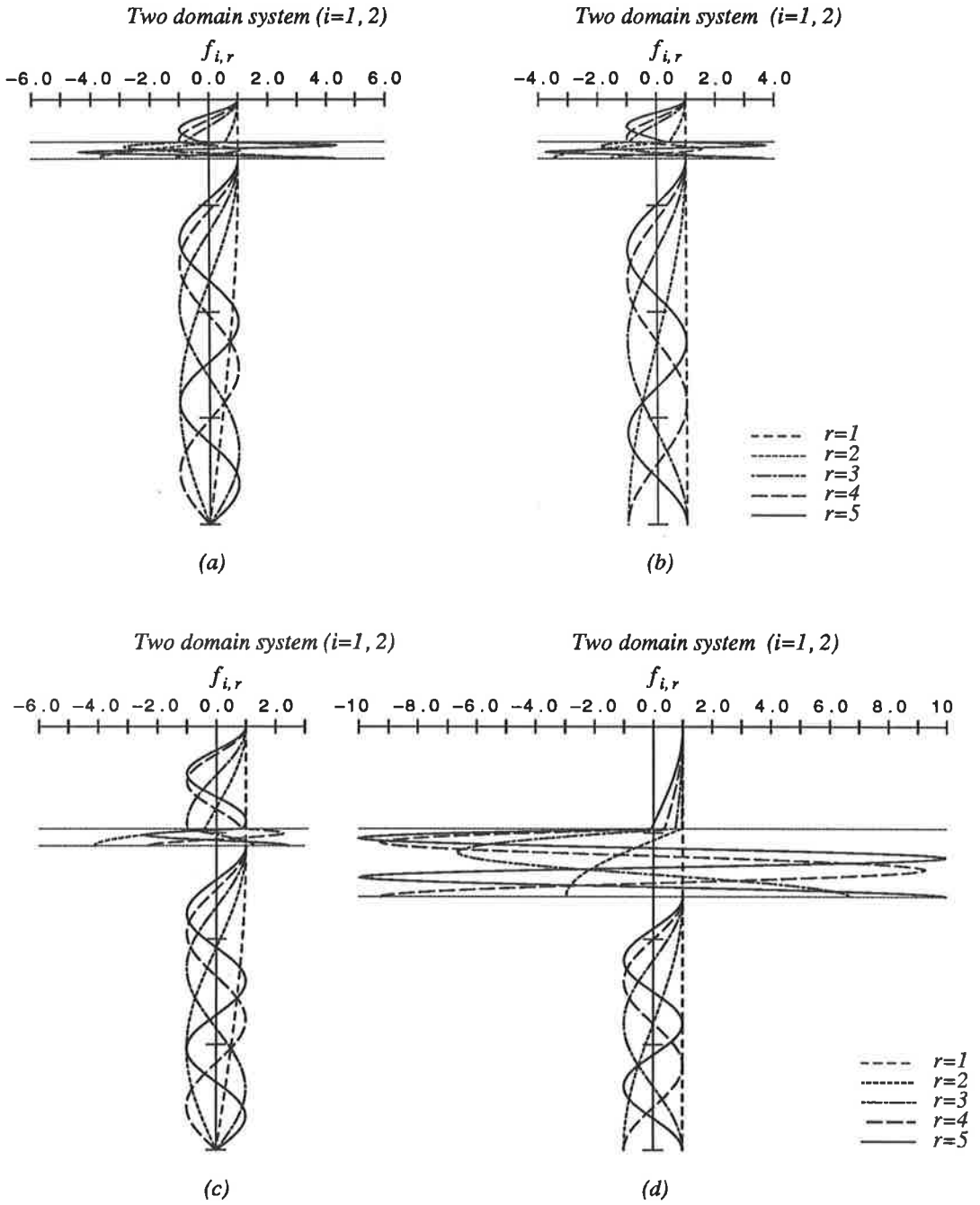

Figure A.3(d) Vertical variations of the first five vertical modes of the two domain system, obtained using the profile in Figure 3.1(d), with: ρ_T=1025.8, ρ_P=1026.5, ρ_B=1027.2 $g\,cm^{-3}$; $\beta_{1,1}$= $\beta_{2,2}$=0; N_P=10, N_B=100 cm^2s^{-1}; and (a) Δ_T=25, Δ_P=10, Δ_B=215 m; N_T =1000 cm^2s^{-1}; $\beta_{1,1}$= $\beta_{2,2}$=∞; (b) Δ_T=25, Δ_P=10, Δ_B=215m; N_T =150 cm^2s^{-1}; $\beta_{1,1}$= $\beta_{2,2}$=0; (c) Δ_T=60, Δ_P=10, Δ_B=180 m; N_T =1000 cm^2s^{-1}; $\beta_{1,1}$= $\beta_{2,2}$=∞; (d) Δ_T=60, Δ_P=40, Δ_B=150 m; N_T =1000 cm^2s^{-1}; $\beta_{1,1}$= $\beta_{2,2}$=0.

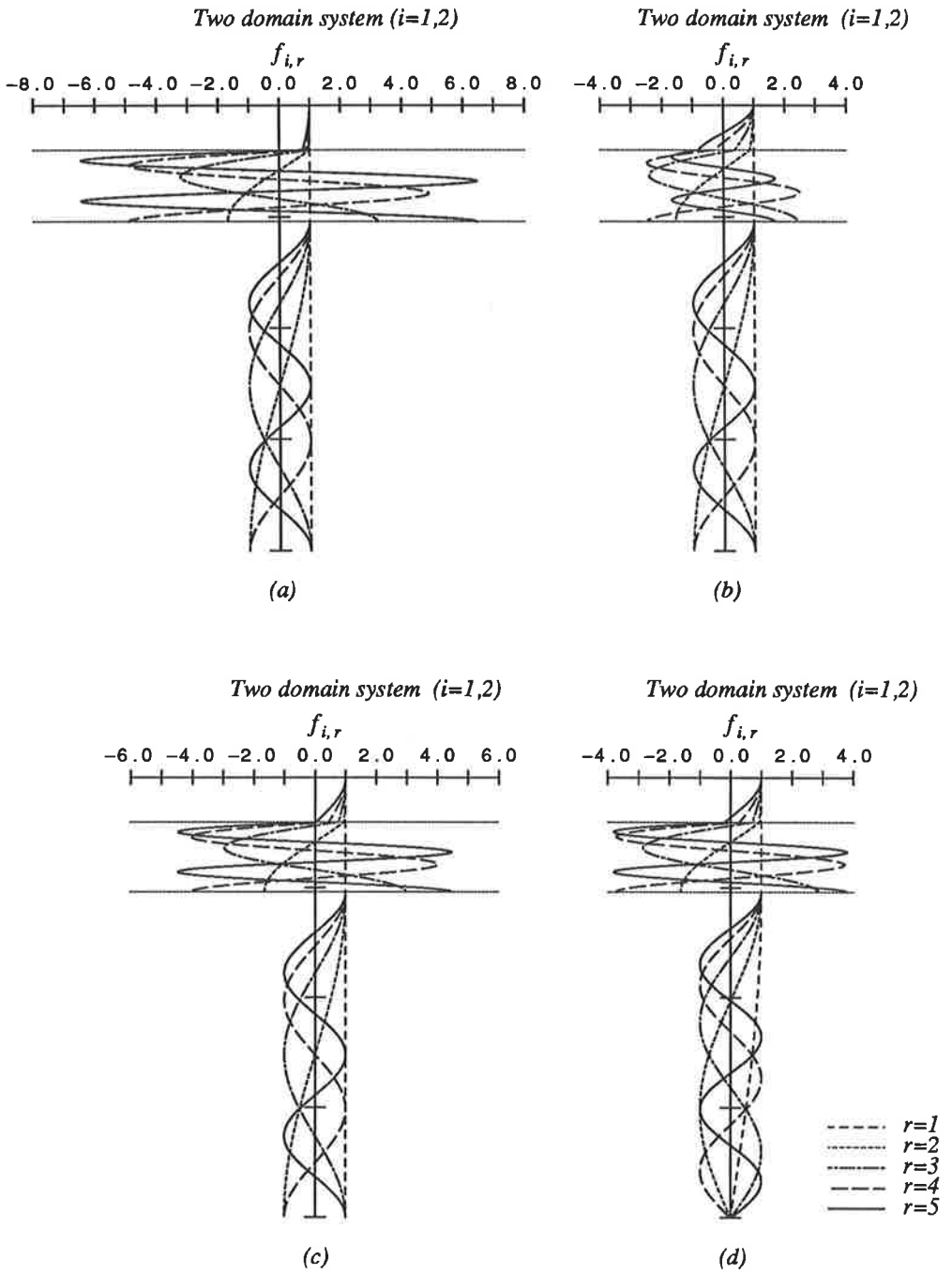

Figure A.3(e) Vertical variations of the first five vertical modes of the two domain system, obtained using the profile in Figure 3.1(d), with: Δ_T=25, Δ_P=40, Δ_B=185 m; ρ_T=1025.8, ρ_P=1026.5, ρ_B=1027.2 $g\,cm^{-3}$; N_B=100 cm^2s^{-1}; and (a) N_T=1000, N_P =10 cm^2s^{-1}; $\beta_{1,1}$= $\beta_{2,2}$=0; (b) as in (a) but with N_P =150 cm^2s^{-1}; (c) as in (a) but with N_P =50 cm^2s^{-1}; (d) N_T=150, N_P =10 cm^2s^{-1}; $\beta_{1,1}$=0, $\beta_{2,2}$=∞.

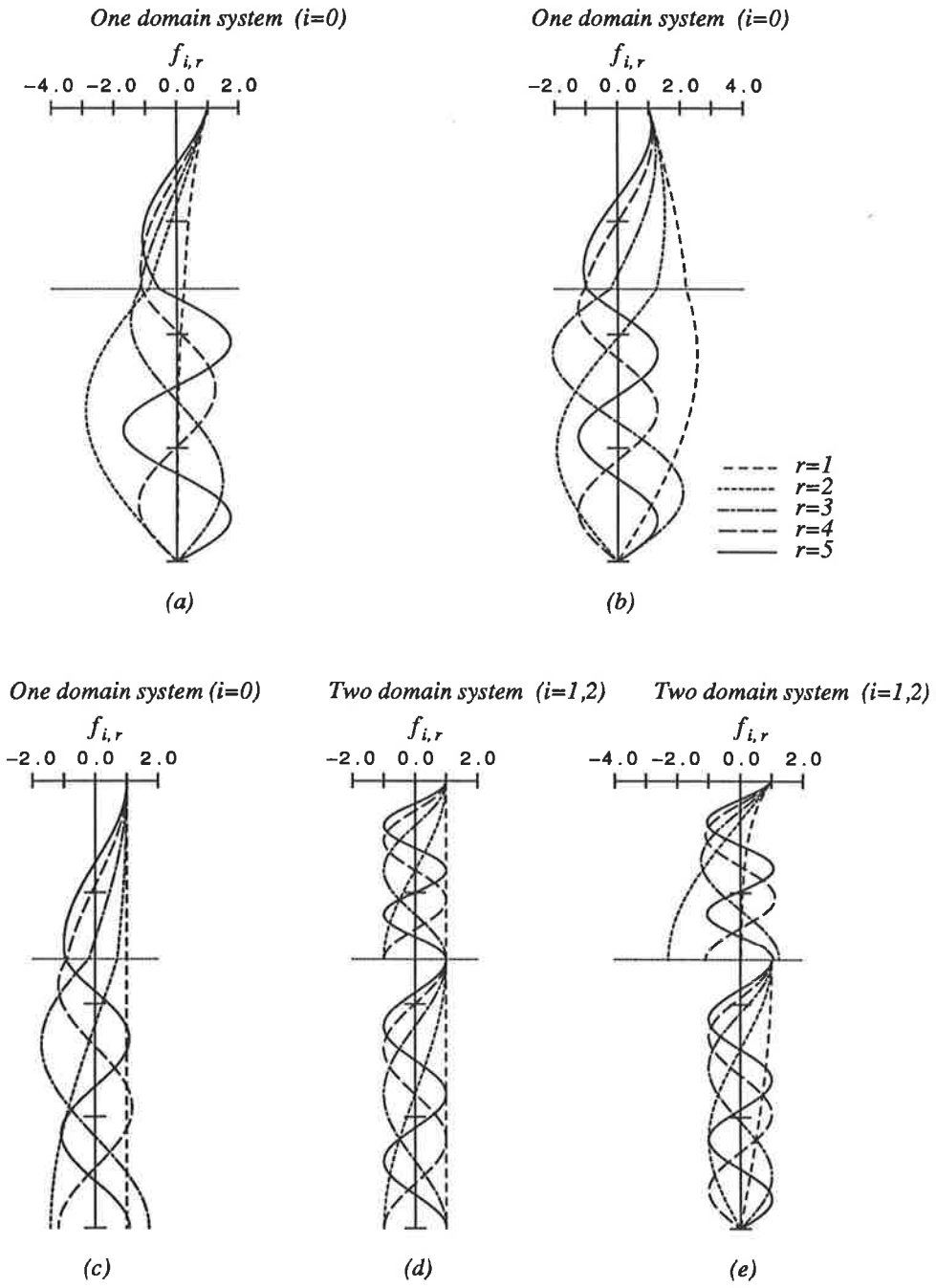

Figure A.3(f) Vertical variations of the first five vertical modes in the two-layered one and two domain systems, obtained using the profiles in Figure 3.1(c), with: Δ_T=40, Δ_B=60 m; ρ_T=1025.8, ρ_B=1027.0 $g\,cm^{-3}$; N_T=300, N_B=100 $cm^2 s^{-1}$; and (a) $\alpha_0\beta_{0,1}$=−0.125 $cm^2 s^{-1}$, $\beta_{0,2}$=∞; (b) $\alpha_0\beta_{0,1}$=0.125 $cm^2 s^{-1}$, $\beta_{0,2}$=∞; (c) $\beta_{0,1}$= $\beta_{0,2}$=0; (d) $\beta_{1,1}$ =$\beta_{2,2}$=0; (e) $\alpha_1\beta_{1,1}$=−0.125 $cm^2 s^{-1}$, $\beta_{2,2}$ =∞.

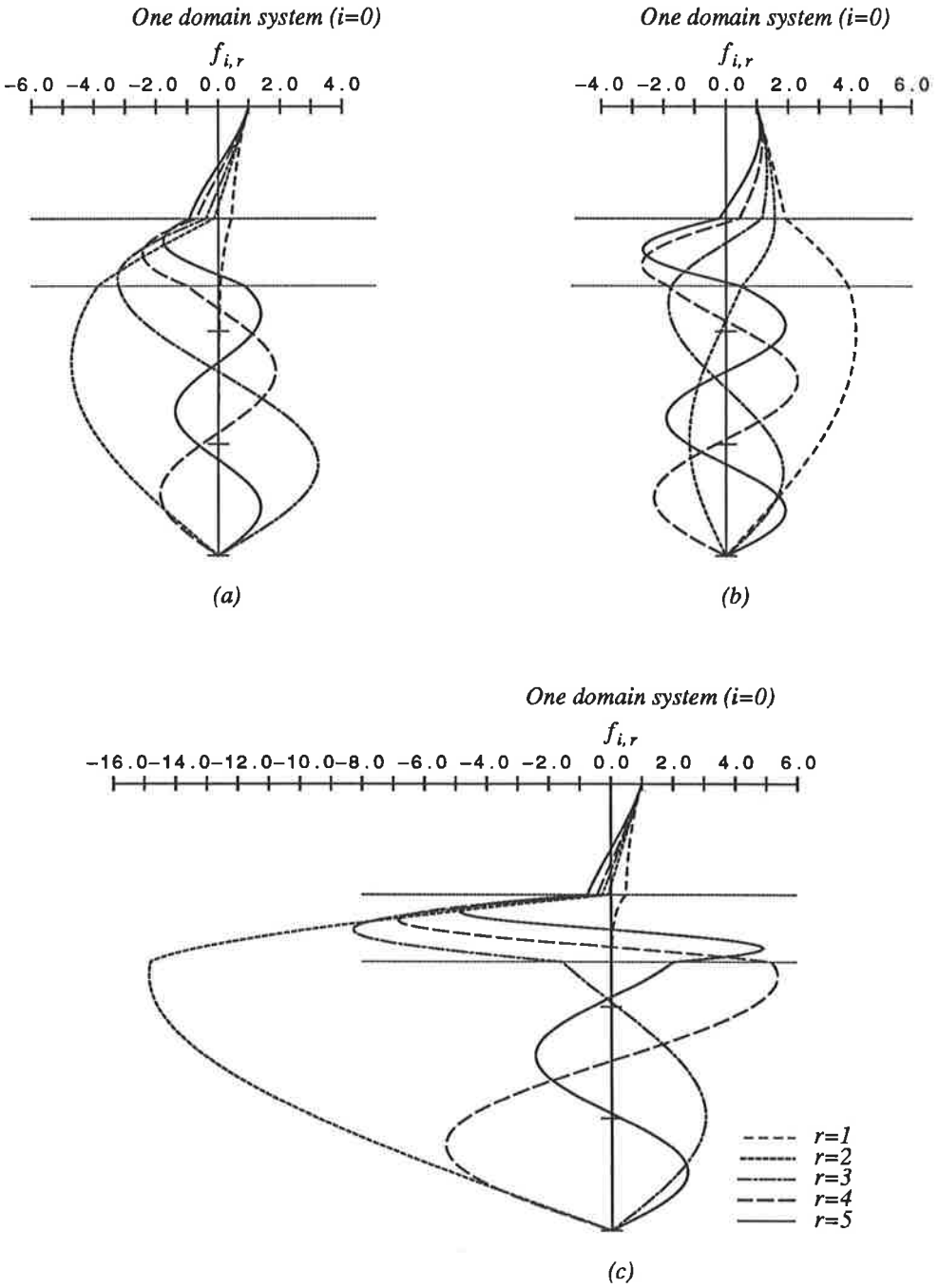

Figure A.3(g) Vertical variations of the first five vertical modes in the one domain system, obtained using the profile in Figure 3.1(d), with: Δ_T=25, Δ_P=15, Δ_B=60 m; ρ_T=1025.8, ρ_P=1026.5, ρ_B=1027.2 $g\,cm^{-3}$; N_T=300, N_B=100 $cm^2 s^{-1}$; and (a) N_P=50 $cm^2 s^{-1}$; $\alpha_0\beta_{0,1}$=−0.125 $cm^2 s^{-1}$, $\beta_{0,2}$=∞; (b) as in (a) but with $\alpha_0\beta_{0,1}$=0.125 $cm^2 s^{-1}$; (c) as in (a) but with N_P=10 $cm^2 s^{-1}$.

Table A.3(*a*) Values of $a_{i,j,r}$, $f_{i,r}(1)$, α_i, $\lambda_{i,r}$ and $\Phi_{i,r}$ of the first six vertical modes computed using various eddy viscosity profiles

$\Delta_T = 25, \Delta_P = 10, \Delta_B = 215m, \alpha_0 = 192.0, \alpha_0\mu_T = 1000, \alpha_0\mu_P = 150, \alpha_0\mu_B = 100\ cm^2s^{-1}$

r	$a_{0,0,r}$	$a_{0,1,r}$	$a_{0,2,r}$	$f_{0,r}(1)$	$\alpha_0\lambda_{0,r}$	$\lambda_{0,r}$	$\Phi_{0,r}$
1	1.00000	0.90000	0.86000	1.000	0.000	0.000	0.998
2	0.00016	−0.09967	−0.13887	−1.058	0.099	5.189	1.806
3	0.00016	−0.09916	−0.13592	1.215	0.407	21.213	1.406
4	0.00015	−0.09828	−0.13090	−1.432	0.939	48.935	1.037
5	0.00015	−0.09702	−0.12385	1.668	1.708	88.979	0.776
6	0.00014	−0.09538	−0.11492	−1.897	2.719	141.643	0.606

$\Delta_T = 25, \Delta_P = 10, \Delta_B = 215m, \alpha_0 = 188.0, \alpha_0\mu_T = 1000, \alpha_0\mu_P = 50, \alpha_0\mu_B = 100\ cm^2s^{-1}$

r	$a_{0,0,r}$	$a_{0,1,r}$	$a_{0,2,r}$	$f_{0,r}(1)$	$\alpha_0\lambda_{0,r}$	$\lambda_{0,r}$	$\Phi_{0,r}$
1	1.00000	0.90000	0.86000	1.000	0.000	0.000	0.998
2	0.00016	−0.09967	−0.13771	−0.999	0.098	5.224	1.984
3	0.00015	−0.09919	−0.13153	1.027	0.388	20.655	1.855
4	0.00015	−0.09841	−0.12164	−1.146	0.867	46.126	1.497
5	0.00014	−0.09729	−0.10820	1.405	1.549	82.410	1.023
6	0.00012	−0.09582	−0.09139	−1.800	2.459	130.818	0.644

$\Delta_T = 25, \Delta_P = 10, \Delta_B = 215m, \alpha_0 = 186.4, \alpha_0\mu_T = 1000, \alpha_0\mu_P = 10, \alpha_0\mu_B = 100\ cm^2s^{-1}$

r	$a_{0,0,r}$	$a_{0,1,r}$	$a_{0,2,r}$	$f_{0,r}(1)$	$\alpha_0\lambda_{0,r}$	$\lambda_{0,r}$	$\Phi_{0,r}$
1	1.00000	0.90000	0.86000	1.000	0.000	0.000	0.998
2	0.00015	−0.09969	−0.13168	−0.703	0.088	4.725	3.329
3	0.00014	−0.09941	−0.11609	0.623	0.263	14.119	3.461
4	0.00012	−0.09886	−0.08752	−1.643	0.609	32.675	0.740
5	0.00009	−0.09785	−0.04267	3.275	1.238	66.436	0.203
6	0.00006	−0.09643	0.00681	−4.533	2.127	114.145	0.107

$\Delta_T = 25, \Delta_P = 10, \Delta_B = 215m, \alpha_0 = 101.4, \alpha_0\mu_T = 150, \alpha_0\mu_P = 10, \alpha_0\mu_B = 100\ cm^2s^{-1}$

r	$a_{0,0,r}$	$a_{0,1,r}$	$a_{0,2,r}$	$f_{0,r}(1)$	$\alpha_0\lambda_{0,r}$	$\lambda_{0,r}$	$\Phi_{0,r}$
1	1.00000	0.90000	0.86000	1.000	0.000	0.000	0.998
2	0.00015	−0.09887	−0.12998	−0.684	0.087	8.636	3.474
3	0.00014	−0.09700	−0.11181	0.602	0.258	25.497	3.677
4	0.00011	−0.09330	−0.07914	−1.581	0.603	59.545	0.803
5	0.00008	−0.08677	−0.03192	2.920	1.232	121.519	0.255
6	0.00004	−0.07803	0.01271	−3.569	2.117	208.830	0.172

$\Delta_T = 25, \Delta_P = 10, \Delta_B = 215m, \alpha_0 = 875.4, \alpha_0\mu_T = 150, \alpha_0\mu_P = 10, \alpha_0\mu_B = 1000\ cm^2s^{-1}$

r	$a_{0,0,r}$	$a_{0,1,r}$	$a_{0,2,r}$	$f_{0,r}(1)$	$\alpha_0\lambda_{0,r}$	$\lambda_{0,r}$	$\Phi_{0,r}$
1	1.00000	0.90000	0.86000	1.000	0.000	0.000	0.998
2	0.00014	−0.09738	−0.11540	−0.179	0.223	2.555	8.103
3	0.00007	−0.08549	−0.02409	3.077	1.359	15.525	0.230
4	0.00000	−0.05424	0.05176	−1.221	4.841	55.305	1.023
5	0.00000	−0.04310	0.04278	0.642	6.328	72.298	2.148
6	0.00001	−0.01119	−0.00431	−1.475	11.928	136.266	0.965

Table A.3(*b*) Values of $a_{i,j,r}$, $f_{i,r}(1)$, α_i, $\lambda_{i,r}$ and $\Phi_{i,r}$ of the first six vertical modes computed using various eddy viscosity profiles

$\Delta_T = 25, \Delta_P = 40, \Delta_B = 185m, \alpha_0 = 198.0, \alpha_0\mu_T = 1000, \alpha_0\mu_P = 150, \alpha_0\mu_B = 100\ cm^2s^{-1}$

r	$a_{0,0,r}$	$a_{0,1,r}$	$a_{0,2,r}$	$f_{0,r}(1)$	$\alpha_0\lambda_{0,r}$	$\lambda_{0,r}$	$\Phi_{0,r}$
1	1.00000	0.90000	0.74000	1.000	0.000	0.000	0.998
2	0.00023	−0.09959	−0.24559	−1.123	0.102	5.169	1.659
3	0.00020	−0.09907	−0.20228	1.354	0.435	21.996	1.205
4	0.00015	−0.09814	−0.13588	−1.477	1.020	51.517	1.016
5	0.00010	−0.09686	−0.06158	1.485	1.833	92.611	0.974
6	0.00006	−0.09525	0.00628	−1.572	2.852	144.080	0.859

$\Delta_T = 25, \Delta_P = 40, \Delta_B = 185m, \alpha_0 = 182.0, \alpha_0\mu_T = 1000, \alpha_0\mu_P = 50, \alpha_0\mu_B = 100\ cm^2s^{-1}$

r	$a_{0,0,r}$	$a_{0,1,r}$	$a_{0,2,r}$	$f_{0,r}(1)$	$\alpha_0\lambda_{0,r}$	$\lambda_{0,r}$	$\Phi_{0,r}$
1	1.00000	0.90000	0.74000	1.000	0.000	0.000	0.998
2	0.00022	−0.09962	−0.22490	−0.845	0.089	4.937	2.448
3	0.00016	−0.09929	−0.14626	0.956	0.320	17.589	1.933
4	0.00008	−0.09864	−0.03241	−1.528	0.764	41.998	0.901
5	0.00002	−0.09756	0.06761	1.723	1.456	80.040	0.693
6	−0.00000	−0.09624	0.10385	−1.596	2.283	125.448	0.716

$\Delta_T = 25, \Delta_P = 40, \Delta_B = 185m, \alpha_0 = 175.6, \alpha_0\mu_T = 1000, \alpha_0\mu_P = 10, \alpha_0\mu_B = 100\ cm^2s^{-1}$

r	$a_{0,0,r}$	$a_{0,1,r}$	$a_{0,2,r}$	$f_{0,r}(1)$	$\alpha_0\lambda_{0,r}$	$\lambda_{0,r}$	$\Phi_{0,r}$
1	1.00000	0.90000	0.74000	1.000	0.000	0.000	0.998
2	0.00019	−0.09973	−0.18500	−0.375	0.040	2.334	4.656
3	0.00007	−0.09962	−0.00603	1.669	0.182	10.364	0.765
4	−0.00000	−0.09922	0.10832	−0.787	0.467	26.617	1.380
5	0.00002	−0.09869	0.05983	2.439	0.771	43.941	0.341
6	0.00012	−0.09749	−0.08974	−2.041	1.436	81.817	0.362

$\Delta_T = 25, \Delta_P = 40, \Delta_B = 185m, \alpha_0 = 90.6, \alpha_0\mu_T = 150, \alpha_0\mu_P = 10, \alpha_0\mu_B = 100\ cm^2s^{-1}$

r	$a_{0,0,r}$	$a_{0,1,r}$	$a_{0,2,r}$	$f_{0,r}(1)$	$\alpha_0\lambda_{0,r}$	$\lambda_{0,r}$	$\Phi_{0,r}$
1	1.00000	0.90000	0.74000	1.000	0.000	0.000	0.998
2	0.00019	−0.09935	−0.18348	−0.371	0.040	4.508	4.728
3	0.00006	−0.09792	−0.00420	1.619	0.181	20.033	0.811
4	0.00000	−0.09495	0.10227	−0.730	0.461	50.930	1.566
5	0.00002	−0.09165	0.05160	2.273	0.767	84.725	0.395
6	0.00011	−0.08482	−0.07838	−1.647	1.421	156.855	0.526

$\Delta_T = 25, \Delta_P = 40, \Delta_B = 185m, \alpha_0 = 756.6, \alpha_0\mu_T = 150, \alpha_0\mu_P = 10, \alpha_0\mu_B = 1000\ cm^2s^{-1}$

r	$a_{0,0,r}$	$a_{0,1,r}$	$a_{0,2,r}$	$f_{0,r}(1)$	$\alpha_0\lambda_{0,r}$	$\lambda_{0,r}$	$\Phi_{0,r}$
1	1.00000	0.90000	0.74000	1.000	0.000	0.000	0.998
2	0.00018	−0.09926	−0.16882	−0.238	0.049	0.654	5.328
3	−0.00000	−0.09470	0.10205	0.225	0.485	6.412	2.112
4	0.00011	−0.08428	−0.08149	−1.061	1.475	19.497	0.751
5	0.00009	−0.07958	−0.06309	2.186	1.952	25.800	0.353
6	0.00000	0.06529	0.06515	−0.407	3.512	46.419	0.764

Table A.3(*c*) Values of $a_{i,j,r}$, $f_{i,r}(1)$, α_i, $\lambda_{i,r}$ and $\Phi_{i,r}$ of the first six vertical modes computed using various eddy viscosity profiles

$\Delta_T = 25, \Delta_P = 15, \Delta_B = 60m, \alpha_0 = 157.5, \alpha_0\mu_T = 300, \alpha_0\mu_P = 150, \alpha_0\mu_B = 100\ cm^2s^{-1}$

r	$a_{0,0,r}$	$a_{0,1,r}$	$a_{0,2,r}$	$f_{0,r}(1)$	$\alpha_0\lambda_{0,r}$	$\lambda_{0,r}$	$\Phi_{0,r}$
1	1.00000	0.75000	0.60000	1.000	0.000	0.000	0.999
2	0.00040	−0.23996	−0.34914	−1.292	0.112	7.126	1.392
3	0.00027	−0.20731	−0.19910	1.555	0.515	32.731	1.018
4	0.00013	−0.15830	0.03564	−1.430	1.195	75.873	1.123
5	0.00002	−0.10283	0.06289	1.421	2.115	134.288	1.158
6	−0.00001	−0.04532	0.07408	−1.356	3.351	212.777	1.299

$\Delta_T = 25, \Delta_P = 15, \Delta_B = 60m, \alpha_0 = 142.5, \alpha_0\mu_T = 300, \alpha_0\mu_P = 50, \alpha_0\mu_B = 100\ cm^2s^{-1}$

r	$a_{0,0,r}$	$a_{0,1,r}$	$a_{0,2,r}$	$f_{0,r}(1)$	$\alpha_0\lambda_{0,r}$	$\lambda_{0,r}$	$\Phi_{0,r}$
1	1.00000	0.75000	0.60000	1.000	0.000	0.000	0.999
2	0.00038	−0.24229	−0.32480	−0.956	0.084	5.910	1.863
3	0.00024	−0.21934	−0.13246	1.789	0.360	25.290	0.724
4	0.00006	−0.17305	0.08249	−2.271	0.972	68.246	0.471
5	−0.00000	−0.12084	0.12243	1.653	1.781	125.003	0.735
6	0.00001	−0.06971	0.05109	−1.635	2.761	193.793	0.841

$\Delta_T = 25, \Delta_P = 15, \Delta_B = 60m, \alpha_0 = 136.5, \alpha_0\mu_T = 300, \alpha_0\mu_P = 10, \alpha_0\mu_B = 100\ cm^2s^{-1}$

r	$a_{0,0,r}$	$a_{0,1,r}$	$a_{0,2,r}$	$f_{0,r}(1)$	$\alpha_0\lambda_{0,r}$	$\lambda_{0,r}$	$\Phi_{0,r}$
1	1.00000	0.75000	0.60000	1.000	0.000	0.000	0.999
2	0.00037	−0.24705	−0.29924	−0.598	0.029	2.153	2.283
3	0.00007	−0.22929	0.12340	3.150	0.241	17.684	0.243
4	0.00000	−0.20766	0.20625	−1.619	0.509	37.343	0.387
5	0.00013	−0.16587	−0.03345	5.338	1.074	78.685	0.091
6	0.00017	−0.12471	−0.12509	−1.637	1.712	125.488	0.338

$\Delta_T = 25, \Delta_P = 15m, \Delta_B = 60m, \alpha_0 = 697.5, \alpha_0\mu_T = 300, \alpha_0\mu_P = 150, \alpha_0\mu_B = 1000\ cm^2s^{-1}$

r	$a_{0,0,r}$	$a_{0,1,r}$	$a_{0,2,r}$	$f_{0,r}(1)$	$\alpha_0\lambda_{0,r}$	$\lambda_{0,r}$	$\Phi_{0,r}$
1	1.00000	0.75000	0.60000	1.000	0.000	0.000	0.999
2	0.00032	−0.22003	−0.25359	−0.527	0.354	5.080	3.061
3	0.00001	−0.09690	0.06819	1.052	2.226	31.916	1.709
4	−0.00002	−0.02344	0.05628	−0.600	3.952	56.661	3.187
5	0.00000	0.04808	−0.05376	0.567	7.786	111.633	2.924
6	−0.00002	0.04996	−0.02013	−1.300	11.557	165.700	1.281

$\Delta_T = 25, \Delta_P = 15, \Delta_B = 60m, \alpha_0 = 676.5, \alpha_0\mu_T = 300, \alpha_0\mu_P = 10, \alpha_0\mu_B = 1000\ cm^2s^{-1}$

r	$a_{0,0,r}$	$a_{0,1,r}$	$a_{0,2,r}$	$f_{0,r}(1)$	$\alpha_0\lambda_{0,r}$	$\lambda_{0,r}$	$\Phi_{0,r}$
1	1.00000	0.75000	0.60000	1.000	0.000	0.000	0.999
2	0.00036	−0.24674	−0.28725	−0.488	0.033	0.493	2.385
3	−0.00000	−0.21027	0.21141	0.479	0.481	7.113	0.552
4	0.00017	−0.12838	−0.12770	−0.815	1.664	24.611	0.418
5	0.00004	−0.07257	0.01064	3.808	2.716	40.150	0.178
6	−0.00000	−0.03123	0.03407	−0.417	3.725	55.075	1.950

Table A.3(d) Values of $a_{i,j,r}$, $f_{i,r}(1)$, α_i, $\lambda_{i,r}$ and $\Phi_{i,r}$ of the first six vertical modes computed using various eddy viscosity profiles

$\Delta_T = 25, \Delta_P = 10m, \alpha_1 \simeq 757.1\ \alpha_1\mu_T = 1000, \alpha_1\mu_P = 150, \alpha_1\mu_B = 100\ cm^2s^{-1}$

r	$a_{1,0,r}$	$a_{1,1,r}$	$a_{2,0,r}$	$f_{1,r}(1)$	$\alpha_1\lambda_{1,r}$	$\lambda_{1,r}$	$\Phi_{1,r}$
1	1.00000	0.28571	1.00000	1.000	0.000	0.000	0.999
2	0.00031	−0.46478	0.00000	−2.578	0.461	6.097	0.764
3	0.00000	−0.00654	0.00000	1.002	1.899	25.087	1.997
4	−0.00010	0.15412	0.00000	−2.567	4.155	54.881	0.769
5	−0.00000	0.00656	0.00000	1.009	7.597	100.342	1.989
6	0.00006	−0.09151	0.00000	−2.545	11.543	152.459	0.779

$\Delta_T = 25, \Delta_P = 10m, \alpha_1 \simeq 728.5, \alpha_1\mu_T = 1000, \alpha_1\mu_P = 50, \alpha_1\mu_B = 100\ cm^2s^{-1}$

r	$a_{1,0,r}$	$a_{1,1,r}$	$a_{2,0,r}$	$f_{1,r}(1)$	$\alpha_1\lambda_{1,r}$	$\lambda_{1,r}$	$\Phi_{1,r}$
1	1.00000	0.28571	1.00000	1.000	0.000	0.000	0.999
2	0.00041	−0.60814	0.00000	−3.717	0.182	2.502	0.428
3	0.00012	−0.17707	0.00000	2.857	1.204	16.534	0.656
4	−0.00001	0.02443	0.00000	−1.112	2.074	28.470	1.872
5	−0.00010	0.15473	0.00000	4.300	3.844	52.769	0.333
6	−0.00003	0.04771	0.00000	−1.978	6.774	92.988	1.090

$\Delta_T = 25, \Delta_P = 10m, \alpha_1 \simeq 717.1, \alpha_1\mu_T = 1000, \alpha_1\mu_P = 10, \alpha_1\mu_B = 100\ cm^2s^{-1}$

r	$a_{1,0,r}$	$a_{1,1,r}$	$a_{2,0,r}$	$f_{1,r}(1)$	$\alpha_1\lambda_{1,r}$	$\lambda_{1,r}$	$\Phi_{1,r}$
1	1.00000	0.28571	1.00000	1.000	0.000	0.000	0.999
2	0.00047	−0.69049	0.00000	−4.394	0.038	0.540	0.320
3	0.00038	−0.55710	0.00000	9.282	0.277	3.863	0.078
4	0.00023	−0.33855	0.00000	−9.270	0.748	10.443	0.079
5	0.00007	−0.11332	0.00000	4.369	1.427	19.906	0.324
6	−0.00000	−0.00000	0.00000	−1.000	1.934	26.974	1.999

$\Delta_T = 25, \Delta_P = 10m, \alpha_1 = 110.0, \alpha_1\mu_T = 150, \alpha_1\mu_P = 10, \alpha_1\mu_B = 100\ cm^2s^{-1}$

r	$a_{1,0,r}$	$a_{1,1,r}$	$a_{2,0,r}$	$f_{1,r}(1)$	$\alpha_1\lambda_{1,r}$	$\lambda_{1,r}$	$\Phi_{1,r}$
1	1.00000	0.28571	1.00000	1.000	0.000	0.000	0.999
2	0.00039	−0.57854	0.00000	−3.477	0.035	3.228	0.479
3	0.00007	−0.10975	0.00000	1.850	0.216	19.650	1.181
4	−0.00004	0.06560	0.00000	−1.556	0.353	32.104	1.421
5	−0.00009	0.13558	0.00000	3.701	0.740	67.327	0.432
6	−0.00000	0.00660	0.00000	−1.022	1.139	103.588	1.974

$\Delta_T = 25, \Delta_P = 10m, \alpha_1 = 121.4, \alpha_1\mu_T = 150, \alpha_1\mu_P = 50, \alpha_1\mu_B = 100\ cm^2s^{-1}$

r	$a_{1,0,r}$	$a_{1,1,r}$	$a_{2,0,r}$	$f_{1,r}(1)$	$\alpha_1\lambda_{1,r}$	$\lambda_{1,r}$	$\Phi_{1,r}$
1	1.00000	0.28571	1.00000	1.000	0.000	0.000	0.999
2	0.00023	−0.34153	0.00000	−1.651	0.111	9.161	1.338
3	−0.00005	0.08301	0.00000	1.159	0.374	30.852	1.820
4	−0.00004	0.06606	0.00000	−1.248	0.963	79.349	1.723
5	0.00005	−0.08311	0.00000	1.562	1.566	128.984	1.415
6	0.00000	−0.00780	0.00000	−1.010	2.555	210.425	1.987

Table A.3(e) Values of $a_{i,j,r}$, $f_{i,r}(1)$, α_i, $\lambda_{i,r}$ and $\Phi_{i,r}$ of the first six vertical modes computed using various eddy viscosity profiles

$\Delta_T = 25, \Delta_P = 40m, \alpha_1 \simeq 476.9, \alpha_1\mu_T = 1000, \alpha_1\mu_P = 150, \alpha_1\mu_B = 100\ cm^2s^{-1}$

r	$a_{1,0,r}$	$a_{1,1,r}$	$a_{2,0,r}$	$f_{1,r}(1)$	$\alpha_1\lambda_{1,r}$	$\lambda_{1,r}$	$\Phi_{1,r}$
1	1.00000	0.61538	1.00000	1.000	0.000	0.000	0.999
2	0.00025	−0.36704	0.00000	−1.553	0.185	3.883	1.068
3	0.00020	−0.30126	0.00000	2.415	0.939	19.709	0.502
4	0.00013	−0.19602	0.00000	−2.481	2.369	49.686	0.478
5	0.00005	−0.08598	0.00000	1.679	4.353	91.291	0.942
6	0.00000	−0.00767	0.00000	−1.010	6.419	134.464	1.973

$\Delta_T = 25, \Delta_P = 40m, \alpha_1 \simeq 415.3, \alpha_1\mu_T = 1000, \alpha_1\mu_P = 50, \alpha_1\mu_B = 100\ cm^2s^{-1}$

r	$a_{1,0,r}$	$a_{1,1,r}$	$a_{2,0,r}$	$f_{1,r}(1)$	$\alpha_1\lambda_{1,r}$	$\lambda_{1,r}$	$\Phi_{1,r}$
1	1.00000	0.61538	1.00000	1.000	0.000	0.000	0.999
2	0.00025	−0.37839	0.00000	−1.649	0.063	1.521	0.971
3	0.00024	−0.35412	0.00000	2.964	0.326	7.867	0.345
4	0.00021	−0.30975	0.00000	−4.033	0.837	20.164	0.192
5	0.00017	−0.24977	0.00000	4.466	1.598	38.492	0.157
6	0.00012	−0.18091	0.00000	−4.146	2.605	62.718	0.182

$\Delta_T = 25, \Delta_P = 40m, \alpha_1 \simeq 390.7, \alpha_1\mu_T = 1000, \alpha_1\mu_P = 10, \alpha_1\mu_B = 100\ cm^2s^{-1}$

r	$a_{1,0,r}$	$a_{1,1,r}$	$a_{2,0,r}$	$f_{1,r}(1)$	$\alpha_1\lambda_{1,r}$	$\lambda_{1,r}$	$\Phi_{1,r}$
1	1.00000	0.61544	1.00000	1.000	0.000	0.000	0.999
2	0.00025	−0.38315	0.00000	−1.689	0.012	0.326	0.933
3	0.00025	−0.37809	0.00000	3.224	0.066	1.698	0.294
4	0.00025	−0.36839	0.00000	−4.891	0.170	4.363	0.132
5	0.00024	−0.35416	0.00000	6.445	0.326	8.351	0.077
6	0.00022	−0.33570	0.00000	−7.785	0.534	13.666	0.053

$\Delta_T = 25, \Delta_P = 40m, \alpha_1 \simeq 88.4, \alpha_1\mu_T = 150, \alpha_1\mu_P = 50, \alpha_1\mu_B = 100\ cm^2s^{-1}$

r	$a_{1,0,r}$	$a_{1,1,r}$	$a_{2,0,r}$	$f_{1,r}(1)$	$\alpha_1\lambda_{1,r}$	$\lambda_{1,r}$	$\Phi_{1,r}$
1	1.00000	0.61538	1.00000	1.000	0.000	0.000	0.999
2	0.00023	−0.34813	0.00000	−1.397	0.059	6.672	1.259
3	0.00015	−0.22772	0.00000	1.724	0.285	32.278	0.902
4	0.00005	−0.08089	0.00000	−1.258	0.669	75.711	1.470
5	−0.00001	0.01861	0.00000	1.025	1.105	124.995	1.938
6	−0.00005	0.07690	0.00000	−1.532	1.709	193.202	1.092

$\Delta_T = 25, \Delta_P = 40m, \alpha_1 \simeq 63.8, \alpha_1\mu_T = 150, \alpha_1\mu_P = 10, \alpha_1\mu_B = 100\ cm^2s^{-1}$

r	$a_{1,0,r}$	$a_{1,1,r}$	$a_{2,0,r}$	$f_{1,r}(1)$	$\alpha_1\lambda_{1,r}$	$\lambda_{1,r}$	$\Phi_{1,r}$
1	1.00000	0.61538	1.00000	1.000	0.000	0.000	0.999
2	0.00025	−0.37644	0.00000	−1.632	0.012	1.971	0.987
3	0.00023	−0.34462	0.00000	2.863	0.064	10.170	0.368
4	0.00019	−0.28766	−0.00000	−3.719	0.166	26.023	0.224
5	0.00014	−0.21344	0.00000	3.801	0.316	49.554	0.215
6	0.00009	−0.13314	0.00000	−3.078	0.512	80.301	0.321

Table A.3(*f*) Values of $a_{i,j,r}$, $f_{i,r}(1)$, α_i, $\lambda_{i,r}$ and $\Phi_{i,r}$ of the first six vertical modes computed using various eddy viscosity profiles

$\Delta_T = 25, \Delta_P = 15m, \alpha_1 \simeq 243.7, \alpha_1\mu_T = 300, \alpha_1\mu_P = 150, \alpha_1\mu_B = 150\ cm^2s^{-1}$

r	$a_{1,0,r}$	$a_{1,1,r}$	$a_{2,0,r}$	$f_{1,r}(1)$	$\alpha_1\lambda_{1,r}$	$\lambda_{1,r}$	$\Phi_{1,r}$
1	1.00000	0.37500	1.00000	1.000	0.000	0.000	0.999
2	0.00024	−0.35818	0.00000	−1.405	0.228	9.358	1.464
3	−0.00002	0.03924	0.00000	1.021	0.863	35.442	1.966
4	−0.00007	0.10881	0.00000	−1.344	2.048	84.022	1.534
5	0.00002	−0.03923	0.00000	1.085	3.467	142.239	1.874
6	0.00003	−0.05403	0.00000	−1.245	5.663	232.342	1.657

$\Delta_T = 25, \Delta_P = 15m, \alpha_0 \simeq 206.2, \alpha_1\mu_T = 300, \alpha_1\mu_P = 50, \alpha_1\mu_P = 100\ cm^2s^{-1}$

r	$a_{1,0,r}$	$a_{1,1,r}$	$a_{2,0,r}$	$f_{1,r}(1)$	$\alpha_1\lambda_{1,r}$	$\lambda_{1,r}$	$\Phi_{1,r}$
1	1.00000	0.37500	1.00000	1.000	0.000	0.000	0.999
2	0.00033	−0.48901	0.00000	−2.296	0.107	5.200	0.768
3	0.00006	−0.09604	0.00000	1.366	0.564	27.376	1.508
4	−0.00005	−0.08236	0.00000	−1.467	1.019	49.408	1.395
5	−0.00007	−0.10615	0.00000	2.212	2.076	100.665	0.812
6	0.00000	−0.00480	0.00000	−1.006	3.079	149.292	1.990

$\Delta_T = 25, \Delta_P = 15m, \alpha_1 \simeq 191.2, \alpha_1\mu_T = 300, \alpha_1\mu_P = 10, \alpha_1\mu_B = 100\ cm^2s^{-1}$

r	$a_{1,0,r}$	$a_{1,1,r}$	$a_{2,0,r}$	$f_{1,r}(1)$	$\alpha_1\lambda_{1,r}$	$\lambda_{1,r}$	$\Phi_{1,r}$
1	1.00000	0.37500	1.00000	1.000	0.000	0.000	0.999
2	0.00039	−0.59202	0.00000	−3.044	0.024	1.275	0.487
3	0.00029	−0.42968	0.00000	5.429	0.159	8.343	0.171
4	0.00013	−0.19248	0.00000	−4.002	0.419	21.937	0.301
5	0.00001	−0.02243	0.00000	1.158	0.706	36.926	1.772
6	−0.00004	0.06089	0.00000	−2.087	0.934	48.874	0.884

$\Delta_T = 60, \Delta_P = 10m, \alpha_1 \simeq 858.5, \alpha_1\mu_T = 1000, \alpha_1\mu_P = 10, \alpha_1\mu_B = 100\ cm^2s^{-1}$

r	$a_{1,0,r}$	$a_{1,1,r}$	$a_{2,0,r}$	$f_{1,r}(1)$	$\alpha_1\lambda_{1,r}$	$\lambda_{1,r}$	$\Phi_{1,r}$
1	1.00000	0.14286	1.00000	1.000	0.000	0.000	0.999
2	0.00049	−0.72509	0.00000	−8.335	0.131	1.532	0.185
3	−0.00009	−0.13453	0.00000	4.335	0.994	11.583	0.564
4	−0.00002	0.03021	0.00000	−1.521	1.443	16.814	1.683
5	−0.00012	0.18164	0.00000	9.992	3.026	35.252	0.132
6	−0.00001	0.01580	0.00000	−1.504	5.180	60.333	1.693

$\Delta_T = 60, \Delta_P = 40m, \alpha_1 = 60.4, \alpha_1\mu_T = 1000, \alpha_1\mu_P = 10, \alpha_1\mu_B = 100\ cm^2s^{-1}$

r	$a_{1,0,r}$	$a_{1,1,r}$	$a_{2,0,r}$	$f_{1,r}(1)$	$\alpha_1\lambda_{1,r}$	$\lambda_{1,r}$	$\Phi_{1,r}$
1	1.00000	0.40000	1.00000	1.000	0.000	0.000	0.999
2	0.00037	−0.59153	0.00000	−2.969	0.022	0.373	0.484
3	0.00037	−0.54857	0.00000	6.661	0.145	2.410	0.108
4	0.00031	−0.46891	0.00000	−9.264	0.389	6.451	0.057
5	0.00024	−0.36262	0.00000	9.963	0.754	12.497	0.049
6	0.00016	−0.24333	0.00000	−8.579	1.239	20.513	0.066

APPENDIX IV

A transient solution for the wind drift current in a two-layered open sea region induced by a step-function wind stress (4.3.4) is derived using the Laplace transform. A linear slip condition (4.3.31) is enforced at the lower domain boundary.

Transforming equation (4.3.28) with respect to the Laplace transform, gives

$$sw_{i,j} + \iota\gamma w_{i,j} = \frac{\alpha_i \mu_{i,j}}{H_i^2} \frac{\partial^2 w_{i,j}}{\partial \sigma_i^2}, \tag{A.4.1}$$

where

$$w_{i,j}(s) = \int_0^\infty e^{-st}\, \varpi_{i,j}(t)\, dt, \quad t > 0 \quad \text{and} \quad i = 0, 1,\ j = 1, 2. \tag{A.4.2}$$

Hereafter, $i = 1$ is used, for convenience.

The boundary and interfacial conditions at the transformed domain take the form:

$$\frac{\alpha_1 \mu_{1,1}}{H_1} \frac{\partial w_{1,1}}{\partial \sigma_1} = -\frac{\tau_{sx}}{\rho_{1,1} s} \qquad \text{at} \quad \sigma_1 = 0, \tag{A.4.3}$$

$$\left.\begin{aligned} w_{1,1} &= w_{1,2} \\ \rho_{1,1}\mu_{1,1} \frac{\partial w_{1,1}}{\partial \sigma_1} &= \rho_{1,2}\mu_{1,2} \frac{\partial w_{1,2}}{\partial \sigma_1} \end{aligned}\right\} \qquad \text{at} \quad \sigma_1 = \xi_{1,1}, \tag{A.4.4}$$

$$\frac{\alpha_1 \mu_{1,2}}{H_1} \frac{\partial w_{1,2}}{\partial \sigma_1} = -k_b w_{1,2} \qquad \text{at} \quad \sigma_1 = 1. \tag{A.4.5}$$

For convenience, we rewrite equation (A.4.1) as follows:

$$\frac{\partial^2 w_{1,1}}{\partial \sigma_1} = \kappa^2 w_{1,1}, \tag{A.4.6}$$

$$\frac{\partial^2 w_{1,2}}{\partial \sigma_1} = \upsilon^2 \kappa^2 w_{1,2}, \tag{A.4.7}$$

where

$$\kappa^2 = (\iota\gamma + s) H_1^2 / (\alpha_1 \mu_{1,1}), \tag{A.4.8}$$

$$\upsilon^2 = \mu_{1,1} / \mu_{1,2}. \tag{A.4.9}$$

Solutions of (A.4.6) and (A.4.7) may be readily written in the form

$$w_{1,1} = ae^{\kappa\sigma_1} + be^{-\kappa\sigma_1}, \tag{A.4.10}$$

$$w_{1,2} = c\Big(\cosh \upsilon\kappa(\sigma_1 - 1) + \overline{k}_b(\upsilon\kappa)^{-1}\sinh \upsilon\kappa(\sigma_1 - 1)\Big), \tag{A.4.11}$$

where a, b and c are to be determined and

$$\overline{k}_b = -k_b H_1/(\alpha_1 \mu_{1,2}). \tag{A.4.12}$$

Using conditions (A.4.3) to (A.4.5), we obtain

$$w_{1,1} = \frac{\tau_1 H_1}{\alpha_1 \mu_T}\left(\frac{K_1 \cosh \kappa(\sigma_1 - \xi_T) - R_1 K_2 \sinh \kappa(\sigma_1 - \xi_T)}{s\kappa K_3}\right), \tag{A.4.13}$$

$$w_{1,2} = \frac{\tau_1 H_1}{\alpha_1 \mu_T}\left(\frac{\cosh \upsilon\kappa(\sigma_1 - 1) + \overline{k}_b(\upsilon\kappa)^{-1}\sinh \upsilon\kappa(\sigma_1 - 1)}{s\kappa K_3}\right), \tag{A.4.14}$$

where

$$\tau_1 = \frac{\tau_{sx}}{\rho_T}, \tag{A.4.15}$$

$$K_1 = \cosh \upsilon\kappa\xi_P - \overline{k}_b(\upsilon\kappa)^{-1}\sinh \upsilon\kappa\xi_P, \tag{A.4.16}$$

$$K_2 = \sinh \upsilon\kappa\xi_P - \overline{k}_b(\upsilon\kappa)^{-1}\cosh \upsilon\kappa\xi_P, \tag{A.4.17}$$

$$J_3 = \sinh \kappa\xi_T\big(\cosh \upsilon\kappa\xi_P - \overline{k}_b(\upsilon\kappa)^{-1}\sinh \upsilon\kappa\xi_P\big) \tag{A.4.18}$$

$$+R_1 \cosh \kappa\xi_T\big(\sinh \upsilon\kappa\xi_P - \overline{k}_b(\upsilon\kappa)^{-1}\cosh \upsilon\kappa\xi_P\big), \tag{A.4.19}$$

$$R_1 = \upsilon(\rho_P\mu_P)(\rho_T\mu_T)^{-1}, \tag{A.4.20}$$

$$\xi_T = \xi_{1,1}, \quad \xi_P = 1 - \xi_{1,1}, \tag{A.4.21}$$

$$\mu_T = \mu_{1,1}, \quad \mu_P = \mu_{1,2}, \tag{A.4.22}$$

$$\rho_T = \rho_{1,1}, \quad \rho_P = \rho_{1,2}. \tag{A.4.23}$$

The solutions in the physical domain can be obtained using the Residue theorem. Simple poles are found at the origin and at the zeros of the term K_3.

With non-zero friction ($k_b \neq 0$):

The solutions in the physical domain are composed of two parts, steady state and transient solutions, namely

$$\varpi_{1,1}(t) = \varpi_{1,1}^{(s)} + \varpi_{1,1}^{(t)}(t), \tag{A.4.24}$$

$$\varpi_{1,2}(t) = \varpi_{1,2}^{(s)} + \varpi_{1,2}^{(t)}(t), \tag{A.4.25}$$

where

$$\varpi_{1,1}^{(s)} = \frac{\tau_1 H_1}{\alpha_1 \mu_{_T}} \frac{J_{1,0}}{\kappa_0 J_{3,0}}, \qquad \varpi_{1,1}^{(t)}(t) = \sum_{r=1}^{\infty} e^{s_r t} \frac{2\tau_1}{H_1} \frac{J_{1,r}}{s_r J_{3,r}}, \tag{A.4.26}$$

$$\varpi_{1,2}^{(s)} = \frac{\tau_1 H_1}{\alpha_1 \mu_{_T}} \frac{J_{2,0}}{\kappa_0 J_{3,0}}, \qquad \varpi_{1,2}^{(t)}(t) = \sum_{r=1}^{\infty} e^{s_r t} \frac{2\tau_1}{H_1} \frac{J_{2,r}}{s_r J_{3,r}}, \tag{A.4.27}$$

and

$$\begin{aligned} J_{1,0} = \quad & \cosh \kappa_0(\sigma_1 - \xi_{_T})\big(\cosh \upsilon\kappa_0\xi_{_P} - \overline{k}_b(\upsilon\kappa_0)^{-1}\sinh \upsilon\kappa_0\xi_{_P}\big) \\ & -R_1 \sinh \kappa_0(\sigma_1 - \xi_{_T})\big(\sinh \upsilon\kappa_0\xi_{_P} - \overline{k}_b(\upsilon\kappa_0)^{-1}\cosh \upsilon\kappa_0\xi_{_P}\big), \end{aligned} \tag{A.4.28}$$

$$J_{2,0} = \quad \cosh \upsilon\kappa_0(\sigma_1 - 1) + \overline{k}_b(\upsilon\kappa_0)^{-1}\sinh \upsilon\kappa_0(\sigma_1 - 1), \tag{A.4.29}$$

$$\begin{aligned} J_{3,0} = \quad & \sinh \kappa_0\xi_{_T}\big(\cosh \upsilon\kappa_0\xi_{_P} - \overline{k}_b(\upsilon\kappa_0)^{-1}\sinh \upsilon\kappa_0\xi_{_P}\big) \\ & +R_1 \cosh \kappa_0\xi_{_T}\big(\sinh \upsilon\kappa_0\xi_{_P} - \overline{k}_b(\upsilon\kappa_0)^{-1}\cosh \upsilon\kappa_0\xi_{_P}\big), \end{aligned} \tag{A.4.30}$$

$$\begin{aligned} J_{1,r} = \quad & \cosh \kappa_r(\sigma_1 - \xi_{_T})\big(\cosh \upsilon\kappa_r\xi_{_P} - \overline{k}_b(\upsilon\kappa_r)^{-1}\sinh \upsilon\kappa_r\xi_{_P}\big) \\ & -R_1 \sinh \kappa_r(\sigma_1 - \xi_{_T})\big(\sinh \upsilon\kappa_r\xi_{_P} - \overline{k}_b(\upsilon\kappa_r)^{-1}\cosh \upsilon\kappa_r\xi_{_P}\big), \end{aligned} \tag{A.4.31}$$

$$J_{2,r} = \quad \cosh \upsilon\kappa_r(\sigma_1 - 1) + \overline{k}_b(\upsilon\kappa_r)^{-1}\sinh \upsilon\kappa_r(\sigma_1 - 1), \tag{A.4.32}$$

$$\begin{aligned} J_{3,r} = \; & \xi_{_T}\cosh \kappa_r\xi_{_T}\cosh \upsilon\kappa_r\xi_{_P} + \upsilon\xi_{_P}\sinh \kappa_r\xi_{_T}\sinh \upsilon\kappa_r\xi_{_P} \\ & -\frac{\overline{k}_b}{\upsilon\kappa_r}\big(\xi_{_T}\cosh \kappa_r\xi_{_T}\sinh \upsilon\kappa_r\xi_{_P} + \upsilon\xi_{_P}\sinh \kappa_r\xi_{_T}\cosh \upsilon\kappa_r\xi_{_P}\big) \\ & + R_1\big(\xi_{_T}\sinh \kappa_r\xi_{_T}\sinh \upsilon\kappa_r\xi_{_P} + \upsilon\xi_{_P}\cosh \kappa_r\xi_{_T}\cosh \upsilon\kappa_r\xi_{_P}\big) \\ & -R_1\frac{\overline{k}_b}{\upsilon\kappa_r}\big(\xi_{_T}\sinh \kappa_r\xi_{_T}\cosh \upsilon\kappa_r\xi_{_P} + \upsilon\xi_{_P}\cosh \kappa_r\xi_{_T}\sinh \upsilon\kappa_r\xi_{_P}\big) \\ & +\frac{\overline{k}_b}{\upsilon\kappa_r^2}\big(\sinh \kappa_r\xi_{_T}\sinh \upsilon\kappa_r\xi_{_P} + R_1\cosh \kappa_r\xi_{_T}\cosh \upsilon\kappa_r\xi_{_P}\big) \qquad r \geq 1, \end{aligned} \tag{A.4.33}$$

and

$$\kappa_0 = H_1(\iota\gamma/\alpha_1\mu_{_T})^{1/2}, \tag{A.4.34}$$

$$\kappa_r = \iota y_r, \quad s_r = -\iota\gamma - y_r^2\alpha_1\mu_{_T}/H_1^2, \quad r \geq 1. \tag{A.4.35}$$

The values of y_r follow from the equation

$$\begin{aligned}&\tan(y_r\xi_{_T})\big[\cos(\upsilon y_r\xi_{_P}) - \overline{k}_b(\upsilon y_r)^{-1}\sin(\upsilon y_r\xi_{_P})\big]\\ &+ R_1\big[\sin(\upsilon y_r\xi_{_P}) + \overline{k}_b(\upsilon y_r)^{-1}\cos(\upsilon y_r\xi_{_P})\big] = 0.\end{aligned} \tag{A.4.36}$$

With a zero-stress condition ($k_b = 0$):

Substituting $\overline{\kappa}_b = 0$ into (A.4.13) and (A.4.14) gives

$$\hat{w}_{1,1} = \frac{\tau_1 H_1}{\alpha_1\mu_{_T}}\frac{\cosh\upsilon\kappa\xi_{_P}\cosh\kappa(\sigma_1 - \xi_{_T}) - R_1\sinh\upsilon\kappa\xi_{_P}\sinh\kappa(\sigma_1 - \xi_{_T})}{ksK_4}, \tag{A.4.37}$$

$$\hat{w}_{1,2} = \frac{\tau_1 H_1}{\alpha_1\mu_{_T}}\frac{\cosh\upsilon\kappa(\sigma_1 - 1)}{s\kappa K_4}, \tag{A.4.38}$$

where

$$K_4 = \sinh\kappa\xi_{_T}\cosh\upsilon\kappa\xi_{_P} + R_1\cosh\kappa\xi_{_T}\sinh\upsilon\kappa\xi_{_P}. \tag{A.4.39}$$

By expanding the solution (A.4.37) into partial fractions, and writing the hyperbolic functions as the power series

$$\sinh\{rq^{1/2}\} = rq^{1/2}(1 + 1/3!\,r^2q + \cdots), \tag{A.4.40}$$

$$\cosh\{rq^{1/2}\} = (1 + 1/2!\,r^2q + r^4/4!q^2 + \cdots), \tag{A.4.41}$$

we can see that $s = -\iota\gamma$ is a simple pole. The other poles are all simple and are found at the origin and at the points where K_4 vanishes.

The solutions in the physical domain can be written as

$$\varpi_{1,j}(t) = \varpi_{1,j}^{(s)} + \varpi_{1,j}^{(t)}(t) + \varpi_{1,j}^{(a)}(t) \qquad j = 1, 2, \tag{A.4.42}$$

where

$$w_{1,1}^{(s)} = \sum_{r=1}^{\infty} \frac{\tau_1 H_1}{\alpha_1 \mu_T} \frac{J_{1,0}}{\kappa_0 J_{3,0}}, \tag{A.4.43}$$

$$w_{1,1}^{(t)}(t) = \sum_{r=1}^{\infty} e^{s_r t} \frac{2\tau_1}{H_1} \frac{J_{1,r}}{s_r J_{3,r}}, \tag{A.4.44}$$

$$w_{1,1}^{(a)}(t) = e^{-\iota\gamma t} \frac{\iota\tau_1}{H_1 \gamma} \left[(\xi_T + (\rho_P/\rho_T)\xi_P \right]^{-1}, \tag{A.4.45}$$

$$w_{1,2}^{(s)} = \sum_{r=1}^{\infty} \frac{\tau_1 H_1}{\alpha_1 \mu_T} \frac{J_{2,0}}{k_0 J_{3,0}}, \tag{A.4.46}$$

$$w_{1,2}^{(t)}(t) = \sum_{r=1}^{\infty} e^{s_r t} \frac{2\tau_1}{H_1} \frac{J_{2,r}}{s_r J_{3,r}}, \tag{A.4.47}$$

$$w_{1,2}^{(a)}(t) = w_{1,1}^{(a)}(t). \tag{A.4.48}$$

Here, k_r and s_r are given by equations (A.4.34) and (A.4.35), respectively, and $J_{\ell,r}$, $r \geq 0$, $\ell = 1, 2, 3$, can be found from equations (A.4.28) to (A.4.34) by setting $\overline{k}_b = 0$.